Spectroscopie Laser avec des cavités résonantes de haute finesse couplées à un peigne de fréquences : ML-CEAS et vernier effet techniques. Applications à la mesure in situ de molécules réactives dans les domaines UV et visible.

Chadi Abd Alrahman Abd Alrahman

UNIVERSITÉ DE GRENOBLE

THÈSE

Pour obtenir le grade de

DOCTEUR DE L'UNIVERSITÉ DE GRENOBLE

Spécialité : PHYSIQUE APPLIQUEE

Arrêté ministériel : 7 août 2006

Présentée par

« ABD ALRAHMAN CHADI »

Thèse dirigée par **«** M. Daniele Romanini**»** préparée au sein du **Laboratoire Interdisciplinaire de Physique (LIPHY),** dans **l'École Doctorale de physique**

Titre de la thèse

Spectroscopie Laser avec des cavités résonantes de haute finesse couplées à un peigne de fréquences : ML-CEAS et effet Vernier. Applications à la mesure in situ de molécules réactives dans les domaines UV et visible.

Thèse soutenue publiquement le **«** 25 Octobre 2012**»**, devant le jury composé de :

M. Marco Prevedelli (Rapporteur)
Professeur, Dipartimento di Fisica, Bologna (Italie)
M. Alfonso Saiz-Lopez (Rapporteur)
Professeur, Laboratory of Atmospheric and Climate Science, Espagne
M. Marco Marangoni (Membre)
Professeur, Physics Department Politecnico di Milano, Italie
M. Erik Kerstel (Président)
Professeur, Laboratoire Interdisciplinaire de Physique
M. Jérôme Morville (Membre)
Maitre de conférences, Laboratoire de Spectrométrie Ionique et Moléculaire, Université Claude Bernard Lyon1
M. Guillaume Méjean (Membre)
Maitre de conférences, Laboratoire Interdisciplinaire de Physique

Abstract

The atmospheric chemistry community suffers a lack of fast, reliable and space resolved measurements for a wide set of reactive molecules (e.g. radicals such as OH, NO_3, BrO, IO, etc). Due to their high reactivity, these molecules largely control the lifetime and concentration of numerous key atmospheric species, and may have an important impact on the climate. The concentrations of such radicals are extremely low (ppbv or less) and highly variable in time and space, which imposes a real challenge during the detection.

In the first part of this thesis, a compact, robust and transportable UV spectrometer is developed, exploiting the Mode-Locked Cavity Enhanced Absorption Spectroscopy (ML-CEAS) technique to measure pptv and sub-pptv levels of atmospherically important reactive molecules, in particular, halogen oxide radicals, to respond to the emerging needs. The ML-CEAS technique is based on coupling a Mode-Locked femtosecond laser to a high finesse optical cavity, which acts as a photon trap to increase the interaction between the light and the intracavity gas sample, which highly enhances the absorption sensitivity. The detection limit obtained for the IO radical is 20 ppqv (part per quadrillion), which is an impressive result.

In the second part of this thesis, a new spectroscopic technique is developed, called Vernier effect, which is also based on the interaction between a mode-locked femtosecond laser with a high finesse optical cavity. This technique provides detection sensitivity similar to that of ML-CEAS technique, but the advantage is that the number of the spectral elements is given by the cavity finesse, so it can reach ten thousands, as well as this technique has a simple setup, where the spectrograph is replaced by a photodiode. Additionally, the time required to measure one output absorption spectrum can be less than 1 ms.

Résumé

La communauté de la chimie atmosphérique souffre d'un manque de mesures rapides, fiables résolues spatialement et temporellement pour un large éventail de molécules réactives (radicaux tels que NO_2, OH, BrO, IO, etc). En raison de leur forte réactivité, ces molécules contrôlent largement la durée de vie et la concentration de nombreuses espèces clés dans l'atmosphère, et peuvent avoir un impact important sur le climat. Les concentrations de ces radicaux sont extrêmement faibles (ppbv ou moins) et très variable dans le temps et dans l'espace, ce qui impose un véritable défi lors de la détection.

Dans la première partie de ma thèse, un spectromètre UV robuste, compacte et transportable est développé, exploitant la technique ML-CEAS (Mode-Locked Cavity Enhanced Absorption Spectroscopy) pour mesurer à des niveaux très faibles (pptv et même en dessous) des molécules réactives d'importance atmosphérique, en particulier, les radicaux d'oxyde d'halogènes, afin de répondre aux besoins émergents. La technique ML-CEAS est basée sur le couplage d'un laser femtoseconde à blocage de modes à une cavité optique de haute finesse, qui agit comme un piège à photons pour augmenter l'interaction entre la lumière et l'échantillon de gaz intracavité. Cela permet d'améliorer fortement la sensibilité d'absorption. La limite de détection obtenue pour le radical IO est de 20 ppqv pour un temps d'acquisition de 5 minutes, ce qui est un résultat impressionnant.

Dans la deuxième partie de ma thèse, une nouvelle technique spectroscopique est développée appelée effet Vernier, qui est également basé sur l'interaction entre un laser femtoseconde à blocage de mode et une cavité optique de haute finesse. Ici, on utilise les battements. Cette technique fournit une sensibilité de détection similaire à la technique ML-CEAS, mais l'avantage est que le nombre des éléments spectraux est donné par la finesse de la cavité optique et donc peut atteindre plusieurs dizaines de milliers. De plus, cette configuration simplifie le montage expérimental par la suppression du spectrographe qui est remplacé par une simple photodiode. Le temps d'acquisition d'un spectre peut être aussi réduit à moins d' 1 ms.

Acknowledgements

First, I must thank Prof. Daniele romanini, not only for his continued guidance as my PhD supervisor, but also for all the opportunities he has encouraged me to embrace, and for being an inspiring role model, mentor and friend.

I would also like to thank Guillaume méjean for his participation in the supervision of this thesis. I am really grateful for accompanying me on this journey, for the many valuable discussions, for making everything a little more fun, for correcting the manuscript of my thesis. Thanks also to Roberto grilli for teaching me most of things I needed to know to build the experimental setup for the ML-CEAS technique, and so much more. I appreciate his effort, and his extensive experience.

I would like to thank all the LAME group members who have contributed to the work presented in this thesis, especially Samir Kassi for sharing his experience in lasers and instrumentation, and his wealth in computer programming. I am really thankful to Prof. Erik kerstel for his very instructive courses in Optical spectroscopy and Experimental methods in atmospheric monitoring. Special thanks go to Irène ventrillard for receiving me in her office and for her comradeship. I valorize the friendly and open atmosphere in LAME group at LIPHY. I was always welcome to ask questions to any of their members and discuss all the ideas flashing in my mind.

I thank very much Hugues guillet de chatellus from OPTIMA group at LIPHY, for his fruitful discussions and for advising me during this thesis.

Thanks to all the technical staffs who had helped me along the way, notably, Jean-Luc MARTIN for his help in electronics, and BEGUIER Serge for his help in programming and using a set of important programs, and all the workers in the mechanical workshop.

I am particularly grateful to Prof. Jacques derouard, the director of LIPHY laboratory, who helped me to easily pass the administration issues.

This work has been financed by Région Rhône-Alpes, I am thankful for this important establishment which gave me the chance to do this thesis.

Great thanks to my family. My parents, you are truly special people. Thank you so much for your endless support, I am so lucky to have you.

And finally my darling wife, I cannot forget you, huge thanks for your love, for your invaluable help.

October 2012

ABD ALRAHMAN Chadi

Introduction

The atmospheric chemistry community suffers a lack of fast, reliable and space resolved measurements for a wide set of reactive molecules (e.g. radicals such as OH, NO_3, BrO, IO, etc). Due to their high reactivity, these molecules largely control the lifetime and concentration of numerous key atmospheric species, and may have an important impact on the climate. The concentrations of such radicals are generally extremely low (ppbv or less) and highly variable in time and space. Measuring their concentration is often extremely laborious, expensive and requires heavy equipment (chemical sampling and treatment followed by mass spectrometry [1] and/or chromatography [2]). Despite the progress in the techniques of laser spectroscopy, monitoring such radicals precisely and in real time is still difficult or impossible by using traditional spectroscopic tools. This challenge motivates the development of new versatile and sensitive optical spectroscopic systems.

In 2002, the LAME research group (LAsers, Molécules et Environnement, at the Laboratoire Interdisciplinaire de Physique, LIPhy, in Grenoble) where this thesis took place, introduced the optical spectroscopy technique "Mode-Locked Cavity-Enhanced Absorption Spectroscopy, ML-CEAS" [3] which turned out to be a promising tool for sounding atmospheric radicals. The LAME research group has indeed a long-standing experience in the development of ultrasensitive spectroscopic techniques, in particular using high finesse (HF) optical cavities coupled with different types of laser sources. While a HF cavity acts as a photon trap capable of greatly enhancing the interaction of light with a gas sample, the laser source defines specific spectral properties and spectral coverage. The ML-CEAS technique is based on the interaction of a ML femtosecond (fs) laser emitting a comb of frequencies over a wide (and usually adjustable) spectral range, with the comb of resonances of a HF optical cavity. At the initial stage, a few demonstrations of possible applications [4] were obtained in the laboratory; however it did not seem reasonable at the time to think of field measurements because the laser source was too complex and sensitive to the environment, needing frequent optimizations. After that, given many flourishing domains of applications (Nobel Prize in Physics 2005 is awarded to John L. Hall and Theodor W. Hänsch, for their contributions to the development of laser-based precision spectroscopy, including the optical frequency comb technique), ML titanium-doped sapphire laser (Ti:Sa) sources were strongly developed to become available as compact and robust, press-button devices, where the pump system and the oscillator are assembled on a single breadboard. These lasers provide impressive characteristics like the broad and easily tunable emission spectrum (680 nm to 1080 nm, for Chameleon Laser from Coherent), and a high peak power which allows to use efficient frequency doubling to access the UV-spectral region, where a host of interesting atmospheric reactive species possess strong absorption bands. The availability of such laser systems opened the way to conceive a transportable comb spectrometer to be deployable during field campaigns for *in situ* measurements of local concentration of traces of reactive molecules. 'In situ' means that measurements should take place directly at the

remote geographical sites of scientific installations. With 'local' it is intended that concentrations are measured in a small air parcel which is admitted into a measurement cell, in contrast with 'remote sensing' where average concentrations are obtained over atmospheric volumes which are several km thick (either vertically or horizontally).

Following first contacts and discussions between our research group and researchers at LGGE (Laboratoire de Glaciologie et Géophysique de l'Environnement, in Grenoble), in particular Michel Legrand et Susanne Preunkert, the idea to develop a transportable instrument based on the ML-CEAS started to grow. Our colleagues at LGGE who are specialists in atmospheric chemistry, strive to achieve a better understanding of the atmospheric photochemistry of the Antarctic marine boundary layer (MBL) at the coastal site of Dumont d'Urville (DDU) station. For this, they require *in situ* measurements of several more reactive atmospheric species, in particular the radicals of BrO and IO as these have a strong influence on the sulphur cycle which in turn affects the chemistry of the Antarctic MBL. Figure 1 displays the role of BrO in the dimethyl sulfide (DMS) oxidation**.** A study published in 2008 [5] showed that at the coastal Antarctic site of British Halley station (located in the Atlantic oceanic sector), BrO and IO radicals strongly influence the atmospheric behaviour of DMS and the rate of production of sulphur aerosol (Methane Sulphonic Acid MSA and Sulfate). Since the level of these oxidants (BrO and IO) strongly depend on sea-ice conditions (controlling the BrO production) and the state of the marine biota (controlling the IO production), which differ from the Atlantic sector (Halley) to the Indian sector (DDU), there is an urgent need to document BrO and IO at DDU.

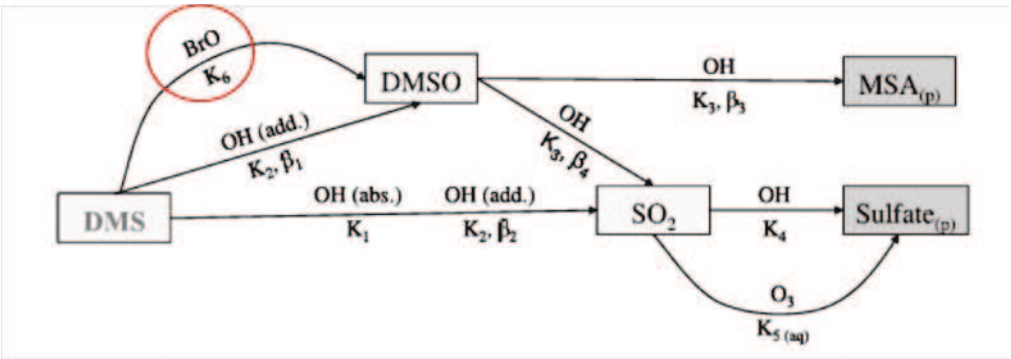

Figure 1: Simplified scheme displays the role of BrO in DMS oxidation [6].

The fruit of the cooperation between our research group and our partners from LGGE is the project MOCAMAR (**Mo**delocked-laser **Ca**vity-enhanced near UV spectrometer for sensitive and quantitative local **M**easurement of **A**tmospheric **R**eactive molecules). This project had been funded by French national agency of research for 3 years, starting from 2008. The main goal is to develop a transportable UV spectrometer based on the ML-CEAS technique, exploitable for field measurements, and allow *in situ* local concentration measurements of several reactive species with excellent selectivity, sensitivity, spatial and temporal resolution. The new instrument will be deployed at the coastal Antarctic site of DDU to

document the levels of IO and BrO. Furthermore, the proposed spectrometer will be also useful for other applications such as urban air quality.

Fortunately, I had the chance to participate in this project during my thesis. There were several technical and scientific challenges concerning how to design such compact and portable instrument and how to improve the previous performance obtained by our group in the laboratory (10^{-8} cm^{-1} detection limit, with an acquisition time of about 30 s [4]) to reach the required detection limit of about 10^{-10} cm^{-1} in 1 s acquisition time. The MOCAMAR project reached its goal as we will see later and achieved impressive results thanks to hard team work of several LAME group members, who did their best to overcome the difficulties and to make this project successful. It was very interesting and motivating to participate to these efforts.

The first axis of this thesis focuses therefore on the realization of the new spectrometer in the framework of the MOCAMAR project. This spectrometer is able to measure concentrations of a wide set of radicals and molecules at extremely low concentrations by accessing their strong electronic transitions in the UV and Visible ranges. As we mentioned above, such development is based on ML fs lasers, and one of the most popular, is the passively ML Ti:Sa laser, where the Kerr effect (taking place in the laser crystal itself) can sustain a stable self-modelocked regime of operation. A single stable pulse is formed in the laser cavity and produces a train of identical pulses as it is partially transmitted through the laser output-coupling mirror at each pass. The repetition rate of this pulse train is given by the round-trip time of the cavity. By the Fourier Transform (FT) principle, the shorter the pulse is the larger its spectrum must be. A typical pulse duration for Ti:Sa lasers is 100 fs with ~10 nm spectral bandwidth (FWHM) around 800 nm. However, the periodicity of the pulse train has also a consequence upon the laser spectrum: it gives a spectrally fine structure (inside the broad envelope) composed by equally spaced very narrow peaks which makes it deserve the name of frequency comb. The uniformity of the mode spacing has been proven experimentally to amazing precision: The relative mode-interval variation over an octave-stretched femtosecond ML laser spectrum is around 10^{-17} [7].

Passive mode locking is thus a simple scheme for producing a train of ultra-short laser pulses with an ultra-stable time periodicity, which corresponds in the frequency domain to a highly regular “frequency comb”. Another practically important feature is that the short duration pulse produces a high peak power: For a 1 W, 100 MHz train of 100 fs pulses; the peak power is typically 0.1 MW. This enhances nonlinear optical processes that are needed to reach the UV-VIS spectral range where relevant reactive atmospheric species have strong absorption bands. Interestingly, the doubled (or tripled) ML laser spectrum has a frequency comb with the same mode spacing, since these nonlinear processes return a pulse train with the same repetition rate.

An optical cavity (or Fabry-Perot resonator) also possesses a uniform comb of frequencies associated with transmission resonances. The basic idea behind the ML-CEAS is then to make

a coincidence between the laser comb and the cavity comb to achieve efficient injection of the whole laser spectrum into the cavity. This is achieved by finely adjusting the cavity length. The radiation transmitted by the injected cavity is analyzed by a high-resolution (0.45 cm^{-1} at 30 000 cm^{-1}) home-made spectrograph. The recorded spectrum will then present absorption features of intracavity molecules with an effective path length given by the cavity length times the cavity finesse (F) which is defined as the ratio of the cavity free spectral range (FSR) and the full width at half-maximum (FWHM) of cavity resonances. This principle works with any broad band light source, such as a lamp or a LED. However, due to their low spatial coherence (large emitting surface and beam divergence) the cavity throughput is poor, it decreases as 1/F, and becomes rapidly useless for cavity finesse higher than F=1000, especially if we want high spectral resolution (less photons available per spectral element). Using broad-band nanosecond or picosecond pulsed lasers, cavity injection has been shown to be rather effective due to the good spatial coherence and high peak power of these sources. However, CEAS with pulsed nanosecond (ns) lasers (dyes or Ti:Sa, principally) was tested by different authors and results were never impressive, mostly due to the noisy laser spectrum. On the other hand, ML fs lasers operating close to the FT limit display a spectral envelope which is smooth and stable: a perfect baseline for observing cavity enhanced absorption spectra. For our commercial laser source which is a “Chameleon” laser (passively ML fs Ti:Sa provided by Coherent), the 338-540 nm range is accessible by using a single doubling crystal. In this range, most reactive atmospheric molecules considered in Figure 2 possess strong absorption bands. It should be noted that the detection limits listed on the vertical right-hand scale are estimated for Long Path Differential Optical Absorption Spectroscopy (LP-DOAS). For molecules with absorption bands falling inside the spectral range of the ML-CEAS instrument (orange and cyan rectangles in Figure 2), the achieved and expected detection limits are mostly the same or better than for LP-DOAS, for example, 1 pptv for BrO and 20 ppqv for IO. In addition measurements will be feasible under any meteorological condition (no open path).

Moreover, the technique does not require calibration with a gas sample to obtain reproducible concentration measurements. Indeed, the HF ring-down [8] time is periodically measured and it is essential to calculate the effective absorption path length used to convert the acquired spectra in absorption units.

The second axis of my thesis was to advance with the exploration of new methods of laser spectroscopy, still using a frequency comb coupled to a HF cavity, in particular trying to exploit the Vernier effect [9] between the HF cavity comb and laser comb in order to obtain a spectral resolution without the need for a spectrograph as in ML-CEAS.

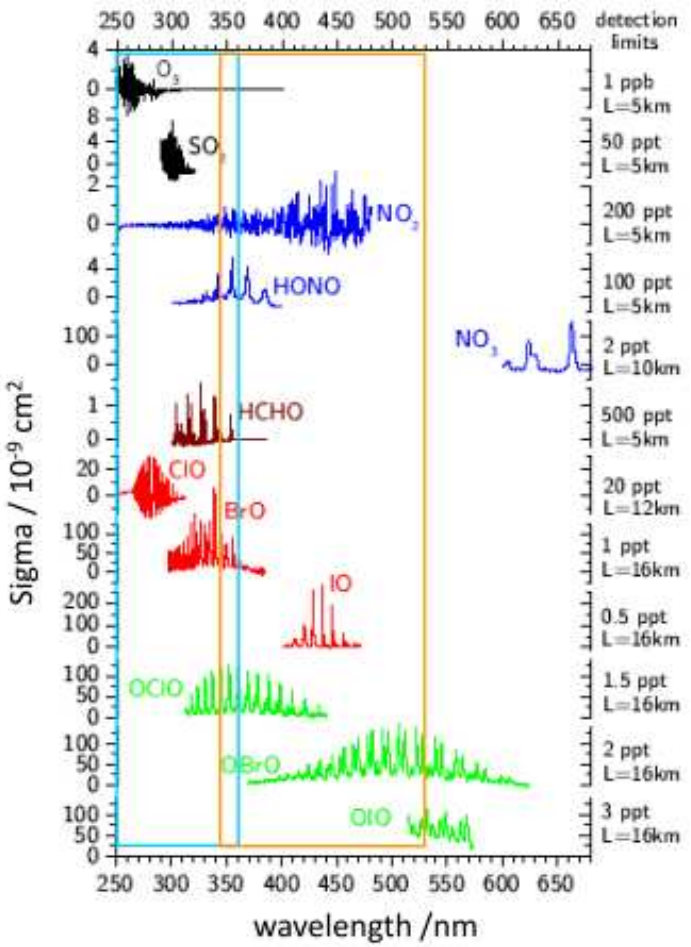

Figure 2: Electronic absorption spectra of several reactive atmospheric species [10]. The spectral region accessible with the frequency doubled Ti:Sa ML laser is given by the orange rectangle, while the cyan rectangle is accessible by frequency tripling. Detection limits (and needed path-lengths) on the right scale are estimated for the well-known LP-DOAS technique.

During the work on the development of the new UV spectrometer, I worked closely with Roberto Grilli, a postdoc hired for the project MOCAMAR, and all my work was supervised by Dr. Daniele Romanini, and Dr. Guillaume Méjean. I mainly participated in the design and building of the second harmonic generation (SHG) setup. As well, I participated actively in BrO and IO sample preparation at the laboratory, at high and low concentrations, using a mixing tank (for ppmv level sample preparation) and building an oven to control the temperature and the effusion rate of a Br_2 permeation tube, for the ppbv concentration range. I also participated in the setup of the home-made spectrograph based on an Echelle grating and UV enhanced Charge Coupled Device (CCD) detector and, in the characterization of this spectrograph. I did a considerable effort to assemble the whole instrument. I designed and fabricated a protection chassis to cover the instrument, and protect it from acoustic noise. I provided this cover with a thermoelectric reversible heat exchanger to control the temperature of the optical setup and the gas cell. I participated in the first field campaign at Marseille to test and reveal potential problems related to the assembly, the disassembly and the operation of the instrument at a remote site, and devise further system improvements. I participated to the analysis of acquired data in the laboratory as well as

during field campaigns, in particular those obtained at the Roscoff station in the North West coast of France (see chapter 3).

For the second part of my thesis concerning the Vernier effect, I worked more independently, I performed all the related modelling, built the setup for the first demonstration and designed basically the LabView program to acquire the data and analyse it. I obtained preliminary results and, I made further improvements to enhance the performance by stabilizing the laser source to a reference cavity, using the tilt lock technique.

This thesis is organized in four chapters, the first one gives an overview of passively ML Ti:Sa laser using Kerr-Lens effect to understand the ML lasers for the generation of frequency combs. We briefly talk about the phase noise of fs combs which will be needed for the Vernier effect technique. This chapter also provides a detailed study about SHG of fs laser pulses in Beta Barium Borate (BBO) and Lithium Triborate (LBO) crystals to reach the UV-VIS spectral range. This study aims to point out the crucial effect of the spatial walk-off, the group-velocity mismatch on the conversion efficiency of SHG. Furthermore, this study includes all the necessary calculations to choose the nonlinear crystal (NLC), to get a compromise between the efficiency of the SHG and the good optical quality of the SH wave, where the optical quality is very important for the injection of the high finesse cavity.

The second chapter describes the principle of ML-CEAS, and the different schemes of coupling the laser comb to a HF cavity, in particular, the “dynamic” or “transient” coupling scheme to obtain the ML-CEAS spectra, where the cavity length is matched to the laser repetition rate, then modulated by a piezoelectric actuator so that all cavity modes go through resonance almost simultaneously.

The third chapter is devoted to the technical developments and the results. This technical development includes the experimental setup, the mode-matching between the laser and the HF cavity, the home-made spectrograph, frequency doubling setup, and the gas sample handling. The data analysis and the automatization process are described in details. The structured absorption bands of the detected molecules are also discussed. A summary of the obtained results in the laboratory and the field campaigns is also presented.

The final chapter is dedicated to describe the Vernier Effect technique, providing the principle of the method, the analytical model, the experimental setup, the performance, and a comparison to ML-CEAS technique. The stabilization of the laser source which is important to enhance the performance is discussed. This chapter ends with conclusion and perspectives.

I should underline that this thesis was completely carried out at LIPHY laboratory at the University of Grenoble and all the experimental work was realized in the LAME group. As well as, this thesis is financed by Région Rhône-Alpes.

Chapter 1. Principle of mode-locked lasers and frequency doubling of femtosecond pulses

1.1. Introduction

Since the demonstration of the first laser in 1960, laser spectroscopy continues to develop and expand rapidly. Today, it plays an important role in physics, chemistry, medicine, biology and environmental sciences. Indeed, laser spectroscopy has been dramatically advanced by the development of mode-locked lasers. It is well known that if lasers can sustain simultaneous oscillation on multiple longitudinal modes, they can emit short pulses, by using a mechanism to lock the phases of all the modes. The lasers that deploy such mechanism are referred to as ‘‘mode locked’’. The importance of ML lasers rises from their capability to generate a train of regularly spaced pulses in the time domain, which results in train of equally spaced sharp lines in frequency domain, and these sharp lines are capable to excite narrow resonances. In addition, ML lasers have a large bandwidth, and a stable envelope of its spectrum. The big advance in ML lasers was due to development of passively Kerr-lens-mode-locked (KLM) Ti:sapphire lasers, because of their simplicity and high performance.

The developed UV-spectrometer to which I contributed during this thesis, is based on the ML-CEAS technique, which in turn depends on injecting a ML femtosecond (fs) Ti:Sa laser into a high finesse (HF) optical cavity. Therefore, I explain in this chapter some basic notions concerning passively mode locked lasers and the generated optical frequency comb, with focus on Ti:Sa lasers and the Kerr lens effect. I will then describe the SHG with fs pulses, which is needed to reach the UV spectral region where the molecules under study possess strong electronic absorption bands.

1.2. Ti:Saphire Kerr-Lens Mode locked (KLM) laser

Ti: Sa lasers have been mode locked by using a variety of techniques, but I will restrict my discussion to the Kerr-lens effect and its control because it affords the best results. Indeed, since it was first demonstrated in 1991 [11], the Kerr-lens mode-locked (KLM) Ti:sa laser has been widely used in ultrafast science because of its relative simplicity and excellent performance in terms of short pulse duration and associated high peak power and wide spectral emission. In the following section, we discuss the properties of the Ti:Sa crystal, which in particular allow for this mode-locking technique.

1.2.1. Properties of Titanium-doped sapphire crystal

This is an optically pumped, solid-state laser material with excellent thermal, physical and optical properties. The lasing medium in Ti:Sa laser is crystalline sapphire (Al_2O_3) doped with Ti_2O_3 to about 0.1 % by weight. The crystal is produced by mixing Ti_2O_3 into a melt of Al_2O_3. When a crystal is grown from this melt, Ti^{3+} ions substitute a small percentage of the Al^{3+} ions. Lasing occurs between the energy levels of the Ti^{3+} ions as shown in Figure 1.1. The ground state $^2T_2$ has a broad sequence of overlapping vibrational levels, as well as the first excited state ^2E also extends upward with a series of overlapping vibrational levels. Excitation takes place from the lower thermally populated vibrational levels of $^2T_2$ state to the broad range of vibrational levels of the ^2E.

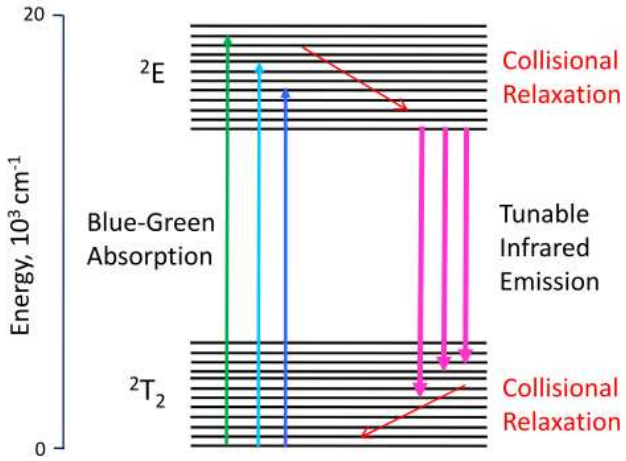

Figure 1.1: Energy level diagram of Ti^{3+} in Ti:Sa crystal.

Figure 1.2 displays typical absorption and fluorescence spectra of Ti:Sa crystal.

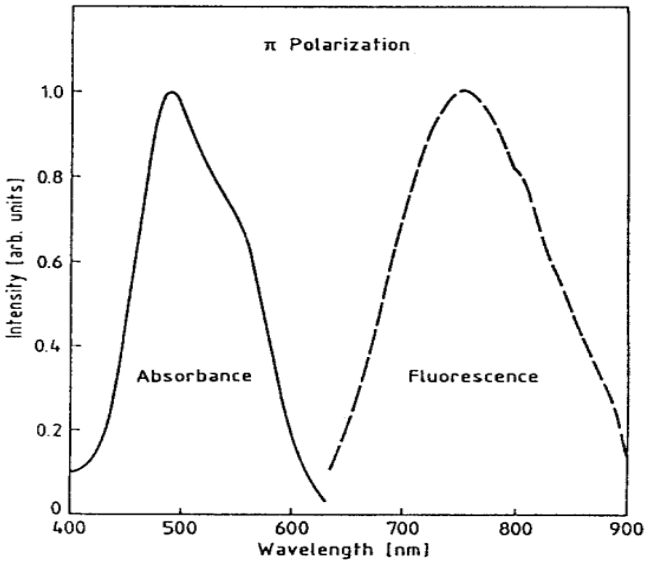

Figure 1.2: Absorption and fluorescence spectra of the Ti^{+3}: Sa crystal [12].

This crystal has an extremely broad fluorescence band (gain band) which extends from wavelengths shorter than 600 nm up to above 1000 nm as shown in Figure 1.2, but the lasing action is possible only up to around 670 nm because of the overlap of the absorption and emission spectrum in this region. However, the shape of the absorption band depends somewhat on the material growth techniques and the Ti^{3+} concentration. In addition, mirror coatings, tuning elements losses, pump power, and pump mode quality have an impact on the tuning range. Nevertheless, this tuning range of about 400 nm, which today is accessible using a single laser cavity configuration, is the broadest tunable range of any known material. Besides the broad tunability, the gain cross section is large, for example, at the center of its tuning range (800 nm), it is half that of Nd: YAG. In addition, we can see that Ti:Sa exhibits a broad absorption band, located in the blue-green region of the visible spectrum with a peak around 490 nm, this broad absorption band allows the Ti:Sa crystal to be pumped with a number of high power laser sources such as Ar^{+} (514 nm) and copper vapor (510 nm) lasers, frequency doubled Nd: YAG (532 nm), Nd: YVO_4 (532 nm), and Nd: YLF lasers (527 nm).

The enormous gain bandwidth of Ti:Sa, is a first advantageous feature as it is necessary for supporting ultrashort pulses by the Fourier relationship. If this entire bandwidth could be mode-locked as a Gaussian pulse, the resulting pulse duration would be only about 4 fs. Moreover, the Ti:Sa crystal also provides an efficient mode-locking mechanism due to its nonlinear refractive index as it will be explained below.

1.2.2. Principle of Mode-locking lasers

Let us consider, a homogeneously broad laser gain medium operating inside an optical cavity without spectrally selective elements: it will oscillate simultaneously over all resonant frequencies of the cavity for which the saturated gain remains above the cavity losses. Saturation here, refers to the fact that the lasing modes will become amplified in time until the extracted power from the gain medium produces a gain reduction to reach the level of the cavity losses (as an average over a given spectral range), which constitutes a steady state operation regime of the total emitted power. This regime is achieved, by the homogeneous laser, very rapidly, with a broad emission spectrum where initially spontaneously-emitted photons succeed inducing lasing of cavity modes. Given that a (small) curvature with a shallow maximum is usually present in the net gain (gain minus losses) as a function of frequency, after a second transient time (much longer than the saturation time) the laser will spectrally collapse over a small spectral region where saturated net gain will be uniformly close to zero. Depending on the flatness of the net gain, and on the intracavity laser power causing nonlinear effects which couple the laser cavity modes, the emission spectrum of such a “free-running” laser will be more or less large. The emission of this laser will be subject to large random spectral fluctuations given by the competition between modes to be amplified by the stimulated emission of the same atoms in the gain medium. This competition causes large fluctuations in the relative phases and amplitudes of the modes, and only the total power is kept stable by the gain saturation condition. A mode-

locked femtosecond laser can also be obtained from a broadband gain medium such as Ti:Sa, which can sustain over 100,000 longitudinal modes in a laser cavity about 1-2 meter long. These random fluctuations are then eliminated by a mechanism which forces all modes to have well defined intensity and the same phase at a given instant in time, producing by constructive interference, a powerful well-defined single pulse circulating in the laser resonator. A few mode locking mechanisms will be discussed in the following.

1.2.3. Mode- locking mechanisms

In mode-locked lasers, phase locking means imposing a fixed phase relationship between all of the lasing longitudinal modes. Forcing all the modes to have an equal phase implies in the time domain that all the waves of different frequency will add constructively at one point in time and space, resulting in an intense and short burst of light. This mechanism requires having higher net gain for regime where one or more pulses circulate in the laser cavity, compared to the CW regime. Typically, a loss modulator inside the laser cavity is used to produce this type of behavior actively or passively (according to the type of loss modulation mechanism) by collecting the laser light in short pulses around the minimum of the loss modulation with a period given by the cavity round-trip time $T_r=c/2L$ (c is the speed of light, L is the optical cavity length) as shown in Figure 1.3.

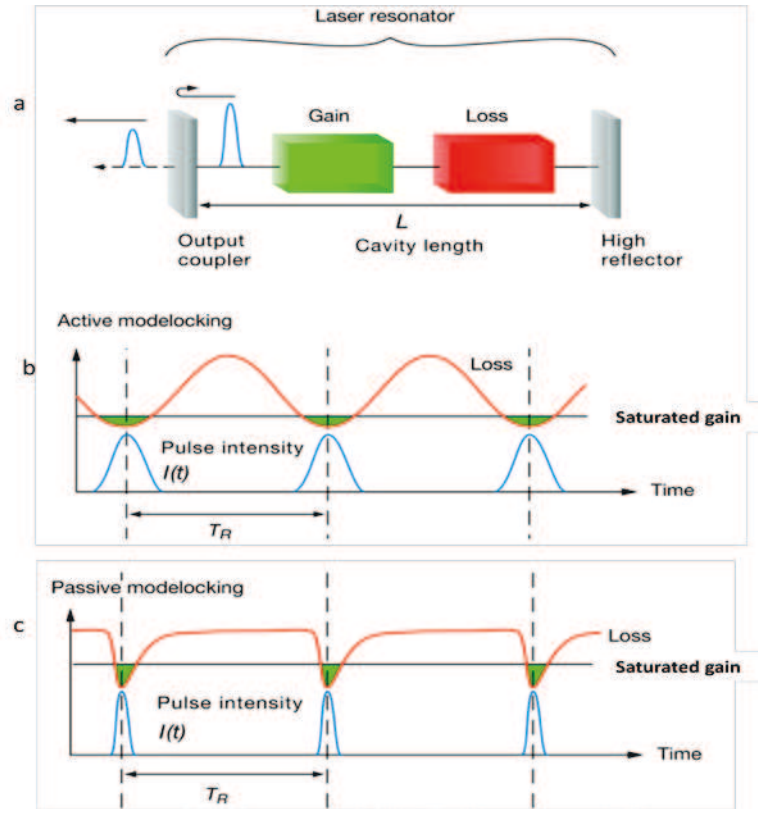

Figure 1.3: Schematic laser cavity setup for active and passive mode-locking [13].

Active methods typically involve applying an external signal to an optical modulator providing a phase or frequency modulation. The most popular modulators are acousto-optic (AOM) or the electro-optic devices. When the AOM is driven with an electrical signal, a sinusoidal amplitude modulation for each cavity longitudinal mode is induced [14]. Making the modulation time close to the cavity round-trip time of a pulse, results in enabling this pulse to exploit the maximum net gain (Figure 1.3.b). In order to have this pulse the modes must develop a precise phase relation, and this is made, because the sidebands generated from each running mode (due to modulation signal) is injected into the neighboring modes of this running mode, which leads to synchronization and locking of neighboring modes. Global phase locking will yield a single oscillating pulse that contains all the energy of the cavity.

Passive methods rely on placing a saturable absorber (real or effective) into the laser cavity as shown in Figure 1.3, which causes self-modulation of the lasing effect. The saturable absorber has the property of intensity-dependent transmission that means: it will allow transmission of high intensity light and will absorb low intensity light. Such an absorber introduces some loss to the intracavity laser radiation, which is relatively large for low intensity in the CW lasing regime, but significantly smaller for a short pulse regime with high peak intensity. Indeed, a short pulse produces a loss modulation, because the high intensity at the peak of the pulse saturates the absorber during the pulse passage in the absorber, more strongly than its low intensity wings. Real saturable absorbers can be made from dyes, semiconductors, or solid-state laser materials. Their main drawback is the long response time associated with relaxation of the excited state, which limits the shortest pulse widths that can be attained. Effective saturable absorption can be obtained exploiting the nonlinear refractive index of some materials together with spatial effects or interference to produce again a higher net gain for shorter and more intense pulses. The most interesting to us is a third order nonlinear effect inside the Ti:Sa gain medium itself which plays the role of a fast saturable absorber through the Kerr lens effect.

1.2.4. Kerr lens effect in Ti:Sa laser

At high intensities, the refractive index in the gain medium becomes intensity dependent. This is manifested in Ti:Sa as an increase of the refractive index when the optical intensity increases, and this can be expressed by the following relation:

$$n = n_0 + n_2 I \tag{1.1}$$

Where,

- I : Optical intensity of the incident light.
- $n_0, n_2 > 0$: Linear and nonlinear refractive index coefficients of the Ti:Sa crystal, respectively.

The nonlinear refractive index describes the strength of the coupling between the electric field and the refractive index (*n*), and is related to the real part of the third-order susceptibility $\chi_R^{(3)}$ by [15]:

$$n_2 = \frac{(4/3)n_0^2 \varepsilon_0 c}{\chi_R^{(3)}} \tag{1.2}$$

Were, ε_0 is the electric permittivity of free space (8.85 x 10^{-12} F/m).

As the beam is less intense at its edges as compared to the center, the index at the center will be higher, and a gradient index lens is formed inside the Ti:Sa crystal. The resulting Kerr lens causes a self-focusing effect that means, the strong pulses circulating in the laser cavity are focused, relative to the continuum laser emission, which is not able to induce appreciable Kerr lensing. Kerr effect is potentially possible only when the light intensity is extremely high, such as the instantaneous intensity of a mode-locked pulse. Introducing a slit or an aperture in the cavity at an appropriate position, then the circulating pulses suffer smaller losses than the continuum which leads to self mode-locking of the laser. The diameter, position and shape of the slit must be calculated precisely. Figure 1.4 displays the Kerr lens effect on the beam profile. Together with a correctly positioned effective aperture, the nonlinear Kerr lens can act as a fast saturable absorber that means high intensities are focused and hence fully transmitted through the aperture while low intensities experience losses.

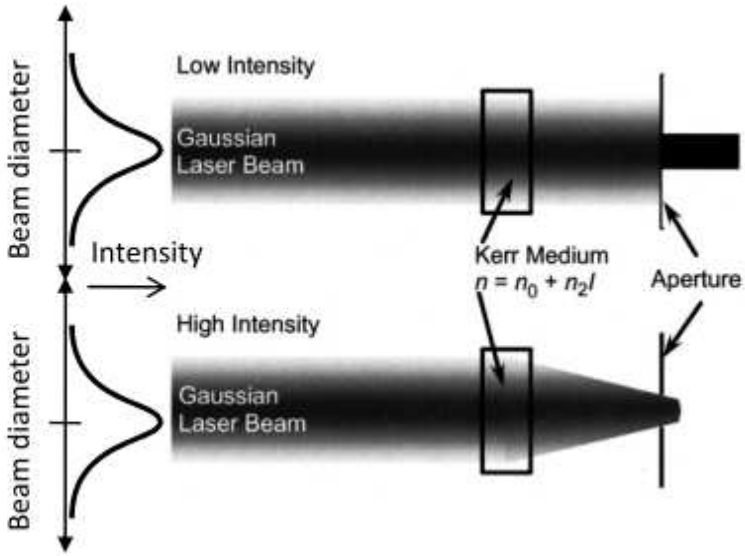

Figure 1.4: Schematic of the Kerr-lens mechanism. The upper diagram shows that, for low intensity, much of the intensity does not pass through an aperture. The lower diagram shows that for high intensity, the Gaussian index profile, which is due to the nonlinear index of refraction, acts as a lens and focuses the beam increasing net transmission through the aperture.

Contrary to actively ML lasers, KLM lasers need a starting mechanism to stimulate the pulsed regime. For this it is enough to introduce a brief intensity spike into the CW-laser resulting

from rapidly enough misalignment of the cavity, and then the intensity spike enjoys more gain than the CW lasing mode and builds up. After the Kerr lens starts, it is self-sustainable. Indeed a KLM laser has basically two stable extreme regimes corresponding to the single circulating giant pulse operation which is more stable, and the CW regime which is less favorable and less stable. When the system is externally perturbed it may fall into one of these regimes, with more chance for the pulse regime. In practice, intermediate regimes with several pulses or mixed pulsed-CW regimes can be observed for non-optimal laser cavity alignments. Today, reliable self-starting passive mode-locking for all types of solid-state lasers is obtained with semiconductor saturable absorbers, first demonstrated in 1992 [16]. Let us now consider in Figure 1.5, a typical realization of a Kerr-lens mode-locked Ti:Sa laser where two prisms are also present to control the dispersion, as explained in the following. The main laser cavity, consisting of mirrors M_1 to M_4, extends up to about 2.0 m, with a Brewster-angled Ti:Sa crystal placed in the center of the cavity, where the length of the crystal ranges from 2 mm to 10 mm according to the doping level of Ti^{3+}. M_4 is a plane output coupler having a transmission of few percent at the lasing wavelengths. The spherical mirrors M_1 and M_2 (radius of curvature ~ 10 cm) are highly reflective over this wavelength range, and highly transmitting for the pump wavelengths. As the Ti:Sa crystal acts like a nonlinear lens, it also disperses the pulses temporally through positive dispersion ($dn_0/dv > 0$), and consequently, a sequence of two prisms may be used to compensate for the group velocity dispersion (GVD) in the crystal. The first prism disperses the pulse according to the angle as a function of wavelength, leading the long wavelengths to traverse more glass in the second prism than the short wavelengths. The angular dispersion is converted to spatially parallel dispersion after the second prism which allows using a flat cavity end-mirror for reflecting exactly backward all dispersed wavelengths.

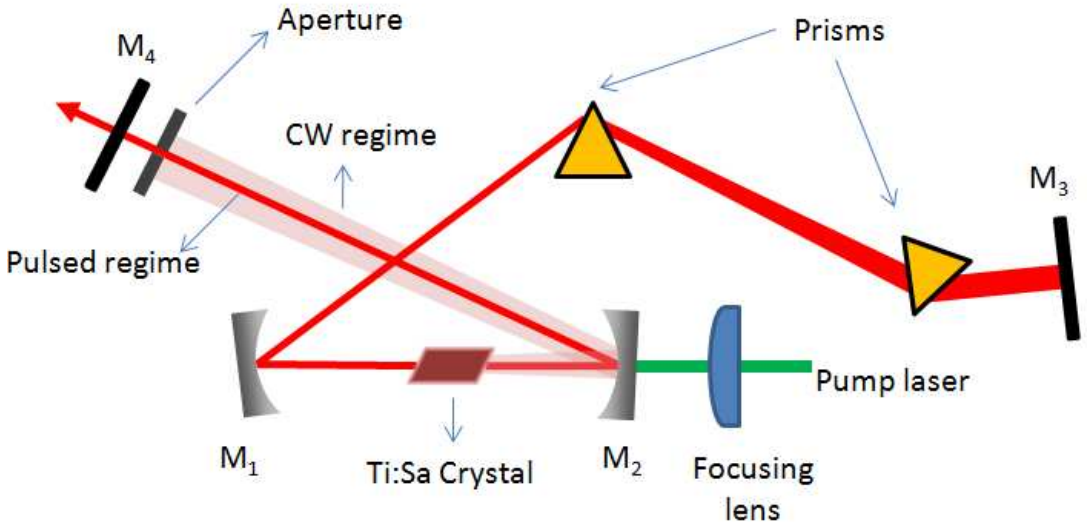

Figure 1.5: Typical Kerr-lens mode-locked Ti: Sa laser with prism based configuration.

The drawback of this modelocking scheme is that KLM is realized near the stability limits, (where the laser mode size is highly influenced by any additional nonlinear lensing), so it is sensitive to the cavity alignment. This means that the optimal cavity condition for efficient

KLM is significantly different from that for the CW lasing. Therefore, in developing a Kerr lens mode-locked Ti:Sa laser, it is important to theoretically investigate the optimal cavity conditions. The big advantage of KLM is that Kerr-lens effect is nearly insensitive to the laser wavelength and has very fast response time in the fs range [17]. The fast response comes from the fact that at sufficient high intensity, the electric field associated with the light can actually distort the electronic cloud of the atoms inside the materials and alter its index to form the Kerr lens. Since the electronic cloud response is much faster than the atomic transitions required in real saturable absorbers, the time response of such nonlinear process is virtually instantaneous (sub fs).

In conclusion, thanks to the large gain bandwidth of Ti:Sa, and giving the ability to sustain simultaneous oscillation on multiple longitudinal modes, it is possible to generate very short pulses (fs range) at the output of a Ti:Sa laser through careful design of the cavity's dispersion and the mode-locking mechanism.

For a deep understanding of how ML lasers can be exploited successfully for the generation of frequency combs with known absolute frequencies, it will be useful to discuss about the specific features of the spectrum emitted by a mode-locked laser, how it arises, and how it can be controlled.

1.2.5. Frequency spectrum of mode-locked lasers

As a result of mode-locking, a single circulating pulse inside the laser cavity is obtained. Due to the action of the saturable absorber (or the Kerr lens effect), which favors the peak against the wings of the pulse, the duration of the pulse is then reduced further at each cavity round-trip, until broadening effects like intracavity dispersion become strong enough to prohibit further pulse shortening. In addition, the circulating pulse inside the cavity will give an output pulse at each round-trip when it strikes the cavity output coupler. Therefore, in the time domain, the mode-locked laser does not emit isolated short pulses, but rather a very regularly spaced train of short pulses with a period defined by the round-trip time τ_{rt}, and the pulse duration τ_p. In the frequency domain, this results in a phase-locked frequency comb with equally spaced sharp peaks (the peaks look like the teeth of a comb), and the constant mode spacing is equal to the pulse repetition rate $f_{rep} = 1/\tau_{rt}$. The spectral width of the envelope of this frequency comb, gives us the well-known broad spectrum of a femtosecond laser and this spectral width is inversely proportional to the pulse duration τ_p. An experiment with a stabilized laser has confirmed that the teeth of the frequency comb, which is the Fourier transform of the pulse train, are equally spaced throughout the pulse bandwidth to 3.0 parts in 10^{17} [18]. This stability makes frequency combs from mode-locked lasers powerful tools for high-precision frequency metrology as well as for high sensitivity laser spectroscopy. We expect that if all of the pulses emitted by the laser are identical, the mode spacing between the frequencies of the comb lines will be integer multiples of the repetition rate of the pulse train. In reality, this is not the case, and the successive pulses are

different of each other due a mismatch between the phase and the group velocities inside the laser cavity. This induces a progressive dephasing of the carrier wave (the central laser emission frequency) with respect to the pulse envelope. Figure 1.6 displays the time and the frequency pictures of frequency comb, where $\Delta\Phi_{ceo}$ represents the carrier-envelope offset (CEO) phase which accumulates from a pulse to the next.

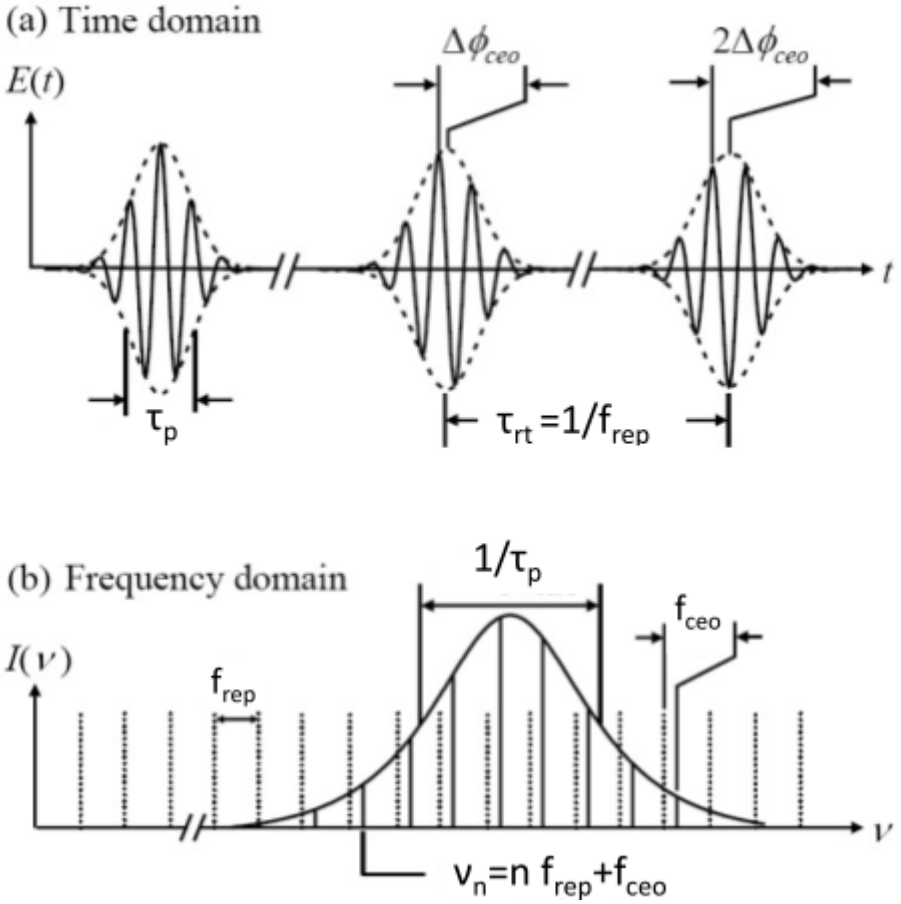

Figure 1.6: Time and frequency domain properties of an optical frequency comb. a: Time domain picture of a pulse train, b: Corresponding frequency domain picture, where dashed lines represent an ideal harmonic frequency grid , while solid lines represent the laser modes. Note: "CEO" stays for carrier-envelope offset.

Figure 1.6.a, illustrates a description of time domain pulse train emitted by a mode-locked laser, while Figure 1.6.b illustrates the frequency domain of the same pulse train. It is obvious from this figure that the lasers modes are shifted from an ideal harmonic frequency comb (dashed lines) by a certain value which is f_{ceo}. We will give a short and simple explanation of this interesting structure [19]. The envelope propagates at the group velocity υ_g, while the carrier propagates at the phase velocity υ_p, and due to the dispersion in the laser cavity we have $\upsilon_g \neq \upsilon_p$. This mismatch causes the envelope to be retarded relative to the carrier during every round-trip. The fractional part of this phase offset gives rise to the (CEO) phase $\Delta\Phi_{ceo}$ (this offset is taken between the carrier wave with respect to the peak of the envelope for each round-trip). To find the relation of $\Delta\Phi_{ceo}$, we start by writing the group velocity as:

$$\upsilon_g = \frac{2L}{\tau_{rt}} = \frac{c}{n - \lambda \frac{dn}{d\lambda}} \tag{1.3}$$

Here, the term $n - \lambda \frac{dn}{d\lambda}$ is the group refractive index n_g.
The phase velocity is given by:

$$\upsilon_p = \frac{2L}{\tau_{phase}} \tag{1.4}$$

Where, τ_{phase} is the time for the carrier to complete one cavity round-trip.

The delay between the pulse envelope and an arbitrary point on the phase front can now be written as:

$$\tau_{ceo} = 2L\left(\frac{1}{\upsilon_p} - \frac{1}{\upsilon_g}\right) \tag{1.5}$$

This yields for the phase shift:

$$\Delta\Phi_{ceo} = 2L\left(\frac{1}{\upsilon_p} - \frac{1}{\upsilon_g}\right)\omega_c \, mod \, 2\pi \tag{1.6}$$

Where, ω_c is the (angular) carrier frequency.
For simplicity, we refer to ($\Delta\Phi_{ceo}$ modulo 2π) by $\Delta\Phi_{ceo}$. This carrier-envelope phase shift $\Delta\Phi_{ceo}$ influences the spectrum of the comb and we will give a simple analytical derivation [19] of this effect by assuming that $\Delta\Phi_{ceo}$ is a constant amount. This assumption is true in the absence of fluctuations of the environmental conditions (temperature, pressure etc) and perturbations to the laser. Let us start by writing the field of a single pulse for a fixed spatial coordinate as following:

$$E_p(t) = \hat{E}(t)e^{i(\omega_c t + \Phi_{ce})} \tag{1.7}$$

Where,

- Φ_{ce}: Carrier envelope phase.
- $\hat{E}(t)$: Pulse envelope.

Here, the electric field is described as the multiplication of carrier signal (CW sinusoidal) by the envelope function. If $\Delta\Phi_{ceo}$ is neglected then $\Phi_{ce} = \Phi_0$ (Φ_0 absolute phase of the pulse), for all pulses of the train but in general the carrier-envelope phase for a pulse *n* is $\Phi_{ce} = n \times \Delta\Phi_{ceo} + \Phi_0$. Then, the field for a train of pulses is given by:

$$E(t) = \hat{E}(t)e^{i(\omega_c t+\Phi_{ce})} \otimes \sum_n \delta(t \quad n\tau_{rt})e^{i\Phi n}$$
$$= \sum_n \hat{E}(t-n\tau_{rt})e^{i(\omega_c t+n(\Delta\Phi_{ceo}-\omega_c\tau_{rt})+\Phi_0)} \tag{1.8}$$

Here, $\Phi_n = -n\times\omega_c\times\tau_{rt}$ is the accumulated phase after *n* round-trips. δ is the Dirac function.

The train of pulses may thus be represented as a convolution product of the electric field of one pulse by a comb of Dirac functions. To obtain the spectrum, we take the Fourier transform of (1.8):

$$\tilde{E}(\omega) = \int\sum_n \hat{E}(t-n\tau_{rt})e^{i\left(\omega_c t+n\left(\Delta\Phi_{ceo}-\omega_c\tau_{rt}\right)+\Phi_0\right)}e^{-i\omega t}dt$$
$$= \sum_n e^{i[n(\Delta\Phi_{ceo}-\omega_c\tau_{rt})+\Phi_0]}\int\hat{E}(t \quad n\tau_{rt})e^{-i(\omega-\omega_c)t}dt \tag{1.9}$$

By definition, we have $\tilde{E}(\omega) = \int\hat{E}(t)e^{-i\omega t}dt$, and by taking into account the identities

$\int f(t-a)e^{-i\omega t}dt = e^{-ia\omega}\tilde{f}(\omega)$, $\int f(t)e^{iat}e^{-i\omega t}dt = \tilde{f}(\omega-a)$, we get:

$$\tilde{E}(\omega) = \sum_n e^{i\left[n\left(\Delta\Phi_{ceo}-\omega_c\tau_{rt}\right)+\Phi_0\right]}e^{-in(\omega-\omega_c)\tau_{rt}}\tilde{E}(\omega \quad \omega_c)$$
$$= e^{i\Phi_0}\sum_n e^{in(\Delta\Phi_{ceo}-\omega\tau_{rt})}\tilde{E}(\omega \quad \omega_c) \tag{1.10}$$

The relevant components in the spectrum are those for which the exponential in the sum add coherently because the phase shift between pulse *n* and *n+1* is a multiple of 2π. That means, $\Delta\Phi_{\text{ceo}} - \omega\tau_{\text{rt}} = 2\text{n}\pi$. This yields a comb spectrum with angular frequencies:

$$\omega_n = \frac{\Delta\Phi_{ceo}}{\tau_{rt}} - \frac{2n\pi}{\tau_{rt}} \tag{1.11}$$

By converting the above relation to a frequency relation, we get:

$$f_n = nf_{rep} + f_{ceo} \tag{1.12}$$

Where, $f_{ceo} = \frac{\Delta\Phi_{ceo}f_{rep}}{2\pi} = \frac{\omega_c\upsilon_g}{2\pi}\left(\frac{1}{\upsilon_g} - \frac{1}{\upsilon_p}\right)$ is the carrier-envelope offset frequency. Here, *n* is the mode order number (10^5-10^6).

Note that the relevant quantity here is ($\Delta\Phi_{ceo}$ modulo 2π) which implies that f_{ceo} is bounded by f_{rep} $(0 < f_{ceo} < f_{rep})$.

It is obvious from the relation (1.12) that the spectrum of the mode-locked femtosecond laser consists of a comb of discrete optical frequencies as shown in Figure 1.6.b, and these frequencies are shifted from the exact harmonics of the repetition rate by f_{ceo} which is proportional to the pulse-to-pulse carrier-envelope phase shift. This structure allows in principle high-resolution and frequency-calibrated spectroscopy across massively parallel (>10^5) detection channels. For the same reason, an efficient coupling is easily realized between the frequency components of the comb and the modes of a high finesse optical cavity as we will see in Chapter 2. Moreover, the relation (1.12) is very important when working with fs frequency comb since it gives the optical frequency as a function of two radio frequencies (f_{rep}, f_{ceo}), which typically vary from hundred MHz up to a few GHz for the shortest laser cavities. For example, as we will see in chapter 3, stabilizing the laser comb by independently acting on these two parameters (f_{rep}, f_{ceo}) is needed in a spectroscopic technique exploiting the Vernier effect, which is under development in our laboratory.

It is interesting to mention that In KML lasers, even though the refractive index is a function of frequency $n = n(\omega)$, the pulse spacing (in time) thus the mode spacing (in frequency) are rigorously constants. The theory of the mode-locked laser shows this "transformation" of the unequal mode spacing of the laser cavity into a perfect comb to be the result of nonlinear optical processes exactly counterbalancing the residual dispersion present after the introduction of the prism compensation system.

1.2.6. Noise in passively modelocked Ti:Sa Laser

In the analytical treatment presented in the previous section, we assumed that $\Delta\Phi_{ceo}$ is constant, but in reality $\Delta\Phi_{ceo}$ is sensitive to changing of laser parameters or fluctuation of environmental conditions. Changes of $\Delta\Phi_{ceo}$ influence the lines of a frequency comb by changing the mode spacing (f_{rep}) or shifting the entire comb by changing (f_{ceo}), or both. The main noise sources are mechanical vibrations of the laser cavity, thermal drifts, pump intensity noise and quantum noise [20] (originating from spontaneous emission in the gain medium which should be a small effect and will not be considered in the following). We will first focus briefly about the CEO phase noise [21] then in particular consider the effects of amplitude-phase coupling [21].

1.2.6.1. CEO Phase noise

In this section, we will discuss the physical mechanisms behind the $\Delta\Phi_{ceo}$ noise. It is instructive to start from the definition of the CEO phase. As mentioned above, when a short pulse propagating through a dispersive material with an index of refraction *n(z)* along the

axis *z*, the pulse will accumulate a phase offset between the carrier and envelope of $\Delta\Phi_{ceo} = \Phi_{ce}(t) - \Phi_{ce}(t - \tau_{rt})$ and this value can be rewritten as follows [21]:

$$\Delta\Phi_{ceo} = \left[\frac{2\pi}{\lambda} \int_0^{2L} n_g(z) \quad n(z) dz \right] \bmod 2\pi$$
$$= \left[\frac{\omega_c^2}{c} \int_0^{2L} \frac{dn(z)}{d\omega} dz \right] \bmod 2\pi \qquad (1.13)$$

Where n_g is the group index, and given by $\mathrm{n_g} = \mathrm{n}(\omega_\mathrm{c}) + \omega_\mathrm{c} \left. \frac{\mathrm{dn}}{\mathrm{d}\omega} \right|_{\omega_\mathrm{c}}$.

From the above relation, we can rewrite the dependence of $\Delta\Phi_{ceo}$ on any laser or environmental parameter X as:

$$\frac{\partial}{\partial X} \Delta\Phi_{ceo} = (1/c)[2\omega_c \frac{\partial \omega_c}{\partial X} \frac{\partial n}{\partial \omega} 2L \quad 2\omega_c^2 \frac{\partial n}{\partial \omega} \frac{\partial L}{\partial X} \quad 2\omega_c^2 \frac{\partial^2 n}{\partial \omega \partial X} L] \qquad (1.14)$$

These partial derivatives $\frac{\partial \omega_c}{\partial X}$, $\frac{\partial L}{\partial X}$, $\frac{\partial^2 n}{\partial \omega \partial X}$ correspond to the variations of the center frequency ω_c (frequency shifting) [22], of the cavity length [23], and of the first-order dispersion of the cavity [24], respectively. If we consider now different possible environmental effects, we can see that any fluctuation in the temperature of the laser crystal or the intracavity optical elements will cause a direct change of the $\Delta\Phi_{ceo}$ according to the second and the third term of (1.14). In addition, air pressure variation in the cavity contributes to $\Delta\Phi_{ceo}$ noise according to the third term. However, such fluctuations are relatively slow and cannot contribute to noise at high frequencies, above a few kHz. In summary, environmental contributions affect CEO noise spectrum at low frequencies, and their effect can be reduced by enclosing the laser system in a box and thermalize the whole system. Therefore, they do not pose any special problem in achieving successful stabilization of the CEO frequency. Another contribution to $\Delta\Phi_{ceo}$ noise arises from geometrical changes of the laser cavity, and the acoustic vibrations which affect the total cavity length *L*, or the tilt of the cavity mirrors (or both). To compensate this noise, a piezo-electric transducer (PZT) can be mounted on the input cavity mirror to finely tune the cavity length. The fluctuation of laser Intensity will also affect $\Delta\Phi_{ceo}$ and generate a noise called amplitude to phase conversion effect.

1.2.6.2. Amplitude-to-phase conversion (APC) effects

To understand the origin of the APC effect, it is sufficient to substitute the parameter X by the intensity in relation (1.14). From the third term in this relation, it is clear that refractive index change induced by the intensity contributes to the $\Delta\Phi_{ceo}$ noise. Notably, inside the

laser crystal the intracavity intensity reaches its maximum leading to the Kerr lensing effect as mentioned in paragraph (1-2-2). If geometric effects and spectral shifting can be avoided, the APC effects are restricted to nonlinear refractive mechanisms, both Kerr-type and an additional thermally induced mechanism at low frequencies. The APC effect is then represented by $\frac{\partial f_{ceo}}{\partial I}$, and when it reaches a value on the order of 10^{-8} Hzm^2/W in a Ti:Sa laser, that means the dominant phenomena in APC dynamics is the nonlinear Kerr effect [21].

1.3. Second harmonic generation of fs pulses in BBO, LBO crystals

1.3.1. Introduction

As we have seen in the introduction, several reactive molecules possess strong electronic transitions in the blue spectral range. In particular, the two principal molecules of interest will be BrO and IO, which absorb at 338.5 nm and 435 nm respectively. Currently, lasers with broad-band tunability in this spectral region are not available. However, one of the main advantages of ML-CEAS is its ability to give access to the blue-UV spectral region via efficient nonlinear optical process. This is possible thanks to the high peak optical intensity delivered by ultrashort pulses. Other advantages are the tunability, and the broad emission spectrum of the KLM Ti:Sa laser. In this section, we will present the type I SHG considering the birefringent phase matching parameters and the limitations of extra-cavity frequency doubling of Ti: Sa fs laser pulses in (BBO) and (LBO) crystals. The choice of nonlinear crystals (NLC) is limited to BBO and LBO because they offer a wide transparency into the blue range, birefringence allowing to obtain phase matching, and high damage thresholds. These crystals are also not sensitive to ambient conditions (temperature fluctuation or humidity), and readily commercially available.

1.3.2. Type-I Second Harmonic Generation

Propagation of two monochromatic waves with frequencies ω_1 and ω_2 in a nonlinear crystal (NLC) with nonlinearity of second order gives rise to new light waves with a sum frequency $\omega_3 = \omega_1 + \omega_2$, and a wave vector mismatch $\Delta k=k_3-(K_1+K_2)$. For SHG, it is then important to fulfill the phase matching condition ($\Delta k=0$) to enhance the efficiency of the nonlinear process as we will see in next paragraphs. The condition of phase matching ($\Delta k=0$) with collinear propagation leads to the following relation:

$$\frac{n_1\omega_1}{c}+\frac{n_2\omega_2}{c}=\frac{n_3\omega_3}{c} \tag{1.15}$$

For the case of SHG, with $\omega_1=\omega_2$, $\omega_3=2\omega_1$, this condition becomes $n(\omega_1)=n(2\omega_1)$, which cannot be achieved in the normal dispersion materials where $n(\omega)$ increases with ω. In birefringent crystals, the refractive index depends not only on wavelength, but also on the polarization direction of the light relative to the crystal. Basically, by choosing orthogonal polarizations between the fundamental input and the SH output waves, the birefringence in the crystal can compensate the normal index dispersion and achieve perfect phase-matching. In uniaxial crystals a special direction exists called the crystal optical axis *Z*. The plane containing the *Z* axis and the wave vector ***K*** of the wave is termed the principal plane. The light beam whose polarization is normal to the principal plane is called ordinary beam (o-beam). The beam polarized in the principal plane is known as an extraordinary beam (e-beam). For this type of crystals, we have phase matching of type (1) in which the fundamental wave propagates as an o-wave, producing a SH e-wave, as in the following examples:

Phase matching type (I): 872 (o) +872 (o) → 436 (e)
Phase matching type (I): 677 (o) +677 (o) → 338.5 (e)

Under certain conditions, where the conversion efficiency (η= SH power /Fundamental power) is small (η<<1), The intensity of the SH wave is given by [25]:

$$I_2=\frac{2\,\pi^2 d_{eff}^2\; I_1^2 L^2}{n_1^2 n_2\,\varepsilon_0\; c_0\lambda_2^2}\operatorname{sinc}^2\left\{\left[\left(\frac{1}{\upsilon_2}-\frac{1}{\upsilon_1}\right)\Omega-\Delta k\right]\frac{L}{2}\right\} \tag{1.16}$$

Where:

- Ω : Angular frequency.
- I_1 : Intensity of the fundamental wave.
- L : NLC length.
- d_{eff}: Effective nonlinear coefficient.
- n_1, n_2: Refractive index of the fundamental and SH waves, respectively.
- υ_1, υ_2 : Group velocities of the fundamental and SH waves, respectively.
- λ_2 : Wavelength of SH wave.

The effective nonlinear coefficient is related to the NLC symmetry, the type of interaction (ooe, or eeo and so on) and the nonlinear dielectric susceptibility $\chi^{(2)}$ which is a tensor of third rank in the general case. The group velocity at the carrier frequency ω_c is defined as:

$$\frac{1}{\upsilon_i} = \frac{n(\omega_i)}{c} + \frac{\omega_i}{c}\frac{dn}{d\Omega}\Big|_{\omega_i} = \frac{n_g}{c} \tag{1.17}$$

Here, n_g is the group index, which determines the group velocity while the ordinary refractive index determines the phase velocity. The term $\left(\frac{1}{\upsilon_2} - \frac{1}{\upsilon_1}\right)$ in the **sinc** function is called the group velocity mismatch GVM. From the relation (1.16), we can see that the SH intensity reaches its maximum when the phase matching condition is achieved that means *GVM,* and *Δk* approach zero. Actually, the *GVM* induces a temporal walk-off between the fundamental and SH waves, causes the broadening of SH pulses, and limits the effective interaction length which also affects the efficiency of the nonlinear conversion. Moreover, the frequency-domain counterpart of temporal walk-off is the effect of limited phase-matching bandwidth. From the above considerations, an appropriate crystal length can be selected to avoid the influence of a non-zero *GVM*, and this length is called the quasistatic interaction length given by [26]:

$$\mathrm{L_{qs}} = \frac{1}{\mathrm{GVM} \times \Delta\omega} \tag{1.18}$$

Where, $\Delta\omega$ is the spectral width of the fundamental pulse. For the Fourier transform (FT) limited pulses ($\Delta\omega\tau_\mathrm{p} = 1$), the effective length could be modified as:

$$\mathrm{L'_{qs}} = \frac{\tau_\mathrm{p}}{\mathrm{GVM}} \tag{1.19}$$

Where, τ_p is the fundamental pulse duration. In many cases, ultrashort pulses are chirped or modulated (not FT limited); hence the relation (1.18) is more realistic. The group velocity dispersion (GVD) can also lead to pulse broadening in the temporal domain which limits the interaction length between the fundamental and the SH beams. To neglect the effect of GVD, the crystal length should be shorter than the dispersive broadening length which is given by [17]:

$$\mathrm{L_d} = \frac{\tau_\mathrm{P}^2}{4 \times \mathrm{GVD}} \tag{1.20}$$

Where, GVD is measured in unit of (fs^2/mm).

The following calculation is made by using **SNLO** program (free software from Sandia National Laboratories, which helps to select nonlinear crystals and model their performance http://www.as-photonics.com/snlo). During the calculation, we took the spectral width of the fundamental wave $\delta\lambda_{FWHM}$ to be 8 nm and 3 nm, at λ=872 nm and λ=677 nm, respectively, which correspond to the spectral width of our laser at both wavelengths.

Table 1.1 presents the calculated values of *GVM* and L_{qs} for BBO and LBO at the desired wavelengths.

Crystal	λ (nm)	$n_{g,\lambda}$	$n_{g,\lambda/2}$	GVM(fs/mm)	$\delta_{\lambda FWHM}$(nm)	L_{qs}(μm)
BBO	872	1.680	1.727	156.7	8	320
	677	1.695	1.785	300	3	275
LBO	872	1.629	1.658	96	8	523
	677	1.639	1.696	190	3	430

Table 1.1: Calculated values of GVM and L_{qs} at 872 nm and 677 nm for BBO, LBO crystals.

Table 1.2 presents the calculated values of *GVD* and L_{d1}, L_{d2} at the fundamental and SH waves, respectively.

Crystal	λ (nm)	GVD_1 (fs^2/mm) at λ	GVD_2 (fs^2/mm) at λ/2	T_p(fs)	L_{d1} (mm)	L_{d2} (mm)
BBO	872	65.4	171.3	130	64.4	12.2
	677	96	260	200	104	15.7
LBO	872	38.5	114.4	130	109.7	15
	677	62.8	162	200	160.2	31

Table 1.2: Calculated values of *GVD* and L_{d1}, L_{d2} at the fundamental and SH waves, respectively.

By comparing the last columns of Table 1.1, and Table 1.2, we can conclude that the crystal length is limited by L_{qs}, and the effective length (L_{eff}) of the NLC should be equal or slightly smaller than L_{qs}. The previous calculation tells us that L_{eff} should be 0.275 mm for BBO, and 0.43 mm for LBO if we want to use the same crystal for both selected wavelengths. In the experiment, we used a BBO crystal with a length of 0.2 mm to optimize the phase matching at 677 nm because the minimum fundamental power delivered by the laser corresponds to this wavelength.

1.3.3. Consideration of angular and spectral bandwidths of phase matching

Respecting the spectral bandwidth $\delta\lambda_{pm}$ of the phase matching allows the whole spectrum of the fundamental beam to be converted. Furthermore, respecting the angular bandwidth $\Delta\theta_{pm}$ of the phase matching is also important when a tight focusing inside the NLC is considered. As ultrashort pulses have a broad frequency bandwidth, $\delta\lambda_{pm}$ and also $\Delta\theta_{pm}$ influence strongly the efficiency of conversion and the SH pulse duration. To obtain a clean SH spectrum, a good optical quality of transverse mode TEM_{00} of SH beam, and an efficient nonlinear conversion, the crystal length has to be carefully chosen with respect to the

angular and the spectral bandwidths of the phase matching. The following calculations are also made by the SNLO program which provides the parameters of phase matching angle θ_{pm}, effective nonlinear coefficient d_{eff}, and the angular acceptance $\Delta\theta.L$ as well as the spectral acceptance $\Delta\lambda.L$. Table 1.3 presents the calculated values of $\Delta\theta.L$, $\Delta\lambda.L$ as well as the angular and spectral bandwidths $\Delta\theta_{pm}$, $\delta\lambda_{pm}$ for BBO and LBO. The angular and the spectral acceptances are calculated for $L.\Delta K$ varies from $-\pi$ to $+\pi$. The strategy of these calculations depends on considering the calculated length that allows neglecting the effect of GVM, at the NLC effective length L_{cr}. The values of $\Delta\theta_{pm}$ and $\delta\lambda_{pm}$ are obtained by dividing the angular and the spectral acceptances by L_{cr}. The LBO crystal is a negative biaxial crystal and the birefringent phase matching depends on two angles (the polar angle θ, and the azimuthal angle ϕ), while the BBO crystal is a uniaxial crystal and the phase matching depends only on θ.

Crystal	λ (nm)	$\Delta\theta.L$ (mrad.cm)	$\Delta\lambda.L$ (nm.cm)	d_{eff} (pm/v)	θ_{pm} (deg)	ϕ_{pm} (deg)	L_{cr} (mm)	$\Delta\theta_{pm}$ (mrad)	$\delta\lambda_{pm}$ (nm)
BBO	872	0.82	1.63	2	27		0.2	41	81.5
	677	0.53	0.51	1.95	35		0.2	26.5	25.5
LBO	872	3.84	2.63	0.78	90	25.3	0.43	89	61
	677	2.21	0.80	0.617	90	46.8	0.43	51	19

Table 1.3: Calculated values of angular and spectral bandwidths at λ =872 nm and 677 nm for BBO.

The last two columns of Table 1.3, show that the whole spectrum bandwidth could be converted, but the small values of phase-matching angular bandwidth ($\Delta\theta.L$) will impose limitations to the focalization inside the NLC as we will see in the next paragraph. The previous calculation helps to compare between LBO and BBO, and enables us to choose the optimal crystal. On one hand, the effective nonlinear coefficient d_{eff} for BBO is larger than the one for LBO. So, we expect to have higher conversion efficiency achieved by BBO than by LBO. On other hand, the angular and spectral bandwidth of LBO are both higher than for BBO, therefore we can compensate the low efficiency of LBO due to its small d_{eff} by using longer crystal and obtaining tight focus inside LBO crystal.

1.3.4. Focalization inside the nonlinear crystal

In fact, the focalization of the fundamental beam has a significant influence on the nonlinear conversion efficiency and the deformation of SH pulses (generation of high-order nonlinear effects such as self-phase modulation and cross-phase modulation). In general, we determine the fundamental beam radius w_0 inside the NLC with respect to the phase matching conditions as follows:

$$\theta = \frac{\Delta\theta_{pm}}{2} \tag{1.21}$$

Where, θ is the divergence half angle of fundamental wave.

A prediction for the focused beam radius w_0 can be made with the following relation:

$$w_0 = \frac{M^2\lambda}{\pi\theta} \tag{1.22}$$

Where, M^2 is the beam quality factor, which for a ML Ti:Sa oscillator is close to 1. In the limit *M=1*, for a diffraction limited Gaussian beam.

According to the value of w_0, we can estimate the focal length of the lens that is needed to focus the fundamental beam inside the NLC, which is given by:

$$f = \frac{\pi\, w_0 D}{2M^2\ \lambda} \tag{1.23}$$

Where, D is the diameter of the fundamental wave before the lens.

The Rayleigh range for a laser beam with a radius w_0 is given by:

$$Z_R = \frac{\pi w_0^2}{\lambda} \tag{1.24}$$

The Rayleigh length should be close to the crystal length to avoid an excessive focusing inside the NLC, and to satisfy the plane waves approximation in the following. In fact, if phase-matching is accomplished at an angle θ_{pm} different from 90° with respect to the optic axis of a uniaxial crystal, there will be double refraction. Therefore, the direction of power flow (Poynting vector) of the fundamental and SH will not be completely collinear but occur at a small angle ρ. This walk-off angle limits the conversion efficiency and influences the output beam shape. The characteristic length to avoid the spatial walk-off effect is called the aperture length, given by [25]:

$$L_a = \frac{d_0}{\rho} \tag{1.25}$$

Where,

- ρ : Walk-off angle
- d_0: Diameter of the focused fundamental beam at the entry of the NLC.

Table 1.4 presents the calculated values of w_0, f, θ, ρ, Z_R, for D=1.2 mm (the beam waist of our laser) for BBO and LBO.

Crystal	λ (nm)	θ (mrad)	L_{cr} (mm)	$w_{0,min}$ (µm)	Z_R (mm)	ρ (mrad)	d_0 (µm)	L_a (mm)	f (mm)
BBO	872	20.5	0.2	14.8	0.79	63.98	29.6	0.462	29
	677	13.25	0.2	18	1.5	76.64	36	0.470	45
LBO	872	44.5	0.43	7	0.18	14.01	14	0.994	14
	677	25.5	0.43	10	0.46	18.94	20	1	25

Table 1.4: Calculated values of w_0, f, θ, ρ, Z_R at λ =872 nm and 677 nm for BBO and LBO.

During the calculation, d_0 is taken to be $2w_{0,min}$ for BBO, and this is justified because the Rayleigh distance is larger than the crystal length. For LBO, the Rayleigh distance is smaller than the crystal length; therefore d_0 should be less than $2w_{0,min}$ but we put the value of $2w_{0,min}$ for approximate calculation. M^2 is taken to be 1.1. The calculated intensity of the fundamental beam (power = 2.5 W at 872 nm, beam waist = 10 µm) is less the 1 MW/cm^2 which is much smaller than the damage threshold of both crystals considered here (in the range of 10 GW/cm^2).

Finally, if we want to use the same crystal for both wavelengths to achieve phase-matching conditions, for BBO crystal, the optimal length is 0.275 mm, the fundamental beam waist w_0 is about 20 µm inside the NLC, and the focal distance of focusing lens is 45 mm**.** For LBO, the optimal crystal length is 0.43 mm, the fundamental beam waist w_0 is about 10 µm inside the NLC, and the focal distance of focusing lens is 25 mm.

1.3.5. Conversion efficiency of SHG

It is very difficult to estimate the conversion efficiency with accurate calculation in the general case, where all the limiting factors are taken into account. For simplicity, we limit our consideration to a field made up of two plane waves propagating in the *Z* direction with frequencies ω_1 for the fundamental input wave, and ω_2 for the output SH wave. The SH wave power can be written in term of the input wave power P_1 as follows [25]:

$$\eta = \frac{P_2}{P_1} = \frac{2\,\pi^2 d_{eff}^2\, P_1 L^2}{n_1^2 n_2\, \varepsilon_0 c\, \lambda_2^2\, A}\,\mathrm{sinc}\left(\frac{|\Delta k| L}{2}\right)^2 \qquad (1.26)$$

Where,

- Δk: Phase mismatch and equal to k_2-2k_1.
- A: Area of the input beam ($A = \pi w_0^2$).

From the above relation, we can see that the generation efficiency of SH wave reaches its maximum value when the phase matching condition is achieved (*Δk = 0*), within the possibility of neglecting the GVM, as the crystal length is well chosen. This relation also gives approximate upper limit values because in ultrashort laser pulses, the input depletion is not negligible and then the input wave should be allowed to depend on *Z*. Hence, it is necessary

to solve the coupled equations of SHG numerically, and these equations are given [25] as follows:

$$\frac{dE_1}{dz} = -\frac{i}{2}\,\kappa\, E_1^{*}\, E_2 e^{-i(\Delta k)z}$$
$$\frac{dE_2}{dz} = -\frac{i}{2}\,\kappa\, E_1^{2}\, e^{i(\Delta k)z} \qquad (1.27)$$

Where, $\kappa = d_{eff}\sqrt{(\frac{\mu}{\varepsilon_0})\frac{\omega_1^2\omega_2}{n_1^2 n_2}}$, and E_1, E_1 are the complex amplitudes of the electric field of the fundamental and the SH waves, respectively.

Table 1.5 presents the calculated value of the output power and the nonlinear efficiency in numerical way by using the SNLO program and compares theses values by the experimental ones for only BBO. The waist inside the BBO crystal is calculated for a lens of 45 mm, for both wavelengths, while the waist inside the LBO crystal is calculated for a lens of f=25 mm for both wavelengths.

Crystal	λ (nm)	P_{in} (W)	L (mm)	w_0 (µm)	$P_{out,\,exp}$(SH) (mW)	$P_{out,\,SNLO}$(SH) (mW)	η (%) exp	η (%) SNLO
BBO	872	2.5	0.2	23	230	280	9.2	11.2
	677	0.7	0.2	20	30	32	4.3	4.5
LBO	872	2.5	0.43	13		520		20
	677	0.7	0.43	10		60		8.5

Table 1.5: Calculated values of P_{out} (SH) and η at λ =872 nm and λ =677 for BBO, LBO crystals.

During the calculation, we used the pulse energy as input parameters for the SNLO program then the output is given as energy density (J/cm^2) which is converted to average power, taking into account the laser repetition rate of 80 MHz, and the SH waist (SH waist = fundamental waist / $\sqrt{2}$). There a good match between the calculated values by the SNLO program and the measured ones for the BBO crystal. We used the approximation of plane waves as the crystal length is smaller than Rayleigh length. We should mention here that all the calculations are made under the supposition of no frequency chirping, and no dispersion or linear absorption inside the NLC. By comparing LBO and BBO with respect to the efficiency, we find that the efficiency of LBO is higher than its value for BBO by a factor of 1.6 which comes from the ratio between the analytical efficiency of LBO and BBO as follows:

$$\frac{\eta_{LBO}}{\eta_{BBO}} = \left(\left(\frac{w_{0,BBO}}{W_{0,LBO}} \times \frac{L_{LBO}}{L_{BBO}} \right) / \left(\frac{d_{eff,BBO}}{d_{eff,LBO}} \right) \right)^2 = 1.6 \tag{1.28}$$

This factor is consistent with the numerical calculation presented in the last column of Table 1.5.

1.4. Conclusion

LBO crystal is expected to provide better performance (higher efficiency and keeping good beam quality), if its length is chosen to be 0.43 mm. We tried the available LBO crystal with a length of 0.6 mm, but the optical quality of the blue mode was not good, in particular the beam was elliptical, likely because of the spatial walk-off even if the calculation in Table 1.4 (column 9) indicates that the length is not limited by the spatial walk-off. It is possible that the relation (1.25) used to calculate the spatial walk-off limited length L_a, gives upper estimation. However as expected, the SH output power obtained by LBO (0.6 mm) was higher than its value for BBO (0.2 mm). On the other hand, the transverse-mode matching between the laser blue mode and the TEM_{00} mode of the HF cavity modes, requires a good optical quality of the blue beam (as we will see in the next chapter), which justifies our preference to work with the BBO crystal (0.2 mm), which produced a nicely circular output with sufficient power.

Chapter 2. Principles of ML-CEAS and comb-cavity coupling

2.1. Introduction

The chemistry and photochemistry of iodine and bromine compounds in the atmosphere, with a particular interest to the highly reactive forms such as the halogen oxides, have progressively captured the attention of the atmospheric community aiming at a better understanding of their oxidizing capacity of Earth's troposphere [27]. During springtime in the Polar Regions, reactive bromine, chlorine and iodine compounds are responsible for the rapid ozone depletion in the Marine Boundary Layer (MBL) [28]. Halogen oxides are also known to be involved in the oxidation of gaseous elemental Mercury (Hg) [29] and dimethyl sulphide (DMS) [5, 6]. Recent studies by Preunkert *et al*. [6] about the catalytic sulphur cycle in the inland and coastal regions of Antarctica to better understand the oxidation of DMS point out that that concentrations of a few pptv (parts per trillion by volume, $1{:}10^{12}$) of BrO radical would make it the most important oxidant of DMS at generally over the whole coastal Antarctica, with respect to other oxidation channels such as the hydroxyl radical [5]. In addition, an accurate model of the sulphur cycle can be used to extract information from the polar ice cores, which constitute a unique archive of climate proxies[6]. Furthermore, monitoring the effects of halogen oxides on the atmospheric oxidative processes helps to get an insight about the global warming. Because of the halogen oxides importance, different spectroscopic techniques are employed to detect them. Indeed, the difficulty to precisely detect such molecules in real time comes from their high reactivity and their extremely low concentrations (on the order of part per trillion or less) which are also variable in time and space.

It is important to have a quick review about the measurements of halogen oxides molecules which have been performed in the last years using different techniques. Each technique has its advantages and drawbacks. Laser Induced Fluorescence (LIF), presented by Whalley *et al*.[30] to measure IO, shows a detection limit of 0.3 pptv (part per trillion by volume, $1{:}10^{12}$) within 300 s of acquisition, and chemical ionization mass spectrometry may provide detection limits down to 2.6 pptv for IO radical within 4 s of integration time [31, 32]. However, both techniques suffer of not being absolute analytical methods, and require regular calibrations using standard samples. Up to now, absorption spectroscopy methods mainly lead to non-spatially resolved techniques such as long-path differential optical absorption spectroscopy (LP-DOAS) [27], or multi axis differential optical absorption spectroscopy (Max-DOAS) [33] using incoherent radiation. On one hand, these techniques offer a large versatility thanks to the spectral coverage of the light source, allowing the monitoring of multiple species. On the other hand, no local information on concentrations are provided because the measurements are integrated over atmospheric volumes which

are several km thick (either vertically or horizontally). In addition, the performances of the open path techniques strongly depend on climatic conditions. The atmospheric box-model calculations performed by Burkholder *et al*. [34] on the iodine chemistry at the marine boundary layer highlight the issue that long-path techniques do not sufficiently account for the presence of inhomogeneous sources of iodine, leading to a mismatch between experimental measurements and calculations. Finally, Wada *et al.* [35] demonstrated an open path cavity ring-down spectrometer for IO measurements injecting a pulsed dye laser into a high-finesse cavity and providing a detection limit of 10 pptv which is, however, not sufficient in most atmospheric situations. In fact, direct and sensitive measurements of halogenated radicals in the atmosphere do not exist; therefore it was motivating to make it possible.

The Modelocked cavity enhanced absorption spectroscopy (ML-CEAS) technique presented in this chapter overcomes most of the mentioned drawbacks. This technique is a laser absorption spectroscopy method recently developed in our research group. It relies on the properties of a high finesse (HF) optical cavity consisting of two high reflective mirrors. Inside the cavity, light is trapped, which enhances the effective interaction length (or life time, equivalently) between this light and the intracavity gas sample, resulting in an increase of the absorption sensitivity. In our case, this technique is applied for atmospheric trace gas sensing. An efficient coupling between the cavity modes and the frequency comb generated from a mode-locked (ML) femtosecond (fs) laser is easily obtained as it was demonstrated in 2002 in our laboratory [3]. In general, achieving the resonance between the laser comb and the corresponding cavity modes requires making the cavity free spectral range equal to an integer multiple or sub-multiple of the laser repetition rate. At the resonance, all the laser frequency components are transmitted from the cavity simultaneously, and they overlap each other in the time domain. Therefore, the transmitted light is spectrally resolved by a home-made spectrograph as we will see later. The absorption spectrum is then recorded with a charge coupled device (CCD) detector.

In the next paragraphs, we will present the basics of direct absorption spectroscopy, then the interesting properties of HF optical cavities which serve to enhance the sensitivity, and enable an efficient coupling with the laser frequency comb. We will discuss in details the key parameters necessary to control the coupling between the HF cavity and the frequency comb.

2.2. Principle of direct optical absorption spectroscopy

In this section, we discuss about the direct optical spectroscopy to identify the detection problem of extremely small absorption, and the key parameters to enhance the detection sensitivity which in turn will be defined to compare different approaches of absorption

spectroscopy. Suppose that the light with an initial intensity $I_0(\nu)$ at a frequency (ν) passes through a closed cell of length *L* which contains a sample gas as shown in Figure 2.1.

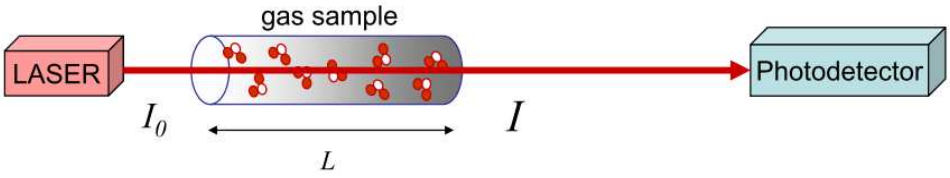

Figure 2.1: Simple setup of optical absorption spectroscopy.

The gas absorbs a portion of the light and the transmitted intensity $I(\nu)$ after one pass is measured by a photodetector. In the approximation of linear absorption, the relation between $I(\nu)$ and $I_0(\nu)$ is given by the Lambert-Beer law:

$$I(\nu) = I_0(\nu)\exp(-\alpha(\nu)L) \tag{2.1}$$

Where $\alpha(\nu)$ is the absorption coefficient (cm^{-1}) and relates to the gas concentration *N* (molecule/cm3) by:

$$\alpha(\nu) = N\sigma(\nu) \tag{2.2}$$

Here $\sigma(\nu)$ is the absorption cross section (cm^2), which gives the unique fingerprint of a given absorbing molecular species present in the gas sample, and may be decomposed as follows:

$$\sigma(\nu) = S_l f(\nu - \nu_c) \tag{2.3}$$

Where S_l is the line strength factor, $f(\nu - \nu_c)$ is the normalized line shape and ν_c is the central frequency.

From the Lambert-Beer law, and in the conventional single pass absorption spectroscopy, the fractional absorption $\frac{I_0 - I}{I_0} = \frac{\Delta I}{I_0}$ can be written in the case of weak absorption $(\frac{\Delta I}{I_0} << 1)$ as follows:

$$\frac{\Delta I}{I_0} = \alpha(\nu)L = S_l f(\nu - \nu_c)NL \tag{2.4}$$

From the previous relation, we can see that the absorption is proportional to the concentration of the absorber, and if the photodetector can detect the change in the light intensity ΔI due to absorption, it will be possible to measure the concentration *N*. But in the case of trace detection where the concentration is very low (*N* is small) and/or the transition

is weak (S_l is small), the absorption is too low to be distinguished from the noise fluctuations of the incoming light intensity, then we say that the detection sensitivity is not sufficient.

In general, the sensitivity is defined as the minimum detectable absorption coefficient $\alpha_{\min}$ (cm^{-1}), and approximately given by:

$$\alpha_{\min} \approx \frac{1}{L \times SNR} \tag{2.5}$$

Where *SNR* is the signal to noise ratio, *S* is the signal and equal to I_0 and *N* is the noise roughly equal to $\Delta I = I_0 - I$.

Sensitivity, as we have just defined, however, does not effectively compare spectroscopic methods together. Moreover, it ignores certain essential characteristics as the width of the probed spectral range, the spectral resolution, and the averaging time of measured spectra. Therefore, we have to use another quantity to compare different methods which is the minimum detectable absorption coefficient per a second and per spectral element (or the normalized bandwidth (BW) minimum absorption coefficient). It is expressed in $cm^{-1}Hz^{-1/2}$, and given by:

$$\alpha_{\min}(BW) = \alpha_{\min} \times \sqrt{\frac{T}{M}} = \frac{1}{L \times SNR} \times \sqrt{\frac{T}{M}} \tag{2.6}$$

Where *T* is the acquisition time. *M* is the number of independent spectral elements, and obtained by dividing the probed spectral range by the spectral resolution. More $\alpha_{\min}(BW)$ is small, better is the sensitivity.

It is clear from the above relation, that to improve the detection limit, there are two solutions. The first is to increase the absorption length without degrading the signal to noise ratio, and the second is to minimize the noise of the acquired signal. In parallel, absorption is enhanced by choosing the strongest available transition to increase S_l. In our case, we reduced the noise until reaching the shot noise limit. The measurement was done in the UV-VIS region where the molecules (IO, BrO) strongly absorb (corresponds to electronic transition, S_l is maximum). Usually, decreasing the pressure leads to less collisional broadening and thus easier discrimination, but lowering the pressure in our case is not so useful due to the self-broadening of the molecules under study.

Increasing the absorption length is a practical solution and there are different ways to do it. A very popular solution is to use multi-pass cell technique. Because laser light has very high spatial coherence and can remain collimated to a small beam size over long distances, multipass cells are used to achieve up to 2 kilometers of path length enhancement, when the base length is on the order of 50 meters as in Figure 2.2. Three commonly used cells are White cells [36], Herriotcells [37], and more recently astigmatic mirror cells [38].

Nevertheless, this technique has several drawbacks. In particular, it suffers from a large sample volume leading to a slow response time which is undesirable in certain applications such as breath analysis or the characterization of rapid chemical reactions. Furthermore, it is limited to a 2-3 hundred passages in the best cases (effective length reaching one or two hundred meters for a typically setup, and exceptionally a few kilometers[39]). In addition, the multiple reflections on the mirror surfaces make the scattered light a limiting factor since it induces interference fringes on the measured spectra. Due to the mentioned shortcomings of the multipass cell technique, the smallest detectable $\Delta I/I$ is typically around 10^{-4}, which together with a respectable 100 m path length for a small cell of 200 cubic centimeter volume, corresponds to a α_{min} of 10^{-8} cm^{-1}. As the required sensitivity for our applications should be better than 10^{-10} cm^{-1}, this technique is not our best choice.

Figure 2.2: Multi-pass cell of White (length=50 m) to increase the absorption length until 2 Km [39].

An elegant solution to increase the absorption length is to use a HF optical cavity which highly enhances the sample absorption. As we will see, this allows significantly higher performance compared to multipass cells.

2.3. Properties of a high finesse optical cavity

Here, we discuss the main properties of a HF optical cavity, which is a stable optical resonator or Fabry Perot (FP) resonator, constructed from two high reflective mirrors (R>0.999) with quarter-wave stack coatings. These properties include the structure of the cavity transmission, the intra-cavity dispersion for the efficient coupling between the cavity and a laser, and the enhancement of light-matter interaction for the sensitivity detection, as well as the cavity time response for the absolute calibration of the absorption.

2.3.1. Cavity transmission and the Finesse

Figure 2.3 displays a configuration of a passive optical cavity consisting of two spherical highly reflective mirrors M_1, M_2 with equal curvatures radius R_C. The two mirrors are opposed at a distance ($L < 2R_C$) and aligned to an optical axis (z).

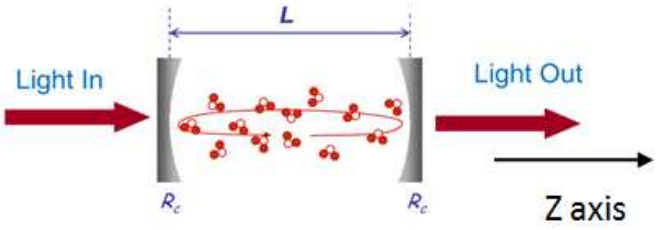

Figure 2.3: Configuration of a passive optical cavity.

Incident light enters the cavity and undergoes multiple reflections between the mirrors, so that it interferes with itself many times. If a constructive interference occurs within the cavity, most of the incident light will be transmitted. The condition for constructive interference (upper window of Figure 2.4) is the round trip phase must be a multiple of 2π, including the contribution of the mirrors. In other words, the optical path between the two mirrors must equal an integral number of half wave length of the incident light. The constructive interference condition is therefore defined by the relation:

$$L = p\frac{\lambda}{2} \tag{2.7}$$

Where, *p* is an integer giving the order of interference. For λ=400 nm, and L=1 m, we get p=5x10^6.

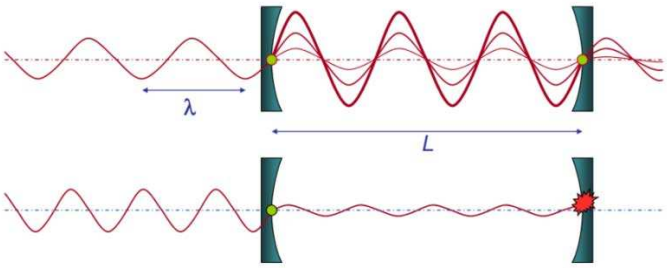

Figure 2.4: Upper window, the resonance inside the FP cavity. Lower window: no resonance.

In the case of no absorption in the cavity, let us consider the incident electric field on the cavity (taken at the input mirror z=0) $E_i(t)$. We can calculate the electric field of light leaving the cavity by adding up all paths that lead to output, which make 1, 3, 5, etc., passes through the cavity. The light making one pass has amplitude of $T_e^2 E_i(t - t_r/2)$ at time t, where $t_r = 2L/c$ is the cavity round-trip time, and T_e is the amplitude transmission coefficient. Each additional round trip through the cavity changes the amplitude by a factor of R_e^2 (R_e is the amplitude reflection coefficient) and leads to an additional retardation of t_r. Summing the contribution of the possibly infinite number of passes (n) leads to the electric field outside the output cavity mirror (at the position z=L) which is given by [40]:

$$E_0(t) = \sum_{n=0}^{\infty} T_e^2 R_e^{2n} E_i(t-(n+\frac{1}{2})t_r) \tag{2.8}$$

The intracavity field at position *z* can also be written by summing the contribution of the possibly infinite number of passes:

$$E(z,t) = \sum_{n=0}^{\infty} T_e R_e^{2n} E_i(t-nt_r-\frac{z}{c}) - T_e R_e^{2n+1} E_i(t-(n+1)t_r+\frac{z}{c}) \tag{2.9}$$

This field contains now two terms of $E_i(z,t)$, the first one corresponds to the propagating wave in the forward direction, and the second term corresponds to the propagating wave in the backward direction. By applying the Fourier Transform (FT) to (2.8), the spectrum of the field is obtained and given by:

$$\tilde{E}_0(\omega) = = \frac{T_e^2 \exp(-\frac{i}{2}\omega t_r)}{1-R_e^2 \exp(-i\omega t_r+\theta)} \tilde{E}_i(\omega) \quad \tilde{T}_{c,e}(\omega)\tilde{E}_i(\omega) \tag{2.10}$$

Where, $\theta = \arg(R_e)$ is the phase shift per reflection on a mirror, $\tilde{E}_i(\omega)$ is the FT of the input field, and $\tilde{T}_{c,e}(\omega)$ is the cavity transmission function for the field. ω is the angular frequency.

The cavity output spectral intensity is proportional to $\left|\tilde{E}_0(\omega)\right|^2$ which gives the cavity transmission function for the intensity $\tilde{T}_C(\omega)$:

$$I_0(\omega) = = \frac{T^2}{(1-R)^2 + 4R\sin^2(\frac{1}{2}\omega t_r - \theta)} I_i(\omega) \quad \tilde{T}_C(\omega) I_i(\omega) \tag{2.11}$$

Where $T = \left|T_e\right|^2$ is the intensity transmission coefficient, and $R = \left|R_e\right|^2$ is the intensity reflection coefficient. $I_i(\omega)$ is the input spectral intensity . The relation (2.11) is called the Airy formula.

The principle of energy conservation of a wave reflected and partially transmitted by a mirror implies:

$$R + T + l = 1 \tag{2.12}$$

Where l represents the losses from the mirror (absorption and scattering losses).

By using the same treatment, we can find the intracavity intensity:

$$I(\omega,z)=T\frac{(1-\sqrt{R})^2+4\sqrt{R}\sin^2(k(L-z)-\theta)}{(1-R)^2+4R\sin^2(\frac{1}{2}\omega t_r-\theta)}I_i(\omega) \tag{2.13}$$

Where, $k=\omega/c$ is the wave vector of the laser radiation.

To obtain the position of the cavity resonances one frequency scale, $\tilde{T}_C(\omega)$ is maximized as a function of frequency, which yields:

$$\sin^2(\frac{1}{2}\omega t_r-\theta)=0\Rightarrow\frac{1}{2}\omega t_r-\theta=K\pi\Rightarrow$$
$$\nu_K=\frac{c}{2L}(K+\frac{\theta}{\pi}) \tag{2.14}$$

Where ν_K is the frequency. The dephasing on reflection (θ) will be neglected in the following treatment because it represents a fixed shift of all cavity modes from the origin on the frequency axis.

At resonance, when the relation (2.14) is satisfied, the laser field at frequency ν_K will make *K* oscillation during a travel interval of one cavity round-trip (*2L*). In this way, the fields add in phase after each cavity round-trip and intracavity field build-up can occur as shown in Figure 2.4. The trace of the cavity transmission obtained by plotting the function given in (2.11) is shown in Figure 2.5, where the resonance peaks at frequencies ν_K make together a comb of modes, called for simplicity, the "cavity comb" which will be matched to the fs laser frequency comb to achieve optimum transmission of the laser spectrum as explained in later paragraphs. It should be mentioned that at resonance, the cavity transmission reaches its maximum value $T^2/(1-R)^2$ as seen from the relation (2.11).

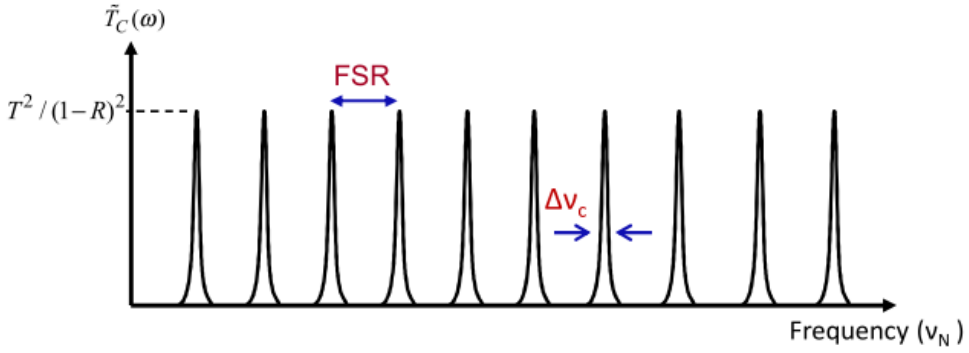

Figure 2.5: Transmission of the passive optical cavity: a comb of modes.

The separation in frequency between two successive peaks is called the Free Spectral Range (FSR) of the cavity and deduced from (2.14) to be FSR=c/2L. To find the cavity mode width, we expand the relation (2.11) around the resonance angular frequency ω_K, we will find the Lorentzian profile for $I_0(\omega)$:

$$I_0(\omega) = \frac{\dfrac{T^2}{(1-R)^2}}{1+\dfrac{4R}{(1-R)^2}\left(\dfrac{L}{C}\right)^2(\omega-\omega_K)^2} I_i(\omega) \tag{2.15}$$

From the above relation (2.15), we can deduce the Full Width at Half Maximum (FWHM) of one cavity peak or the spectral width $\Delta\nu_c$ of the cavity mode as a function of mirrors reflectivity:

$$\Delta\omega_c = 2\times\sqrt{\frac{(1-R)^2}{4R}\left(\frac{c}{L}\right)^2} = \frac{c(1-R)}{L\sqrt{R}} =$$
$$\Delta\nu_c = \frac{c(1-R)}{2\pi L\sqrt{R}} = \frac{FSR}{F} \tag{2.16}$$

Where F is called the cavity finesse, and given by:

$$F = \frac{\pi\sqrt{R}}{1-R} = \frac{FSR}{\Delta\nu_c} \tag{2.17}$$

From the relation (2.16), we can see that $\Delta\nu_c$ becomes narrower if the cavity length *L* is increased or the mirror reflectivity (equivalently the finesse) is increased. The cavity finesse has a significant importance since the enhancement factor of the absorption sensitivity is directly related to its value as explained in the next paragraph.

2.3.2. Absorption sensitivity enhancement factor

In this section, the enhancement factor of the detection sensitivity is estimated for two limiting cases. The first one corresponds to a monochromatic laser mode which is perfectly resonant with the cavity mode, while the second case corresponds to a uniform (constant speed) scan of the cavity mode relative to the laser mode. We start by writing the output intensity in the presence of the absorption of the sample gas, and calculating the cavity transmission. An easy way to get that is to use the same expression (2.11) and replacing the reflectivity $R(\nu)$ by the effective reflectivity per pass which includes the gas absorption, $\mathrm{R}_{\mathrm{e}ff} = R(\nu)e^{-\alpha(\omega)L}$. Then, the cavity transmission can be rewritten as:

$$\tilde{T}_c(\nu) = \frac{T^2 e^{-\alpha(\omega)L}}{(1-R_{eff})^2 + 4R_{eff}\sin^2(k(\omega).L)} \tag{2.18}$$

2.3.2.1. Enhancement factor at the resonance

At the resonance as shown in Figure 2.6, the cavity transmission reaches its maximum, which is given as:

$$T_c^{res} = \frac{T^2 e^{-\alpha L}}{(1-R_{eff})^2} \tag{2.19}$$

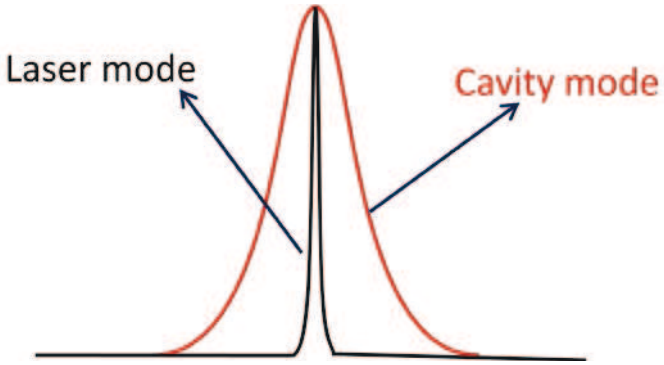

Figure 2.6: Resonance between the cavity mode and the laser mode.

In practice, we do not measure the transmission given in (2.19), but we need to measure the ratio between the transmitted spectra with and without the intracavity sample gas, to cancel out all the common factors (laser emission and spectrometer response profiles), and all other conditions will be identical. The ratio can be written as

$$s^{res}(\nu) = \frac{T_c^{res}(\alpha \neq 0)}{T_c^{res}(\alpha = 0)} = \frac{(1-R)^2 e^{-\alpha L}}{(1-Re^{-\alpha L})^2} \tag{2.20}$$

By applying a first-order Taylor expansion for small α corresponding to weak absorption, this yields:

$$s^{res}(\nu) = 1 - \frac{2}{(1-R)}\alpha L = 1 - \frac{2F}{\pi}\alpha L \Rightarrow$$
$$1 - s^{res}(\nu) = \frac{\Delta I}{I_0} = \alpha(\nu) \times L \times (2F/\pi) \tag{2.21}$$

Where, the term $(1-R)$ is nearly equal to F/π from the relation (2.17) in the high reflectivity limit $(\sqrt{R} \square 1)$.

By comparing (2.21) and (2.4), we can see the advantage of using the HF cavity where the absorption sensitivity is increased by a factor of $2F/\pi$. We may conclude that the absorption path length is enhanced by this factor, and we define an effective absorption path length by:

$$L_{eff}^{res} = (2F/\pi) \times L \tag{2.22}$$

For *L*=1 m, and *R*=0.99995 %, the finesse is *F*=62830 calculated from (2.17) leading to an effective absorption length of 40 km. Obviously, it is difficult to reach such value of the absorption path length by using a multi-pass cell technique explained earlier.

2.3.2.2. Enhancement factor when scanning the cavity mode around the resonance

If we modulate the optical cavity length over one FSR around the resonance at constant speed, as shown in Figure 2.7, then the time averaged transmission T_c for one cavity mode is obtained by the integral of the transmission given in the relation (2.18) over one full FSR (argument of sinus from 0 to 2π), and this yields:

$$T_c = \frac{1}{FSR}\int \tilde{T}_c(\nu)d\nu \quad \frac{T^2 e^{-\alpha L}}{(1-R_{eff})^2} \Rightarrow \frac{1}{2\pi}\int_0^{2\pi} \frac{1}{1+\xi.\sin^2(\psi)} d\psi$$

$$T_c = \frac{T^2 e^{-\alpha L}}{1-R_{eff}^2} \tag{2.23}$$

Where $\xi = 4\,\mathrm{R}_{e\,ff}/(1-\mathrm{R}_{e\,ff})^2$, and $\psi = k(\omega).L$.

We should mention that the modulation is made by a piezo electric transducer (PZT) mounted on one of the optical cavity mirrors, and this situation corresponds to our experimental implementation to couple the laser to the passive optical cavity.

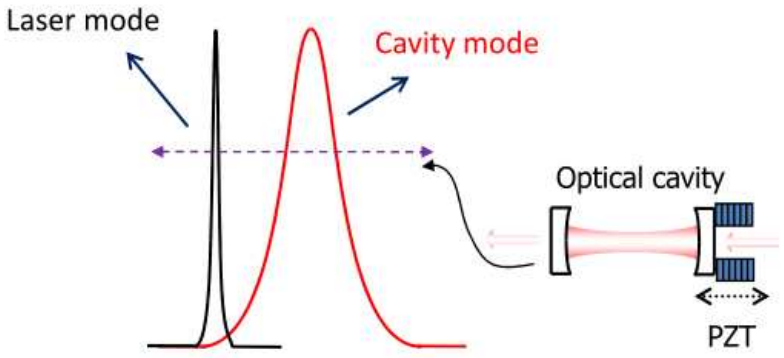

Figure 2.7: Scanning one cavity mode around the resonance, the scan is made by a PZT mounted on one of the cavity mirrors.

The ratio $S(\nu)$ between the transmitted spectra with and without the intracavity sample gas can be expressed as follows:

$$S(\nu) = \frac{T_c(\alpha \neq 0)}{T_c(\alpha = 0)} = \frac{(1-R^2)e^{-\alpha L}}{1-R^2 e^{-2\alpha L}} \tag{2.24}$$

Which can be rewritten with respect to the sample absorbance (keeping only the solution making physical sense):

$$\alpha(\nu) = -\frac{1}{L}\ln\left(\frac{R^2 - 1 + \sqrt{(R^2-1)^2 + 4s^2R^2}}{2sR^2}\right) \tag{2.25}$$

By applying a first-order Taylor expansion for small (1 – R) as a new variable for the expansion, we obtain:

$$\alpha(\nu) = \frac{(1-s)(1-R)}{sL} \times \frac{(1-s)}{s} \quad \frac{\pi}{LF} \tag{2.26}$$

The above equation can be rewritten as a function of the cavity finesse and the fractional absorption as:

$$\alpha(\nu) \times L \times (F/\pi) = \frac{\Delta I}{I} \approx \frac{\Delta I}{I_0} \tag{2.27}$$

By comparing (2.27) and (2.4), we can see that the absorption sensitivity is increased by a factor of F/π, and the relevant effective absorption path length is given by:

$$L_{eff} = (F/\pi) \times L \tag{2.28}$$

From (2.22) and (2.28), we can see that the absorption lines appear at cavity transmission doubled in strength in the case of injection at the resonance compared with the case of modulating the cavity length around the resonance.

In summary, the finesse determines the absorption enhancement factor inside the cavity, and the fractional change in laser intensity $\frac{\Delta I}{I}$ transmitted through the cavity is given by:

$$\frac{\Delta I}{I}(\nu) = \alpha(\nu) \times L \times (\gamma F/\pi) \tag{2.29}$$

Where $1 \leq \gamma \leq 2$ is a factor that depends the coupling scheme between the laser mode and the cavity mode. The effective absorption path length is then given by:

$$L_{eff} = (\gamma F/\pi) \times L \tag{2.30}$$

This large effective path length L_{eff}, up to tens of kilometers, obtainable in a relatively compact space, make the ML-CEAS an extremely sensitive and convenient technique for detection of very weak absorptions. In practice, we need to measure the absorption coefficient $\alpha(\nu)$ as experimental spectroscopic data. To retrieve $\alpha(\nu)$ (see relation(2.26)), the measured signal $S(\nu)$ is required as well as the cavity finesse which depends only on the

mirrors reflectivity. Indeed, the finesse is usually estimated by measuring the ring-down time τ_{rd} that we are going to define in below.

2.3.3. Cavity response time (Ring-down time)

When a photon enters the cavity, it may be reflected backward and forward, thus "ringing" hundreds or thousands times between the cavity mirrors, before it is transmitted through the cavity. When the input light is switched off, the photon life time of a cavity mode is defined as the characteristic time of the decay of optical energy stored in that cavity mode. Since light circulating inside the cavity experiences constant fractional losses per pass given by $(1-R)$ for an empty cavity (no gas absorber), the intensity will decay exponentially as $\exp(-t/\tau_{rd})$, where τ_{rd} is the decay time or the ring-down time, defined as the time for which the detector signal decreases to 1/e of its maximum value, and given by:

$$\tau_{rd} = \frac{L}{c(1-R)} \approx \frac{L \times \pi F}{c} \tag{2.31}$$

Here, $(1-R)$ represents the energy losses by the transmission and the mirrors.

In the presence of the intracavity gas sample, the absorption at the resonance frequency will create an increase in the losses results in decreasing the ring-down time. By combining the relations (2.26) and (2.31) we can write $\alpha(\nu)$ as a function of the measured signal $S(\nu)$ and τ_{rd}:

$$\alpha(\nu) = \frac{(1-s)}{s} \times \frac{1}{\tau_{rd} \times c} \tag{2.32}$$

From the above relation we can see the importance of the precise measurement of τ_{rd} to retrieve $\alpha(\nu)$. Figure 2.8 displays the experimental method for the ring-down measurement (RD), which is performed by injecting the laser light into a resonant mode of the cavity and then rapidly switching off the incident light when the photodetector signal reaches a certain threshold. To switch the incident light off, an acousto-optic modulator is used that can provide switching times on the order of 1 microsecond, sufficiently shorter than the HF cavity life time τ_{rd}.

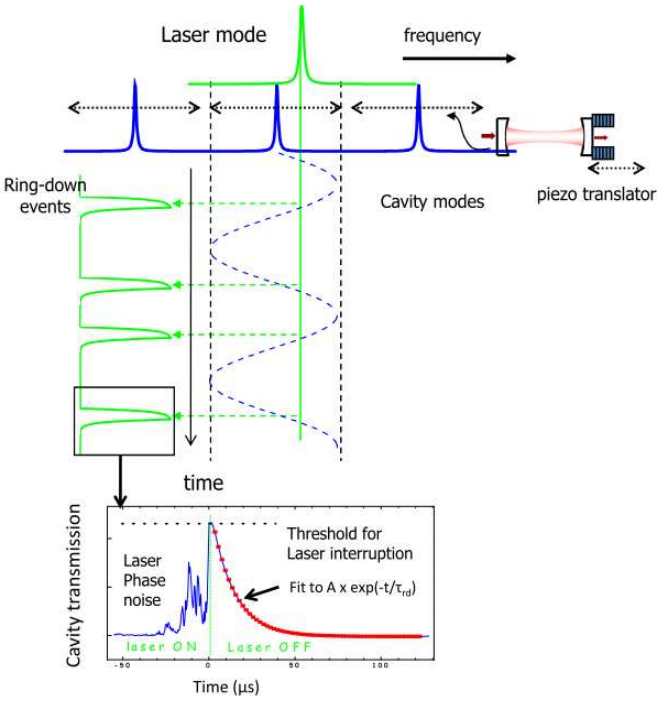

Figure 2.8: Experimental method used for the ring-down measurements.

The single-frequency RD measurement explained here can be generalized to a comb, which makes sense if the comb is not too large relative to the mirror stopband, otherwise one also needs to add a spectral filtering system to obtain the RD over a sufficiently narrow spectral region. Then the RD value can be used to normalize the ML-CEAS spectrum.

2.3.4. Intracavity dispersion of a high finesse optical cavity

To effectively couple a frequency comb into a cavity, each comb mode must be maximally matched with the corresponding cavity mode, and this requires a cavity mode spacing (FSR) equal to the comb modes spacing (f_{rep}). We have seen that the frequency comb consists of regularly spaced modes, but unfortunately, the cavity FSR varies with the optical frequency due to the intracavity dispersion. In the following, we study the effect of this dispersion on the coupling efficiency. In the absence of dispersion, the cavity modes are separated by $FSR_0=c/2n_0L$. But in general, the FSR is given by [19]:

$$FSR = \upsilon_g / 2L = \frac{c}{2L\left(n_0 + \omega\frac{\partial n}{\partial \omega}\right)} \tag{2.33}$$

The term $\frac{\partial n}{\partial \omega}$ shows the dependence of the FSR on the intracavity dispersion, and by using first order Taylor expansion in $\frac{\partial n}{\partial \omega}$, the FSR is rewritten as:

$$FSR = \frac{c}{2Ln_0\left(1+\frac{\omega}{n_0}\frac{\partial n}{\partial \omega}\right)} = \frac{c}{2Ln_0}\left(1-\frac{\omega}{n_0}\frac{\partial n}{\partial \omega}\right) \rightarrow$$
$$FSR = \frac{c}{2Ln_0} - \frac{\omega.c}{2Ln_0^2}\frac{\partial n}{\partial \omega} = FSR_0 + \Delta FSR(\omega) \quad (2.34)$$

The frequency of the cavity mode of order *m* can be given by:

$$\nu_{m,cav} = \sum_{i=0}^{i=m} FSR_i(\omega) = \sum_{i\ 0}^{i\ m}(FSR_0 + \Delta FSR_i(\omega))$$
$$= mFSR_0 + f_{0,cav} \quad (2.35)$$

Where $f_{0,cav} = \sum_{i=0}^{m} \Delta FSR_i(\omega)$ accounts for the dispersion and depends on the frequency, and the position of the mode.

As a comb mode of order n is given by ($\nu_n = nf_{rep} + f_0$), to match this mode to a cavity mode of order m given by (2.35), we can see the importance of the dispersion effect. Indeed, the consequence of a frequency dependent $f_{0,m,cav}$ is that it limits the perfect matching between the laser comb and the cavity modes. The perfect overlap between the entire bandwidth of frequency comb and the cavity modes is then generally possible over a limited spectral window over which the maximum deviation of the FSR is less than the combined width of the cavity and laser modes (more precisely one should consider the width of the convolution of the two comb line profiles). However, this effect of the intracavity dispersion does not exist for the laser cavity due to the nonlinear mechanism of mode-locking leading to the femtosecond regime where all the laser modes are in phase. Moreover, the separation between two ML laser modes has been shown to be uniform to a precision of 10^{-17} [18]. The dispersion measurement can be made by measuring the FSR over a large bandwidth by injecting single-frequency lasers or a comb into the optical cavity under characterization [41]. In the following section we discuss how to couple the laser comb modes with the corresponding resonant cavity modes, and how to control the coupling process to minimize the impact of dispersion.

2.4. Coupling comb-cavity

2.4.1. Introduction

I describe the comb-cavity interaction in the frequency and time domain, and how to control this interaction. It is easy to start by the frequency domain where a simple physical static image can be made about the two combs of modes which characterize the laser emission and the cavity transmission spectra as shown in Figure 2.9.

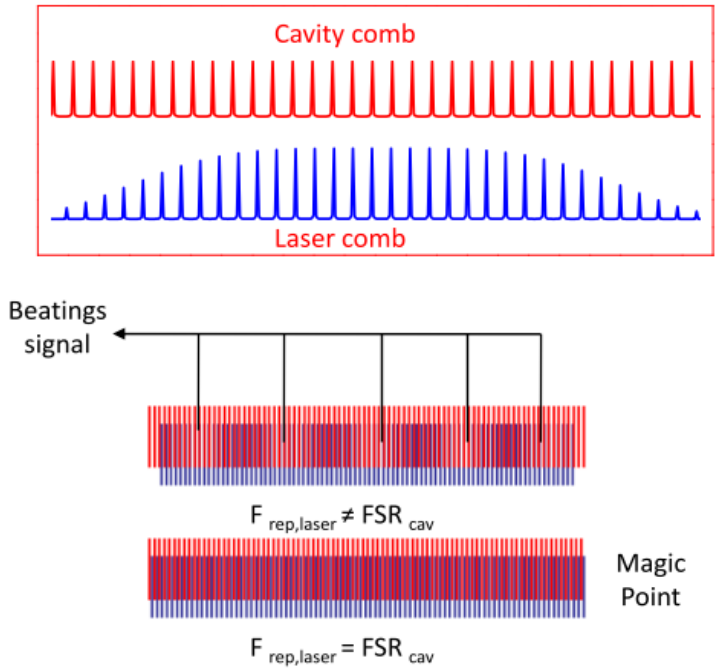

Figure 2.9: Top window: Cavity comb (in red), and laser comb (in blue). Bottom window: Different positions between the two combs. Beatings signal appears when f_{rep}≠FSR. Perfect matching (magic point) is obtained when f_{rep}=FSR.

2.4.2. Concept of comb-cavity coupling

To transmit the laser spectrum through the cavity, an overlap between the two combs is required, that implies making the cavity FSR equal to the laser repetition rate (f_{rep}) (or an integer number of f_{rep}). This is true if we neglect initially the presence of frequency offsets (f_0, $f_{0,cav}$) affecting these combs. In our case, this match can be achieved by adjusting the cavity length; and during the adjustment procedure, when the two combs are far from the perfect matching position; a periodic signal of beating peaks between the two combs appears as shown in Figure 2.10. The beating signal here is formed by groups of laser modes from different laser spectral regions which go in resonance with the cavity modes all at the same time. Here, the cavity length displacement δL is obtained by a translation stage mounted on the input cavity mirror, and there is no modulation to the cavity length. The beating peaks period $\Delta\nu_b$ is related to δL by [3]:

$$\Delta\nu_b = \frac{c}{2N_c\delta L} \tag{2.36}$$

Where N_c accounts for the ratio between the FSR_{cav} and f_{rep}. In our case N_c =2.

When the mismatch δL between the two combs decreases, the period $\Delta\nu_b$ gets larger as indicated from the above relation, and thus the number of the beating peaks decreases.

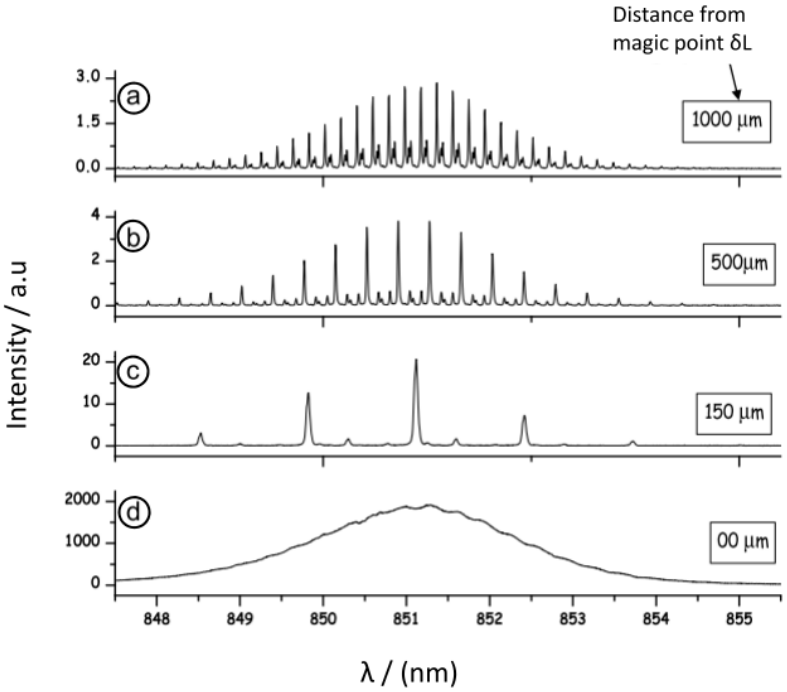

Figure 2.10: Output laser spectrum registered after the cavity at different distances from MP [3]. a,b,c: display the beatings signal when a mismatch occurs between the two combs, d: displays the perfect matching (MP) between the two combs, and the whole laser spectrum is efficiently transmitted.

Indeed, when δL decreases, the width of each peak becomes larger (as shown in Figure 2.10) due to matching an increasing number of laser modes to corresponding cavity modes simultaneously. When the perfect matching (Figure 2.10.d) between the two combs (which is called magic point (MP) for simplicity) approaches ($\delta L = 0$), the cavity starts flickering with giant bursts of light appearing according to the occasional passage through the resonance of all cavity modes at a time. The resonance is not persistent in the absence of active control of the laser or the cavity parameters (f_{rep}, FSR_{cav}) due to the laser jitter and the mechanical instability of the optical cavity. When the two combs are perfectly matched, all the laser modes go in resonance with the corresponding cavity modes and the laser spectrum is efficiently transmitted as a whole, with no beating pattern over it, and the absorption lines of the sample gas may be obtained. The spectrum in Figure 2.10.d was recorded at the MP when the cavity length modulation was used to produce several bursts during the integration time of the charge coupled device (CCD) detector. To observe the interaction between the two combs in the time domain at different position, a systematic and periodic modulation is applied to the cavity length by using a piezoelectric transducer (PZT). The cavity transmitted signal is monitored by a photodetector and shown in Figure 2.11.

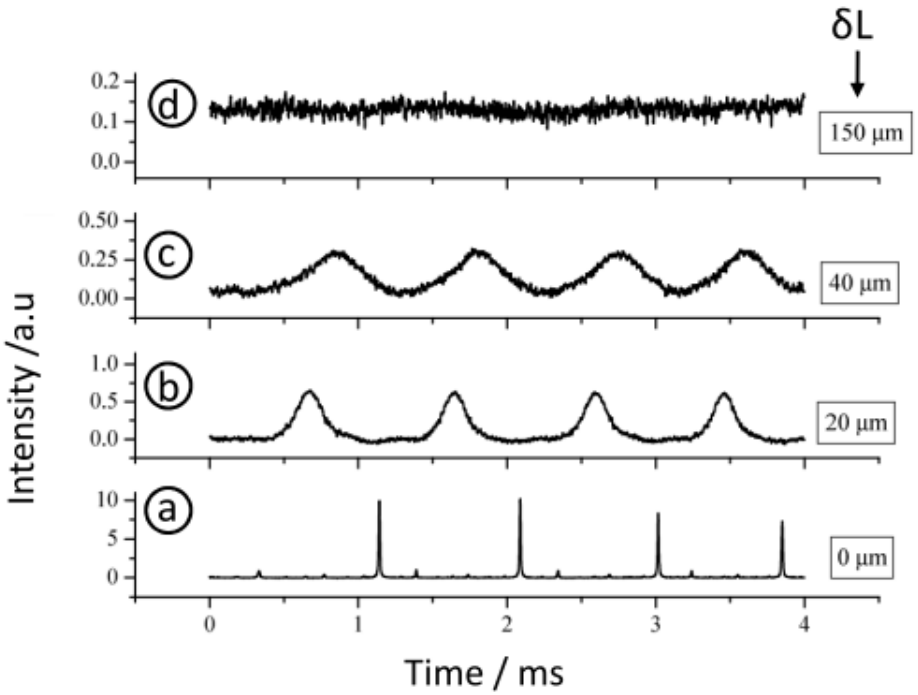

Figure 2.11: Cavity transmission as a function of displacement from MP. These oscilloscope traces correspond to a PZT scan of about 1 λ=4 FSR [3].

Here, the cavity displacement δL is obtained by a translation stage. When the two combs are close to the MP position δL < 150 µm, resonance peaks are observed, whose width becomes narrower when δL decreases to get closer to the MP as well as their intensity increases as shown in (Figure 2.11). A varying width of the resonance peaks is observed, because the modes in different parts of the laser spectrum pass through resonance with cavity modes at different times (temporal dispersion) as the cavity length scans. It is to be noted that, as long as resonances are well resolved, their area is constant due to the fact that the duration time to inject each laser mode into the cavity is constant. In Figure 2.11.d, the resonance peaks have nearly disappeared in the time domain. That means the overlap between the two combs consists of more than one beating peak in the frequency domain. Indeed by comparing with Figure 2.10.c, one can see that the distance from the MP (150 µm) corresponds to appearing of the beating pattern (about 3 beating peaks) in the transmitted spectrum. When getting closer to the MP as much as possible, very narrow peaks are observed as shown in Figure 2.11.a. One of these resonance peaks (close to 2 ms) is more intense as it corresponds to the best comb match, while the other resonances are less intense due to a small cavity length mismatch that is sufficient for not allowing simultaneous transmission of all laser modes. By looking closer, the resonances on the two sides of the strongest resonance are not equal in intensity. Modeling of the intensity of these resonances points out that this asymmetry relates to the laser carrier-envelop offset frequency (f_{ceo} or f_0). This effect could actually be explored as an alternative method to control the laser comb origin [42] as it will be explained later in Chapter 4.

To make a useful measurement, we need to maintain the resonance between the two combs, and to do this there are two strategies. The first one is to tightly lock the comb to the

cavity that means to stay exactly at the peak of the resonance, while the second one implies to make fast repeated scans around the resonance (Tracking). In the following subsections, we describe these strategies, their advantages and disadvantages.

2.4.3. Cavity injection by tight frequency Locking

The principle of the locking technique is to maintain a situation of perfect matching where all the comb modes are in resonance with the cavity modes simultaneously. Perfect coupling between the laser comb and the resonant cavity modes is shown in Figure 2.12.

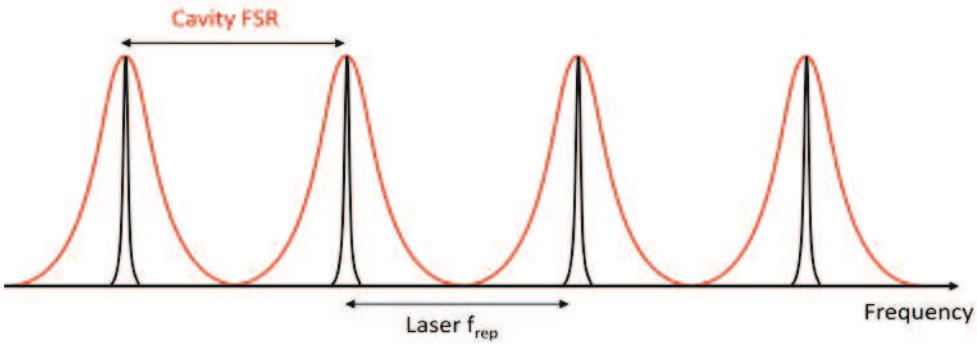

Figure 2.12: Perfect coupling between the two combs, in red: cavity comb, in black: laser comb.

To get the overlap, it is required to control the laser repetition rate f_{rep} to be equal to the cavity FSR (or an integer multiple), but because of (f_{ceo}), it may still exist a horizontal shift of the whole laser comb. If one tries to compensate for this mismatch by modifying the f_{rep}, this results in partial comb alignment, for example with only laser modes over the central region of the laser comb being sufficiently well in resonance with the cavity modes, while the laser modes at the edges of the laser comb will be out of resonance and rejected by the cavity. Controlling f_{ceo} in parallel with f_{rep} is thus necessary to avoid such a spectral filtering effect and increase the laser bandwidth injected into the cavity. However, the entire laser spectrum may not be completely injected due to the dispersion of the HF cavity, whose mode spacing FSR changes slightly with frequency as discussed earlier. The resulting spectral filtering effect may become significant when the cavity finesse is increased and the laser comb is sufficiently well stabilized, so the laser mode line width is comparable or smaller than that of the cavity mode. For example in ref [43], the spectral bandwidth injected into the cavity is limited to less than 10 % of the center frequency. Figure 2.13 displays the effect of the intracavity dispersion on the coupling between the two combs.

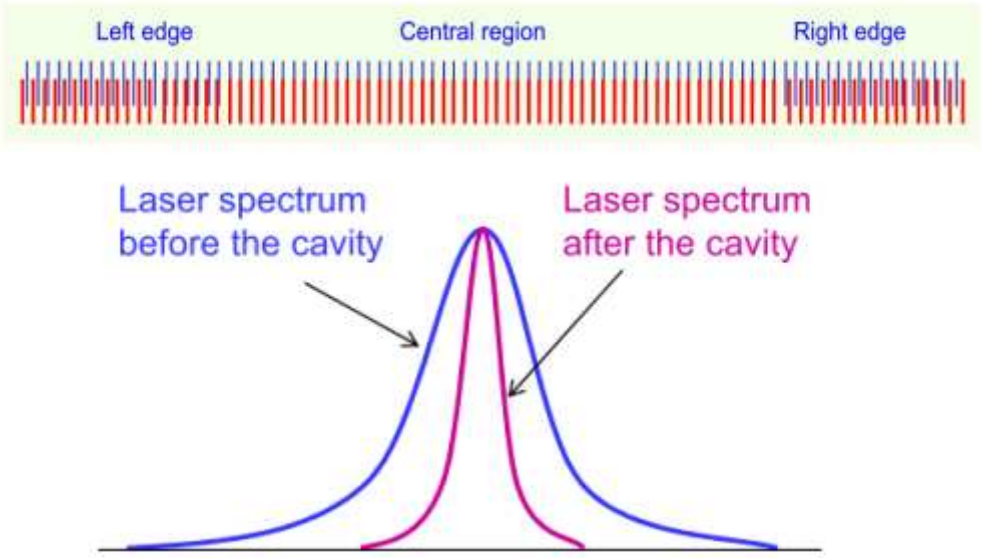

Figure 2.13: Top window: Cavity modes (in red), laser modes (in blue). Lower window: Effect of intracavity dispersion results in excluding the edges from the laser spectrum.

To frequency lock a laser to an optical cavity, different methods are available. One of the most widely used is the Pound-Drever-Hall (PDH) technique [44], which exploits the beat between the carrier field and non-resonant phase modulation sidebands. The sidebands provide a reference for the phase of the carrier reflected from the cavity. Another attractive technique is the Tilt lock [45], which uses a misalignment of the laser with respect to a reference cavity to produce a non-resonant spatial mode (TEM_{01}). By observing the interference between the carrier (TEM_{00}) and the (TEM_{01}), an error signal can be recorded. The Tilt locking technique offers a number of potential benefits over existing locking schemes including low cost, high sensitivity and simple implementation. This technique will be carefully explained in chapter 4. The main advantage of the locking is that the optical power transmitted through the cavity is maximized. Furthermore, the cavity transmission is continuously present. These two features yield a high signal to noise ratio (SNR) for measurements of the cavity transmitted light, and a fast averaging time. The main drawback of the locking is the spectral filtering, with only the frequency components in a more or less wide spectral window being simultaneously in resonance with the cavity modes, and the frequency components at the edges of this window going gradually out of resonance. As a consequence, in order to cover the entire laser spectrum, several measurements with different lock points on the laser bandwidth must be made. Another drawback is that a tight locking is sensitive to vibrations which lead to intensity noise of the cavity transmission and degradation of the detection sensitivity. Indeed, the last problem also makes a locking technique inconvenient for field measurements. Therefore, we developed another coupling mechanism described in below.

2.4.4. Cavity injection by modulation and resonance tracking

In this case, the cavity length is modulated around the resonance comb in a way that all the laser comb frequencies scan over the cavity modes or vice versa. This type of locking is called

a transient coupling [43]. Figure 2.14 displays a configuration of tracking technique when the cavity length is modulated by a PZT to scan the cavity modes over the laser modes.

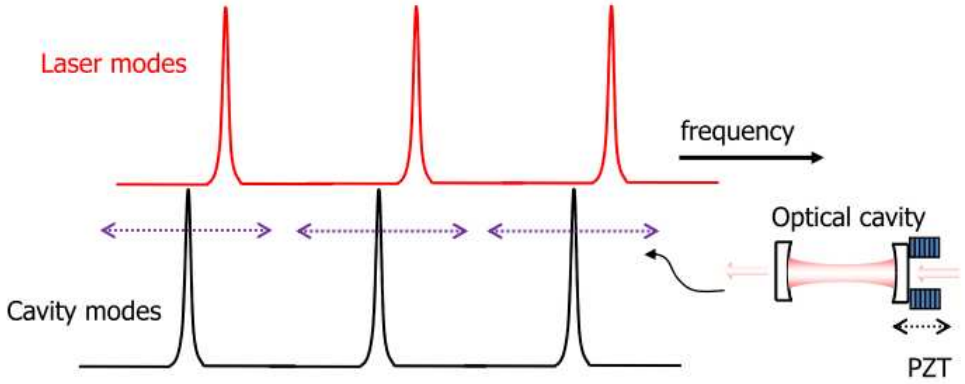

Figure 2.14: Configuration of tracking technique. In red: laser modes, in black: cavity modes. Cavity length is modulated by a PZT.

Here, there is no need to make a precise and simultaneous overlap between the laser comb frequencies and the HF cavity modes. The modulation permits all the laser modes in different parts of the laser spectrum to pass through resonance with cavity modes at slightly different times, but at the same speed, as the HF cavity length is modulated. Consequently, the injected spectral bandwidth is increased to the whole laser spectrum, and this is one of the advantages. Another advantage is that the intracavity dispersion effect is not a significant issue as long as the exact overlap is no longer needed. It should be underlined that a uniform scanning speed during a passage through resonance insures that the laser spectrum is transmitted without distortion. The scan frequency is chosen in order to reach a large number of fast passages through resonance within the integration time of the CCD. Applying higher modulation frequencies is useful to avoid the effect of mechanical vibrations and laser jitter, but the maximum value of the modulation frequency is limited by the cavity response time. This technique is more robust (it is insensitive to mechanical vibrations), and suitable for field measurements. The primary disadvantage is the loss in the useful cavity transmission due to the modulation duty cycle, but this is not a problem in our case, because of the high injected input power. Figure 2.15 illustrates the cavity transmission, and the ramp signal applied to the PZT in order to finely modulate the cavity length. A tracking electronic card is used to maintain the center of the modulation range on the comb resonance peak. This card requires the cavity transmission signal to detect the position of the resonance peak on the ramp and generate an error signal used to change a bias voltage applied to the PZT to move the ramp, as it will be explained later in more details.

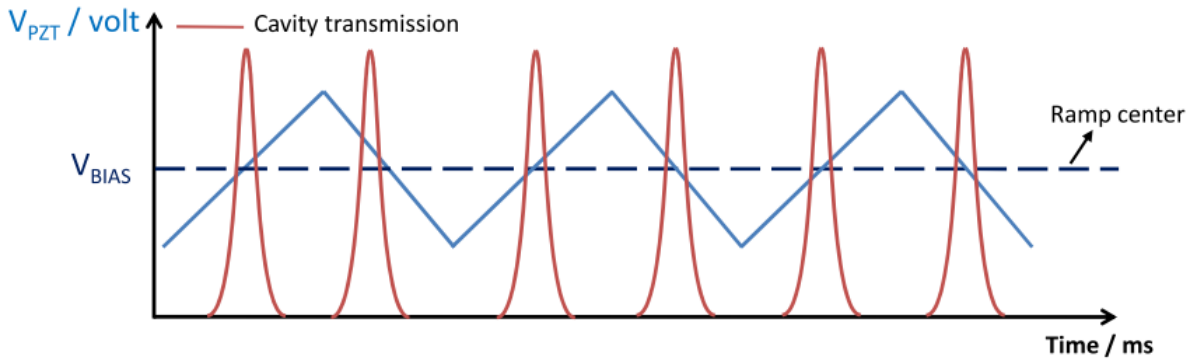

Figure 2.15: Cavity transmission peaks with a ramp signal at low frequency sent to a PZT.

2.5. Conclusion

We have explained in details the principle of the ML-CEAS technique, including the optical properties of the HF cavities, the sensitivity enhancement and the comb-cavity coupling. This technique provides ultrahigh sensitivity detection, a high spectral resolution, and rapid time acquisition. We will see, in a typical experiment, that more than 2000 data channels are recorded simultaneously over a bandwidth of about 2 nm with detection sensitivity better than 10^{-12} cm^{-1}. The spectral resolution can be better than 5 pm. In the next chapter, we describe the experimental realization of the developed instrument based on the ML-CEAS, all the related technical developments, and the measurements performed at the laboratory and at the field campaigns.

Chapter 3. Technical development and experimental data

3.1. Introduction

After explaining the principles of comb-CEAS and the different implementations of comb-cavity coupling in the second chapter, I describe in this one, the technical development of the instrument and the experimental measurements as well as the results and the perspectives. The technical development covers the spectrometer setup, the tracking electronic circuit, the automatism routines, the gas line and sample handling. The data analysis and the method to derive the detection limit from the measured spectra are presented. In addition, Allan variance study is made to investigate the instrument stability for long term measurements. The experimental measurements include the measurements made in the laboratory and at the field campaigns.

3.2. Technical development

In this section a complete description of the experimental setup is given, together with a detailed overview about the double cavity design, frequency doubling process, transverse-mode matching arrangement, tracking system to perform a transient coupling of the laser to the cavity, and a description and characterization of the homemade spectrograph. After that, the automatisms processes that control the adjustment of the instrument during long term measurements will be presented, ending on the gas sample circuit description and the samples preparation and test procedures.

3.2.1. Spectrometer Setup

Figure 3.1 shows a schematic diagram of the experimental setup. The instrument consists of a compact femtosecond (~100 fs, 80 MHz) laser oscillator (Chameleon, Coherent Inc.) with a laser head of 61x37x19cm^3 (which includes the doubled Nd:Yag pump laser). The laser source can automatically and rapidly be tuned from 677 nm to 1080 nm. it provides 700 mW of average power within 2 nm (full width at half max, FWHM) of bandwidth centred at 677 nm, and 2.5 W within 5 nm of bandwidth at 872 nm, which are the two wavelengths of interest for our application. The laser head is fixed under a 120 × 60 × 6 cm^3 aluminium honeycomb breadboard (Thorlabs), while the optical components are placed above. The laser radiation is frequency doubled with a 0.2 mm thick, type-I, BBO (β-barium borate) crystal (Fujian CASTECH Crystals, Inc.). The BBO crystal is mounted on a motorized rotation stage (AG-PR100, Newport) that allows computer controlled phase-matching optimization, which is crucial when the wavelength is switched from 338.8 nm to 436 nm. The lens L_1 of focal length of 40 mm is employed to focus the fundamental beam inside the BBO crystal.

The laser beam is spatially mode matched to the cavity mode (TEM_{00}) with a single lens (L_2, f=75 mm) placed after the doubling crystal. The mode matching means that the laser waist is equal to the HF cavity mode waist (TEM_{00}), and the two waists have the same position. The lens is mounted on a translation stage used to finely adjust the position of the focus which should fall in the center of the HF cavity. Three dichroic steering mirrors (DM_1, DM_2, and DM_3) are used as a band-pass filter to clean the beam from the fundamental radiation before injecting the optical cavity. An acousto-optic modulator (AOM), with 80 % efficiency on the first order diffracted beam which is injected into the cavity, acts as a fast optical switch: by interrupting the radiofrequency (RF) driving power, it allows to regularly perform ring-down measurements to determine the cavity finesse needed to calibrate the CEAS spectrum. Secondly, it is equivalent to a dispersive grating, acting thus as an additional filter that suppresses the residual fundamental radiation.

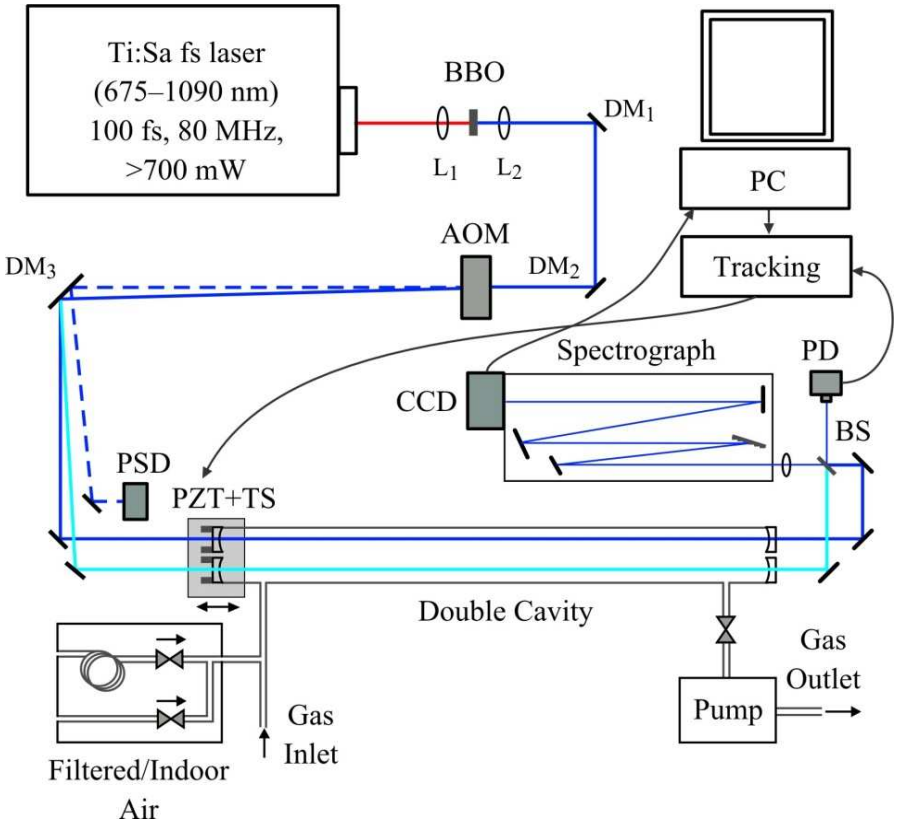

Figure 3.1: Schematic diagram of the experimental setup. BBO: Doubling crystal, L_1: Focusing lens, L_2: Matching lens, AOM: Acousto-optic modulator. DM_1, DM_2, DM_3: Dichroic mirrors, PZT: Piezo-electric transducer, TS: Translation stage, BS: Beam splitter, PD: Photodiode, CCD: charge-coupled device detector, PSD: Position sensitive detector.

Finally, by acting on the amplitude of the RF driving the AOM, the module can be used as a variable attenuator. This point, as we will see later on, it will be important for the detection at 436 nm, where attenuation (by a factor of 5) is needed in order to avoid saturation of the charge-coupled device (CCD) detector within its minimum integration time of 12 ms. A

double cavity is used to detect our target molecules at the two wavelengths (338.5 nm and 436 nm). By using a beam splitter, half of the cavity output is resolved by a laboratory-developed spectrograph based on an Echelle diffraction grating (Thorlabs, GE2550-0863, blaze angle = 63°, order @ 400 nm ~ 55, 79 grooves per mm) and a TE-cooled back-thinned CCD camera (Hamamatsu, C10151, 2048 × 250 pixels) providing high sensitivity in the UV region. The second half of the cavity output is sent to an avalanche photodiode to monitor the cavity transmission and to lock the cavity frequency around the comb resonance by tracking control electronics. The tracking technique is exploited to compensate for laser jitters and mechanical instabilities (vibrations and drifts) of the system by sending an error signal to the PZT together with a fast sinusoidal modulation (20 kHz and 5 kHz at 338.5 nm and 436 nm, respectively). Indeed, this type of locking scheme is more robust with respect to tightly lock the frequency of the oscillator to an optical resonator. Therefore, this scheme is more suitable for field measurements purpose, where the instrument is supposed to work in a rough environment. Data from the CCD camera are acquired in binning mode (the array becomes effectively 2048 H × 1 pixels V) by a 16-bits resolution acquisition card (NI-PCIe-6251, National Instrument). A position sensitive detector (PSD, Hamamatsu, S5990) with a surface of 4x4 mm^2 is placed to collect the zero order radiation transmitted by the AOM and reflected by DM_3 (as well as the 1^{st} order beam which is injected into the optical cavity), this detector helps the automatic procedure used to re-optimize the alignment of the beam and enhance its long term performance. The whole spectrometer is confined in an aluminium box covered by a thermal insulating material, thermalized by a peltier air-air exchanger (AA-040-12-22) module coupled to a PID temperature controller (Supercool, TC-PR-59). Figure 3.2 displays two pictures of the instrument from upper and lateral sides. The pictures also show the electronic parts of the instrument and the gas line. In the following sub-sections, we discuss in details the frequency doubling setup, the double cavity design, the tracking card, the gas line, and the automatism procedure to re-optimize the alignment of the instrument.

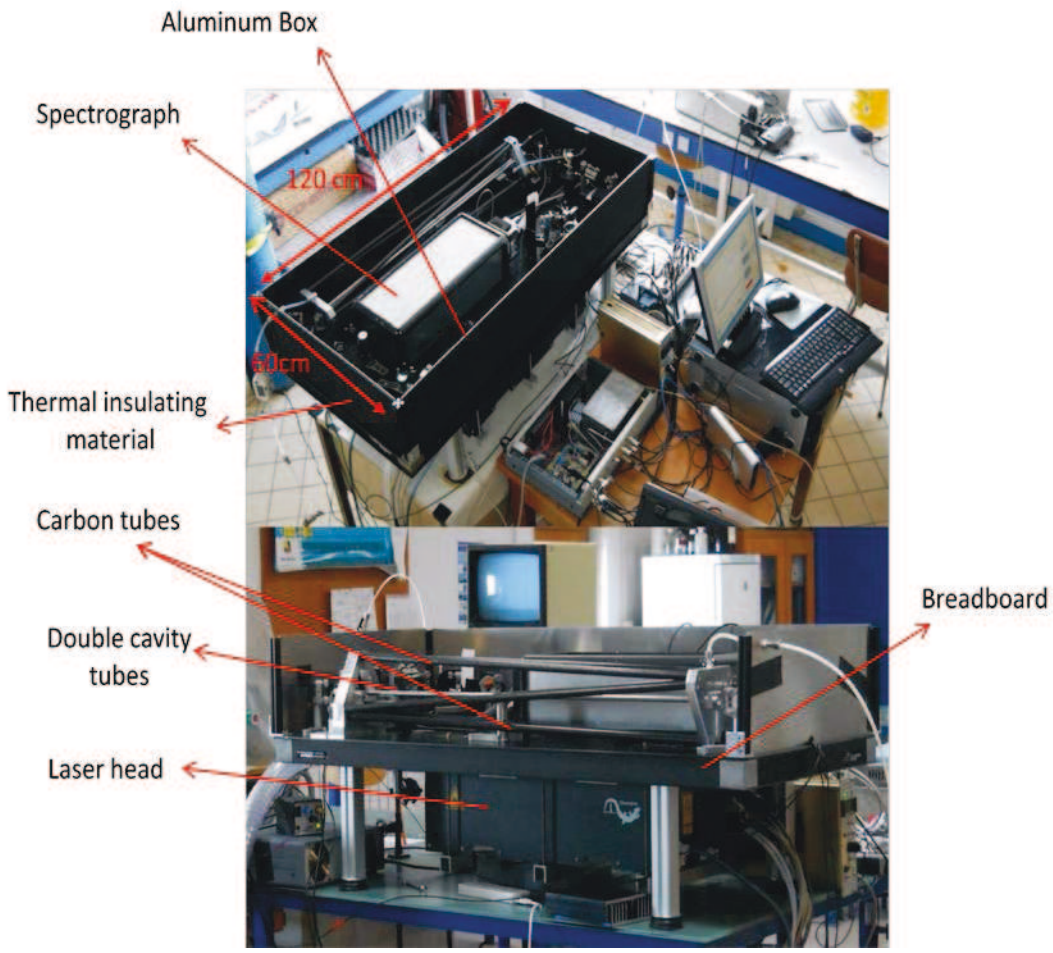

Figure 3.2: Two pictures of the transportable instrument. The laser head is attached under a honeycomb breadboard, which carries the rest of the optical system. The computer, the gas lines and other electronic devices are also visible.

3.2.2. Frequency doubling setup

Figure 3.3 displays a picture of the frequency doubling arrangement used in the experimental setup. A BBO crystal (Fujian CASTECH Crystals, Inc.) of length of L_C=0.2 mm thick is used for the type-I frequency doubling to reach the UV-VIS spectral range. The crystal thickness and the focusing lens were chosen (as seen in chapter 1) to get a good compromise between maximizing the SHG process while keeping a small walk-off and preventing astigmatism of the harmonic output beam due to chromatic dispersion. This is important to obtain clean and efficient single transverse mode cavity injection. The lens L_1, f=40 mm (see Figure 3.1) is used to focus the fundamental beam inside the BBO crystal to a waist of about 12 µm, which allows respecting the phase-matching conditions for both wavelengths of interest (338.5 nm, 436 nm). By rotating the BBO crystal by small steps, in order to optimize the phase-matching for either shorter or longer wavelengths, no shifts of the laser spectrum were observed, which indicates that the laser spectral width is not limited by phase-matching.

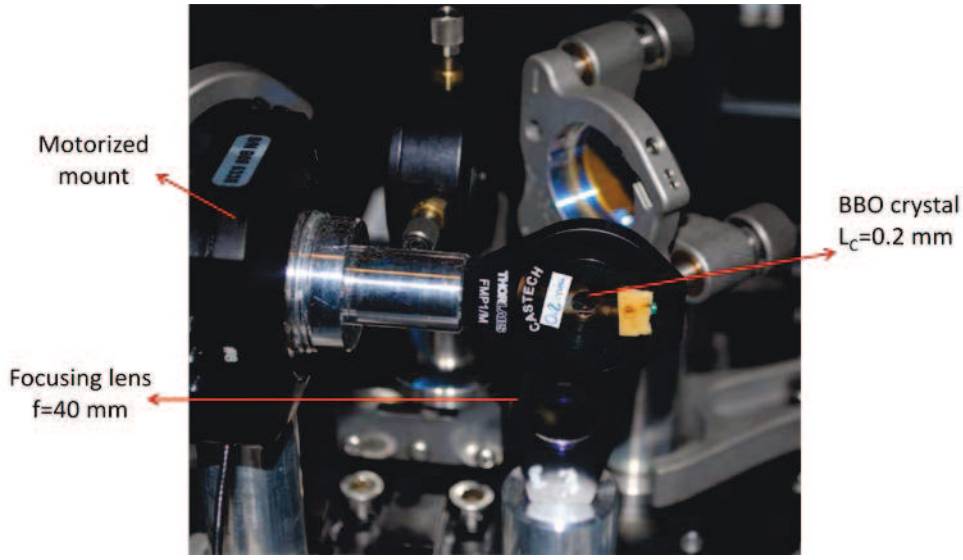

Figure 3.3: Picture of the frequency doubling arrangement which starts by the focusing lens F=40 mm. BBO crystal is fixed by a metallic black mount which is attached to a motorized mount.

Because of the small acceptance angle and the large walk-off of the BBO crystal (see chapter 1), to obtain a high SH conversion efficiency, a good laser beam quality is highly important. Generally, Ti:Sa fs laser sources satisfy this requirement while providing short pulses with a high peak power, which is another condition for an efficient second harmonic generation. Table 3.1 summarizes the measured SH power (P_{SH}), and the conversion efficiency (η) at the selected wavelengths.

λ_I(nm)	λ_{SH}(nm)	P_{in} (mW) at λ_I	P_{SH} (mW)	$\eta=P_{SH}/P_{in}$ (%)
677	338.5	750	32	4.2
872	436	2500	245	10

Table 3.1: Experimental results of the SH power at the selected wavelengths.

We should underline that the bandwidth of the measured SH spectrum $\Delta\lambda_{SH}$ was narrower than the bandwidth of the fundamental spectrum $\Delta\lambda_I$. The measured values of $\Delta\lambda_{SH}$ at the selected wavelengths are presented in Table 3.2, which coincide with the following relation:

$$\Delta\lambda_{SH} = \frac{\Delta\lambda_I}{2\sqrt{2}} \tag{3.1}$$

This relation comes from the fact that the product of the pulse temporal duration and its bandwidth (in frequency) is constant for the fundamental beam and the SH pulse, then we should consider that the SH pulse duration is shorter than the fundamental by a factor of $\sqrt{2}$.

λ_I (nm)	λ_{SH} (nm)	$\Delta\lambda_I$ (nm)	$\Delta\lambda_{SH}$ (nm)
872	436	5	1.8
677	338.5	2	0.7

Table 3.2: Measured values of the fundamental and the SH bandwidths.

3.2.3. Double cavity design

Given the separation of the two wavelengths of interest (of 100 nm between IO and BrO detection), it was not possible to find a single set of mirrors covering the whole range with high reflectivity. However, rather than setting up two independent cavities each with a motorized translation stage control and a solid structure to maintain the optical alignment, it was preferred to have a single structure and a single translation stage. This double high-finesse linear cavity is built inside six carbon bars mounted in a telescope-like arrangement (used in Dobsonian telescopes [46]) as shown in Figure 3.4. This configuration was chosen to provide the best stability for the HF double cavity to respond to constraints associated with field campaigns. The gas tubes are made of stainless steel where inside thin-walled PFA tubes are inserted to limit surface effects with the reactive halogen oxide radicals. A motorized translation stage (T-LS28, Zaber) is incorporated in the cavity to adjust its length around 90 cm, where the cavity FSR becomes twice the laser repetition rate. Metallic flexible bellow connections are fixed between each tube and the input-side cavity block mounted on the translation stage. The role of these flexible pieces is to allow the translation stage action on the cavity length.

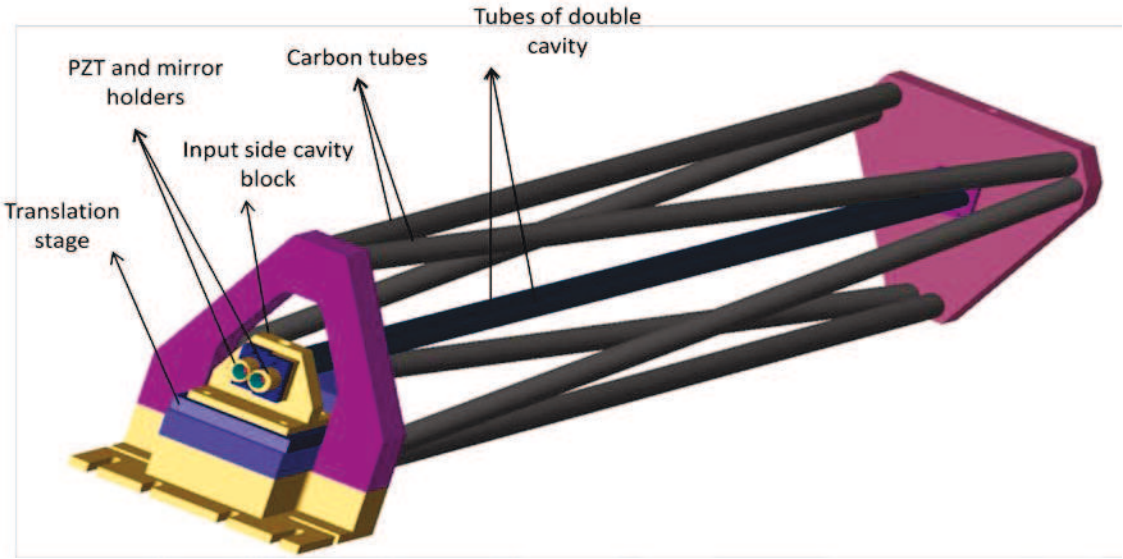

Figure 3.4: Telescope-like arrangement of double high finesse cavity to enhance the stability.

On one side of the cavity, the mirrors are mounted on piezo-electric tube transducers (PZT, type PT130.20 from PI) as shown in Figure 3.5 to modulate the cavity length across the comb resonance condition (while finely controlling the cavity FSR). The two sets of cavity mirrors (Layertec) are selected for their maximal reflectivity: 99.948 % and 99.990 % at 338.5 nm and 436 nm, respectively. The mirrors are pre-aligned and glued on aluminium holders that can be removed for cleaning and replacement purpose without affecting the optical alignment.

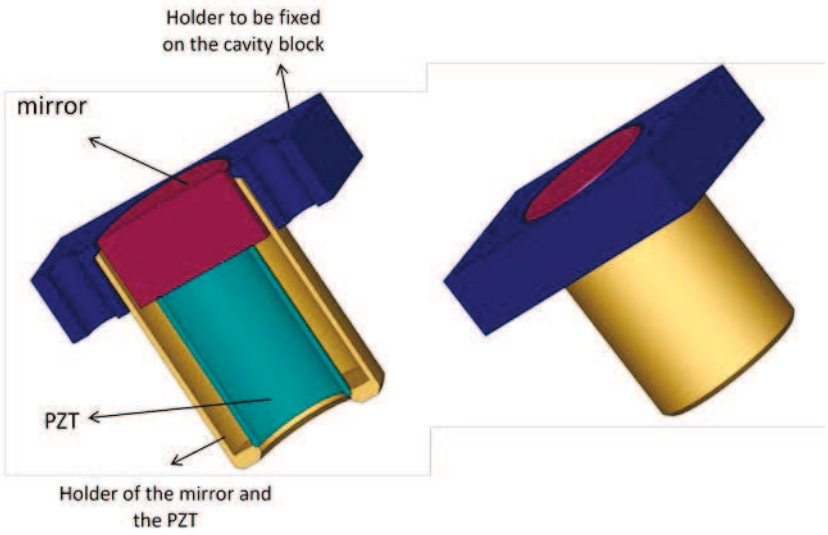

Figure 3.5: Right side, Holder of the mirror with PZT actuator. Left side: a section view of the holder.

The length of the cavity used at 338.5 nm is 93.7 cm, while the length of the cavity used at 436 nm is 93.3 cm. This difference in length is due to the difference (371 kHz) in the laser repetition rate at the two wavelengths, and compensated directly by the cavity design. Each cavity length is calculated to have a cavity free spectral range twice the laser repetition rate.

To obtain an optimal and reproducible cavity injection, the transverse-mode matching between the laser beam and the fundamental cavity mode is necessary, as discussed in the next section.

3.2.4. Transverse mode-matching and cavity alignment

As the laser beam is a diffraction-limited Gaussian beam (beam quality factor close to 1) that means most of the laser energy is concentrated in the fundamental transverse mode of the laser cavity. Therefore, to get efficient injection of the laser comb into the HF cavity (optical resonator) and maximize the cavity output intensity the laser beam has to match the fundamental transverse cavity mode (TEM_{00}). If this is not achieved, part of the laser power will be distributed among the cavity higher order modes, and this depends on the overlap of the laser beam with these modes. The matching [47] implies that, for a

symmetric resonator, the laser beam should have the same waist in the cavity center as the waist of the cavity mode TEM_{00}, and the beam at each cavity mirror have the same size. To obtain the mode matching, a lens L_2, with a focal of 75 mm (Figure 3.1) was placed at D_1=80 mm after the BBO crystal, and at D_2=730 mm before the cavity in order to focalize the second harmonic beam at the center of the cavity with the right size. D_1, D_2 are calculated taking into account the laser waist inside the BBO crystal of about 12 µm, and the waist in the center of the HF cavity of about 232 µm. The distances (D_1, D_2) are calculated at λ=338.5 nm, and they are slightly different at λ=436 nm. Therefore, the position of the lens L_2 is manually controlled to find the best position to get a good mode matching at both wavelengths. Here the cavity length is roughly adjusted by a translation stage to approach the MP. The cavity length is then carefully adjusted by moving the translation stage at slow speed using the smallest steps (about 1 µm which corresponds to the resolution of the translation stage) to detect the position when a spot starts flashing irregularly on a camera located after the cavity. The spot flashes are due to random fluctuations in the cavity length or the laser comb. This occurs when the MP is approached, and it corresponds to a single beating peak, of a period larger than the laser spectral width, between the laser and cavity comb. For the moment, this peak appears and disappears alternately according to the occasional matching between the two combs as the cavity or the laser comb fluctuates. The broader the laser spectrum, the narrower is the region around the MP where a single combs beating may be observed. The tuning of the cavity length can be also monitored by looking at the laser spectrum transmitted through the cavity with a high resolution spectrograph. When the two combs are mismatched, a particular comb beating is observed (chapter 2-Figure 2.10). When the cavity length approaches to the MP, the separation between two successive peaks becomes larger as well as the width of each peak. Here, by modulating the cavity length by one FSR, and monitoring the signal transmitted through the cavity with a photodiode, passages through comb resonance positions are visible as more or less narrow peaks depending on the closer match to the MP (Chapter 2, Figure 2.11).

After adjusting the cavity length and the input beam path to achieve the MP condition and the best mode matching, the photodiode signal is sent to the tracking electronic card to ensure that the transient resonance between the two combs occurs at the center of the cavity length sweep. In the following section, the principle and operation of the tracking card to perform transient coupling of a frequency comb to an optical resonator is described.

3.2.5. Tracking control

We had explained in the second chapter, the different implementations of the comb-cavity coupling, in particular, the transient coupling that is deployed in our application. The coupling procedure is realized by a home-made tracking card. The aim of this electronic card is to produce a periodic symmetric triangular signal (V_{PZT}) to be applied to the cavity mirror PZT to modulate the cavity length around the resonance between the cavity and the laser comb. This triangular modulation has a bias voltage which is controlled to obtain the

passage through resonance at the center of at each ramp composing the triangular modulation. The frequency of the modulation should be as fast as possible to avoid the laser field phase fluctuations producing amplitude fluctuations at the cavity output [47, 48]. In other words, the duration of the passage through resonance must be comparable or shorter than the laser coherence time. In our case, we make the modulation frequency large enough that the shape of the passage through resonance begins to appear asymmetric since its duration is close to the cavity response time, which is about 6 µs (30 µs) at 338.5 nm (436 nm). This also ensures that all laser modes pass through resonance at the same speed, but with a small temporal dispersion since we do not control the comb offset nor the cavity dispersion effects. This avoids non-uniform injection across the laser spectrum which would produce distorted cavity-enhanced spectra. Given that the modulation frequency is high and the duration of the passage through resonance is limited by the cavity response time, the piezo modulation amplitude has to be rather large in order to still obtain well separated peaks in time. In our case, we used the largest setting which corresponds to FSR/2 (notice that since f_{rep} is half the cavity FSR, there is actually one resonance when scanning the cavity over one FSR/2).

To track the cavity PZT bias to satisfy the above mentioned centering condition, the output cavity transmission is recorded by a PD, whose signal is sent to the tracking card. The card generates a gate signal (Figure 3.6.c), when the PD signal becomes higher than a certain threshold (Figure 3.6.b). A sample-and-hold circuit (in the card) is then used to sample the value of the modulation signal (without any bias, as a triangle centered around zero voltage) at the gate pulse time. This generates an error signal, since the sample-and-hold output will be zero only when the resonance occurs at the center of the modulation ramps. This error signal is sent to an integrator circuit (in the card) to produce a correction to be used as a piezo modulation bias voltage (a summing circuit adds this bias to the original triangle modulation). It should be noticed that the integrator makes this bias increase or decrease each time the error signal is not zero, with the effect of bringing the error towards zero if the sign of the control loop is correctly chosen (there is an inverting circuit on the tracking card which can be activated if this sign is not right).

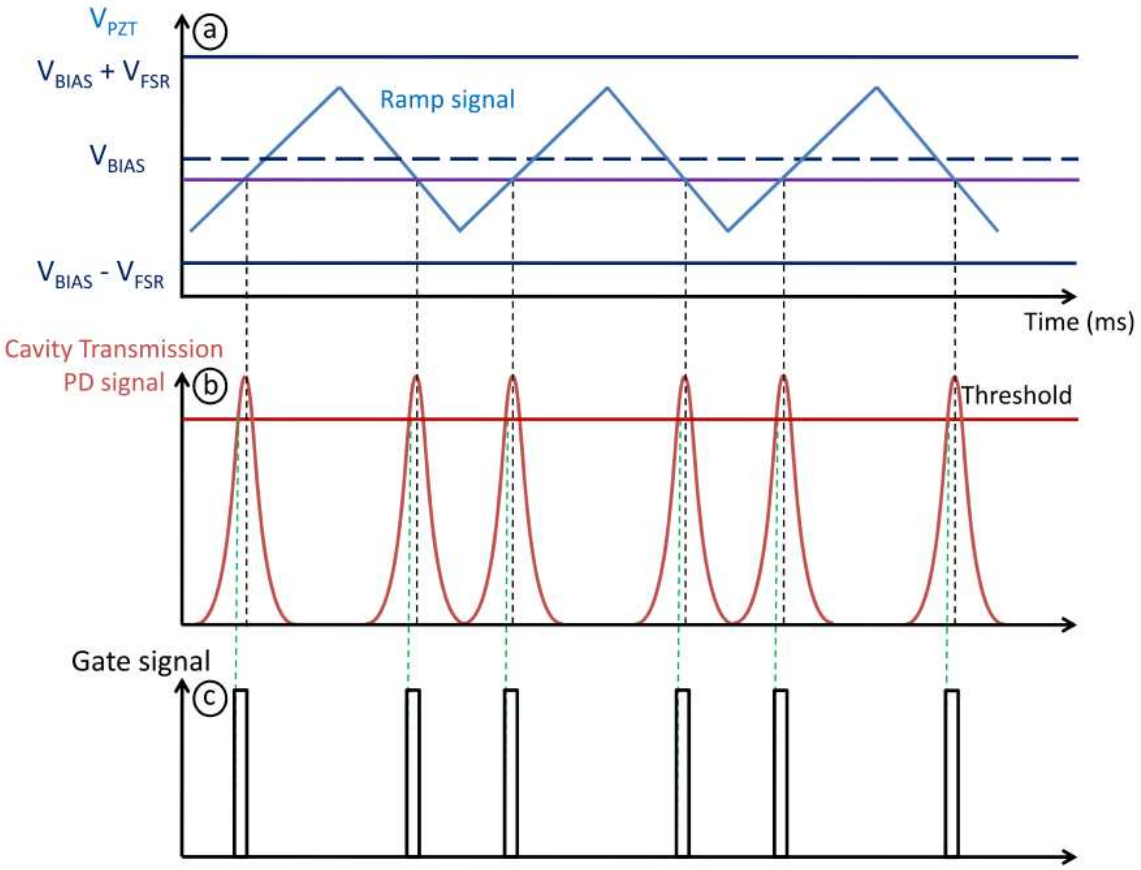

Figure 3.6: a: Output signals (V_{PZT}, V_{BIAS}), of the card, sent to the PZT, b: PD signal which is the input signal of the card, c: The gate signal generated inside the card. The error signal is given by the violet level with respect to the center of the modulation V_{BIAS}, thus it is a negative error which is sent to the integral to reduce the V_{BIAS} value. As V_{BIAS} decreases, the modulation signal V_{PZT} is shifted down which makes the resonance occurs closer to the center of the modulation ramps.

If the detected resonance peaks occurs in the negative part of the modulation ramp (below the ramp center, violet level in Figure 3.6.a, the input error signal of the integrator is negative leading to reduce the value of the bias voltage sent to the PZT. This will re-center the position of the resonance peak with respect to the PZT ramp. Inversely, if the detected peaks are above the center of the ramp, the input error signal of the integrator is positive leading to increasing the value of the bias voltage sent to the PZT to shift the ramp vertically to a higher position, and re-center the peak position. The modulation amplitude must be less than FSR/2 in order to avoid multiple transmissions within the cavity modulation window. Additionally, the used modulation frequency is above the resonance frequency of the PZT. This allows us to modulate the PZT at higher frequency, but an inversion in phase occurs, which means that the phase of the bias signal should be reversed as well.

As we have seen, by a successful tracking procedure, all the laser frequencies are transmitted by the HF cavity almost simultaneously, so it is necessary to use a spectrograph to separate them and recover the laser spectrum which contains the intracavity sample absorption information. For this, a home-made spectrograph is built as described in below.

3.2.6. Home-made spectrograph

A home-made spectrograph has been realised which can combine both compactness and high resolution. For this aim, a specific high order reflection grating has been employed. This grating is called Echelle Grating or blaze grating [49], resembling a saw tooth with steps inclined at the angle θ (blaze angle) relative to the grating plane as shown in Figure 3.7. The interest of using such grating is in its ability to concentrate the diffracted energy at higher order which increases the spectral resolution as it will be explained later. The grating is operated near the Littrow configuration (see Figure 3.7.b). In addition to using a blaze grating, particular design of the spectrometer has been chosen in order to achieve 5 pm resolution within a 2 nm spectral window. Our experiment requires such high resolution to resolve the rotational structure of the absorption bands of the target molecules, IO and BrO. The commercial available spectrographs providing such resolution are very bulky, not suitable for a transportable instrument to make field measurements.

3.2.6.1. Basic property of diffraction gratings

The main properties of a spectrograph depend on the characteristics of its diffraction grating, including the angular dispersion, the spectral resolution, and the free spectral range. Here, a brief overview is presented to explain these properties.

3.2.6.1.1. Angular dispersion of a grating

Suppose a parallel light beam incident onto two adjacent grooves of a grating as shown in Figure 3.7.a.

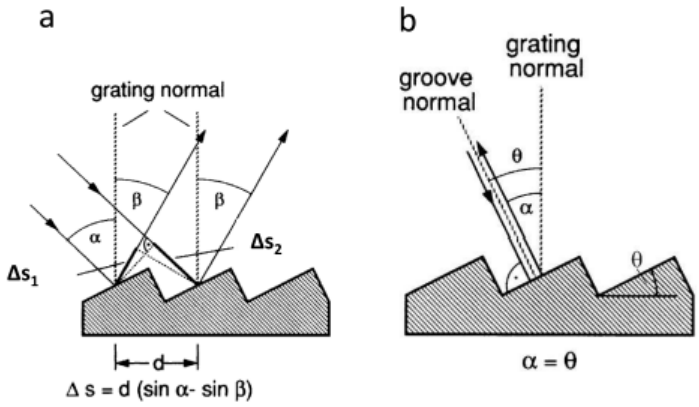

Figure 3.7: (a) Illustration of an Echelle grating, (b) Littrow configuration [49].

At an angle of incidence α to the grating normal (which is normal to the grating surface, but not necessarily to the grooves), one obtains constructive interferences at the far field of the reflected light for which the path difference, $\Delta s = \Delta s_1 - \Delta s_2$, is an integer multiple m of the wavelength λ. With $\Delta s_1 = d \sin \alpha$ and $\Delta s_2 = d \sin \beta$, this yields the grating equation:

$$d(\sin\alpha \pm \sin\beta) = m\lambda \tag{3.2}$$

Where *m* is the order of diffraction, *d* is the grating constant which corresponds to the distance between grooves, and β is the reflection angle measured from the grating normal. The plus sign has to be taken if β and α are on the same side of the grating normal; otherwise the minus sign has to be taken.

For near Littrow-grating configuration ($\theta = \alpha \square \beta$), the grating equation (3.2) for constructive interference becomes:

$$2d\sin\beta = m\lambda \tag{3.3}$$

By differentiating the above relation with respect to λ, we obtain for a given angle α, the angular dispersion *D* measured in (mrad/nm):

$$D = \frac{d\beta}{d\lambda} = \frac{m}{d\cos\beta} = \frac{\sin\alpha \pm \sin\beta}{\lambda\cos\beta} = \frac{2\tan\theta}{\lambda} \tag{3.4}$$

3.2.6.1.2. Spectral resolution of the grating

The spectral resolution of grating is given in terms of spectral resolving power *R* by the expression [49]:

$$R = \left|\frac{\lambda}{\Delta\lambda_{\min}}\right| = mN \tag{3.5}$$

Where $\Delta\lambda_{min} = \lambda_1 - \lambda_2$, is the minimum separation of two closely spaced monochromatic wavelength (λ_1 and λ_2) that are considered to be just resolved by the instrument. *N* is the total number of illuminated grooves, and *m* is the diffraction order. The previous formula is derived from the Rayleigh criterion [49] .

The special type of Echelle grating which is optimal to work on the higher order (m=10-100) helps to increase the resolution as indicated from (3.5).

3.2.6.1.3. Free Spectral Range of a grating

The grating free spectral range (FSR_g) is the maximum spectral bandwidth that can be obtained, with a specific diffraction order, without spectral interference (overlap) from two adjacent orders. For a given diffraction order, *FSRg* is calculated by the difference between two wavelengths, λ_1 *and* λ_2, such that $m\ \lambda_1 = (m+1)\lambda_2$. These two wavelengths will be diffracted at the same angle (see relation (3.2)) and overlapped at the spectrograph output.

$$FSR_g = \lambda_1 - \lambda_2 = \frac{\lambda_2}{m} \tag{3.6}$$

Thus the grating free spectral range decreases as the order increases. The disadvantage of an Echelle grating is therefore its small *FSRg*, which makes it not appropriate for a

broadband light source. However, in our case the limited laser bandwidth makes an Echelle grating a reasonable choice. In the spectrograph design, FSR_g was calculated to be at least 2 times larger than the laser bandwidth to avoid overlap between two adjacent orders.

3.2.6.2. Spectrograph design

The designed spectrograph is compact (42 cm x 15 cm), and provides high spectral resolution for the UV and visible region. It is based on reflection grating used at a near Littrow configuration at high order with a large blaze angle (an Echelle grating from Thorlabs, GE2550-0863, blaze angle = 63°, order @ 400 nm ~ 56, 79 grooves per mm), and a high-sensitivity blue enhanced TE-cooled CCD (Hamamatsu, C10151, 2048 × 250 pixels). This CCD detector is a two-dimensional image sensor, and it can operate as a linear sensor having a large active area by transferring all the pixel signals in the vertical direction to the buffer line (this process is called "line binning"). The obtained resolution is about 5 pm at 338.5 nm (corresponding to 0.45 cm^{-1} at 30000 cm^{-1} and to a resolving power of 65000) as we will see later. Calculation of the spectrograph was carried out in order to evaluate the optimal configuration to achieve such high resolution in a small space. The best configuration is shown in Figure 3.8, where f_1 is the focal length of the entry lens, f_2, f_3 are the focal lengths of the concave mirrors, and f_4 is the focal length of the convex mirror.

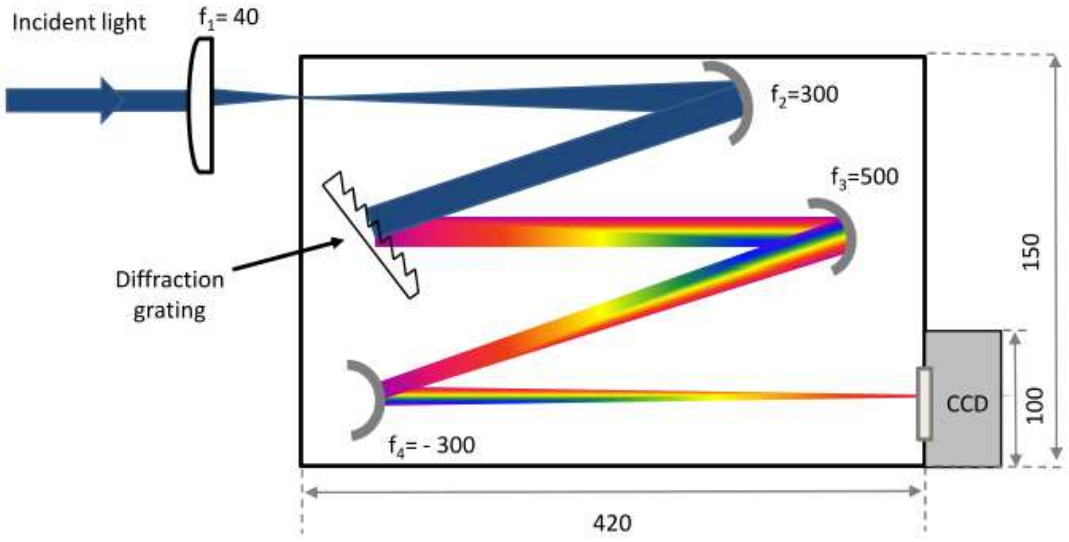

Figure 3.8: Compact spectrograph, dimensions in mm. f_1: Focusing lens at the entry of the spectrograph, f_2, f_3: Focal lengths of concave mirrors, f_4: Focal length of a convex mirror, CCD: Charge coupled device detector.

Since we have to spectrally analyze the radiation transmitted through the high finesse cavity, TEM_{00} modes are predominantly excited, it is easy to calculate the focusing lens needed to obtain the appropriate spot size at the spectrograph input. This should correspond to a diverging beam which optimally fills the grating after collimation by the first spectrograph mirror. For this, f_1 = 40 mm lens is placed at a distance of about 30 cm from the cavity, to give a waist of 10 µm at the entry of the spectrograph. The divergent beam is

collimated by a concave mirror (f_2=300 mm focal length) towards the grating. The diffracted radiation is focused into the CCD camera by using a concave and a convex mirror telescope with focals f_3=500 mm and f_4= −300 mm, respectively. These two mirrors f_3 and f_4 are equivalent to a concave mirror of f_{out}=1.15 m as given by the relation:

$$\frac{1}{f_{out}} = \frac{1}{f_3} + \frac{1}{f_4} - \frac{e}{f_3 \times f_4} \tag{3.7}$$

Where, *e* is the distance between f_3 and f_4 which is 33 cm in our design.

This configuration allows a remarkable reduction of the spectrograph size, while the diffracted beam travels a large effective distance before to reaching the CCD. This is required in order to achieve sufficiently large beam dispersion and to have just few CCD pixels corresponding to the grating resolution. Figure 3.9 displays a picture of the spectrograph.

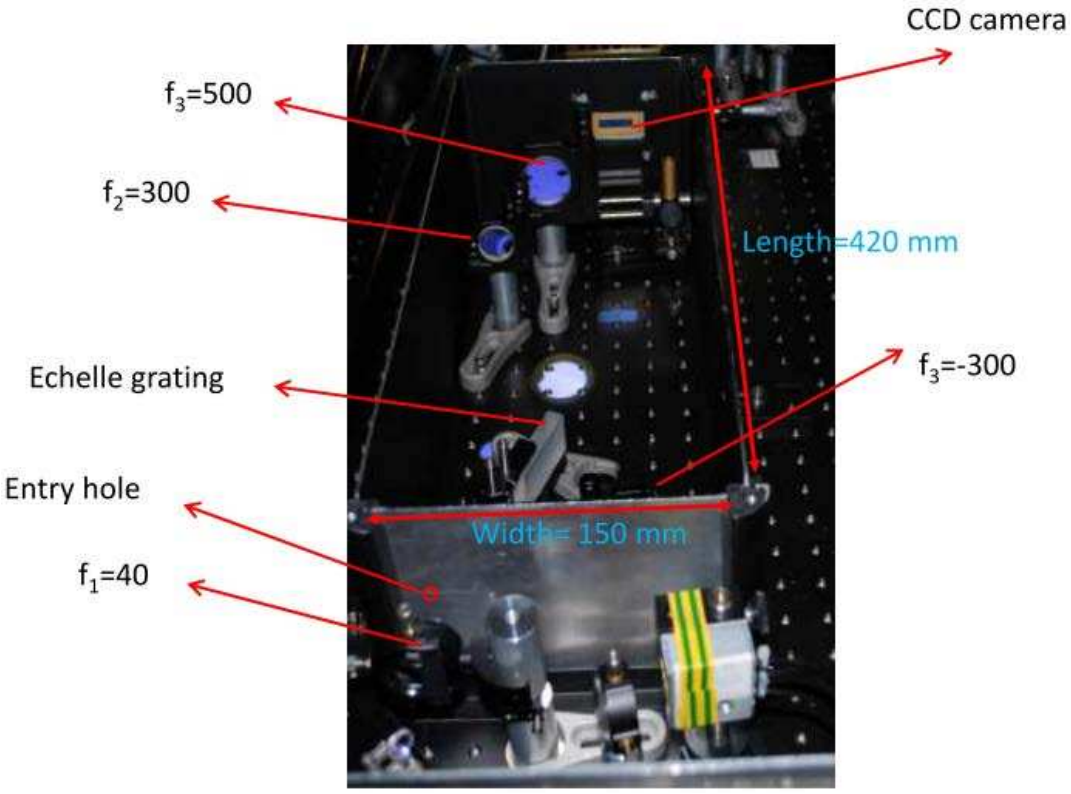

Figure 3.9: Picture of the spectrograph.

3.2.6.3. The resolution and calibration of the spectrograph

In the following subsection, we present different methods to estimate the resolution and the calibration values of our spectrograph.

3.2.6.3.1. Resolution measurement by a narrow bandwidth laser

We tried several methods to estimate the resolution of the spectrograph, one of them involved using a narrow bandwidth external cavity diode laser (ECDL). This allowed testing different configurations where the input spot size was varied and the resolutions were compared with the theoretical values. Because of the narrow bandwidth of the ECDL laser (~100 kHz), its spectrum will be broadened by the spectrograph resolution, thus the measured full width at half maximum (FWHM) of the spectrum gives directly the spectral resolution $\Delta\lambda_{min}$ in pixel. Figure 3.10 reveals the spectra with f_1 = 50, 100, and 150 mm corresponding to input spot size D_{in} of 20 µm, 42 µm, 64 µm, respectively.

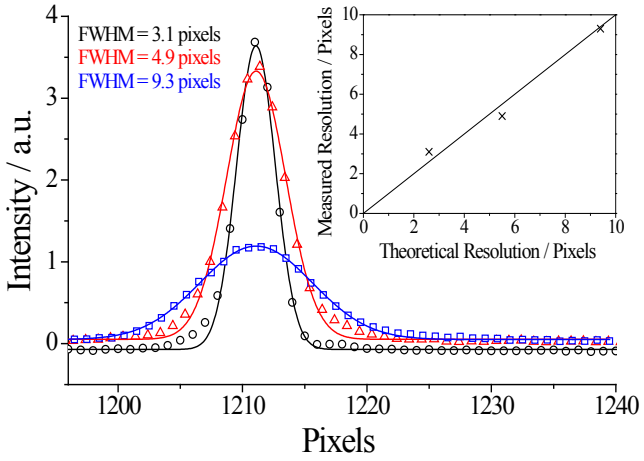

Figure 3.10: The resolution measured by using a narrow bandwidth laser. In the main window: laser spectrum with input waist of 20 µm (black), 42 µm (red) and 64 µm (blue). In the inset, the measured resolution (in pixels) for the different spectrograph configurations plotted against its theoretical value (in pixels).

Each spectrum is fitted by a Lorentzian function to estimate the FWHM which corresponds to the measured resolution $\Delta\lambda_{min}$ in pixels. Table 3.3 presents the input parameters used to calculate the theoretical resolution $\Delta\lambda_{min}$ in pm unit from the relation (3.5). These parameters are: λ=410 nm, blaze angle $\theta = 63\,\mathrm{deg}$, number of grooves per mm n=79 grooves/mm resulting in d= (1/n) = 2.66 µm. In addition to the beam size Z_B on the grating, given by:

$$Z_B = 2\frac{\lambda f_2}{\pi(D_{in}/2)\cos\theta} \tag{3.8}$$

The above relation is true for one frequency component of the broadband input radiation. The division by $\cos\theta$, accounts for the beam projection on the grating. The diffraction order m is calculated from the grating equation (3.3). N is calculated by the equation $N=Z_B/d$, R is derived from (3.5), and then the theoretical resolution $\Delta\lambda_{min}$ is calculated by $\Delta\lambda_{min}= \lambda/R$.

m	f_1 (mm)	D_{in} (µm)	Z_B (mm)	N (grooves)	R
55	50	20	29.4	2270	$1.25x10^5$
55	100	42	14	1081	$6x10^4$
55	150	64	9	709	$4x10^4$

Table 3.3: Input parameters of the resolution calculation.

In the inset of Figure 3.10, the measured resolution is plotted against the theoretical resolution. which is calculated in pm unit, then transferred to pixel unit by the calibration value of 1.2 pm per pixel, This value (1.2 pm per pixel) was roughly estimated by dividing the calculated extended laser spectral range $\Delta\lambda_c$=2.6 nm over the number of the CCD pixels (2048 pixels): the good agreement between the two values highlight the reliability of our calculation. Table 3.4 presents the theoretical and experimental resolutions.

$\Delta\lambda_{min}$ (pixels) calculated	$\Delta\lambda_{min}$ (pixels) measured	$\Delta\lambda_{min}$(pm) calculated	$\Delta\lambda_{min}$(pm) measured
2.8	3.1	3.3	3.7
5.7	4.9	6.9	6
8.7	9.3	10.5	11

Table 3.4: Theoretical and experimental values of the resolution $\Delta\lambda_{min}$ in pixels and pm units.

The following calculation is made at λ=338.5 nm, corresponding to Chameleon laser wavelength to characterize the spectrograph at the operating wavelength. To obtain a spectral resolution of $\Delta\lambda_{min}$= 5 pm when using Chameleon laser, a focusing lens at the entry of the spectrograph f_1=40 mm is used, resulting in D_{in}= 10 µm. The experimental spectral resolution is estimated by the beating patterns between the laser comb and the cavity comb as we will see in the next sub-section. Then, it is also important to calculate the number of pixels (n_{PIXEL}) corresponding to the spectral resolution (apparatus function), where its value should be small as much as possible (close to 1 pixel), and given by:

$$n_{pixel} = (f_{out} \times \Delta\theta_{\min}) / a \tag{3.9}$$

Where, a is the distance between two pixels of the CCD (a = 12 µm), and $\Delta\theta_{\min}$ is the angular resolution, given by:

$$\Delta\theta_{\min} = D \times \Delta\lambda_{\min} \tag{3.10}$$

Here, the angular dispersion D is calculated from the relation (3.4) for blaze angle θ=63 deg, and λ=410 nm.

The laser spectral range $\Delta\lambda_c$ covered by the CCD camera is given by:

$$\Delta\lambda_c = \frac{p \times \Delta\lambda_{\min}}{n_{pixel}} \tag{3.11}$$

Where p is the number of CCD pixels (p=2048 pixel). $\Delta\lambda_c$ should be bigger than the laser bandwidth, otherwise, a part of the laser spectrum will be lost.

Table 3.5 presents the calculated values of D, $\Delta\theta_{min}$, n_{pixel}, FSR_g (grating free spectral range), and the ratio $FSR_g/\Delta\lambda_l$, where $\Delta\lambda_l$ is the Laser band width. It is necessary to mention that the ratio $FSR_g / \Delta\lambda_l$ should be greater than 2 to avoid the interference of adjacent orders. The FSR_g is calculated from the relation (3.6) for m=55.

D (mrad/nm)	$\Delta\theta_{min}$ (mrad)	f_{out}(m)	n_{pixel}	$\Delta\lambda_c$ (nm)	$\Delta\lambda_l$ (nm)	FSR_g (nm)	$FSR_g/\Delta\lambda_l$
11.54	0.057	1.15	5	2	0.72	5	7

Table 3.5: Calculated values of D, Δθmin, npixel, FSRg, Δλc, FSRg / Δλl.

3.2.6.3.2. Calibration and resolution measurements by the comb beating patterns

Another method to measure the spectrometer resolution and the dispersion at the CCD camera is to use the comb beating patterns. We have seen from the second chapter (section 2.4.2), that when the cavity length is changed away from the magic point length, by using a motorized translation stage, different comb beating patterns can be observed at the CCD as shown in Figure 3.11. Here δL represents the displacement from the magic point length.

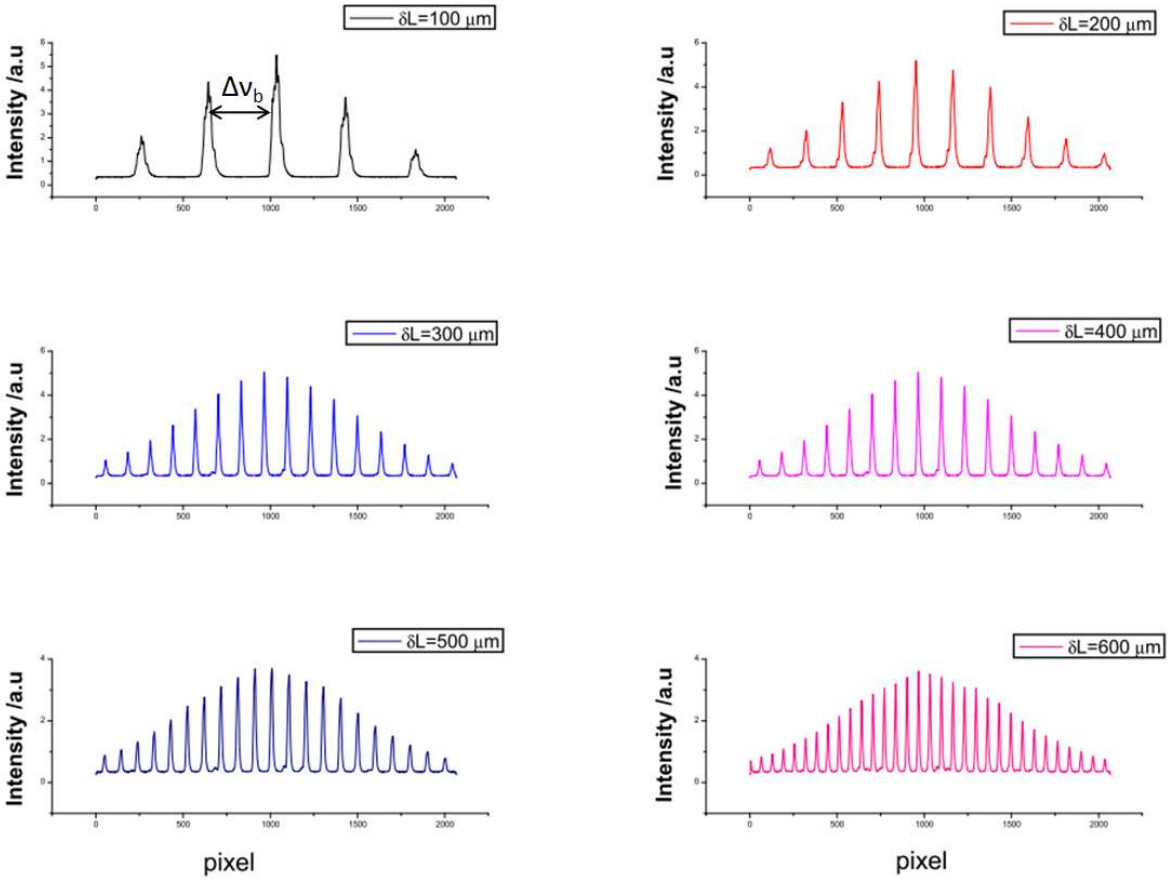

Figure 3.11: Beatings signal resulting from the mismatch between laser and cavity combs for different cavity displacements δL from the magic point length. δL is ranged from 100 µm to 600 µm.

In such case, the frequency spacing $\Delta\nu_b$ in pixels between two adjacent beating peaks of the transmitted signal can be directly measured, while $\Delta\nu_b$ in frequency unit can be derived from the relation $\Delta\nu_b = \frac{c}{2N_c\delta L}$ for each value of δL (see chapter 2, section 2.4.2). In this relation $N_c = 2$ accounts for the fact that the cavity FSR is twice the laser repetition rate. Then, $\Delta\nu_b$ value is transformed to wavelength unit by using $\Delta\lambda = \left|\Delta\nu_b \times \lambda^2 / c\right|$. By plotting the measured values of $\Delta\nu_b$ in pixel versus the calculated $\Delta\nu_b$ values in wavelength unit, a calibration value of 0.72 pm per pixels was found as shown in Figure 3.12.

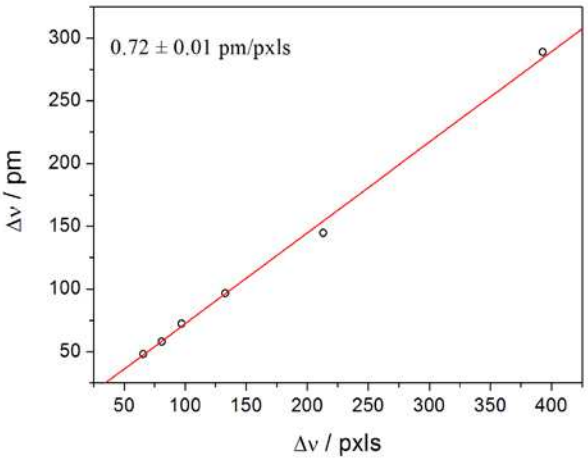

Figure 3.12: Calibration value of the spectrograph, estimated by analyzing the beatings period between laser and cavity combs.

In addition, by monitoring the width of the beating peaks as a function of increasing *δL* value, the spectrograph resolution can be measured. Indeed, we have seen from (chapter 2, section 2.4) that increasing *δL* results in decreasing the beating peak width, which is consistent with the fact that the number of comb modes, participated in the peak, decreases. However, for large *δL* values, the widths stop decreasing, while they should theoretically continue to narrow down, indicating that the spectrograph resolution has been reached. Here, the width of the narrowest beating peaks reaches a value of (FWHM= 8 pixels), which gives a resolution of about 5.7 pm at 338.5 nm, taking into account the calibration value of 0.72 nm.

Another method to estimate the resolution is to use the vertical distribution of the laser beam on the CCD pixels, while all the laser modes have the same width but they are horizontally dispersed, and this is true when the CCD camera is positioned exactly at the focal point. Figure 3.13 displays this distribution and the FWHM is estimated to be 7 pixels resulting in 5 pm resolution at 338.5 nm.

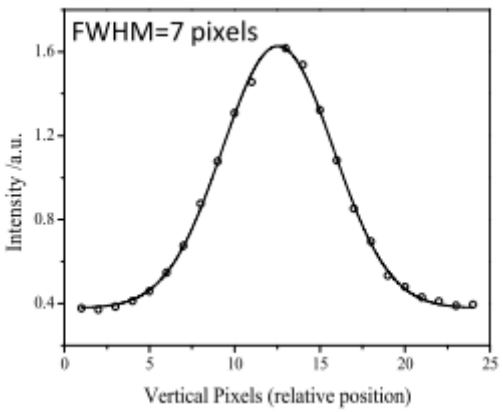

Figure 3.13: Vertical cut of the spectrograph image on the CCD camera.

In Summary, we tried different techniques to estimate the resolution, and all of them give approximately the same value of 5 pm. The spectrograph resolution can, in principle, be enhanced to 1 pm by changing the actual input lens f_1=40 mm to 10 mm, but at the expense of losing a part of the laser power, because the new value of the beam size on the grating (Z_B=4.8 cm) will be greater than the height of the grating (2.5 cm). However, increasing the resolution will not increase the contrast for the absorption spectra of IO and BrO, since they are limited by lifetime broadening.

3.2.6.4. Noise of the spectrograph

In this section, the performance of the CCD camera is described as well as the noise of the detection. This back-thinned CCD camera (Hamamatsu, C10151, 2048 × 250 pixels) provides high sensitivity in the UV spectral region (where strong absorptions of our target molecules are present), thanks to a high quantum efficiency (40 % at 340 nm, 60 % at 436 nm), and to its structure. In a normal CCD camera that receives light from the front surface, the active area is covered with electrodes for charge transfer. These electrodes cut a fraction of the radiation incident on the image sensor thus reducing the quantum efficiency especially at shorter wavelengths. In back thinned CCD image sensors, the substrate of the active area is removed to allow light to enter from the back surface, which is used as the CCD input side. In a well-designed CCD camera, the noise performance is limited by the CCD sensor rather than by associated system electronic components. The signal to noise ratio (SNR) for a CCD image sensor specifically represents the ratio between the measured signal and its noise, which consists of undesirable signal components arising in the device, and inherent natural variation of the incident photon flux. The measured signal from a CCD imaging system is proportional to the photon flux incident on the CCD photodetectors (expressed as photons per pixel per second), the quantum efficiency of the device, and the integration time (exposure time) over which the signal is collected. The three primary components of noise in a CCD system are photon noise, dark noise, and readout noise, whose contributions we are going to consider now separately.

3.2.6.4.1. Photon shot noise

It results from the inherent statistical variation on the number of photons stricking the CCD and collected in its charge wells (pixels) [50]. Photoelectrons generated within the sensitive area constitute the signal, and the quantum efficiency is defined as the number of electrons or holes that can be detected as a photocurrent divided by the number of the incident photons. The interval between photon arrivals is governed by Poisson statistics, and as a result, the photon noise on a number *N* of measured photons is equal to the square root of *N*. In general, the term shot noise is applied to any noise component reflecting such a statistical behavior, and sometimes it is used in place of photon noise. It is important to notice that as *N* increases, the SNR for photon noise also improves as the square root of *N*. It should be underlined that it is really the number of detected photons which has to be considered, and not the initial number of signal or source photons, which is a characteristic

of this quantum noise. It should be noticed that (vertical) binning a number of pixels, to give a single (one dimension) readout, produces a photon noise which is relative to the total number of collected electrons in those pixels. Unfortunately, the readout buffer in our CCD, which is used to gather the charges accumulated in the CCD pixels before readout, has charge wells which possess only twice the capacity of the CCD pixels.

3.2.6.4.2. Dark noise

Dark noise arises from statistical variation in the number of electrons thermally generated within the sensitive area of the CCD, which is independent of photon induced signal, but it exponentially depends on the device temperature (proportional to *exp(-E/kT)*, where *E* represents the energy barrier for the production of a thermal electron, T is the absolute temperature, k is Boltzmann constant). The generation rate of thermal electrons at a given CCD temperature is referred to as dark current. Similarly to photon noise, dark noise follows Poisson statistics, and its standard deviation is thus also the square-root of the number of thermal electrons generated within the image exposure time. Cooling down the CCD sensor largely reduces the dark current, and in practice, high-performance cameras are usually cooled to a temperature at which dark current is negligible, with respect to the shot noise, over the chosen exposure time interval. Our peltier cooled CCD camera produces at most 15 dark electrons per pixel per second when operated at -10°C, whose associated fluctuations are totally negligible relative to the photon noise of a filled pixel. On the other hand, for precise spectral measurements, the dark background spectrum of the CCD should be measured and subtracted from the acquired spectra using the same exposure time. It should be underlined that this background corresponds to a stable pattern as long as the CCD temperature is fixed.

3.2.6.4.3. Readout noise

This is a combination of system noise sources generated from the process of converting CCD charge carriers into a voltage signal, followed by the analog-to-digital (A/D) conversion process. High-performance camera systems exploit design enhancements that dramatically reduce the readout noise down to the level of a few electrons (20 electrons rms/pixel for our CCD).

3.2.6.5. Signal to noise ratio

The following equation is commonly used to calculate the SNR of the CCD camera [50]:

$$SNR = F_p Q_e t / \sqrt{F_p Q_e t \quad Dt \quad N_r^2} \tag{3.12}$$

Where F_p is the incident photon flux (photons/pixel/second), Q_e is the CCD quantum efficiency (%), *t* is the integration time (seconds), *D* is the dark current value given in (electrons/pixel/second), and N_r represents the readout noise in electrons rms /pixel (rms means a root mean square). This equation simply results from the ratio of the total signal

generated during the exposure time divided by the sum of the three primary not correlated noise components mentioned above: the first term under the square root accounts for the photon noise, the second term for the dark noise and the last corresponds to the readout noise component. In our experiment the camera is cooled down to -10° C to reduce the dark current noise between 1.5 and 15 electron/pixel/s. The readout noise ranges between 20 and 45 electron rms /pixel. In this case, the dark noise and the readout noise are negligible compared to photon noise which is estimated to be 360 electrons rms /pixel, and this value corresponds to the square root of the number of photoelectrons (150000 e−/pixel ≈ 360^2) needed to fill up the well capacity of the CCD camera. In practice, when two successive single spectra are recorded with our CCD the ratio between them gives roughly a flat (zero absorption) spectrum with a SNR consistent to the expected shot noise value. In fact, our ML-CEAS system provides shot noise limited measurement [51] as it will be discussed later in more details.

3.2.7. Gas line and sample handling

Our target molecules, the halogen oxides radicals, are highly reactive species with a life time on the order of 1 s in a remote environment, and so it is important to choose a tube material which is able to efficiently transport them inside the cavity. Different types of tubes had been tested such as stainless-steel, PA (Polyamide), PFA (Perfluoroalkoxy), and stainless-steel treated with halocarbon wax (Wax 600, Halocarbon Products Corporation). The PFA (Perfluoroalkoxy) gave the best performances [52]. Therefore, the gas line (shown in Figure 3.14) is entirely composed by PFA tube.

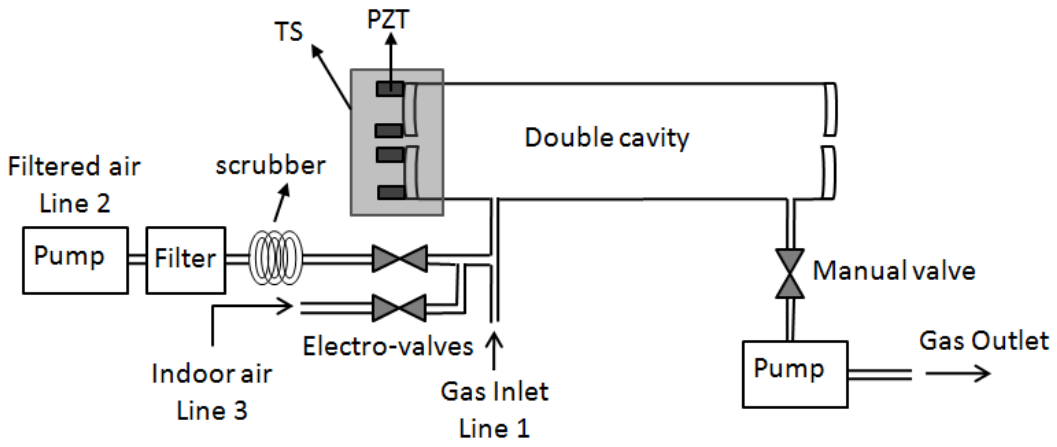

Figure 3.14: Gas line. TS: Translation stage, PZT: Piezoelectric tube transducer.

At the cavity output, a diaphragm pump and a manual proportional valve are employed to provide a constant gas flow of 800 SCCM (Standard Cubic Centimetres per Minute), and this value of gas flow was practically chosen to provide rapid refreshing (1 second) of the gas inside the cavity avoiding turbulent flow condition which will perturb the stability of the resonator. The cavity inlet can sample three different lines through a cross connection. The main line (line 1) is the outdoor sample that is collected with a 6 mm diameter PFA tube.

The second line is linked to a filtered air generator, composed by a second diaphragm pump, a particle filters and a scrubber that are employed to provide a flow rate greater than 800 SCCM, which dynamically replaces the main input flow. This filtered air flow, free of NO_2, IO and BrO, is switched on/off by a software controlled electro-valve and allows acquiring reference spectra and ring-down events essential for the absolute calibration of the absorption scale. Filtering NO_2 and Formaldehyde (CH_2O) is necessary because they absorb at the same wavelength of IO, and BrO respectively. However, recently has been found that Formaldehyde is not completely removed by this filtering system and an additional filter such as the commercial Hopcalite can be required to remove volatile organic compounds from the air sample; in alternative a zero air cylinder can be employed to acquire reference spectra, which is, however, less functional for field campaign purpose. A second electro-valve allows partially collecting indoor air which is naturally enriched in NO_2 and Formaldehyde: the recognition of their spectra by the fitting routine allows adjusting the fit parameters (in particular the spectral centring).

3.2.8. Gas preparation and permeation tube sources

In this section we will discuss how BrO and IO radicals were generated in the laboratory. Initially, BrO and IO were prepared at relatively high concentration (ppb - ppm levels) to easily detect them, and then later on at extremely low concentration (ppt levels) to test the performance of our instrument before the field campaign measurements.

3.2.8.1. BrO preparation

In the first tests to detect BrO, this highly reactive molecule was produced directly in the cavity, at relatively high concentration, by photolysis of Br_2 in a gas mixture containing O_3 and O_2 according to the following reaction:

$$\begin{aligned} Br_2 &\xrightarrow{h\nu} 2Br \\ Br + O_3 &\rightarrow BrO + O_2 \end{aligned} \qquad (3.13)$$

A home-made gas cylinder contains Br_2 diluted in O_2 (0.13 % mixing ratio of Br_2) was used to provide highly concentrated Br_2 samples. Ozone was produced by flowing pure O_2 (Alphagaz I, Air Liquid) through an ozonizer based on a high voltage electric discharge (Yanco Industries Ltd). The Br_2 sample from the cylinder was further diluted with a flow of carrier O_2 and mixed to a small flow of O_3 before entering the cavity. The concentration of O_3 was adjusted to be in excess relatively to the concentration of Br_2. With respect to the photodissociation of Br_2, the absolute quantum yield as a function of excitation wavelength reported in the literature shows a peak of 87 % at 500 nm [53]. For this reason, a 10 cm long LED array composed by ten cyan LEDs (Philips Lumileds, emission angle of 140°) was used to photolyse Br_2 efficiently by shining their light through a glass section in the HF cavity. Each LED provides a spectral emission with a full width at half maximum of 30 nm, centred at 505 nm, and a typical optical power of 20 mW. The concentration of Br_2 and its

photodissociation efficiency was estimated by cavity ring-down spectroscopy (CRDS) [54] measurements using the absorption cross-section of Br_2 at 338.5 nm, which is spectrally broad and unstructured at this wavelength, with a value of 9.5×10^{-21} cm^2 $molecule^{-1}$ [55]. Indeed, the change in the cavity ring-down time in the absence and presence of Br_2, at atmospheric pressure (in absence of O_3) gives the concentration of Br_2, while measuring the depletion in Br_2 signal when switching on the LEDs gives the photodissociation efficiency. For different dilution levels, about 4 % efficiency in the production of bromine atoms (expressed in terms of [Br] / [Br_2]) could be estimated as shown in Figure 3.15.

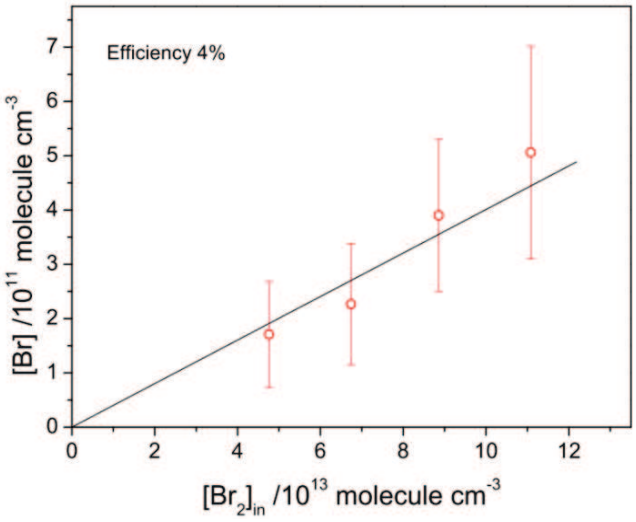

Figure 3.15: Photodissociation efficiency of Br_2. Horizontal axis: Br_2 concentration provided from a prepared cylinder, Vertical axis: Br concentration resulted from Br_2 photodissociation.

Substantial efforts have been made in fabrication of a calibrated and reproducible source of BrO. In Figure 3.16, concentration of BrO is plotted versus the concentration of Br_2. The concentration of BrO was measured by the fit procedure explained later.

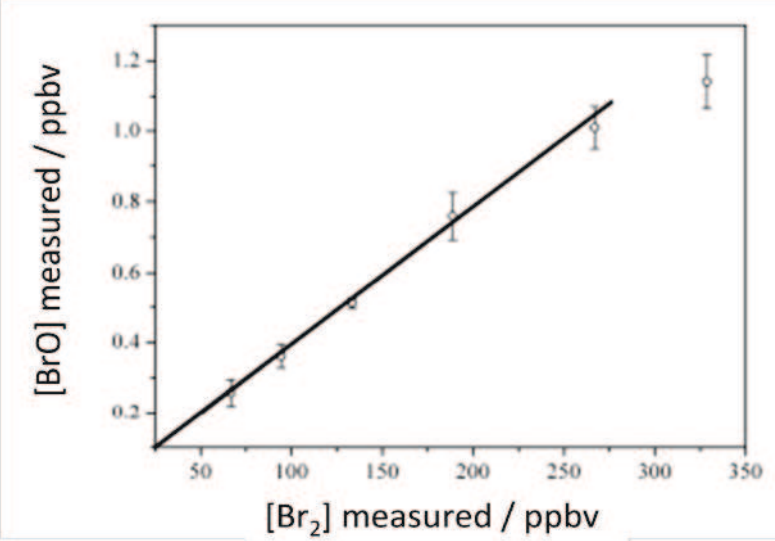

Figure 3.16: Concentration of BrO versus the concentration of Br_2.

The concentration of BrO linearly depends on the Br_2 concentration only at low concentration level of Br_2 up to ~300 ppbv, and in this linear region, the BrO concentration are in agreement with the concentration expected from the photolysis efficiency of Br_2. At higher concentration of Br_2, BrO depletion occurs due to the self-reaction of BrO according to the relation (3.14), and to its reaction with atomic bromine according to the relation (3.15).

$$BrO + BrO \rightarrow 2Br + O_2$$
$$BrO + BrO \rightarrow Br_2 + O_2 \quad (3.14)$$

$$Br + BrO \rightarrow Br_2O \quad (3.15)$$

At low concentration level of BrO (few pptv), this kind of calibrated source is no longer valid, because the Ring-down measurements were unable to detect the low concentration of Br_2 (less than ppb). O_3 concentration in the cavity was also measured using an absorption cross-section at 338.5 nm of 1.41×10^{-21} cm^2 $molecule^{-1}$ [56].

In a second series of experiments, in order to reach lower concentrations of Br_2, a permeation tube (KIN-TEK Laboratories, Inc.) was employed to deliver 954 (nanogramm/min) of bromine molecules when heated at 40°C. This tube acts as a flow control mechanism for dispensing a very small flow of permeating vapor through a polymeric membrane (usually Teflon). It can supply small flows of Bromine (Br_2), where the emission rate is set by the operating temperature of the tube (according to a precisely known dependence), and it is essential to carefully control the tube temperature (to better than ± 0.1°C). Therefore, the permeation tube was installed into a home-made temperature stabilized oven (Figure 3.17) flushed with 10 SCCM of O_2 carrier gas. The oven consists of an aluminium block (5x5x15 cm^3) where a hole of 16 mm diameter was drilled to insert the permeation tube of Br_2 (5 mm diameter, 50 mm length). This block is thermalized by a peltier device and a fan fixed on the top to dissipate the heat. The entire block is covered by a thermal insulating material.

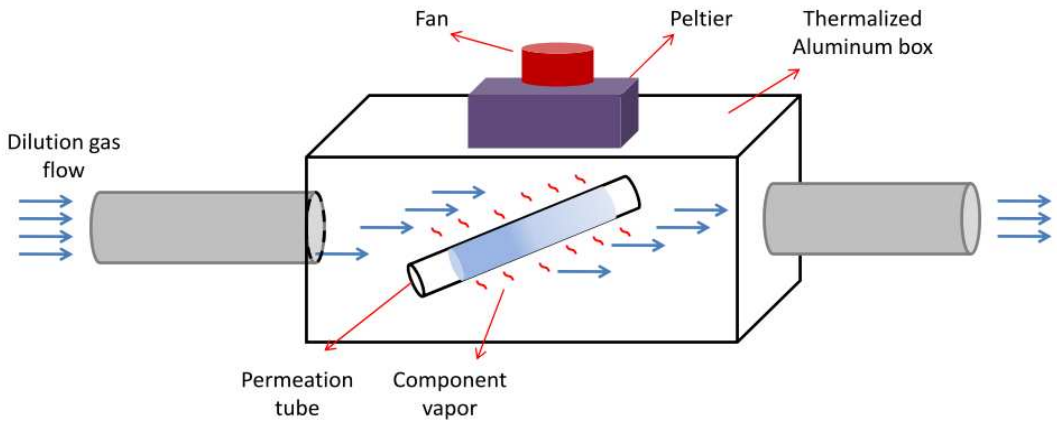

Figure 3.17: Home-made oven to control the temperature of the permeation tube.

The resulting Br_2-carrying flow was then mixed with a 50 SCCM of ozone-carrying flow, as well as a larger air flow (~ 500 SCCM) before being injected into the sample cavity. The LEDs array for the photolysis was placed along the PFA tube a few centimeters before the cavity gas inlet. The concentration of Br_2 was adjusted by changing the oven temperature. This system is producing less BrO than expected (only about 20 %) and its reproducibility is not very high due to the losses on surface of the oven walls, as well as the losses in the stainless-steel connections used in the gas line. Therefore, A systematic study of the concentration losses on the delivery of BrO was performed by introducing in the gas line between the BrO source (~50 pptv) and the cavity 25-cm tubes made of different materials: stainless-steel, PA (Polyamide), PFA (Perfluoroalkoxy), and stainless-steel treated with a halocarbon wax (Wax 600, Halocarbon Products Corporation). The study showed that PFA and treated stainless-steel lead to undetectable BrO losses (limited by 12 % fluctuations of the BrO production system). Moreover, no additional losses in the mixing ratio of BrO measured in the cavity were observed when the length of the PFA tube was increased up to 7 meters (using a flow of 500 SCCM), which indicates that PFA is excellent for the delivery of BrO containing air samples over relatively long distances. In the current setup, the gas line tubes are all in PFA and the double cavity tubes, which are made in stainless steel, where internally covered by thin-walled PFA tubes.

3.2.8.2. IO preparation

Similarly to BrO, IO was obtained by photolysis of I_2 (iodine) in the presence of O_3 under flow conditions, according to the following reaction:

$$\begin{aligned} I_2 &\xrightarrow{h\nu} 2I \\ I + O_3 &\rightarrow IO + O_2 \end{aligned} \tag{3.16}$$

A small concentration of iodine in a regulated oxygen flow (1–10 SCCM) was obtained placing a small iodine crystal inside a cold trap. This trap consists of a section of a thin copper tube attached to a thermoelectric plate. The trap placed in a sealed plastic bag flushed with dry N_2, which allows to avoid water condensation and therefore to reach low temperatures: at −33°C, an iodine vapour pressure close to 10^{-6} bar was achieved. Ozone is generated in the same manner as for the BrO production, together with a larger O_2 flow used for dilution. These flows were mixed at the HF cavity gas inlet close to the input mirror. The gas outlet was placed close to the other mirror and connected to an atmospheric pressure exhaust line. By changing the flow through the cold trap, the iodine concentration in the cavity could thus be adjusted in the range from 10 to 100 ppbv, while ozone was present in excess. The total flow inside the cavity was kept to 800 SCCM to have a reasonably high cavity volume exchange time (~1 second) independent to the small added iodine carrying flow. Here, the radiation for the photolysis was directly provided by the intracavity laser beam at 436 nm, and no external photolysis source was needed.

3.3. Automatization procedures

Automatization routines have been developed and included in the main Labview program used for the spectra acquisition and data analysis. The aim of the procedure is to recover the signal during a long term measurement when degradation of the instrument sensitivity occurs. Each routine is called by the Labview software only when needed (centring the laser frequency, alignment of the beam injected into the optical cavity, matching the cavity FSR to the laser repetition rate, controlling the diffraction grating, re-optimize the multicomponent fit procedure.

The first routine is used to center the laser frequency. The Chameleon laser has a build-in spectrometer (USB4000, Ocean Optics) which allows monitoring the central frequency of the laser. By acting on the position of one of the two prisms (that compensate for dispersions) inside the laser cavity, it is possible to perform adjustments on the laser wavelength with a resolution of 0.2 nm.

The second routine is used to align the beam injected into the optical cavity, by acting on the alignment of the dichroic mirror DM_3, which is mounted on a motorized optical mount (AG-M100, Newport). A position sensitive detector (PSD, Hamamatsu, S5990) with a surface area of 16 mm^2 is placed (see Figure 3.1) to collect the zero order radiation transmitted by the AOM and reflected by the DM_3 (as well as the 1^{st} order beam which is injected into the optical cavity). This allows retrieving the laser beam trajectory by controlling AG-M100 which is connected to the PSD. By scanning the steering mirror DM_3 on the X and Y axis, the intensity of the TEM_{00} mode transmitted by the resonator reachs a maximum which corresponds to the best alignment, and thus the best mode matching of the laser to the cavity.

The third routine is used to tune the cavity FSR to the magic point. For a large mismatch between the two combs, the beating signal generated at the CCD camera (therefore in the frequency domain) is employed: the distance between two adjacent peaks, $\Delta\nu_b$, is increased by changing the cavity length L, in the direction where the displacement from the magic position, δL tends to zero (see chapter2, section 2.4.2). This first part of the procedure is conducted without modulating of the cavity length. After reaching a $\Delta\nu_b$ of about 40 cm^{-1} ($\delta L \approx 60$ µm), the sinusoidal modulation is sent to the PZT and the procedure keeps approaching the magic point by monitoring the intensity of the transmitted signal recorded by the PD where the maximum of the peak intensity corresponds to a perfect matching of the two combs. Both, the mode matching and the magic point routines are called only if the maximum in intensity of the TEM_{00} mode recorded at the photodiode goes below a given threshold.

The fourth routine is deployed to control the diffraction grating inside the spectrometer, where this grating is also mounted on a motorized rotation stage (AG-PR100, Newport). The fifth routine is used to re-optimize the multicomponent fit procedure (described in the next

section), which allows a horizontal shift of the reference spectrum with respect to the experimental spectrum, in order to minimize the residuals. The tolerance of this shift is normally fixed to ~25 pm (~5 pixels), and when a misalignment of the laser beam or a shift in frequency of the optical comb occurs such that a larger shift is needed to optimize the fit, a degradation of the fit performances will be observed, and a reoptimization of the fit parameters will take place. For small changes in the spectral shift, the parameter corresponding to the initial shift of the reference spectrum will be adapted, while for larger changes (greater than 0.5 nm) the spectrometer will be automatically re-centered by rotating the diffraction grating. During the re-optimization routine the ideal initial shift for the fitting is found by injecting into the cavity indoor air, which contains a relatively high level of NO_2 and H_2CO. A large tolerance of the horizontal shift of the reference spectrum is then selected and the best shift is guessed for five different experimental spectra. Afterwards the average value becomes the new initial shift, and the tolerance is again reduced to the previous value.

3.4. Data Analysis

This section describes the data analysis performed by the Labview software which controls the ML-CEAS spectrometer, to retrieve the concentrations of the target molecules. In addition, we present a method to estimate the detection limit directly from the measured spectrum to take into account the structure of absorption cross section of the molecules.

3.4.1. Fit procedure

We have seen from (chapter 2, section 2.3.3) that the frequency dependent absorption coefficient can be expressed as a function of the cavity transmission $S(\nu)$, and the ring-down time of the empty cavity τ_{air} :

$$\alpha(\nu) = \left(\frac{1}{S(\nu)} - 1 \right) \frac{1}{\tau_{air}\ c} \tag{3.17}$$

The ring-down time is measured by performing cavity ring-down spectroscopy when 800 SCCM zero air (or filtered air) was continuously flowed into the cavity. In our calculations, τ_{air} corresponds to an average photon life-time of the entire broad-band radiation circulating inside the cavity. We may assume that τ_{air} (proportional to the finesse) is almost constant over the injected laser spectrum which is spectrally narrow (~2nm) relative to the mirror reflection bandwidth (~40nm). The transmission spectrum $S(\nu)$ is calculated by the ratio between the intensities of the light transmitted through the optical cavity in presence and absence of the absorbers, both subtracted by the dark signal containing the CCD camera background. Spectral data, $\alpha(\nu)$ are analysed in real time by a standard linear

multicomponent fit routine [57], where spectra of known concentration of absorbers $\alpha_i(\nu)$ are used as references for the fit, and the respective coefficient c_i (c_{BrO} , $c_{IO,}$ etc.), which gives the sample concentration, retrieved according to the following relation:

$$\alpha(\nu) = \sum_i \alpha_i(\nu) \cdot c_i + p(\nu) \qquad (i = BrO, CH_2O;\ \ or\ IO, NO_2) \tag{3.18}$$

Where $p(\nu)$ is a polynomial function necessary to adapt to slow defects in the spectral baseline. The presence of a non-zero baseline on our spectra is mainly due to the fact that the femtosecond oscillator is not stabilized. The free-running laser can therefore shift in frequency between the two spectra acquired in absence and in presence of absorbers. Furthermore, contribution from scattering and broad (no structured) absorptions will also be included in the baseline fit.

The coefficient c_i is referred to the concentration N_i of the reference spectrum, and the concentration of the species C_i is given by:

$$C_i = c_i \times N_i \tag{3.19}$$

The reference spectra are experimental data, which are inherently taking into account the instrumental function and the wavelength calibration of our spectrometer. The concentrations of the reference spectra were calculated by using the wavelength dependent absorption cross-sections found in the literature for BrO [58, 59], H_2CO [60], IO [61, 62], and NO_2 [63]. The output parameters of the fit are the coefficients, c_i (c_{BrO} , c_{IO}, etc.) used to retrieve the concentration of the absorbers, and the coefficients of the baseline polynomial. The uncertainty of the measurement for the radical species is limited by the uncertainty of the literature absorption cross-sections (evaluated to be about 10 % for the halogen oxides), while the precision on the measured ring-down times is around 0.1 %. The ring-down times are recorded regularly (around every 15 min) according to the system stability. We recall from (chapter2, section 2.2), that the detection limit defined as a bandwidth normalized minimum absorption coefficient per spectral element, $\alpha_{\min}(BW)$ is given by:

$$\alpha_{\min}(BW) = \alpha_{\min}(cm^{-1}) \times \left(\frac{t}{M}\right)^{1/2} = \frac{\Delta I_{\min}}{I_{out}^0} \frac{1}{\tau_0\ c} \cdot \left(\frac{t}{M}\right)^{1/2} \tag{3.20}$$

Where I_{out}^0 is the cavity output intensity, $\Delta I_{\min}$ represents the minimum detectable change of the output intensity, t is the integration time and M is the number of fitted pixels (corresponding to 1000 and 1500 for the detection at 338.5 nm and 436 nm, respectively). In fact, in terms of noise the total number of pixels should be considered, and not the

apparatus function which will be important later to determine the detection limit in terms of concentration.

We should mention that the relation (3.20) is true only for the case of white Gaussian noise.

For the experimental spectra, the detection limits are expressed in terms of minimum detectable mixing ratio at atmospheric pressure, which takes into account the whole band absorption, and derived as the following.

3.4.2. Detection limit derived from the measured spectrum

If the absorption of the molecules of interest is not structured then the fitting routine will include of the spectrum in the baseline, and the resulting concentrations from the fit procedure are zeros. The fit procedure is sensitive to the structure of the absorption cross section of the molecules, and the more the spectrum is structured, the better it will be identified by the fitting routine. The question is how to link the noise in absorbance units (cm^{-1}) provided from the fit procedure to the detection limit given in Allan variance plot (given in units of concentration) which will be explained later. Our idea is to fit the measured spectrum with a polynomial function of the same order than the one used to fit the baseline of the experimental spectra, and then the standard deviation of the fit, which corresponds to the contrast (*ct*) of the spectrum (in cm^{-1}) is multiplied by the square root of the independent spectral elements ($\sqrt{n_{se}}$) to take into account the whole broadband absorption. To get the signal to noise ratio *SNR*, the value of the product $(ct \times \sqrt{n_{se}})$, which presents the signal, is divided by the standard deviation of residuals for one spectrum (α_{min}), which presents the noise, provided from the fit procedure. The detection limit (DL in units of mixing ratio) is obtained by dividing the measured concentration (c: also in mixing ratio) by the *SNR* as following:

$$\begin{aligned} \mathrm{DL} &= c(ppt) / SNR \\ &= c(ppt) / \left[\frac{ct(cm^{-1}) \times \sqrt{n_{se}}}{\alpha_{\min}(cm^{-1})} \right] \end{aligned} \qquad (3.21)$$

3.5. Structured absorption band of BrO, CH_2O and IO, NO_2

The absorption cross sections of the molecules of interest are like fingerprints that our fit procedure recognizes. This is essentially why we are interested in the absorption bands having a high rotational structure. In addition, having the sufficiently high resolution to resolve these lines will improve the contrast leading to increase the detection limit. In the following, the absorption bands of the molecules from the literature are presented, and compared to the experimental references spectra exploited in the fit procedure. The UV absorption spectrum of BrO is assigned to the electronic transition $A^2\Pi_{3/2} \leftarrow X^2\Pi_{3/2}$, and it

has well-defined vibrational band structure, but not all the transitions exhibit the rotational structure at high resolution, due to the predissociative character of the excited state. Indeed, the main contribution to the width of the absorption feature is given by the natural lifetime broadening, which implies that dissociation occurs faster than collisions. Because the width of the absorption line is limited by natural lifetime broadening, reducing the pressure inside the cavity does not increase the detection sensitivity. Moreover, the dissociation of the radical species immediately after detection does not affect the measured concentration due to the fast diffusion of the molecules through the laser beam in the cavity (t_{diff} = 8 ms), and to the low photolysis rate of BrO of ~ 20 molecules s^{-1} (that means the time to photolyse one molecule is 50 ms which is longer than t_{diff} = 8 ms). The same calculation for IO, and gives (t_{diff}=12 ms, the time to photolyse one molecule is 14 ms). To check that the dissociation had no effect on the measured concentration, the intracavity power was decreased by a half, and no changes in the measured BrO concentration were observed. The spectral features of the vibrational band (7,0) provide the characteristic signature that has been used to detect BrO in the atmospheric and laboratory measurements. Figure 3.18 displays the UV absorption spectrum of BrO at 300 K.

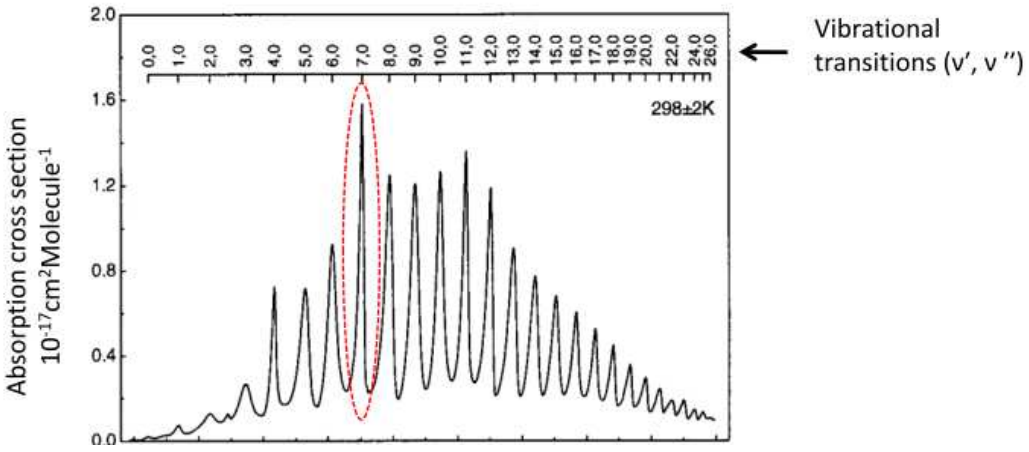

Figure 3.18: UV absorption spectra of the electronic transition $A^2\Pi_{3/2} \leftarrow X^2\Pi_{3/2}$ of BrO at (298 ± 2 K). Spectra were acquired at a resolution of 10 cm-1. Vibrational band (7,0) inside the ellipse [58].

(7,0) vibrational band is the strongest absorption band of BrO in the UV region , and presents a rotational structural as shown on the high resolution spectrum of Figure 3.19 (in red). This literature spectrum was used to retrieve the concentration of the experimental reference spectra (Figure 3.19, in blue) employed for the fit procedure. A labview program has been developed to compare the experimental reference spectrum with the literature spectrum which is interpolated and convoluted with an apparatus function. Moreover, on the experimental spectrum, a baseline can be added to correct the distortion of the experimental data, as well as a calibration parameter (pixel/nm) to convert the horizontal axis in wavelength units. The input of the program is the literature wavelength dependent absorption cross section (sigma) given in (cm^2), the experimental data given in absorbance unit (cm^{-1}). The literature cross section is then multiplied by a guessed concentration value

(input parameter of the program) in order to match the literature and the experimental one. The concentration found, is then the concentration of the experimental reference spectrum, which it will be used later on by the fitting routine.

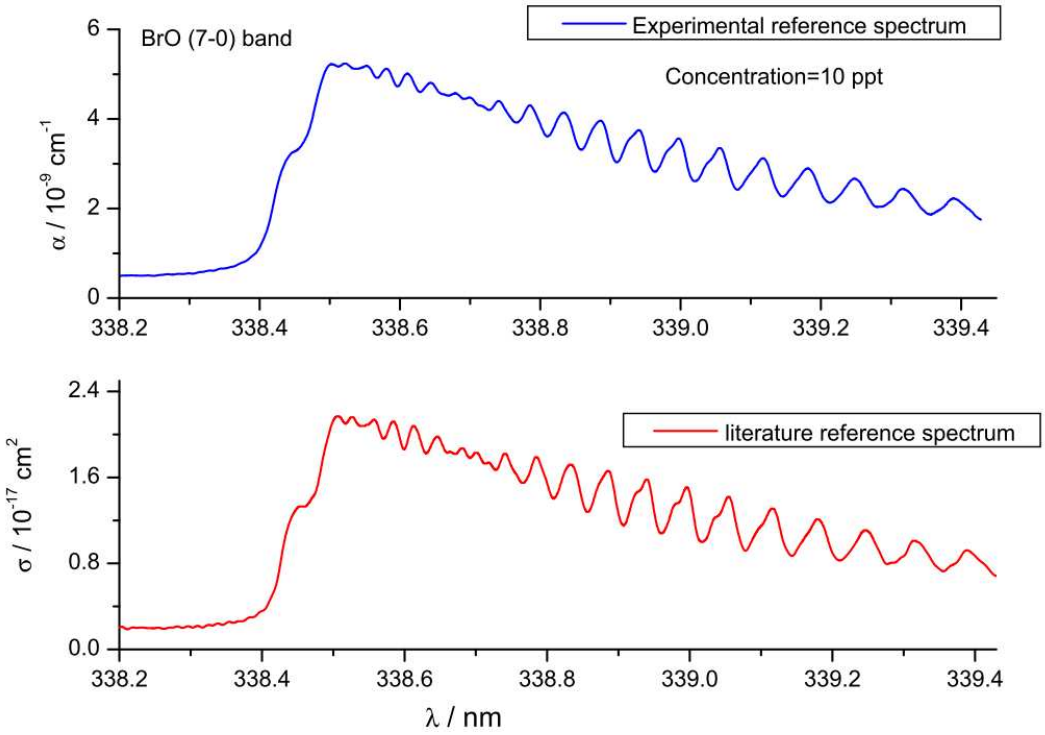

Figure 3.19: In blue, the experimental spectrum at atmospheric pressure and room temperature acquired by the ML-CEAS spectrometer. In red, the literature rotational structured (7,0) vibration band of BrO , acquired at a resolution of 1 cm^{-1} at 35 Torr and 300 K [58].

In the same spectral window chosen for BrO detection, CH_2O is also absorbing. Thanks to the versatility of our instrument, it is possible to detect BrO and CH_2O simultaneously. It should be noticed that this gas exists naturally in the ambient air. The absorption of UV radiation by formaldehyde in the wavelength range 260-360 nm is assigned to an electronic transition which exhibits a rotational structure around 338.5 nm [60]. Figure 3.20 (in red) displays the literature absorption spectrum of formaldehyde around 338.5 nm [60], and the experimental spectrum , which is used to fit CH_2O.

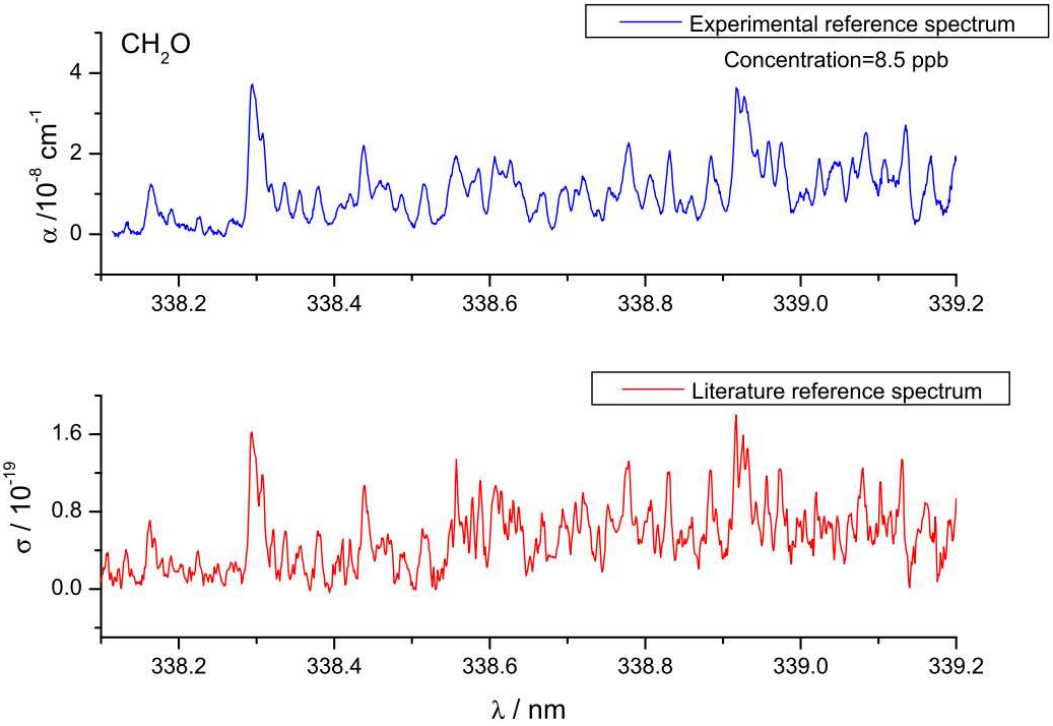

Figure 3.20: In blue, the experimental spectrum acquired at atmospheric pressure, used as a reference by the fit procedure. In red, UV absorption spectrum of CH_2O around 338.5 nm from the literature [60], acquired at atmospheric pressure, and at a resolution of 0.35 cm^{-1}.

The UV absorption spectrum of IO is assigned to the electronic transition ($A^2\Pi_{3/2} \leftarrow X^2\Pi_{3/2}$) which has well defined vibrational band structure [61]. The vibrational band (3,0) was chosen to detect IO around 436 nm because this band is strong and exhibits an extensive rotational structure which helps to define IO molecules. Figure 3.21 displays the rotational structure of IO (3,0) vibrational band around 436 nm from the literature (in red) [61], and the experimental reference spectrum (in blue). Figure 3.22 displays the UV absorption spectrum of NO_2 around 436 nm from literature (in red) [63], and the experimental reference spectrum (in blue). We underline that the structure of NO_2 is not completely resolved. Here, NO_2, which exists naturally in the ambient air, absorbs in the same spectral window of IO, and they are detected simultaneously.

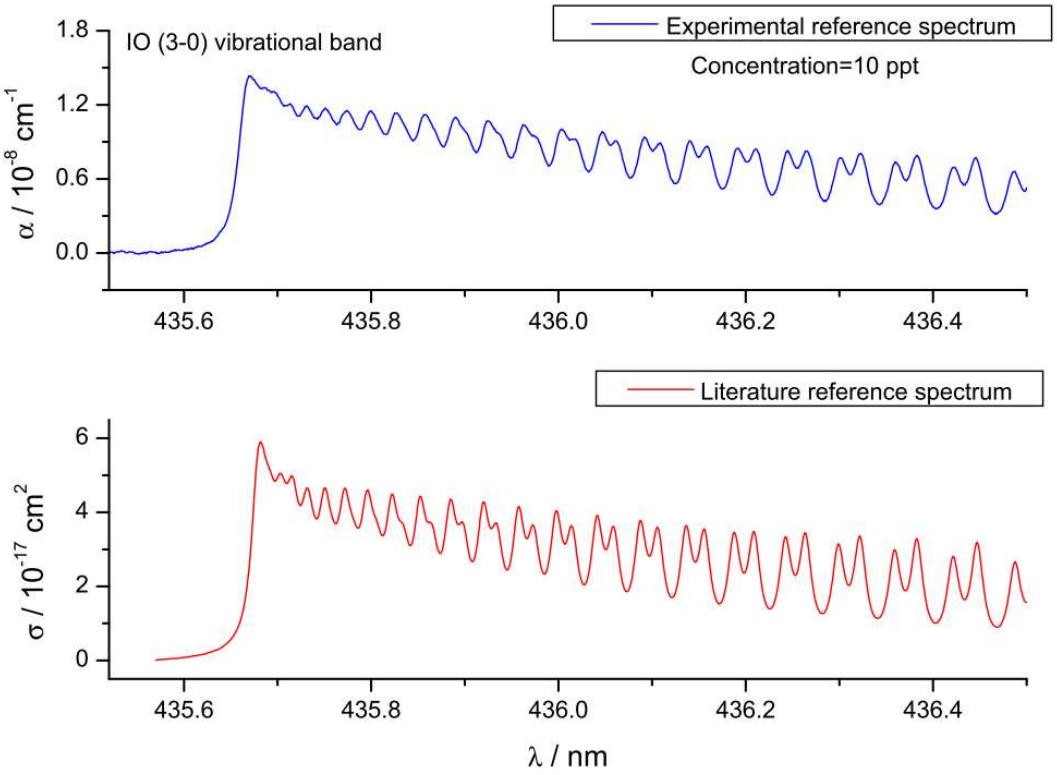

Figure 3.21: In blue, the experimental reference spectrum at atmospheric pressure. In red, rotational structure of (3,0) vibrational band of IO around 436 nm from the literature [61].

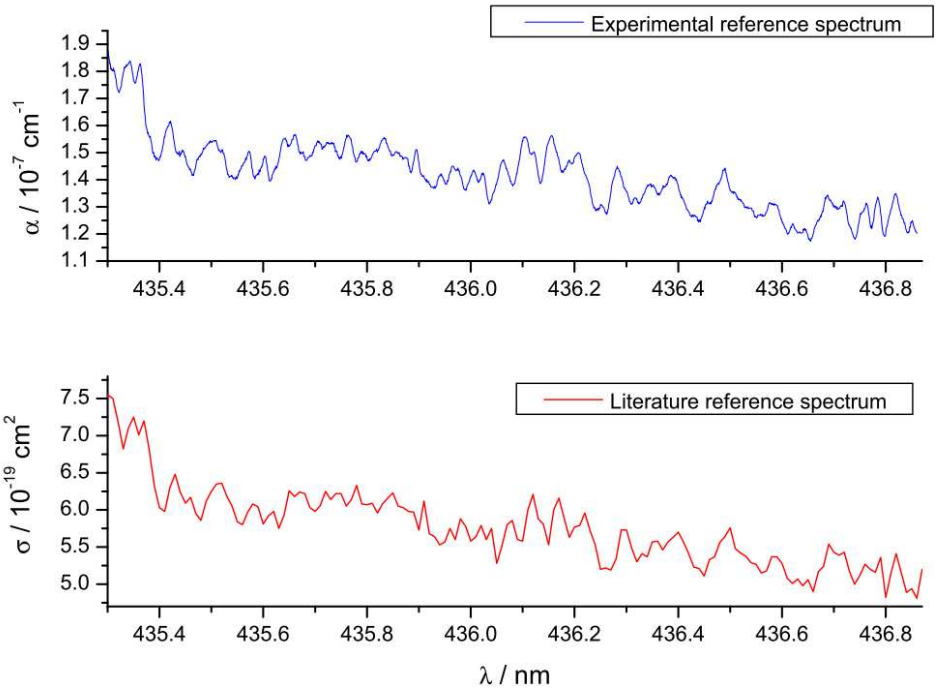

Figure 3.22: In blue, the experimental reference spectrum at atmospheric pressure. In red, UV absorption spectrum of NO_2 around 436 nm from the literature [63].

3.6. Results and discussion

I am presenting here the measurements done in the laboratory and during field campaigns. The measurements in the laboratory concentrate on the characterization of the Rayleigh scattering losses, the characterization of the HF cavities, and the measurement of the absorption spectra. The first field campaign was carried out at the Centre d'Océanologie de Marseille in the spring of 2011 for one week. This first filed campaign was only aimed to test the mechanical robustness of the instrument, discover the problems related to disassembly and assembly of its components, and think about further improvements of the system, as well as testing the ability of the work outdoor. A second field campaign took place at the CNRS Biologique Station of Roscoff in the North West Atlantic coast of France, during June 2011. The goal of this campaign was to prove that the instrument was able to perform long term measurement of the halogen oxides radical together with NO_2 and CH_2O, before sending it to Dumont d'Urville station in Antarctica at the end of 2011, which corresponds to the Austral summer. The measurements performed at Roscoff and Dumont d'Urville stations are discussed, and a brief conclusion is presented at the end.

3.6.1. Measurements at the laboratory

3.6.1.1. Rayleigh scattering

As the measurements are performed in the UV-visible spectral region, it was necessary to calculate the losses imposed by Rayleigh scattering, and analyze the effect of these losses on the cavity ring-down time, τ_{air}. Firstly, a brief introduction of Rayleigh scattering is presented and then the summary of the calculations. Rayleigh scattering is an elastic scattering of light radiation by particles much smaller than the wavelength of the light, and its intensity is proportional to λ^{-4}, therefore it dominates elastic-backscatter signals at short light wavelengths. If we take into account the depolarization effects [64], and the adjustments for temperature and pressure, the Rayleigh scattering coefficient is given by [65]:

$$\beta_{m,th} = \frac{8\pi^3 (m^2-1)^2 N}{3N_s^2 \lambda^4} \left(\frac{6+3\gamma}{6-7\gamma}\right)\left(\frac{P}{P_S}\right)\left(\frac{T_S}{T}\right) \tag{3.22}$$

Where, *m* is the real part of the gas refractive index, *N* is the number of molecules per unit of volume (number density) at the pressure *P* and temperature *T*, and N_s is the number density of molecules at standard conditions (N_s = 2.547 x 10^{19} cm^{-3} at T_s = 288.15 K and P_s = 101.325 kPa). γ is the depolarization factor, and its current recommended value, for dry air, is $\gamma = 0.0279$ according to [65].

If one accounts for Rayleigh scattering β_m, the ring-down time measured in the air τ_{air} (in the absence of absorbers) for a cavity of length *L* is given by :

$$\tau_{air} = L/\left[(1-R+\beta_m L)\times c\right] \tag{3.23}$$

While the ring-down time measured in the vacuum τ_{vac} is given by:

$$\tau_{vac} = L/\left[(1-R)\times c\right] \tag{3.24}$$

Then, the Rayleigh scattering β_m can be deduced from τ_{vac} and τ_{air} values:

$$\left(\frac{1}{\tau_{air}} - \frac{1}{\tau_{vac}}\right)\times\frac{1}{c} = \beta_{m,\exp} \tag{3.25}$$

Table 3.6 presents the experimental and theoretical Rayleigh scattering coefficients at 338.5 nm $\beta_{m,\exp}$, $\beta_{m,th}$, respectively. The mirror reflectivity (*R*) was calculated in vacuum conditions from the relation (3.24).

λ (nm)	τ_{air} (µs)	τ_{vac} (µs)	$\beta_{m,\exp}\ \left(\mathrm{cm}^{-1}\right)$	$\beta_{m,th}\ \left(\mathrm{cm}^{-1}\right)$	R(%)	$\frac{\beta_{m,th}-\beta_{m,\exp}}{\beta_{m,th}}$
338.5	6.0	7.1	$7.70\text{x}10^{-7}$	$7.82\text{x}10^{-7}$	99.953	1.3 %

Table 3.6: Values of τ_{air}, τ_{vac}, $\beta_{m,exp}$, $\beta_{m,th}$, R at 338.5 nm.

From Table 3.6, we can see a good agreement between the measured and the theoretical Rayleigh scattering coefficient. The values of τ_{air} and τ_{vac} comes from an average of 100 ring-down events, and the standard deviation of the measured ring-down time was ranging between 0.02 % and 0.05 %. To compare the effect of Rayleigh scattering to the losses induced by the cavity mirror l_{mir}, Rayleigh scattering losses l_{ray} for half cavity roundtrip (1 m path length). Table 3.7 presents the calculations at relevant wavelengths for trace gas sensing. The values of l_{ray} were calculated from the relation (3.22). Mirror reflectivities were measured only at 338.5 nm and 436 nm, while their values at other wavelengths were estimated with respect to the specification for the high reflective mirrors available in the market.

λ (nm)	**l_{ray}**	**l_{mir}= (1-R)**	**l_{ray} / l_{mir} (%)**
436	$2.82\text{x}10^{-5}$	$1\text{x}10^{-4}$	28
355	$6.55\text{x}10^{-5}$	$5\text{x}10^{-4}$	13
338.5	$8.15\text{x}10^{-5}$	$5\text{x}10^{-4}$	16
340	$7.82\text{x}10^{-5}$	$5\text{x}10^{-4}$	15.6
308	$1.19\text{x}10^{-4}$	10^{-3}	19

Table 3.7: Rayleigh scattering losses for 1 meter path length compared to the losses by reflection on the cavity mirror.

The calculation points out that the losses due to available mirror reflectivity are more important than Rayleigh scattering. Furthermore, the ring-down time used to calibrate the spectra is measured at atmospheric pressure (Since is easier to detect highly reactive molecules), so it takes into account the total losses provided by the mirrors and the Rayleigh scattering.

3.6.1.2. Measurements of ring-down time and mirror reflectivities

To estimate the mirror reflectivity of the cavity used to detect BrO and CH_2O, the ring-down time τ_{air} was measured at 338.5 nm with filtered air flowing in the cavity to eliminate absorption from BrO and CH_2O (the absorption interference from potential molecules that absorb in this spectral region like O_3, or Br_2 is negligible compared to the absorption of the molecules of interest. The measured value of τ_{rd} was 6.0 µs corresponding to a mirror reflectivity of R = 99.948 %, and then a cavity finesse of 6000 leading to an effective path length L_{eff} of 1.8 km (see chapter 2, section (2.3.2) for the calculations). In the same way, τ_{air} of the cavity deployed to detect IO and NO_2 was measured to be 30 µs. This value corresponding to a mirror reflectivity of R = 99.990 %, a cavity finesse of 32000 leading to an effective path length of 10 km. Table 3.8 summaries the measured and calculated values for both cavities. It is to be noticed that the mirror reflectivity, the finesse, and the effective length are calculated at atmospheric pressure. The correct value of the mirror reflectivity comes from τ_{vac}, but for the calculation, we considered roughly the mirror reflectivity corresponds to τ_{air}.

λ(nm)	τ_{air}(µs)	R (%)	Finesse	L_{eff} (km)
338.5	6	99.948	6000	1.8
436	30	99.990	32000	10

Table 3.8: Measured τ_{air}, and calculated values of R, Finesse, L_{eff}.

The ring-down time was estimated from an average of 100 ring-down events, and the fluctuation of τ_{air} value was between 0.02 % and 0.04 %.

3.6.1.3. Results of BrO measurements

3.6.1.3.1. Low pressure measurements

The first measurements of BrO in the laboratory were conducted at low pressure, in order to be in the same conditions than for the literature spectra and to better resolve the rotational structure of the $A^2\Pi_{3/2} \leftarrow X^2\Pi_{3/2}$ (7,0) BrO band. As we mentioned in gas preparation section, the spectra were taken by continuously flowing Br_2 and O_3 in O_2 carrier

gas through the cavity (the Br_2 source was the cylinder containing 0.13 % of Br_2 diluted in O_2). The pressure in the cavity was reduced down to 35 Torr by using a vacuum pump connected at the cavity output through a manual adjustable valve. The photolysis of Br_2 was performed by a LED array as described earlier. The measured low pressure spectrum of $A^2\Pi_{3/2} \leftarrow X^2\Pi_{3/2}$, (7,0) band of BrO is plotted in Figure 3.23 (2), corresponding to 1 ppbv (2.7×10^{10} molecule cm^{-3}) of BrO inside the cavity. For comparison, the equivalent high-resolution (1 cm^{-1}), and low pressure (35 Torr) spectrum available in literature [58] is plotted in Figure 3.23 (1). The estimated concentration of BrO is given by the fit procedure described earlier. The difference between the two spectra is plotted at the bottom of Figure 3.23, showing a good agreement between the experimental and literature spectra, and confirming that the high resolution achieved by the compact spectrograph is enough to resolve the residual rotational structure of the low-pressure spectrum.

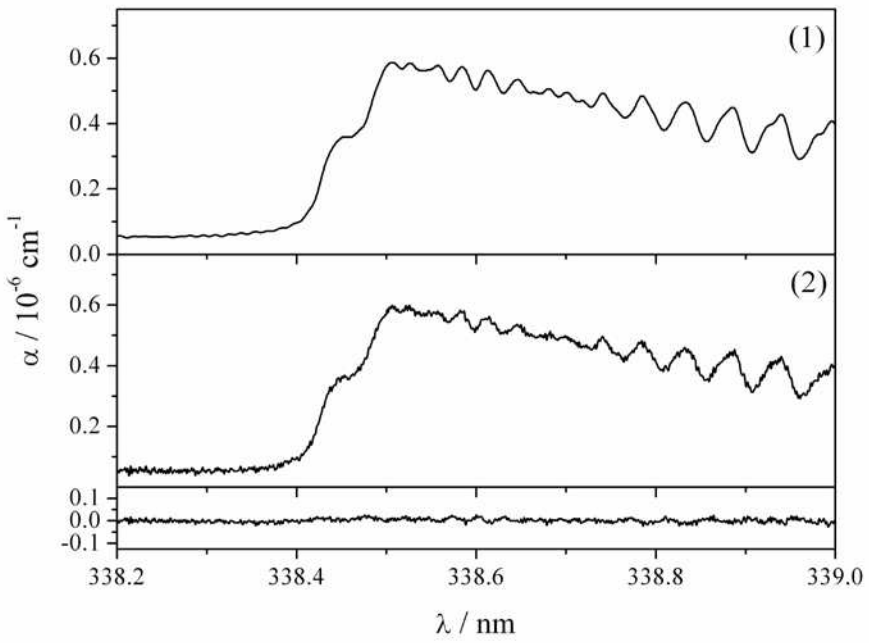

Figure 3.23: (1) Literature spectrum of BrO from reference [58]. (2) A low pressure (35 mBar) experimental spectrum for BrO at 1 ppb. The difference between the two spectra is reported at the bottom of the plot.

3.6.1.3.2. Atmospheric pressure measurements

Atmospheric pressure spectra at relatively high concentration of BrO (ppb level) were acquired by continuously flowing about 800 SCCM of gas mixture (Br_2 from the cylinder, O_3 and O_2) inside the cavity. The outlet of the cavity was connected to a pump. The cavity transmission spectrum in absence of BrO (reference spectrum) is plotted in the top window of Figure 3.24 (in black): during the acquisition the LED array was off to ensure that no Br_2 was photolyzed to form BrO. The top window of Figure 3.24 (in red) also displays the cavity transmission spectrum, when the LED array was on to form BrO (absorption spectrum). The ratio between the spectrum containing the absorption feature and the reference spectrum

(CCD dark signal was subtracted from both recorded spectra) provides the transmission spectrum, S(v). By knowing the empty cavity photon life-time τ_{air}, the frequency dependent absorption coefficient *α(v)* is calculated according to (3.18). The experimental spectral data *α(v)* was analyzed in real time by a standard linear multicomponent fit routine. The output parameters of the fit are the coefficients c_{BrO} used to calculate the concentration of BrO, and the coefficients of the polynomial function for the baseline. The experimental data *α(v)* is plotted in black on the bottom window of Figure 3.24, which also displays (in red) the fitted spectrum. The retrieved concentration of BrO was 5.1×10^{10} molecules cm^{-3}, which corresponds to a mixing ratio of 2 ppbv.

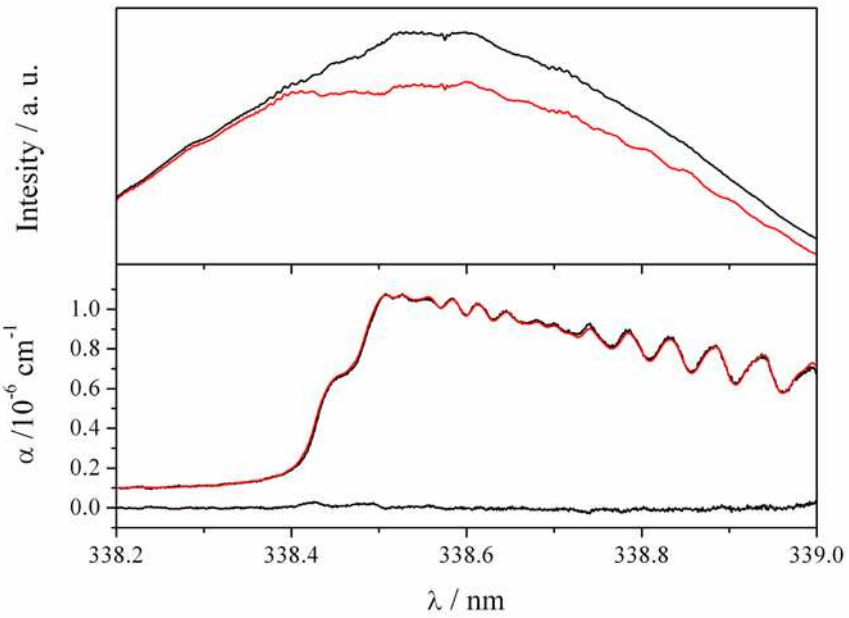

Figure 3.24: Top window: Raw spectra transmitted from the cavity in absence (black) and in presence (red) of BrO at ambient pressure. Bottom window: in red is the fitted spectrum, and in black is the measured spectrum at atmospheric pressure. The residuals of the fit are plotted on the bottom of the window.

Low concentrated sample of BrO were obtained in the laboratory using the permeation tube as source of Br_2. Figure 3.25 displays an example of a low concentration spectrum of BrO (6.4×10^8 molecules cm^{-3}, corresponding to 26 pptv) at atmospheric pressure, acquired within 26 s. The low concentration of BrO was obtained by fixing the temperature of the permeation tube oven at 25°C. Different concentration of Br_2 precursor was achieved by changing the flow rate of the carrier gas O_2. The acquisition time of 26 s corresponds to an average of 1000 elementary spectra. From the rms (root mean square) noise of the residual, the minimum absorption coefficient estimated was 1×10^{-9} cm^{-1} leading to a detection limit (1σ) of 1.7 pptv.

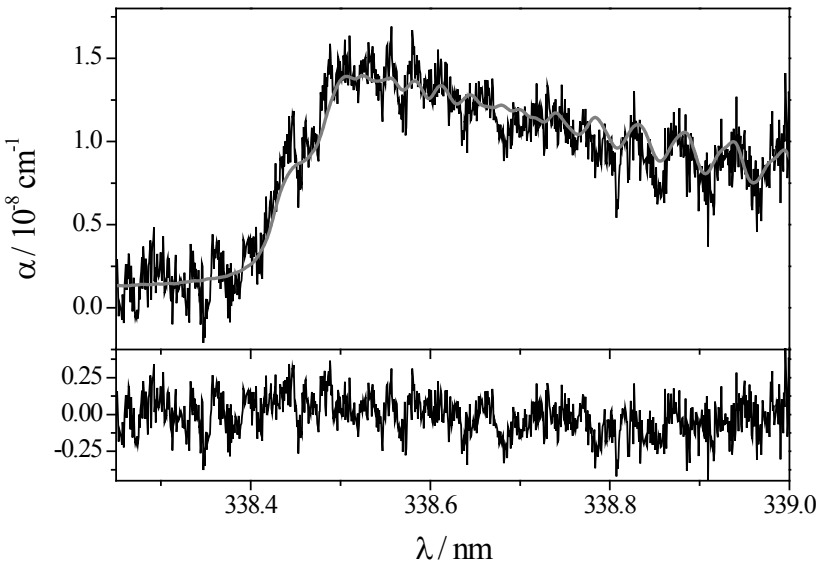

Figure 3.25: In black: Experimental spectrum. In gray: Fitted spectrum. The minimum absorption coefficient is 10^{-9} cm^{-1} estimated from the residuals reported in the lower window, leading to a detection limit of 1.7 pptv in air.

3.6.1.3.3. Long term measurement of BrO

An example of long-term measurement performed in the laboratory is reported in Figure 3.26, where a low-concentration sample of BrO (~ 60 pptv) was monitored for about 80 minutes. The observed fluctuations of ± 12 pptv are due to the source of BrO. Indeed; this source is based on the permeation tube inside a temperature controlled oven as explained earlier. This source exhibits fluctuations during the long term, and not reproducible from one day to another. Covering the internal surface of the oven with PFA would improve the system.

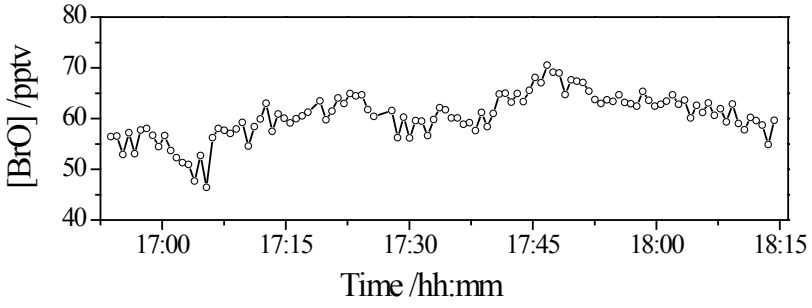

Figure 3.26: An example of long-term measurement performed in the laboratory by the ML-CEAS spectrometer. Measurements of about 60 pptv of BrO sample performed during 80 minutes with an acquisition time of 26 s.

3.6.1.4. Results of IO measurements

Figure 3.27 displays the absorption spectrum of IO at atmospheric pressure, prepared in the laboratory (as described earlier in sub-section (3.2.8.2)) at high concentration (1 ppbv) then rescaled to 10 ppt concentration to employ it as an experimental reference spectrum for the fit procedure.

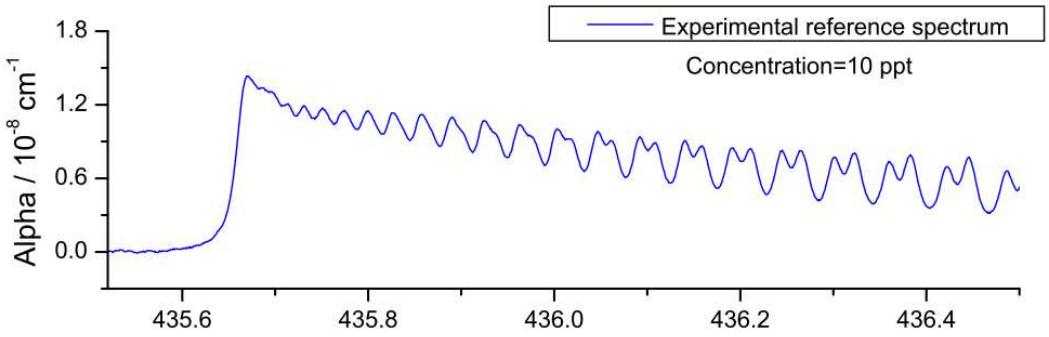

Figure 3.27: Experimental absorption spectrum of IO.

Further laboratory measurements at low concentrations of IO are not needed as the instrument performance has been fully characterized for the detection of BrO at 338.5 nm. At 436 nm, better performance is expected, since the mirror reflectivity is higher and the laser is more stable. In addition, to generate IO radicals at low concentration (few pptv), a permeation tube oven for IO, similar to the one build for the BrO generation, should be made, which will probably lead to the already observed issues of non-uniform reproducibility and instability of the concentration of the produced radical.

3.6.1.5. Allan variance and long-term stability

In order to better characterize the long-term stability of the spectrometer, an Allan variance [66] study was performed. In the case of a dataset where the only source of noise is the white noise, Allan variance decreases as the square root of the number of averages. Consequently, the sensitivity enhances for longer signal averaging until it reaches a point where long-term instabilities (due to drift in alignment, fluctuations of environmental conditions or laser power, etc.) induce an increase or a constant Allan variance value. Then, the Allan variance study gives the optimum averaging time which corresponds to the minimum Allan variance value. Allan variance measurements have to be performed at a constant concentration. As previously explained, it was difficult to get a stable source of halogen oxides in the laboratory due to high reactivity and chemical properties of these molecules. Thus the study was performed for zero levels of BrO and IO. This was done by continuously flow air from outside our laboratory (St Martin d'Hères-France) into the cavity. Because of the polluted environment and to the remoteness with respect to a marine boundary layer environment, the analysed outdoor air contains NO_2 and H_2CO but zero

levels of IO and BrO. We should underline that CH_2O (NO_2) absorbs at the same wavelength for BrO (IO) which allows to clearly fit experimental spectra even in the absence of BrO and IO. The top window of Figure 3.28 reports the long term simultaneous measurements of CH_2O and BrO for the outdoor air. The concentration of CH_2O varied during the experiment between 10 and 14 ppbv due to changes in the composition of the gas sample. Each acquired spectrum is averaged 10 times before being fitted, while the spectra in the absence of absorbers (reference spectra) were recorded at the beginning of the measurement averaging 10 thousands spectra. The time for one acquisition was 26 ms, which corresponds to the time needed to nearly saturate the CCD camera. The zero-level dataset of BrO was used to compute Allan standard deviation study shown in the bottom window of Figure 3.28. We use Allan standard deviation value which is a square root of Allan variance value, to get directly the vertical axis of the figure in concentration unit. In the log-log plot, the white noise is dominating for about 20 s, and the trend reaches a minimum value of 0.9 pptv after about 1 min of integration. For time average smaller than 20 s, Allan deviation values correspond to photon shot noise, estimated by considering the number of photons collected on the CCD pixels during the acquisitions as it will be explained later. At longer integration time, the Allan deviation increases mainly due to poor laser stability when running close to the limit of its tuning range (677 nm) to get the harmonic wavelength at 338.5 nm. This stability analysis points out that in order to obtain the best sensitivity for the measurement of BrO ($\sim$ 0.9 pptv), acquisition times on the order of 1 min should be used.

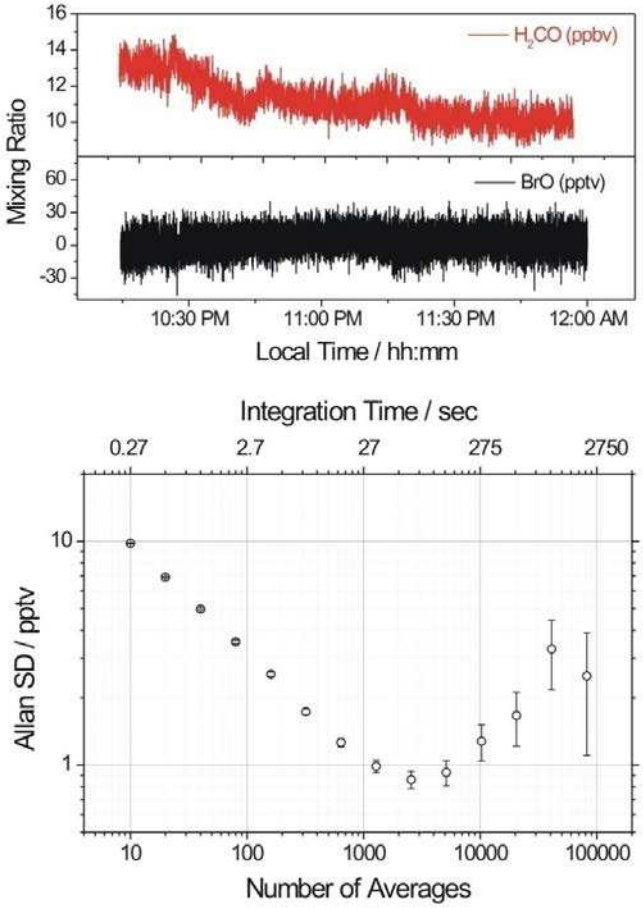

Figure 3.28: The top window reports long term measurements of CH_2O and BrO for outdoor air sampled outside our laboratory (in the absence of BrO). The bottom window shows the Allan standard deviation for the derived BrO concentration around zero.

The bottom window of Figure 3.29 displays Allan standard deviation plot for zero-level of IO in the log-log scale. The data analysis was performed for zero levels of IO in presence (top right) and absence (top left) of NO_2. The presence of NO_2, with high concentrations, (black dots) gives an Allan standard deviation values higher than what is observed in the case of zero level of NO_2 (blue triangles). This can be explained by the presence of a residual structure of NO_2 after the fit, indicating that the NO_2 reference spectra were probably not optimized. The detection limit reaches a minimum value of 20 ppqv (parts per quadrillion by volume, $1:10^{15}$) after 5 min of acquisition. Concentration of NO_2 of 2-5 ppb are 1000 times higher that detection limit. This affects the detection of IO by only 20 %, which shows the high dynamic range of the instrument. However taking a reference spectrum for NO_2 exactly at the same conditions that in the real measurement (same temperature and alignment) would reduce the effect of NO_2 presence on the detection of IO. It should be noticed that the possibility to average for longer time compared to the BrO situation is due to the better stability of the femtosecond laser source at the fundamental wavelength of 872 nm with respect to 667 nm.

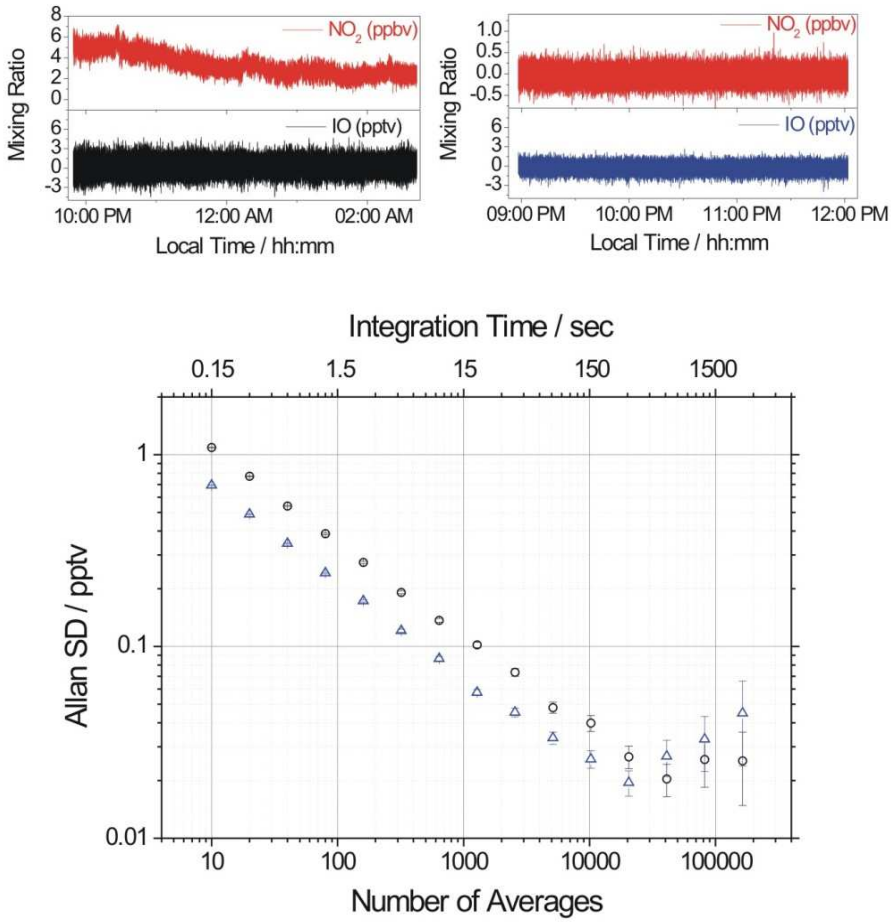

Figure 3.29: Top plots report the long term measurements of the air, outside the laboratory, contains NO_2 (left) and filtered air (right) free of NO_2, and zero levels of IO are expected in both cases. The Allan standard deviation plot for IO in presence of NO_2 (black circles) and with filtered air (blue triangle) is shown in the log-log plot at the bottom.

3.6.2. Measurements at Roscoff station

Here, a summary of the measurements made in the marine boundary layer of Roscoff on the North West coast of France throughout June 2011 for two weeks, is presented. The presence of halogen oxides radicals in the semi-polluted area of Roscoff is due to the active seaweeds (macroalgal species) [67]. When these species are fully or partially exposed to air during the low tide, they can emit iodine and bromine in forms of hydrocarbons (RX), ions or in form of I_2 and Br_2 [67]. For the displacement of the instrument, the laser head was detached from the breadboard (see Figure 3.2) and transported in a separate box. The rest of the spectrometer (optics, cavity and spectrograph) was left mounted on the breadboard, while the electronics and the gas manifold were also disassembled and transported separately. Reassembling and optimizing the whole setup took about one day.

3.6.2.1. Results of IO and NO_2 measurements

Figure 3.30 (in black) displays typical measured absorption spectra of IO, NO_2 around 436 nm. A continuous flow of 800 SCCM was provided by the membrane pump placed after the cavity. The experimental data were obtained after averaging 1000 spectra, while each spectrum needed 12 ms (the minimum integration time of the CCD camera) to be recorded. The fitted data are reported in red, which correspond to the sum of IO (blue) and NO_2 (green) spectra.

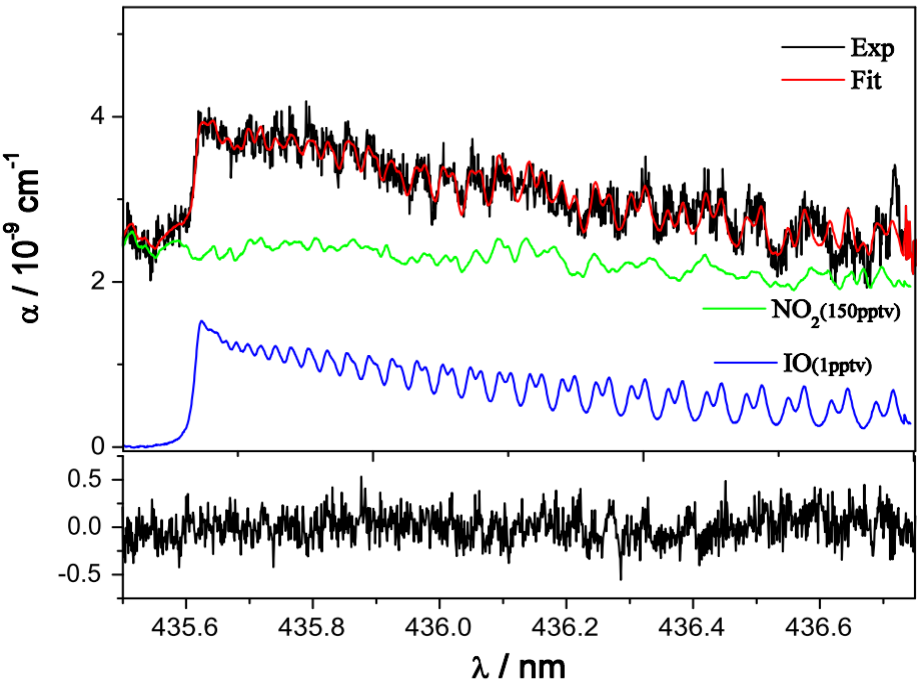

Figure 3.30: A typical spectrum of low concentration of IO and NO_2 recorded around 436 nm in Roscoff station. The experimental data and the fit are reported in black and red, respectively. The spectra of IO (1pptv) and NO_2 (150 pptv) are shown in blue and green, respectively. The residual of the fit is reported in the bottom window, corresponding to a rms of 1.5 x 10^{-10} cm^{-1}. With an acquisition time of 12 sec, a detection limit of 60 ppqv and 11 pptv of IO and NO_2 were achieved.

The experimental data are treated by the home-developed LabView software based on a linear multicomponent fit routine described in section (3.4), and the output parameters of the fit give the measured concentrations: 1 pptv and 150 pptv for IO, and NO_2, respectively. The residuals of the fit are reported in the bottom window of Figure 3.30. The rms noise is 1.5×10^{-10} cm^{-1} which corresponds to the minimum absorption coefficient. The normalised noise equivalent absorption achieved is then 1.3×10^{-11} cm^{-1} $Hz^{-1/2}$ per spectral element, according to the relation (3.20) taking into account the integration time of 12 s and 1500 independent points.

The derived detection limit from the measured spectra is 60 ppqv and 11 pptv, for IO and NO_2, respectively. The noise is limited by a residual structure in the fitting process which becomes significant for relatively high concentrations of NO_2.

During the field campaign, long-term measurements of IO and NO_2 were performed on outdoor air, and reported in Figure 3.31. Concentrations of IO of few pptv were observed during the day, while NO_2 concentration is about few ppbv. From Figure 3.31, an anti-correlation between the concentration of IO and NO_2 is observed as expected in a semi-polluted environment of Roscoff due to their reaction to form $IONO_2$. $XONO_2$ (X=Br or I) is known to be a temporary reservoir of halogen atoms in a NO_x-rich environment [68]. No particular correlation with the tide level was noticed. The rms noise (Each point is integrated for 2 min) is estimated to 40 ppqv and 20 pptv on IO and NO_2, respectively.

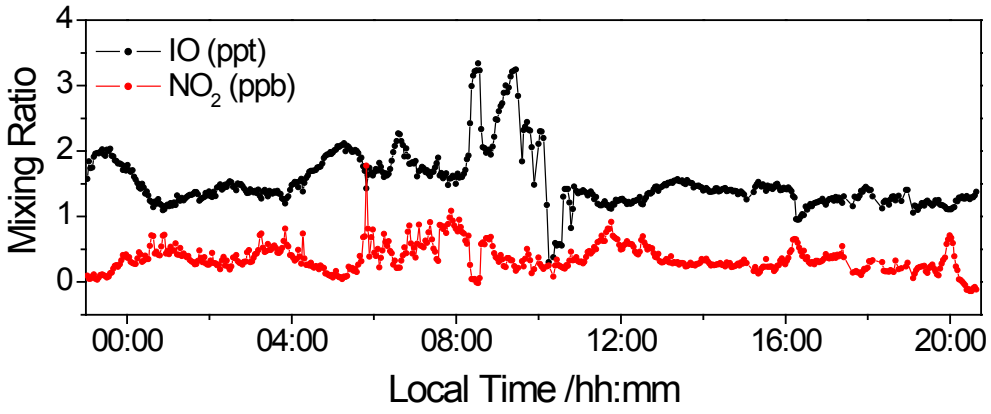

Figure 3.31: Long term measurements of IO and NO_2 performed at Roscoff station on June 18th 2011. Each point is integrated for 2 min. The rms noise corresponds to 40 ppqv, 20 pptv on IO and NO_2 traces, respectively.

3.6.2.2. Measurements of BrO and CH_2O

Figure 3.32 displays the absorption spectra of BrO and CH_2O obtained around 338.5 nm. The experimental data was also obtained by averaging 1000 spectra. The time needed to record one spectrum was 26 ms, corresponding to the time needed to fill the pixels of the CCD camera. The data were fitted by the labview program, and a concentration of 8.9 pptv and 5.6 ppbv for BrO, and CH_2O, were respectively found. The residuals of the fit are reported in the bottom window of Figure 3.32, corresponding to a rms of 1.0×10^{-9} cm^{-1} which is the minimum absorption coefficient. The normalised noise equivalent absorption achieved was $\alpha_{min} = 1.6 \times 10^{-10}$ cm^{-1} $Hz^{-1/2}$ per spectral element calculated from the relation (3.20) taking into account the integration time of 12 s and 1000 independent points. The derived detection limits from the measured spectra are estimated to be 1.4 pptv, 146 pptv, for BrO and CH_2O, respectively.

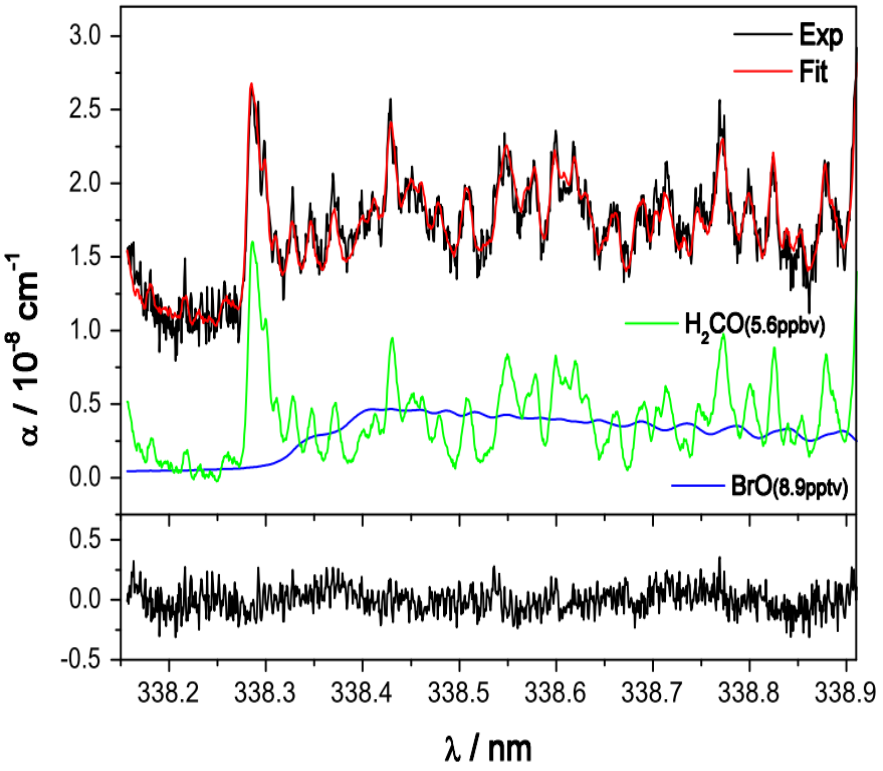

Figure 3.32: A typical low concentration spectrum of BrO and CH_2O obtained around 338.5 nm with 26 s of acquisition time. The blue and the green traces are the spectra of BrO (8.9 pptv) and CH_2O (5.6 ppbv), respectively. Experimental data (black) and fit (red) were offset by 10^{-8} cm^{-1} for better display. Fit residuals are reported at the bottom, and correspond to a rms value of 1.0×10^{-9} cm^{-1}. The derived detection limits were 1.4 pptv, 146 pptv, for BrO and CH_2O, respectively.

An example of a long term measurement of BrO and H_2CO is reported in Figure 3.33, where an increasing of the concentration of BrO up to (4 ±1) pptv was observed at 17 h00 on June 21st in correspondence of a low tide. Our observations are in agreement with previous measurements performed by Mahajan *et al*. [69] in the same site using LP-DOAS technique, where few ppt of BrO where observed and a strong dependence to the tide level was observed.

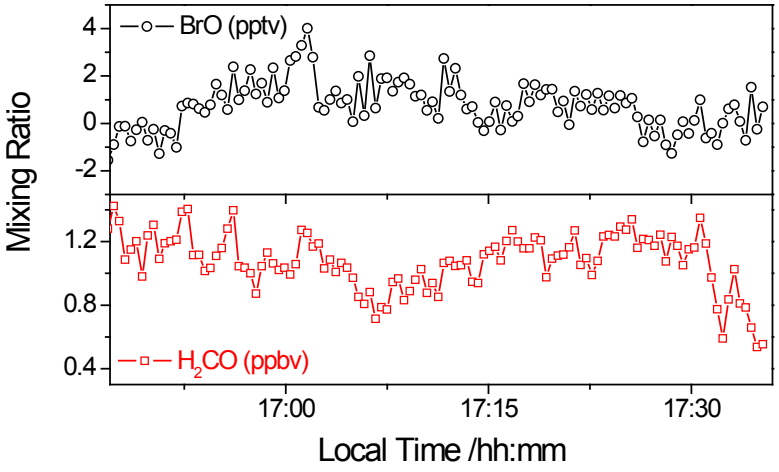

Figure 3.33: Long term measurements of BrO and CH_2O at Roscoff station on June 21st 2011.

3.6.3. Measurements in Antarctica at Dumont d'Urville

The instrument was sent at the end of 2011 for 3 months to Antarctica to make measurements of BrO and IO molecules. I did not participate in this campaign, but I present some measured data. I would like to say that the obtained data from Antarctica was completely analysed in a cooperation between the expert of atmospheric chemistry from laboratory of Glaciology and Geophysical environment (LGGE) in Grenoble, and our team in particular, our postdoc, Roberto Grilli who accompanied the instrument to Antarctica and made the measurements. The result of this analysis will be the subject of the next article under the title "First investigations of IO, BrO, and NO_2 summer time atmospheric levels at a coastal East Antarctic site using mode-locked cavity enhanced absorption spectroscopy".

In summary, IO, BrO, and NO_2 were measured for the first time at Dumont d'Urville (East Antarctica) during Austral summer 2011/2012. IO mixing ratios ranged from the detection limit (0.02 pptv) up to 0.1-0.2 pptv. BrO remained close or below the detection limit (1 pptv) of the instrument. Daily averaged NO_2 values ranged between 3 and 57 pptv (21 ± 14 pptv) being far higher than levels of a few pptv commonly observed in the remote marine boundary layer. The measured concentration for BrO (~1 pptv), is at least 3 times lower than the recorded one (3 pptv) at Halley station (British Antarctic Survey), by [30]. The measured concentration for IO are more than one order of magnitude lower than those observed (3 pptv) at Halley station in the summer, recorded by [30]. Example of IO and NO_2 measurements is shown in Figure 3.34.

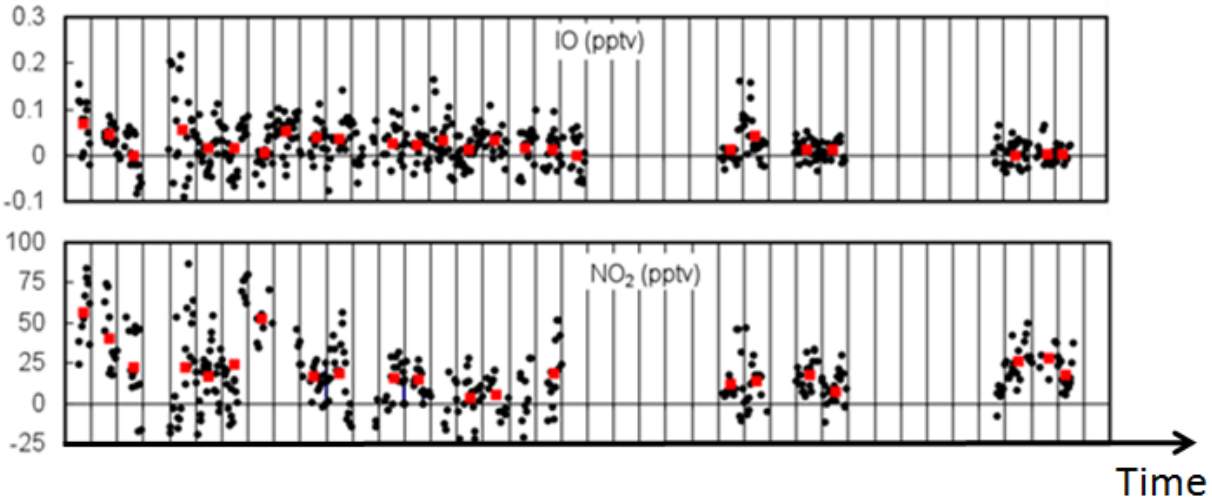

Figure 3.34: IO and NO_2 mixing ratios at DDU in January/February 2012. Black and red points (top) refer to 1 h averages and daily means, respectively.

3.6.4. Photon shot noise limited Detection

Here, we demonstrate that our detection is shot noise limited. This is achieved by using CCD detector arrays with sufficiently high spectral resolution.

3.6.4.1. Shot noise calculation

The minimum absorption coefficient is ultimately limited by the photon shot noise. For a spectrally multiplexed detection, this limit is given by [70]:

$$\alpha_{\min}^{SN} = \sqrt{2eM / \eta PT}\,(\pi / FL) \tag{3.26}$$

Where, e is the electron charge, η is the detector response factor (which includes the quantum efficiency), P is the total power, T is the integration time, L is the cavity length, F is the cavity finesse, and M is the number of independent points. The factor 2 accounts for the fact that one elementary spectrum is actually the ratio of two CCD acquisitions carrying the same noise. The terms under the square root corresponds to the reciprocal of the number of photons per pixel.

3.6.4.2. Estimation of the shot noise limit for IO and BrO detection

The calculation for the BrO shot noise detection is well explained in our article [52], I use the same approach for IO shot noise detection limit as follows:

The power P received by the CCD detector is given by the following relation:

$$P = p_{in} \times T_c \times r_{FSR} \times \frac{f_{\mathrm{mod}}}{F} \times T_{BS} \times T_{gr} \times M_{mat} \times S \tag{3.27}$$

Where, p_{in} is the laser power at the cavity input (p_{in} =30 mW), T_c is the cavity transmission at resonance (T_c=16 %), $r_{FSR}=(f_{rep}/FSR_{cav})$ =0.5, f_{mod} is the duty cycle of the modulation with

respect to the cavity FSR (f_{mod}=90 %), *F* is the finesse cavity (F=32000), T_{BS} is the transmission of the beam splitter towards the CCD (T_{BS}=*50 %*), T_{gr} is the grating efficiency (T_{gr}=*50 %*), M_{mat} is the spatial mode matching coefficient (M_{mat}=99 %), and *S* is the spectral coverage of the CCD (70 %=1500/2048).

Here, the estimation of the power *P* received by the CCD at 436 nm is firstly discussed. The laser beam is attenuated by a factor of 6 to reach 30 mW at the cavity input. This reduction is necessary to avoid the CCD saturation even at its minimum integration time. We estimate T_c=16 % cavity transmission at resonance, where the measured mirror transmission T_m is 60 ppm at 436 nm, leads to $T_c=T_m^2/(1-R)^2$=16 %, here, the mirror reflectivity is calculated from the ring-down measurement to be 0.9999 %. Furthermore, only half of the laser modes are being injected because FSR_{cav}= 2 x f_{rep}. The duty cycle of cavity injection has also to be taken into account by the factor f_{mod} /F. It is given by the cavity modes width over the cavity modulation range: about 0.9/F for modulation over f_{mod}=90 % of the cavity FSR. Finally, we take into account that 50 % of the cavity output power is sent to a photodiode used for ring-down measurements and cavity length tracking. Then only 30 % of the cavity output power reaches the CCD array after dispersion at the spectrograph Echelle grating (losses of about 50 % imposed by the grating). The power *P* received by the CCD is then 14 nW (9 pW per pixel, considering M=1500) calculated from (3.27).

Now, the photon shot noise calculation can be computed with the following values. The CCD response in the UV-visible region is η = 0.23 A/W, and M = 1500 is the number of independent pixels. The CCD wells capacity is 150 000 photoelectrons which are usually filled up to about 80 % of their capacity. Let us remove first the factor of 2 in the relation (3.26), as our single exposure CEAS spectra are normalized using a low noise averaged zero absorption spectrum. This yields a shot noise limited minimum absorption coefficient $\alpha_{\min}^{SN} = 3.2\times10^{-9}\,\mathrm{cm}^{-1}$ for 12 ms acquisition time. This value is in a very good agreement with the rms value (α_{min}=3.3x10^{-9} cm^{-1}) obtained from the residuals related to a spectrum obtained for a single CCD exposure as shown in Figure 3.35 (upper window, left side). This highlights that at short averaging time, the experimental spectra are photon shot noise limited.

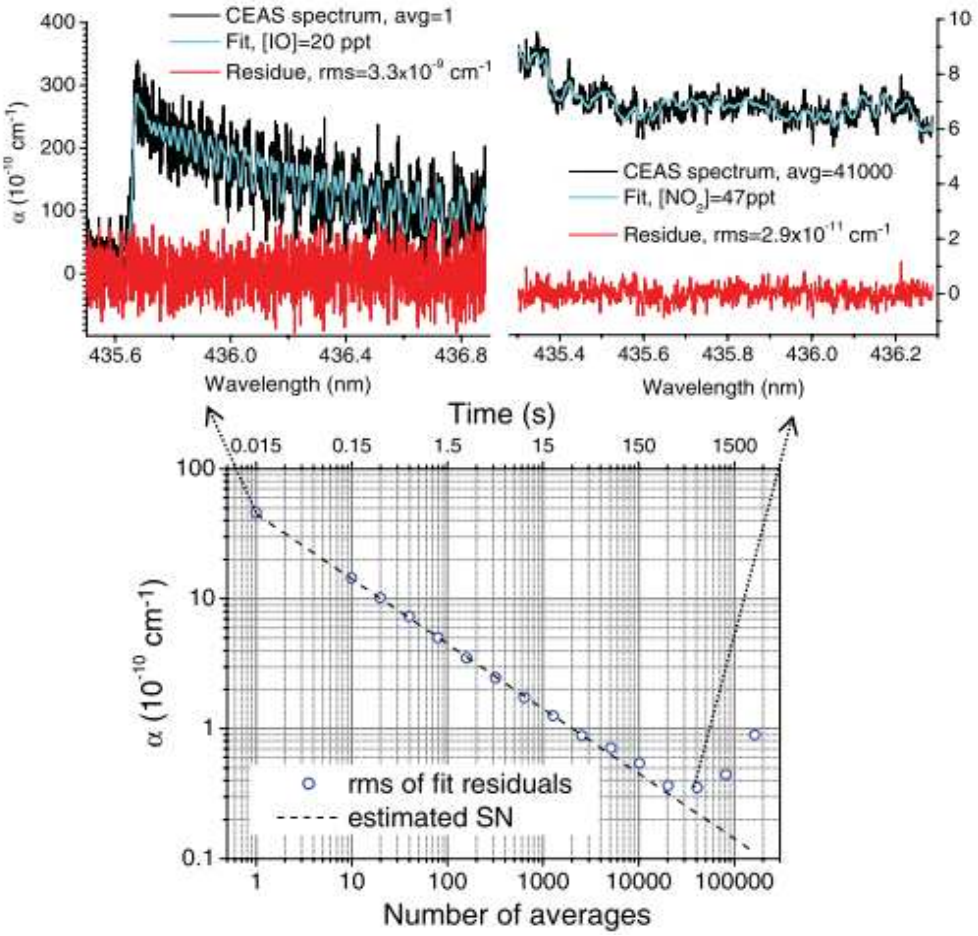

Figure 3.35: Top left: IO spectrum for a single 12 ms CCD exposure. Top right: spectrum of NO_2 from averaging 41 000 CCD exposures. Spectral fits using a linear combination of literature cross sections for IO and NO_2 yield the displayed molecular concentration. Fit residuals have rms values corresponding to the expected level of photon shot noise. At the bottom is a plot of the rms versus the averaging number.

If we now include the factor 2 accounting for a reference with the same averaging, and further consider the reduced sampling bandwidth of the total sample and reference acquisition time (24 ms), we obtain a normalized spectral detection limit of 7×10^{-10} cm^{-1} $Hz^{-1/2}$, which is the noise level over a spectrum. If we finally account for the number of simultaneously acquired spectral elements (divided by $\sqrt{1500}$), we obtain an absorption sensitivity of 1.8×10^{-11} cm^{-1} $Hz^{-1/2}$ (per spectral element), which is a widespread figure of merit useful for comparison between different absorption spectroscopy techniques.

The bottom window of Figure 3.35 displays a plot of the resulting rms noise versus the number of averaged CCD acquisitions, *N*. As the first point of plot is shot noise limited measurment, the $1/\sqrt{N}$ dependence implies shot-noise limited measurements from the shortest acquisition times all the way to about 10 min averaging. The lowest rms noise obtained here for spectra averaged up to 10 min is rather impressive: 3×10^{-11} cm^{-1}, or 7×10^{-13} cm^{-1} when normalizing per spectral element.

At longer time scales, drift of interference fringes or CCD pattern noise begin dominating the residuals of the spectral fit. We should underline that each point in the rms noise plot is obtained by using the same averaging for the reference and the signal, while the spectra displayed as examples of short and long times averages are normalized using references averaged over even longer times. This explains the factor $\sqrt{2}$ smaller rms levels displayed on these spectra. We reported the IO spectrum for one acquisition, and the NO_2 spectrum for long time acquisition in Figure 3.35, because it was easier to get a stable source of NO_2 during the measurement, compared to IO.

3.6.5. Calculation of detection limit from the measured spectrum

From the relation (3.21), the DL values can be calculated directly for the measured absorption spectra reported in Figure 3.30 for (IO, NO_2), and in Figure 3.32 for (BrO, IO). Table 3.9 presents a comparison between these calculated values and the respective values (DL_{AV}) extrapolated from Allan variance analysis in Figure 3.28 and Figure 3.29 for BrO and IO, respectively. The value (n_{pxl}), which is the number of the spectral elements, is taken (300=1500/5), (250=1000/5) for IO and BrO, respectively. We divided the number of pixels 1500 (1000), covered by the measured spectrum of IO (BrO), by the apparatus function (5 pixels).

Molecule	λ (nm)	T(s)	$ct \times \sqrt{n_{ne}}$ (10^{-10} cm^{-1})	Noise (10^{-10} cm^{-1})	Concentration (ppt)	DL (ppt)	DL_{AV} (ppt)
IO	436	12	33	1.5	1	0.04	0.06
NO_2			19	1.5	150	11.5	
BrO	338.5	26	71	10	8.9	1.4	1.3
CH_2O			426	10	5600	132	

Table 3.9: Comparison between the detection limit values estimated directly from the measured spectra to the detection limit values derived from Allan variance plot.

The values of DL calculated directly from the experimental spectra (for BrO and IO) are in good agreement with the DL_{AV} values. Here, the intrinsic structure of the molecular spectra plays an important role, which leads to a lower detection limit for IO with respect to BrO, together with the greater cavity finesse and a better laser stability.

3.7. Conclusion and perspectives

A compact and transportable instrument (~200 kg Total weight) based on a mode-locked cavity-enhanced absorption spectroscopy to measure pptv and sub-pptv levels of atmospherically important halogen oxide radicals has been developed. Thanks to the

double-cavity setup, alternative measurements of BrO and IO, at 338.5 nm and 436 nm respectively, were possible. Due to the broad-band character of the instrument, H_2CO and NO_2 could also be measured by the instrument together with the halogen oxides which were the principal target species of this development. This compact and robust instrument is suitable for *in situ* measurements of local concentrations of BrO / H_2CO and IO / NO_2. The detection limit and the bandwidth normalized minimum absorption coefficient for each measured molecule is presented in Table 3.10. It should be noticed that the performance of the instrument in the laboratory and in the field are identical, leading to the same stability results as well as the same detection limits at both wavelengths.

Molecule	λ(nm)	α_{min} (BW)($cm^{-1}Hz^{-1/2}$)	T(s)	Detection limit(pptv)
IO	436	1.3×10^{-11}	300	0.02
NO_2				2.3
BrO	338.5	1.6×10^{-10}	60	0.90
CH_2O				96

Table 3.10: The detection limit and the bandwidth normalized minimum absorption coefficient of BrO, CH_2O, and IO, NO_2.

We proved that our method to calculate the detection limits directly from the measured spectra was consistent with the values estimated from Allan variance plot, for BrO and IO. Therefore, we can extrapolate the detection limit of NO_2 (2.3 pptv) and H_2CO (96 pptv) with respect to the detection limit for IO and BrO (within the white noise regime). From the previous table, it is clear that the performance of the instrument around 436 nm is better than around 338.5 nm. This can be explained since at 436 nm higher reflectivity mirrors (R = 99.990 %) are commercially available, while at 338.5 nm, the best mirror reflectivity achievable at the moment is 99.95 %. Furthermore, the Ti:Sa laser is more stable at the fundamental wavelength of 872 nm, compared to its operation at 667 nm, which is close to the limit of its tunability range. The large tunability and versatility of the system will allow trace detection of several other important atmospheric species such as OBrO, OClO, OH, HONO, and SO_2 for which absorption cross sections in the near UV-visible are available in literature. In fact, by frequency doubling or tripling the fundamental radiation, the laser source could cover continuously all the wavelengths between 230 and 1080 nm. By taking into account the reflectivities of the mirrors available in the market and the molecular cross-sections, it is easy to extrapolate the achievable detection limits for the different species from the performance obtained at 436 nm. Table 3.11 presents the potential detection limits estimated for each molecule. To make these estimations, we do not consider the Rayleigh scattering since the losses per passage do not exceed 30 % of losses due to mirror

reflectivity even in the UV region (see Table 3.7). The extremely low detection limits reported here would be sufficient to detect those highly interesting atmospheric molecules in unpolluted environments. In particular, for the OH that is considered one of the most important radical in the atmosphere with an abundance of 10^6 molecules cm^{-3} (40 ppqv), the expected detection limit for the instrument would be 6 x 10^5 molecules cm^{-3} (20 ppqv), which should be enough to probe the strong rotational transitions of the OH radical at 308 nm. For this reason, the possibility to perform *in situ* measurements of this radical by using the ML-CEAS technique is promising.

Molecule	λ(nm)	Mirror reflectivity %	Detection limit (pptv)
HONO	355	99.95	15
OBrO	505	99.99	0.1
OClO	340	99.95	0.6
OH	308	99.9	0.02
SO_2	300	99.9	12

Table 3.11: Detection limit of other environmental important molecules.

As the sensitivity of the developed system is limited by the photon shot noise, we could in principle achieve a better performance on our current setup by using a CCD allowing shorter exposure times and/or larger well capacity. In addition, the sensitivity can be increased at least by a factor of 3 as concluded from Table 3.7 (as long as the Rayleigh scattering is not dominant) by using higher reflective mirrors at both wavelengths (338.5 nm, 436 nm), which are unfortunately not commercially available at the moment.

Chapter 4. Vernier effect technique

4.1. Introduction

In the second and third chapter, we have explored the principle, the technology, and some applications of the ML-CEAS technique. We have also discussed its enormous potential, in particular, the high spectral resolution, the ultrahigh detection sensitivity, and the rapid acquisition.

Nevertheless, the problem associated with this technique is that its performance does not reach very high resolution on a broad spectrum. At the end, we are limited by the number of pixels of the CCD which is for instance 2048. To analyze a spectrum of 10 nm broad, the resolution will be limited at 5 pm, and even worse since we have to consider the apparatus function of the spectrometer which covers at least 2 or 3 pixels. Consequently, the spectral resolution, in the best case, will be in the range of 10 pm when analyzing a spectrum 10 nm broad. This drawback was not a real problem in our application, since the laser bandwidth after the frequency doubling was narrow (1 or 2 nanometers), but for broadband detection, this imposes a crucial limit. To overcome this point, it is possible to use the virtually-imaged phased array (VIPA) based spectrometer [9, 71] as detection system which provides for example (1000 x 1000 pixels). However, the VIPA system suffers from the fact that it is an etalon, so the fringe pattern is extremely sensitive to optical alignment which makes the reproducibility and calibration, difficult procedures [72].

We intended to develop a new technique which allows broadband trace gas detection with a high sensitivity, a high spectral resolution, and keeps a simple setup. This new technique is based on a Vernier effect between the laser comb and the cavity comb. Like in the ML-CEAS technique, the frequency comb generated by a mode locked laser is injecting into a high finesse (HF) optical cavity. The main difference is that the cavity length is not adjusted around the perfect matching between the two combs, but small mismatch is intentionally left between them to get the resonance in the frequency domain for only one group of adjacent laser modes inside the spectrum of the laser. Then, the cavity length is tuned around this mismatch position, to scan the whole laser spectrum instead of being at the perfect matching position between the two combs, and then all the laser modes go in resonance with the cavity modes at slightly different times like in the ML-CEAS technique.

Indeed, the name of this technique is chosen in analogy with the Vernier caliper tool, which is used to measure the distances more precisely than the simple rulers. Usually, when we measure a distance with a ruler, we can give a reading with an accuracy of about 1 mm range. Thanks to the two parallel scales of the Vernier tool, the fixed one (main scale) and the sliding one (Vernier scale), it is possible to improve the accuracy of our measurement.

The main scale is divided so that its marks are one millimeter apart (its interval (Int_1) = 1 mm). The Vernier scale marks are 9/10 millimeter apart (its interval (Int_2) = 9/10 mm), that means ($10 \times Int_2 = 9 \times Int_1$), as shown in Figure 4.1. Now, if the Vernier scale is moved just Δ_{Int}= 1/10 mm from the zero points aligned position (initial matching position between the main scale and the Vernier scale (N=0 on Figure 4.1), the Vernier marks all moves away together, which brings the first Vernier mark into coincidence (N=1 on Figure 4.1) with the main scale's 1 mm mark (first mark). Each time, the Vernier scale is moved Δ_{Int}=1/10 mm further, the next higher value of Vernier mark lines up with a main scale mark.

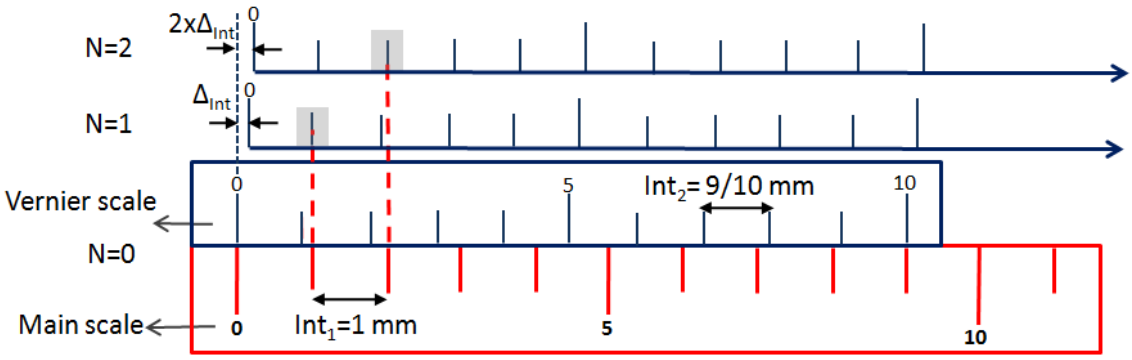

Figure 4.1: Principle of Vernier scale.

An example of reading by a Vernier caliper tool is shown in Figure 4.2, If the Vernier scale is moved from the zero points aligned position by a small amount, the large marked number on the main scale to the left of the zero line on the Vernier scale gives the reading of the deviated distance, or the starting number of the measurement. By comparing the Vernier scale lines to the ones on the main scale, there will be only one line on the Vernier scale best matches one line on the main scale. The best match between those lines gives the last digit of the measurement or the precision of the measurement as indicated in Figure 4.2, where the 0.2 value can be read off the main scale and the 5th Vernier mark is the matching mark that means the reading measurement should be 0.25.

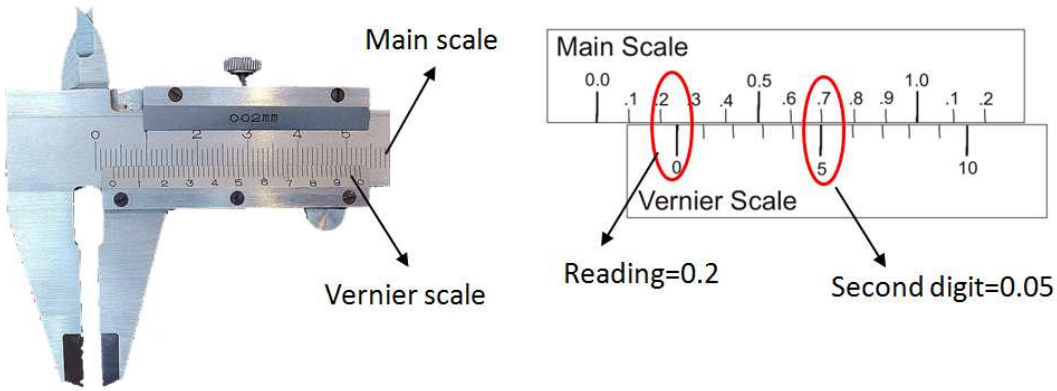

Figure 4.2: Left, Vernier caliper tool. Right, Vernier Scale with its zero mark aligned at 0.25 on the Main Scale.

We apply the same idea in the Vernier effect technique, but in the frequency domain, where the HF cavity modes (like Vernier scale) are mismatched with the laser modes (like the main scale). The only difference that is the cavity mode has a certain width, therefore, there is a group of laser modes matchs with the cavity mode, and there is more than one matching position due to the periodicity of the comb.

We should underline that the high sensitivity is provided by means of the HF cavity that vastly extends the interaction length with the gas sample under study, and the enhancement factor is again F/π as for ML-CEAS, since this technique is using also a transient coupling between the laser mode and the cavity mode.

4.2. Principle of Vernier effect technique and the analytical model

4.2.1. Principle of Vernier effect

We have seen from the second chapter that the ML-CEAS technique works at the magic point (MP) position which corresponds to the perfect matching between the laser comb and the cavity comb. The MP is obtained by making the cavity FSR equal (or integer multiple) to the laser repetition rate f_{rep}, ($FSR=f_{rep}$ or $FSR=N_c x\ f_{rep}$, and N_c is an integer). For the rest of the discussion, we will consider the situation where $N_c = 1$.

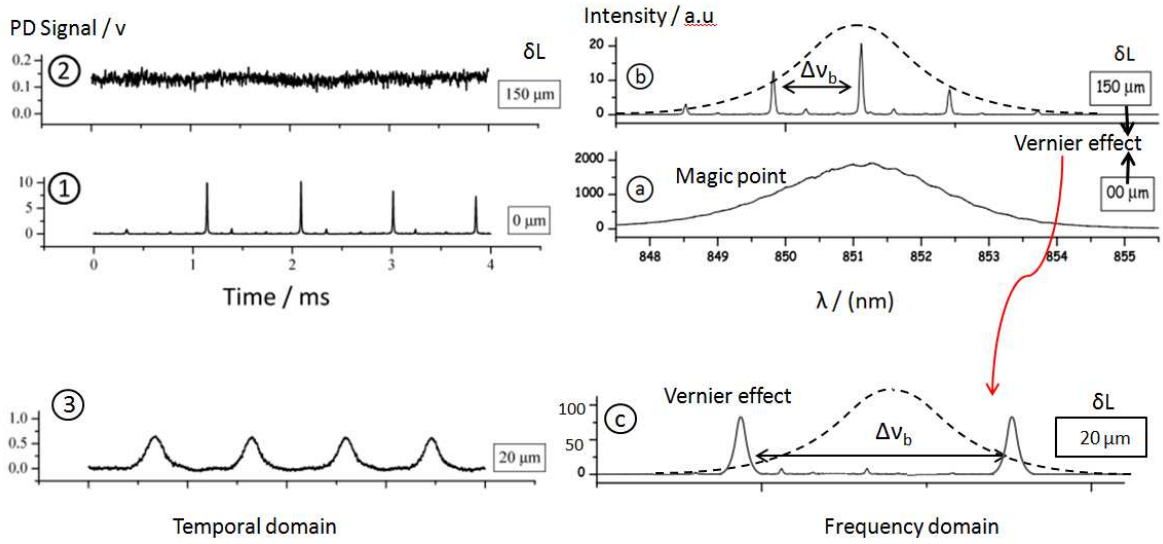

Figure 4.3: Right: Laser spectra by a spectrometer after the cavity in the frequency domain at MP (a), and at δL=150 µm (b), δL=20 µm (c) [3], the beat signal appears in b and c. Left: Photodiode signal at MP (1), and at δL=150 µm (2), δL=20 µm (3), the PD signal is acquired when the cavity length is modulated by a PZT.

As we have seen in (Chapter 2, section 2.4.2), at the MP position, all the laser modes go in resonance with the corresponding cavity modes simultaneously, and the whole laser

spectrum is transmitted (Figure 4.3.a) without any beatings pattern. When the cavity length is modulated around the MP position, the PD signal displays sharp peaks (Figure 4.3.1), and each passage through resonance results in transmitting all the laser modes at the same moment, that is why the resonance peaks are very narrow.

In Figure 4.3.b, the cavity length is changed by δL=150 µm (about 300 x λ/2) away from the MP. At this position, the cavity FSR is not equal to the repetition rate f_{rep} but changed of Δ_{FSR} as follows:

$$FSR = f_{rep} \mp \Delta_{FSR} \tag{4.1}$$

Where Δ_{FSR} is related to the change of cavity length δL by:

$$\Delta_{FSR} = FSR_0 \times \frac{\delta L}{L} = f_{rep} \times \frac{\delta L}{L} \tag{4.2}$$

Due to the mismatch between the two combs, a periodic signal of beating peaks in the frequency domain appears as shown in Figure 4.3.b. Each beating peak is produced by a group of laser modes which go in resonance with the corresponding cavity modes and are transmitted simultaneously.

Here, I define two key parameters, $\Delta\nu_b$ the spacing between two beating peaks (period of the beatings signal in the frequency domain), and W_b the width of each beating. Both of them depend on δL. As we had seen in (Chapter 2, section 2.4.2), the period $\Delta\nu_b$ is given by:

$$\Delta\nu_b = c/(2\times N_c \times \delta L) \tag{4.3}$$

Because of the important change of the cavity length (δL=150 µm), the period $\Delta\nu_b$ is small, and several beating peaks are located inside the laser spectrum. If the cavity length is modulated around this position by a PZT, then the PD gives roughly a continuous signal (Figure 4.3.2), since at every moment, the PD receives light transmitted by the cavity coming from the different beating peaks inside the laser spectrum. In other words, each peak scans the input laser spectrum during the cavity modulation, and partially contributes to the PD signal. As there are always several beating peaks transmitted by the cavity, there is always a signal on the PD, and the signal is approximately constant. The light received by the PD is coming from different parts of the laser spectrum. For the Vernier effect, we cannot be in this situation, since if there is an absorption in one part of the spectrum, it will be impossible to determine where this absorption takes place.

To avoid the overlap, the mismatch δL between the two combs should be small enough to increase the separation between two successive peaks $\Delta\nu_b$ as indicated from the relation (4.3). Indeed, to ensure that there is only one beating peak inside the input laser spectrum (Figure 4.3.c) during the cavity modulation, the period $\Delta\nu_b$ should be equal or greater than the input laser spectrum $\Delta\nu_l$. The Vernier effect technique corresponds to the position

illustrated in (Figure 4.3.c), where $\Delta\nu_b \geq \Delta\nu_l$. For δL = 20 µm (about 40 x λ/2). If the cavity length is modulated around this position, then the PD gives approximately identical resonance peaks, and each peak corresponds to the same output laser spectrum (Figure 4.3.3). The resonance peaks in Figure 4.3.3 are lower in intensity, but they are wider compared to resonance peaks in Figure 4.3.1. However, the energy inside each resonance peak in these figures is the same. The width of the resonance peak increases due to passing the laser mode through resonance at slightly different times as the cavity length is deviated from the MP position.

At a given moment, the PD will receive light from a beating peak inside the laser spectrum; therefore the spectral resolution of Vernier effect technique is given by the width W_b of this beating beak. Indeed, W_b decreases when δL increases due to the fact that the number of laser modes participating in one beating peak is reduced. Therefore, the resolution enhances when it gets further from the magic point. But in parallel, increasing δL will reduce the beating period $\Delta\nu_b$ as indicated from (4.3) which may lead to the overlap problem. Thus, there is an optimal value of δL to enhance the resolution, and to avoid the overlap of output spectra.

In the case of a well stabilized frequency comb that provides a comb linewidth narrower than the optical cavity mode width $\Delta\nu_c$, the spectral resolution is only limited by the cavity mode width which in turn, determines the width of the beating peak. Otherwise, the resolution will be limited by the comb linewidth. In the following discussion, we will make the assumption that the comb linewidth is narrower than $\Delta\nu_c$, a particularly interesting regime for the Vernier effect.

Figure 4.4 illustrates the principle of the technique. To simplify this scheme, the laser carrier envelope frequency f_{CEO} and the $f_{0,cav}$ of the cavity are supposed to be zero. The lower part (Figure 4.4.a) corresponds to the perfect match between both combs ($FSR_0 = f_{rep}$) at the MP position (N=0). Here, the frequency scale starts from zero, and the possible laser modes start from the m^{th} mode number. When the cavity length is increased by δL=λ/2, from the MP length (Figure 4.4.b), the mismatch between the two combs occurs, then there will be a matching between the laser modes and the cavity mode at the position n on the end of the comb, where (n x f_{rep} = (n-1) x FSR), which forms the beating peak of order N=1 (Figure 4.4.c). The continuous change in the cavity length allows the beating peak to move, and scan the whole input laser spectrum, in the frequency domain, to give an output spectrum in the time domain recorded by a PD. When the cavity length change reaches δL=2xλ/2, there will be another matching, at the position n on the comb where (n x f_{rep} = (n-2) x FSR), which forms the beating peak of order N=2, and this peak moves due to the change of the cavity length, and scans the whole laser spectrum, in the frequency domain to give the output spectrum of order N=2 in the time domain, and so on. The beating peak of order N is larger (in frequency) than the beating peak of order $N+1$, because moving to

higher order requires to increase δL, which yields to decrease the width of the resulting beating peak due to reducing the number of the laser modes that participate in the peak as explained earlier.

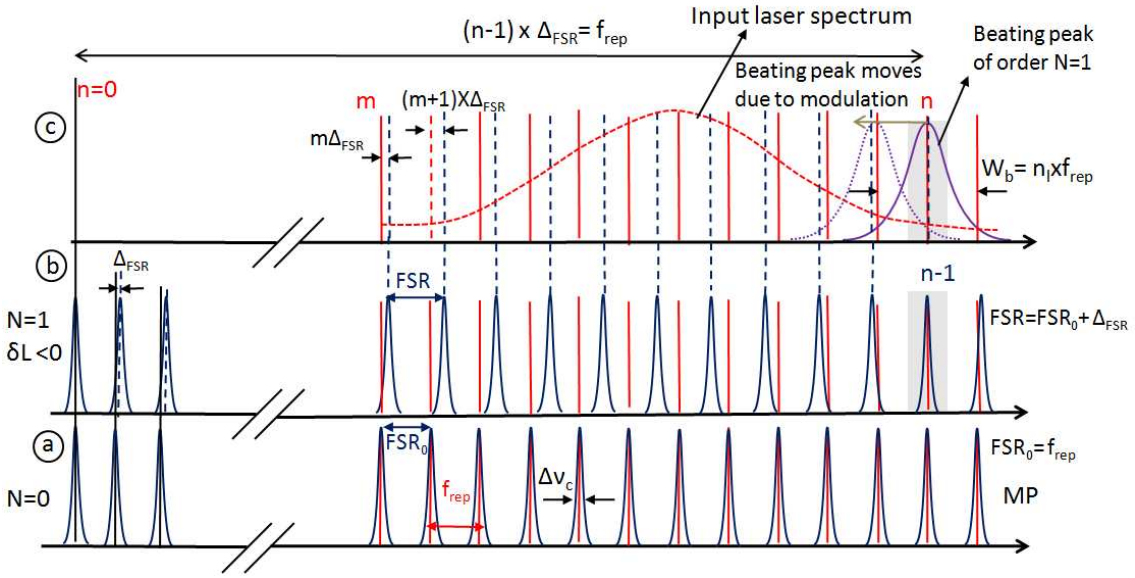

Figure 4.4: (a) The magic point between the Laser comb (red) and the cavity comb (blue), which corresponds to *N*=0. (b): Cavity length is reduced of $\delta L=\lambda/2$ from the MP length, and then the first matching occurs at the position n on the laser comb, which corresponds to *N*=1. (c) Beating peak of first order is illustrated at the position n which is transmitted through the cavity (violet peak which contains here three laser modes). Δ_{FSR} corresponds to the change in the cavity FSR due to δL.

The upper window (left) of Figure 4.5 displays the ramp signal applied to the PZT to modulate the cavity length around the MP position, while the lower window illustrates the measured output spectra in the time domain, recorded by a PD, when the cavity length is modulated. At the MP, we have seen that the resonance peak is very narrow, and corresponds to output spectrum of order *N*=0. Each time the cavity length is changed by $\delta L=\lambda/2$, a beating peak is formed and starts to scan the input laser spectrum during the modulation to give a new output laser spectrum. The right part of this figure, displays the scanning of the input laser spectrum by a beating peak of order 5 to give the output spectrum of the same order shown in the inset on the left.

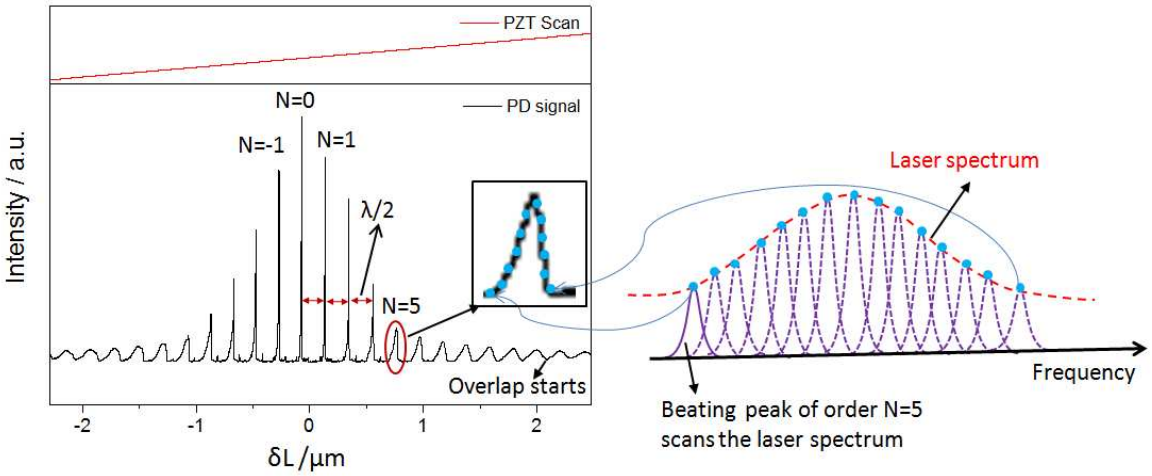

Figure 4.5: Left, Upper window: Ramp signal applied to the PZT. Lower window: PD signal when the cavity length is modulated around the MP position. Each change in cavity length of λ/2 gives an output spectrum in the time domain. Right: Beating peak of order 5 scans the input laser spectrum in the frequency domain, during the modulation. The blue circles corresponds the sampling point of the input laser spectrum by the scanning peak, and these circles form the spectrum of order *N*=5 (inset at left), recorded by the PD in the time domain.

We recall from (Chapter 2, section 2.4.2) that the intensity of the spectrum *N*, and the spectrum *–N* are not the same due the fact that f_0 is not controlled. Furthermore, the spectrum of order *N* is not symmetric due to the intracavity dispersion.

4.2.2. Analytical model

In this section we present the analytical model of the Vernier effect technique. The aim is to characterize the performance of this technique in terms of the spectral resolution and the acquisition time. The starting point is the coupling condition to obtain a beating peak of order *N* at the position *n* on the laser comb, and then the spectral position of this peak is calculated as a function of *N*, and the deviated distance δL from the MP position.

From the previous section, we have demonstrated that the coupling condition between the laser comb and the cavity comb to get the peak of order *N* (Figure 4.4,b) can be written as follows:

$$\nu_n^N = n \times f_{rep} = (n \mp N) \times FSR \tag{4.4}$$

From the relation (4.1), we have $FSR = f_{rep} + \Delta_{FSR}$, so by replacing the value of FSR in the above relation, we find that:

$$(n \mp N) \times \Delta_{FSR} = N \times f_{rep} \tag{4.5}$$

The negative sign corresponds to reducing the cavity length (increasing the cavity FSR, *FSR= f_{rep} + Δ_{FSR}*), while the positive sign corresponds to increasing the cavity length (reducing the cavity FSR, *FSR= f_{rep} - Δ_{FSR}*).

From the above relations, it is possible to derive the relation which gives the absolute spectral position of the beating peak of order *N* (or the position of the output spectral elements) as a function of *δL* and *N*, by writing *FSR=f_{rep}+ Δ_{FSR}*, and taking into account that *f_{rep}=FSR_0=c/2L*.

$$\begin{aligned} n \times f_{rep} &= (n-N) \times (f_{rep} + \Delta_{FSR}) \\ n \times f_{rep} &= (n-N) \times f_{rep}(1 + \Delta_{FSR} / f_{rep}) \Rightarrow \\ n &= (n-N) + n\frac{\Delta_{FSR}}{f_{rep}} \end{aligned} \tag{4.6}$$

To reach the final relation, I used the approximation $N\frac{\Delta_{FSR}}{FSR_0} \square\ n\frac{\Delta_{FSR}}{FSR_0}$, where *N* is of the order of 10^2 and *n* is of the order of 10^6.

From the relation (4.2), we have $\frac{\Delta_{FSR}}{f_{rep}} = \frac{\Delta_{FSR}}{FSR_0} = \frac{\delta L}{L}$, and from the relation (4.4), we have $\nu_n / f_{rep} = n$, we replace the relevant terms in the relation (4.6) to get:

$$\nu_n(N, \delta L) = N\frac{c}{2\delta L} \quad \lambda_n(N, \delta L) \quad \frac{2\delta L}{N} \tag{4.7}$$

Now, If we consider that in our case, *FSR_0=N_c x f_{rep}*, where *N_c*=2, then the above relation can be rewritten as follows:

$$\nu_n(N, \delta L) = N\frac{c}{2N_c\delta L} \Rightarrow \lambda_n(N, \delta L) = \frac{2N_c\delta L}{N} \tag{4.8}$$

The above relation is very important when the calibration of the measured output spectrum is made to move from the δL scale (length unit) to the wavelength scale.

Figure 4.6 displays the beating peak position, where *δL* ranged between the magic point position and 6 µm (~12 x λ/2), and *N* ranged between 1 and 16.

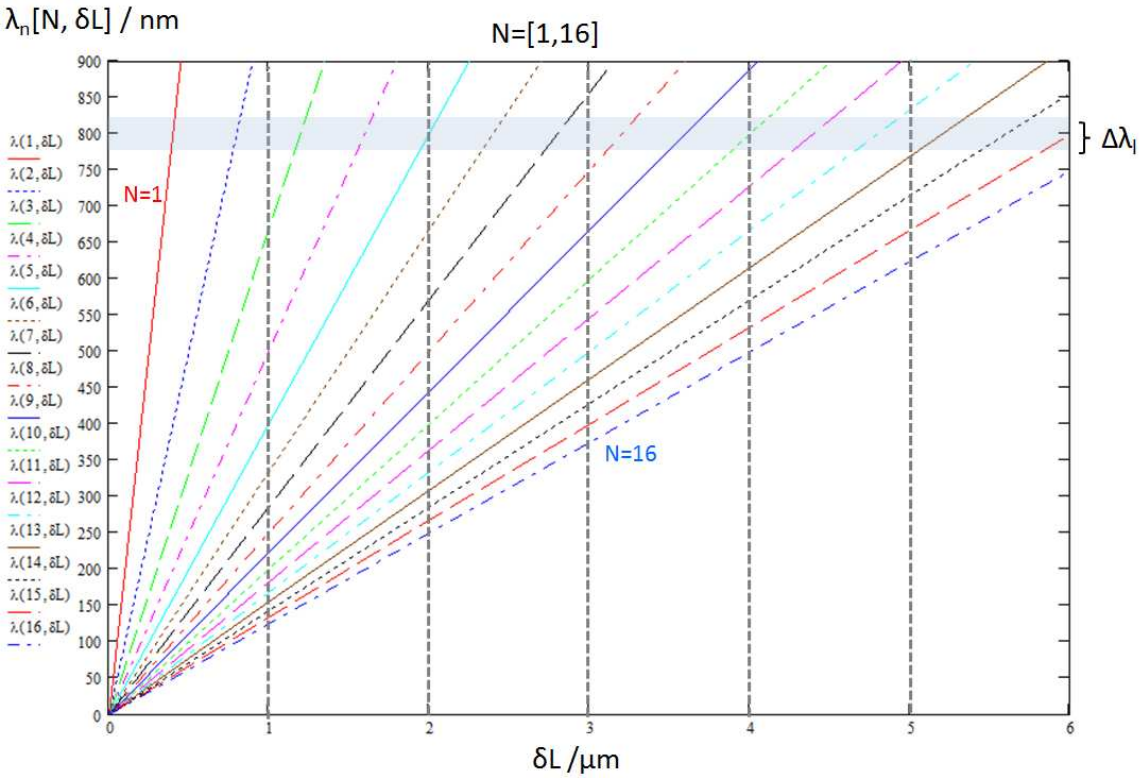

Figure 4.6: Position of the Beating of order *N* as a function of *N* and *δL*. *Δλ*$_l$ corresponds to the laser bandwidth centered at λ=800 nm, and illustrated as a horizontal rectangle. The intersection, between the rectangle and the peak position at certain value of *N*, gives the spectral range scanned by this peak. It is clear that the scanned range increases with *N*.

From the above plot, we can see that for given *δL*, the spectral range scanned by one beating is dependent on the order *N* of this beating. For one position *δL,* only one wavelength for the order *N* is transmitted by the cavity. As *δL* is changing in time, it means that the wavelength transmitted by the cavity is changing in time. The slope decreases with *N* and we can see in Figure 4.7, that eventually when *δL* is large enough, two orders can be transmitted in the same position corresponding to two different *N*, and so wavelengths from different parts of the spectrum are transmitted at the same time to the PD. So the distance *δL* is limited. This means that there is a dispersion which increases the width of the scanned range when the value of *N* increases. Furthermore, the spectral ranges scanned by the beatings overlap after a certain value of *N* as shown in Figure 4.7. When *N* is bigger than 15, the end of the scan of the laser is overlapping with the beginning of the next scan. We should underline that each scanned spectral range is equivalent to the laser bandwidth.

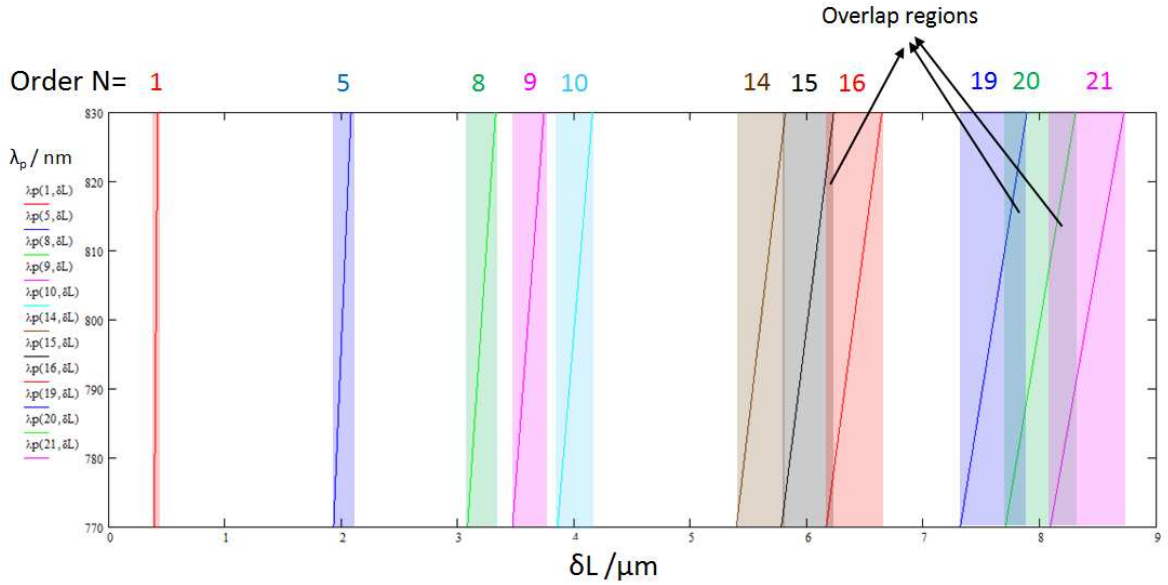

Figure 4.7: Overlap starts to appear between two spectral ranges scanned by two successive beatings, when *N* is bigger than 15, for a laser bandwidth of about 40 nm. The colored rectangles correspond to the width of scanned range.

4.2.2.1. Resolution of the Vernier effect technique

From Figure 4.4.c, we can deduce a relation that gives the width W_b of the beating peak. If the laser comb of order n is perfectly matched with the cavity mode of order q, the distance in frequency between the laser comb of order n-1 and the cavity mode of order q-1, will be Δ_{FSR}. It is easy to prove that the distance between the laser mode of order n-p and the cavity mode of order q-p is $p\,\Delta_{FSR}$. The laser adjacent modes will go in resonance with one cavity mode, and be transmitted, if $p\,\Delta_{FSR}$ is smaller than the cavity mode width $\Delta\nu_c$. We deduced n_l the number of the laser modes which contributes in one beating peak as follows $n_l=\Delta\nu_c/\Delta_{FSR}$.

The laser modes, which form the beating peak, are separated by the laser repetition rate, and thus the width of the peak is given by:

$$W_b = n_l \times f_{rep} \tag{4.9}$$

We mentioned earlier that the spectral resolution is equal to the spectral width of one beating which itself is related to δL, and to the cavity mode width or the cavity finesse. From the definition of n_l, Δ_{FSR} and the optical cavity finesse as well as $f_{rep}=FSR_0=c/2L$, we rewrite the above relation as follows:

$$\begin{aligned}\Delta\nu_{res} &= W_b = n_l \times f_{rep} \\ &= \frac{\Delta\nu_c}{\Delta_{FSR}} \times f_{rep} = \frac{FSR_0 / F}{FSR_0 \times \delta L / L} \times f_{rep} \Rightarrow \\ \Delta\nu_{res} &= \frac{c/(2\times\delta L)}{F} = \frac{\Delta\nu_b}{F}\end{aligned} \tag{4.10}$$

To avoid the overlap between two successive output spectra, $\Delta\nu_b$ should be equal or broader than the laser bandwidth $\Delta\nu_l$. By taking the limit of the overlap condition ($\Delta\nu_b = \Delta\nu_l$), the resolution reaches its maximum value, and can be written as:

$$\Delta\nu_{res}^{\max} = \frac{\Delta\nu_l}{F} \Rightarrow \Delta\lambda_{res} = \frac{\Delta\lambda_l}{F} \tag{4.11}$$

The limit of overlap condition ($\Delta\nu_b = \Delta\nu_l$) gives the maximal distance δL_{max} deviated from the MP length which also corresponds to the maximal resolution, and δL_{max} is expressed as:

$$\delta L_{\max} = \frac{c}{2\times\Delta\nu_l} \tag{4.12}$$

From the relation (4.11), we can see that at the maximum resolution, the number of spectral elements is equal to the cavity finesse. At this position, two successive output spectra are adjacent, one is finishing when the other one is starting, it is required to modulate the cavity length by (δL =λ/2, if we consider N_c=1) to scan the whole input laser spectrum (or δL =λ/4, if we consider N_c=2) by the relevant beating peak in the frequency domain. Therefore to move the beating peak from one spectral element to the next one on the input laser spectrum in the frequency domain, it is required to modulate the cavity length by one cavity mode width $\Delta\lambda_{cav}$ ($\lambda/2/F = \Delta\lambda_{cav}$, where $\Delta\lambda_{cav} = (\Delta\nu_c \times \lambda^2 / c)$.

4.2.2.2. Modulation frequency

Moving from one spectral element to the next one requires that there is no memory effect of the cavity, so that the minimum delay between two consecutive spectral elements must be longer than the ring-down of the cavity. Therefore, the modulation time is limited by the product of the number of the spectral elements (equal to F) and the HF cavity ring-down time (τ_{rd}) which characterizes the cavity resonance. Then, the maximum modulation frequency can be expressed as:

$$f_{scan} = \frac{1}{F\times\tau_{rd}} \tag{4.13}$$

It is clear that when the finesse in increased, the modulation frequency decreases, but the minimum frequency will be limited by the instability of the laser source.

4.2.2.3. Resolution and acquisition time values for a typical mode-locked Ti:Sa Laser

We consider a mode-locked femtosecond Ti:Sa laser with f_{rep}= 80 MHz, $\Delta\lambda_l$ =10 nm at λ=800 nm, injected into an optical cavity of length (L=0.94 m). The cavity length is chosen to have $FSR = 2\ f_{rep}$=160 MHz (N_c=2). In this case, to go from a cavity resonance to the next one, the cavity length change is equal to λ/4=200 nm. Table 4.1 presents the calculated values of the resolution for different values of cavity finesse. Here, the order N in the table is calculated from the following relation:

$$N \approx \frac{\delta L(\mu m)}{\lambda / 2N_c} \tag{4.14}$$

R	F	δL_{max} (µm)	$\Delta\nu_c$ (kHz)	Δ_{FSR} (kHz)	n_l (mode)	N	$\Delta\lambda_{res}$ (pm)
0.995	626	16	255	2.7	94	80	16
0.9997	10470	16	15	2.7	5	80	0.95
0.9999	31414	16	5	2.7	2	80	0.3

Table 4.1: Resolution is calculated for different cavity finesse values.

Table 4.2 presents the calculated values for the maximum modulation frequency of the PZT signal, from the relation (4.13).

F	τ_{rd} (µs)	f_{scan} (Hz)
626	0.62	2576
10470	10.4	9
31414	31.2	1

Table 4.2: Maximum modulation frequency is calculated for different cavity finesse values.

The last columns of previous tables indicate that increasing the finesse results in enhancing the resolution, but leads to reducing the maximum modulation frequency down to a level for which the laser stability is not guaranteed during the modulation time. Therefore, there is a compromise between the high resolution and the rapid acquisition time. However, by using a cavity finesse of 10000, the same number of spectral elements can be obtained, resulting in high spectral resolution (0.9 pm) with 100 ms acquisition time per spectrum. We can see here that the number of spectral elements is largely increased, compared to ML-CEAS.

4.2.3. Experimental setup

Figure 4.8 outlines the experimental setup which consists of a free running commercial modelocked Ti:Sa femtosecond laser (Coherent MIRA laser) which delivers pulses of 30 fs with a repetition rate of 77 MHz. The laser spectrum is about 35 nm broad and the central wavelength is tunable between 780 nm and 820 nm. The laser oscillator is pumped by a 5 W diode-pumped frequency-doubled Nd:YVO_4 laser (Coherent Verdi). An acousto-optic modulator (AOM) allows cavity ring-down measurements to estimate the intracavity photons life time which serves to determine the cavity finesse. The laser radiation is injected into the HF cavity by using a mode matching system consisting of two plano-convex lenses (L_1=10 cm, L_2=15 cm) and a pinhole (diameter of 50 µm) located at the focal distance of L_1. This system allows matching the laser mode to the principle transverse cavity mode TEM_{00}. The pinhole is needed to spatial filtering the input laser beam which is elliptical. The HF cavity consists of two highly reflective concave mirrors (radius of curvature is r = 0.5 m). The distance D_1 between the pinhole and the lens L_2 is 18 cm, and the distance D_2 between L_2 and the input cavity mirror is 61.2 cm. D_1, D_2 are calculated for the transverse mode matching between the laser mode and the cavity mode TEM_{00}. The laser waist at the center of the optical cavity is 14.7 µm, and at the cavity mirrors is 851 µm. All these distances and the waists values are calculated for λ= 816 nm.

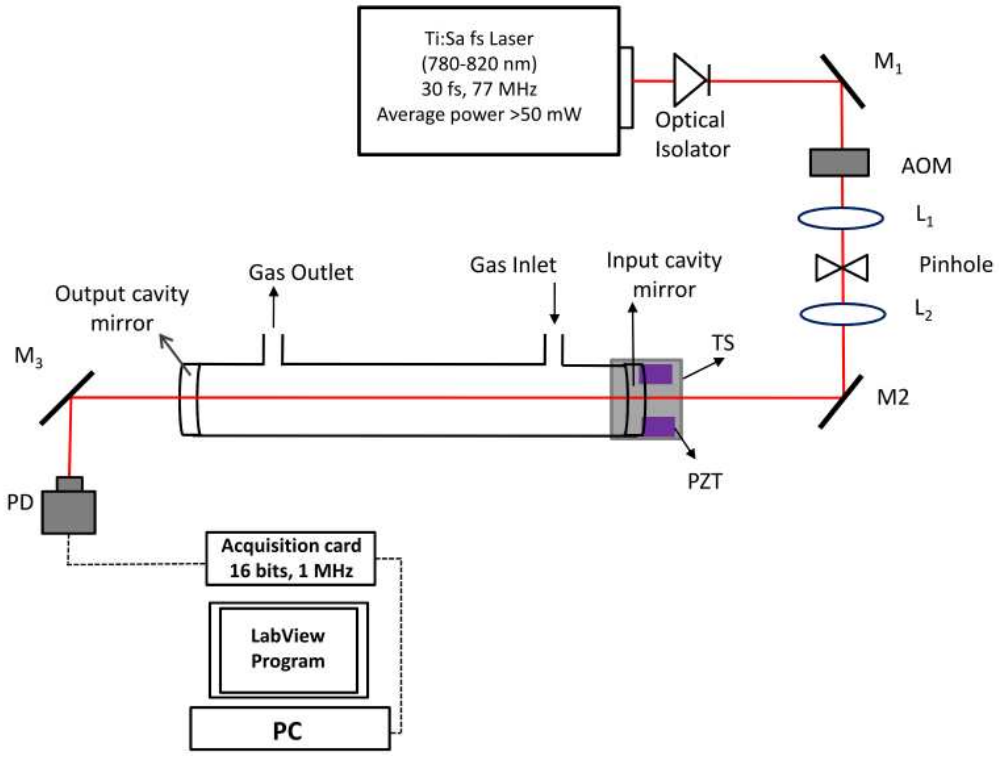

Figure 4.8: Experimental scheme based on a Ti:Sa fs oscillator, and a mode matching lens to inject a high finesse cavity whose length is finely controlled by a translation stage (TS), and modulated by a piezoelectric actuator (PZT). An acousto-optic modulator (AOM) allows laser interruption for ring-down measurements. A fast photodiode (PD) is located after the HF cavity to record the output absorption spectra by using an acquisition card connected to a PC.

The cavity length is adjustable by a step-motor translation stage (TS) with USB control, and modulated by a tubular piezoelectric actuator mounted on the input cavity mirror. Indeed, the HF cavity length is chosen (L=0.973 m) to get a FSR equal to twice the laser repetition rate. The transmitted light through the cavity is recorded by a photodiode with a response time of about 1 µs. The data are acquired by an acquisition card (16 bits, 1 MHz sampling rate) connected to a PC. After that, the acquired data are treated by a home-made LabView program.

4.3. Preliminary results and discussion

Two sets of experiments had been done. In the first one, the laser was centered at 790 nm, and the cavity finesse was low (F=626). The cavity was filled with pure acetylene C_2H_2. In the second experiment, the finesse of the cavity was increased (F=10470), and we tested the technique with water vapor in the air of the laboratory. This time, the laser was centered on the water absorption band around 816 nm. The PZT was controlled by a high voltage ramp signal providing a maximal extension of the piezo of 5 µm which corresponded to (12 x λ/2). The scan frequency was 30 Hz, and 13 Hz for C_2H_2 and H_2O, respectively. In the C_2H_2 experiment, as the laser is broadband (~35 nm), and the cavity finesse is low, the expected spectral resolution is low on the range of 50 pm. Therefore to improve the resolution, a spectrograph is used to take a part of the laser bandwidth (~7 nm), and then the expected resolution is about 10 pm. Indeed, reducing the probed laser spectrum permits to decrease the separation between the beating peaks ($\Delta\nu_b$), which in turn enables increasing the deviated distance δL from the MP position, and the overlap between the output spectra takes place at higher value of the spectrum order N as indicated from the relation (4.3).

In Figure 4.9.a, the C_2H_2 output spectra at low order values, recorded by a fast PD are presented, when the cavity length is modulated far away from the MP position which is the starting point N=0. Each change in the cavity length of δL =λ/4, leads to the next output spectrum, because $FSR=2 \times f_{rep}$. In the inset of Figure 4.9.a, the output spectrum of order N=9 is illustrated, which contains the C_2H_2 absorption features. Figure 4.9.b displays the output spectra at higher order values, where the maximum deviated distance δL can reach (17 µm) leading to record output spectra of order (N= $\delta L^{max} / (\lambda/4)$ =87, for λ=0.79 µm, and δL^{max}=17 µm). The output absorption spectrum of order N=87 is treated by the home-made Labview program to solve the problem of the dispersion, and to estimate the calibrated factor in nm/pixel, and to build the absolute wavelength scale. The treated output spectrum is shown in the upper window of Figure 4.10, while the lower window illustrates the C_2H_2 absorption spectrum from the literature [73].

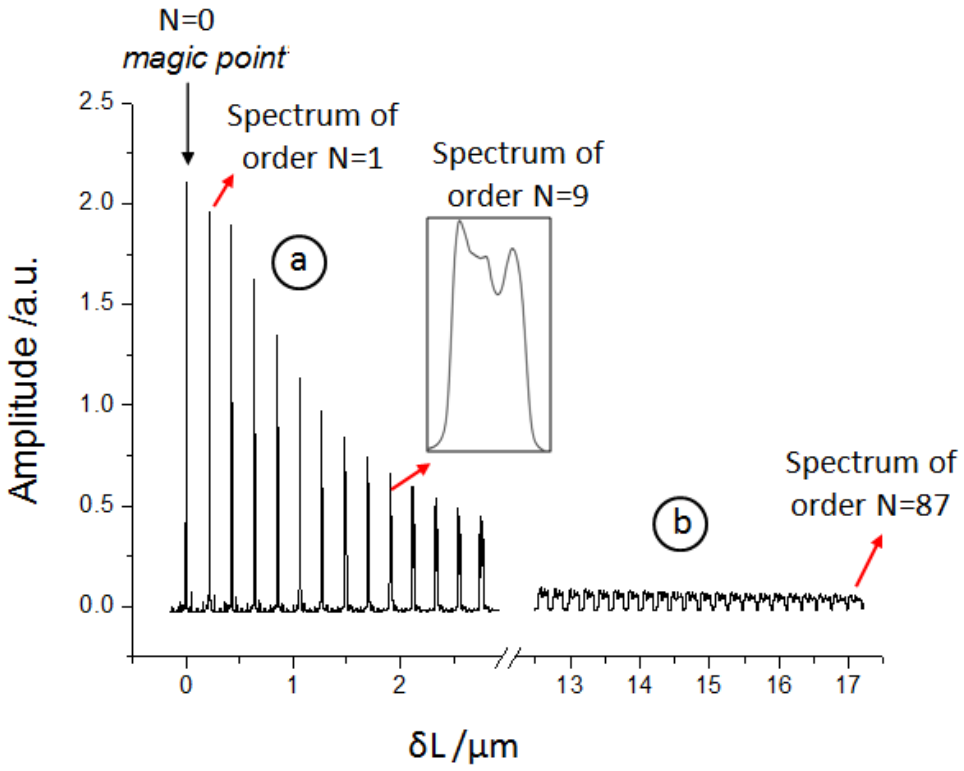

Figure 4.9: a: Displays the output spectra at low order values recorded by a PD when scanning the cavity length by a PZT to deviate it far away from the MP position. b: Displays the output spectra at high order values, where the maximum deviated distance is δL=17 µm permitting to record the output spectrum of order N=87.

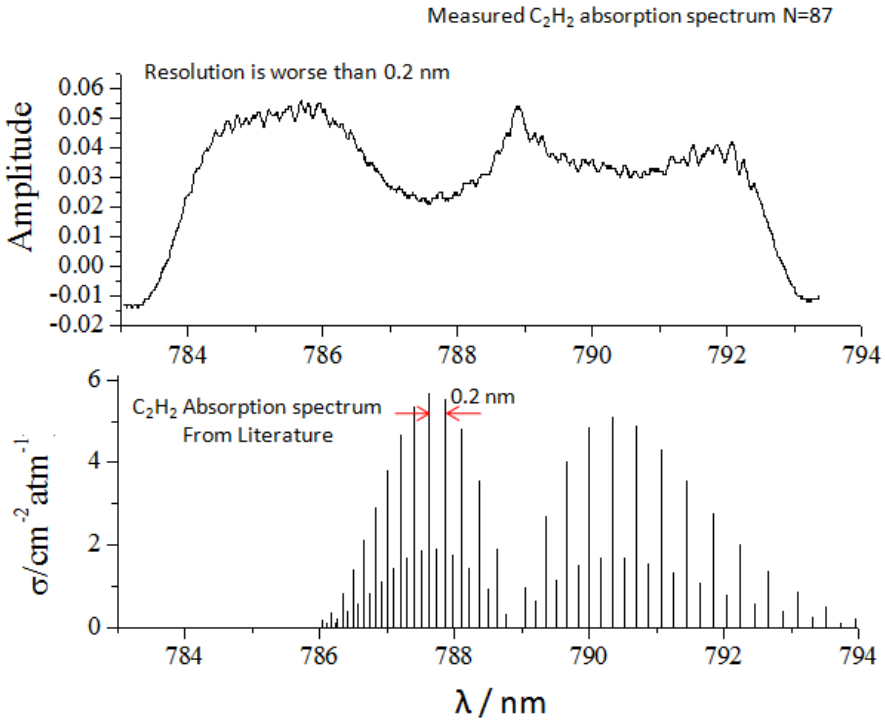

Figure 4.10: Upper window: C_2H_2 output absorption spectrum resulting from scanning the laser spectrum by the beating peak of order N=87. Lower window: C_2H_2 absorption spectrum from the literature [73].

The estimated resolution was worse than 0.2 nm, because the strong absorption lines in the measured spectrum are not resolved, and the distance between two lines is about 0.2 nm as indicated on the lower window of Figure 4.10. The expected resolution is about 10 pm which is better than the measured one and I will give an explanation for this discrepancy later.

To improve the performance, we tried to make a step forward by using a cavity with a higher finesse (R =0.9997 and F =10470). Indeed, in this case the absorption by acetylene was too strong, so we decided to observe the water vapor band around 816 nm. The laser was manually tuned to this wavelength. Here, we did not use a spectrograph to take a part of the output laser, because the transmitted power was already low (due to the high finesse value), and taking a part of the spectrum would make the output signal undetectable by the PD. Figure 4.11 displays the obtained H_2O output spectrum of order N=21, superimposed to a HITRAN H_2O absorption spectrum around 816 nm. The HITRAN spectrum is convoluted by a Lorentzian of 3.15 cm^{-1} width, and the corresponding resolution is 0.2 nm. We should underline that N=21 corresponds to the maximum deviated distance (δL^{max} = 4.3 µm) from the MP position, leading to the maximum spectral resolution.

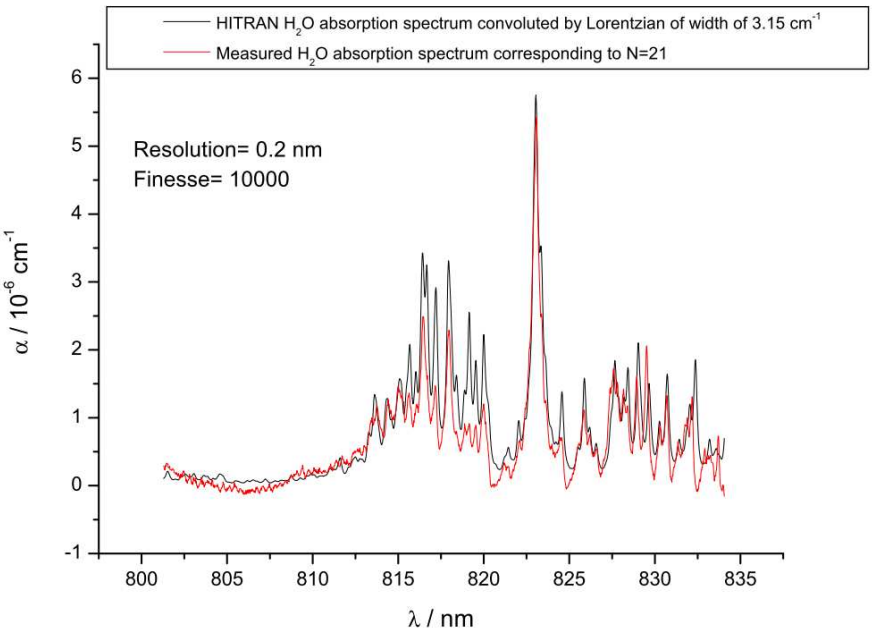

Figure 4.11: In red: Measured H_2O absorption spectrum around 816 nm, corresponding to N=21. In black: HITRAN H_2O absorption spectrum convoluted by a Lorentzian of 3.15 cm^{-1} width.

In summary, the maximum resolution achieved is 0.2 nm corresponding to H_2O output absorption spectrum of order N=21 ($N=(4.3\ \mu m) / (\lambda/4)$), and the relevant cavity finesse is 10470. By comparing this result to that of C_2H_2 output absorption spectrum, where the low finesse cavity is used but a part of the laser spectrum is taken to enhance the resolution which is equivalent to increasing the finesse, we find that the resolution for H_2O is slightly enhanced, but the maximum resolution is not achieved. We expect (for H_2O) about 10 000

spectral elements (equal to the cavity finesse), which gives a resolution of about 3 pm, taking into account the laser bandwidth of about 35 nm. This discrepancy between the calculated resolution and the measured one is due to the fact that the laser mode width is neglected. Indeed, the resolution is limited by the laser mode width and not by the cavity mode width. We roughly estimate the laser mode width from the measured resolution which corresponds to effective finesse of 175, leading to a mode width of about 0.6 MHz. Thus, the laser stabilization is required to reduce the width of the laser mode [74], in order to enhance the resolution. For example, if we succeed to reduce the laser mode width to about 20 kHz, then the measured resolution enhances by roughly a factor of (0.6 MHz/20 kHz = 30) to reach a value of 6 pm, but If we succeed to reduce the laser mode width to be less than the cavity mode width ($\Delta\nu_c$=15 kHz), then the theoretical resolution (calculated in Table 4.1, for F=10470) can be achieved (less than 1 pm=0.01 cm^{-1}). Moreover, when the laser is stabilized, it will be possible to highly increase the resolution by increasing the optical cavity finesse. We should underline that as the performance is limited by the laser mode width, the resolution cannot be enhanced by increasing the finesse. So, the resolution for (C_2H_2) should be better than for (H_2O). This is due to the fact that when the laser bandwidth was reduced to (7 nm), it was possible to go further away from the MP position (δL=17 µm) which badly affected the cavity alignment and resulted in appearing high order transverse modes that degraded the resolution. In the usual case, we deal with lasers of large bandwidths which limit the deviated distances to few microns, and the problem of misalignment no longer exists.

4.4. Laser stabilization

4.4.1. Introduction

We have seen from (Chapter 1, section 1.3) that the frequency spectrum of a mode-locked laser is a comb, and the position of the comb line depends on two parameters, the repetition rate f_{rep} and the absolute position of the comb f_0 or f_{ceo}. Then, the optical frequency of a comb mode with order number n is given by:

$$\nu_n = n \times f_{rep} + f_0 \tag{4.15}$$

As our experiment of Vernier effect is sensitive to the laser mode width, the laser stabilization is required to reduce the laser mode width. The stabilization is possible by acting independently on the two parameters (f_{rep}, f_0), and this can be implemented electronically because of (f_{rep}, f_0) are in the radio frequency range.

4.4.2. Controlling the frequency comb parameters

From (Chapter 1, section 1.2.5), I recall that the mode spacing f_{rep} is given by:

$$f_{rep} = \frac{1}{t_g} = \frac{v_g}{2L} \tag{4.16}$$

Where t_g is the round-group delay, v_g is the average group velocity, and L is the cavity length.

The absolute comb position f_0 presents the carrier-envelop offset frequency which is proportional to the carrier-envelop offset phase $\Delta\phi_{ceo}$, and given by:

$$f_0 = \frac{\Delta\phi_{ceo}}{2\pi} f_{rep} = \frac{v_c}{t_g}(t_g - t_p) \tag{4.17}$$

Where t_p is the round-trip phase delay and relates to the average phase velocity v_p by $t_p = 2L/\upsilon_p$. v_c is the carrier frequency. It is to be noticed that the envelope of the pulse propagates at v_g, while the carrier propagates at υ_p.

The pulse repetition rate f_{rep} can be controlled by adjusting the cavity length using a piezoelectric transducer (PZT) to translate one of the end mirrors (M_4 or M_6) as shown in Figure 4.12.

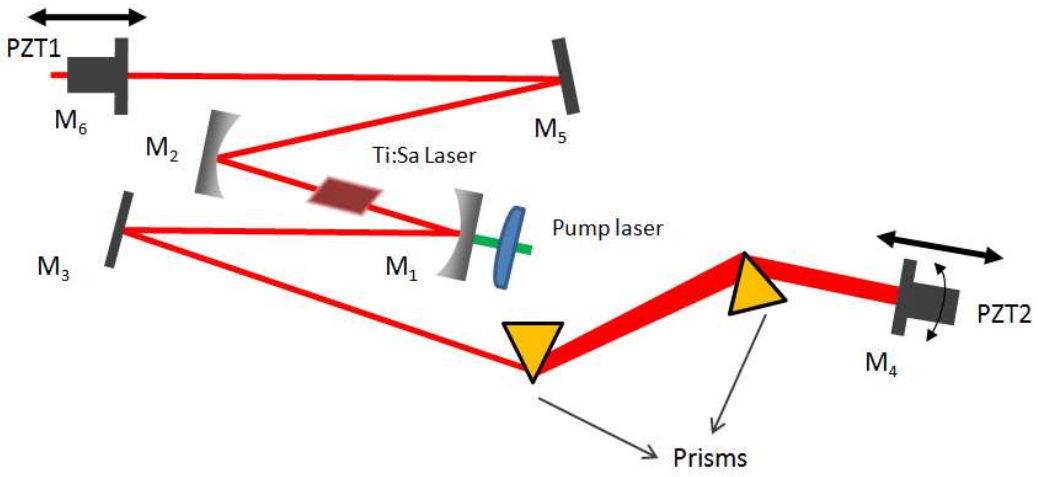

Figure 4.12: Modelocked Ti:Sa laser with a configuration of controlling both f_{rep} and f_0.

Both f_{rep} and f_0 depend on the cavity length L through the dependence of t_g and t_p on L. Therefore, to obtain independent control of both, the comb spacing and its position, an additional parameter, besides the cavity length, must be adjusted; the comb position f_0 can be controlled by a small rotation about the vertical axis (the direction of the incoming beam) of the laser end mirror M_4 after the sequence prisms as shown in Figure 4.12. After these prisms, there is a linear spatial dispersion of the wavelength; the different spectral components are spatially separated across the end mirror. Hence a mirror tilting provides a linear phase with frequency, and the first derivative of this phase with respect to the frequency will give a group time delay [75]. Consequently, tilting the end mirror changes f_0 as indicated in the relation (4.17). The tilt angle should be very small (compared to the

angular aperture of the beam at the end mirror) to affect only the difference between the group and phase delay in the cavity while leaving the other laser parameters nearly unchanged, in particular, the intracavity power and the effective cavity length. A tilt angle of few microradians is sufficient to control f_0 within one spectral range [21]. If we assume that the mirror tilt only changes the group delay by an amount αθ, where θ is the tilt angle and α is a constant that depends on the spatial dispersion on the mirror and has units of s/rad, then we rewrite [19]:

$$f_{rep} = \frac{1}{2L/\upsilon_g + \alpha\theta}$$
$$f_0 = \nu_c \left(1 - \frac{2L/\upsilon_p}{2L/\upsilon_g + \alpha\theta}\right) \tag{4.18}$$

From the relations above we can derive how the comb frequencies depend on the control parameters, *L* and θ. To get this, the total differential of f_{rep} is calculated as follows:

$$\begin{aligned} df_{rep} &= \frac{\partial f_{rep}}{\partial\theta} d\theta + \frac{\partial f_{rep}}{\partial L} dL \\ &= \frac{\alpha}{(2L/\upsilon_g + \alpha\theta)^2} d\theta \quad \frac{1/\upsilon_g}{(2L/\upsilon_g + \alpha\theta)^2} dL \\ &= \alpha \frac{\upsilon_g^2}{4L^2} d\theta \quad \frac{\upsilon_g}{4L^2} dL \end{aligned} \tag{4.19}$$

By the same way, the total differential of f_0 with respect to *L* and θ is given by:

$$\begin{aligned} df_0 &= \nu_c \frac{2L\alpha}{\upsilon_p} \frac{1}{(2L/\upsilon_g + \alpha\theta)^2} d\theta \quad \nu_c \frac{\alpha\theta/\upsilon_p}{(2L/\upsilon_g + \alpha\theta)^2} dL \\ &\cong \nu_c \frac{\upsilon_g^2 \times \alpha}{2\upsilon_p L} d\theta \end{aligned} \tag{4.20}$$

Where the final formula of the total differential (df_{rep}, df_0) are obtained under the approximation of small tilt angle, $\alpha\theta \ll 2L/\upsilon_g$. We can see that f_0 is controlled only by θ from the relation (4.20) and f_{rep} slightly changes as a function of θ as indicated from the relation (4.19), but the associated change can be compensated for by changes in the cavity length. As the optical frequency of the comb mode at position *n* is given by ($\nu_n = n x f_{rep} + f_0$), then the change in the position is ($d\nu_n = n x df_{rep} + df_0$), which indicates that the change in f_{rep} is more important than the change in f_0, because df_{rep} is multiplied by n (n~10^6). From (4.19) and (4.20), we can find:

$$n\frac{\partial f_{rep}}{\partial\theta}/\frac{\partial f_0}{\partial\theta}=(n\times\alpha\frac{\upsilon_g^2}{4L^2}d\theta)/(\nu_c\frac{\upsilon_g^2\times\alpha}{2\upsilon_p L}d\theta)$$
$$=\frac{n\lambda}{2L}\approx 1 \qquad (4.21)$$

The calculation is made for typical values of λ=800 nm, L=1 m, and n=2.3x10^6.

The maximum allowed change in f_0 due to the tilt angle is one laser repetition rate (80 MHz), which means that the change in f_{rep} is on the order of ($df_{rep}=df_0/n$=35 Hz) as indicated from (4.21). To compensate a change of about 35 Hz in f_{rep} due to change the angle θ, the cavity length should be changed by 0.4 µm.

Other control methods of f_0 are possible, for example, changing the amount of glass in the cavity [22] changes the difference between the group delay and the phase delay due to dispersion in the glass. The amount of glass can be changed by moving a prism or by introducing glass wedges. However, this method has the disadvantage of also changing the effective cavity length which prevents the independent control (orthogonality) of the two parameters (f_{rep}, f_0). Furthermore, rapid response time in a servo loop cannot be achieved because of inertia of the prism or the wedge which have a relatively high mass to provide the required amount of dispersion. This disadvantage can be eliminated when using the tilt technique by choosing low mass mirrors. Another widespread method to control f_0 is to modulate the pump power either with an acousto-optic modulator [76] or with an electro optic modulator [77]. Changing the pump power changes the power of the intracavity pulse which modifies the carrier-envelop phase offset. The required pump power modulation is on the order of 10^{-3} [21], and it is easy to reach servo bandwidths of several tens to hundreds of kHz driven by an optical modulator which is considered the main advantage of this method. We should underline that a direct stabilization of f_0 is possible by using the self-referencing technique [21] which requires the laser comb to span an entire octave. The heterodyne beat between the frequency-doubled infrared portion of the comb and the high-frequency portion provides the radio frequency f_0. The octave-wide spectrum needed for this method can be achieved externally by using a highly nonlinear microstructured fiber to broaden the laser spectrum [78] or by using femtosecond lasers which directly emit octave-spanning spectra [79].

4.4.3. Laser stabilization to a reference cavity

The aim is to stabilize the laser frequency to that of the reference cavity [80]. For this purpose we use the tilt-lock technique [45] which derives an error signal for locking a laser to a reference cavity by using spatial-mode interference as explained later. This technique is chosen because of its simplicity compared to other techniques such as Pound Drever Hall (PDH) technique [44]. In addition, this technique does not require a modulation to obtain the error signal. In the following, I explain the final configuration of the experimental setup including the mode-matching system, the double cavity design, and the double piezo setup

to move the end mirror (M_4), as well as the tilt-lock technique. A brief description is made about the electronics to generate the error signals and the two bias voltages to control the double piezo system. The general configuration is used to make Vernier technique experiments, and to stabilize the laser by generating two error signals that contain a mixture of the two degrees of freedom (f_{rep}, f_0). This is possible when the error signals correspond to two different positions of comb lines inside the spectrum. To get two error signals, we use two split photodiodes, and a reflection grating to disperse the laser light before the photodiodes as shown in the lower window of Figure 4.13. Then, the laser input is matched to the fundamental modes of two cavities (in mono-block double cavity design) by a matching system consisting of two lenses (L_1, L_2) and a pinhole as described earlier. The double cavity design contains a low finesse cavity which is used as a reference cavity for the tilt lock technique to stabilize the laser, and a high finesse cavity which is used as a gas chamber for the Vernier technique.

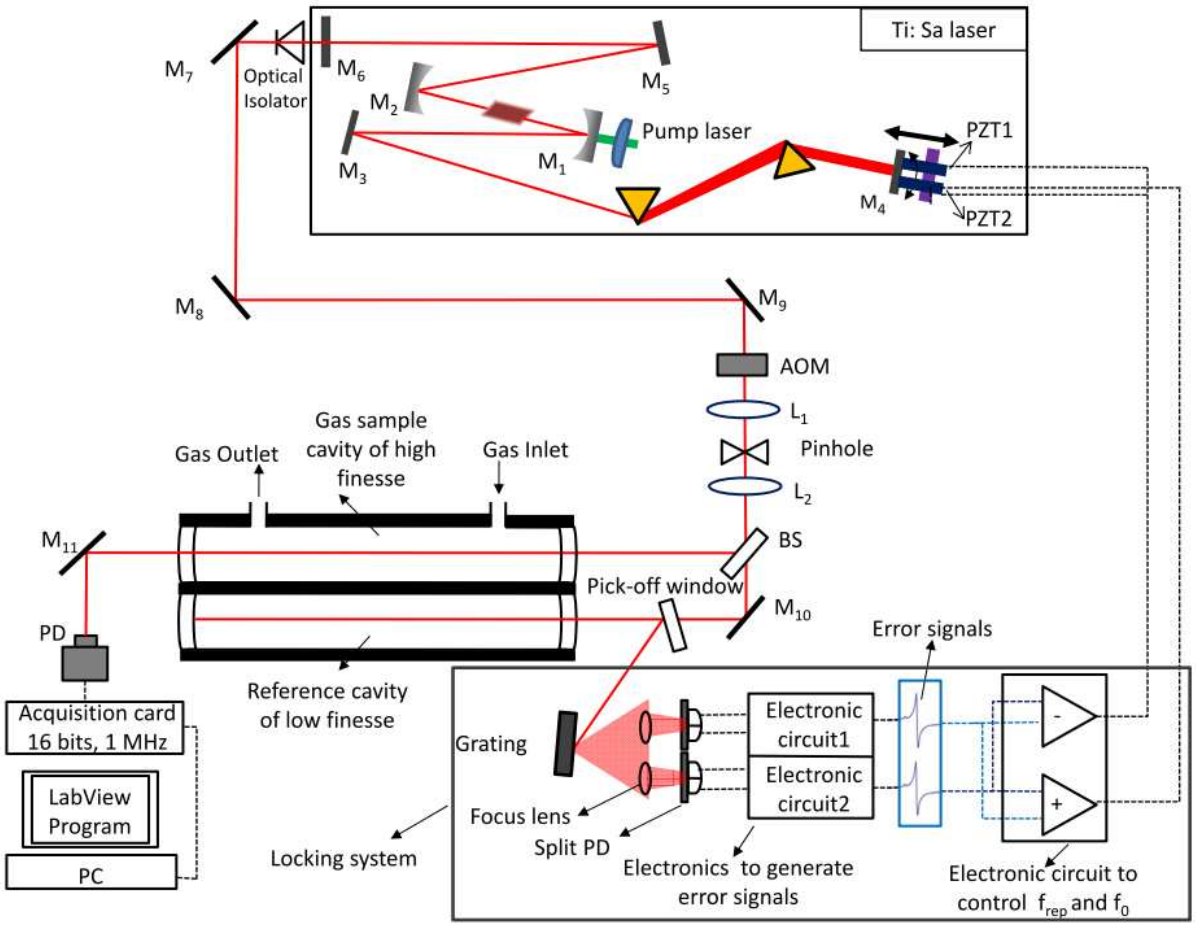

Figure 4.13: Final configuration to stabilize the laser by a tilt lock technique and realize the Vernier effect technique. The mode matching system (L1, L2, and pinhole) is used to match the laser mode to the fundamental modes of the two cavities. BS: Beam splitter. The Vernier effect detection system consists of a fast photodiode (PD), acquisition card and a PC. The tilt lock setup consists of the reference cavity, grating, two split photodiodes and electronic circuits to generate the error signals.

A beam splitter is used before the double cavity design, to divide the input beam into two beams. The output signal of the gas sample cavity is monitored by a fast photodiode, obtained by an acquisition card, and processed by a labview program. The steering mirror M_{10} is slightly tilted to misalign the input beam to couple light into a nonresonant reference cavity TEM_{10} mode, which directly reflects off from the input cavity mirror. The signal reflected from the input reference cavity is directed to a grating by a pick-off-window. This grating disperses the laser light to enable two split photodiodes to monitor two different parts of the laser spectrum. Two error signals are generated and contain a mixture of the two laser parameters f_{rep}, f_0. Two PID controllers [81] are needed to electronically process the signal errors to generate two independent bias voltages, and send them to the double piezo setup to control both f_{rep} and f_0. This double piezo setup is described in below.

4.4.3.1. Double piezo setup

We want to design a mechanical system that provides at the same time, tilt and translation movements with high speed (resonance frequency > 100 kHz). At the beginning, a single PZT system is made, and its speed is tested, and then the double piezo system is designed and tested. The mechanical system consists of two identical PZT mounted on the end mirror in the sequence prism arm as shown in the upper part of Figure 4.13. It provides a translation movement to control f_{rep}, when the two PZT are activated together or a tip/tilt movement to control f_0, when one of them is activated. As the noise frequency of ML Ti: Sa laser (in free running regime) is in the range of 100 kHz, the resonance frequency of the mechanical setup, used to move the end mirror, should have a resonance frequency higher than 100 kHz. It is possible to use the differentially-driven PZT to provide the tilt movement, but the bandwidth of the system is usually limited to few kHz. Here, the deployed PZT (P-010.00P, ϕ=10 mm, H=8 mm, from PI France S.A.S) has several important features: the operating voltage ranges from 0 to 1000 V, long lifetime without performance loss, displacement of 5 µm (for 1000 volts), low electrical capacitance, integrated sensor to measure the PZT displacement , extreme reliability $>10^9$ cycles. But the most important feature is its high resonance frequency of about 129 kHz, when it is unloaded and both sides are not clamped. Indeed, the resonance frequency value is halved if clamped at one side. Therefore, to benefit from this high frequency value, the PZT is fixed at its lower half by three metallic screws with plastic heads, keeping both sides free. Firstly, we realized a mechanical mount for a single PZT to test the resonance frequency, as shown in Figure 4.14. Then, we realized the double PZT setup as shown in Figure 4.15.

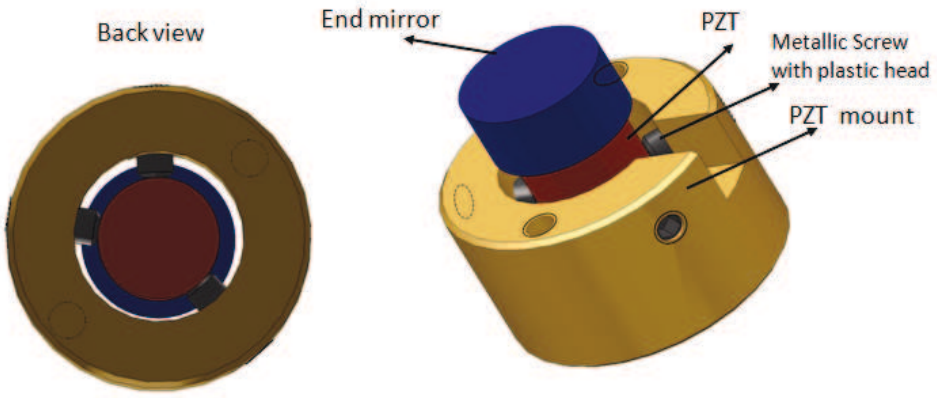

Figure 4.14: Mount of single piezo with a mirror, the piezo end sides are free.

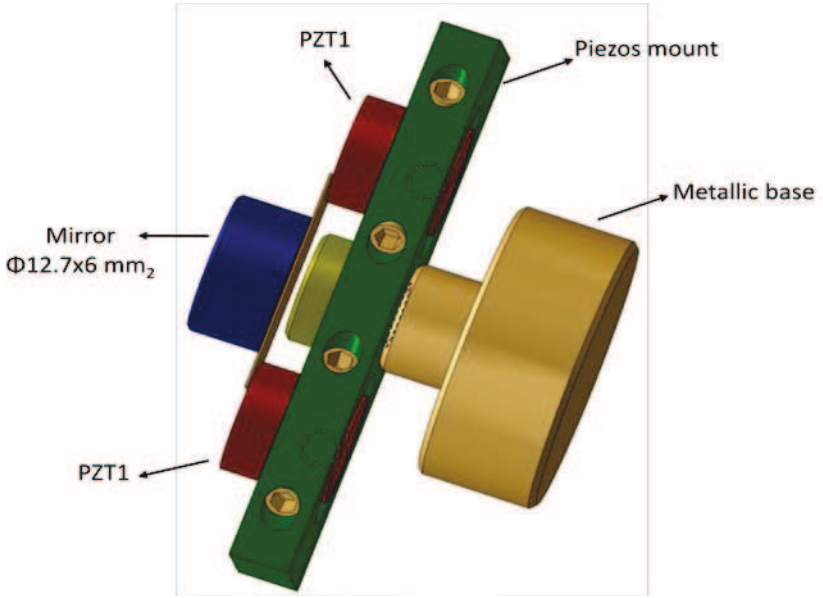

Figure 4.15: Double piezo setup to provide a translation and tip/tilt movements. The end sides of each piezo are unclamped.

4.4.3.2. Characterization of a Piezo by a Michelson interferometer

We use a Michelson interferometer to determine the resonance frequency for the single piezo (Figure 4.14) and for the double piezo (Figure 4.15) configurations, whereas each configuration is loaded with the operating mirror M_4. Generally, this optical technique is used for displacement measurements with micrometer or even nanometer resolution, and it is preferred because of its simplicity, its high resolution, and sensitivity. The interferometer setup is illustrated in Figure 4.16.

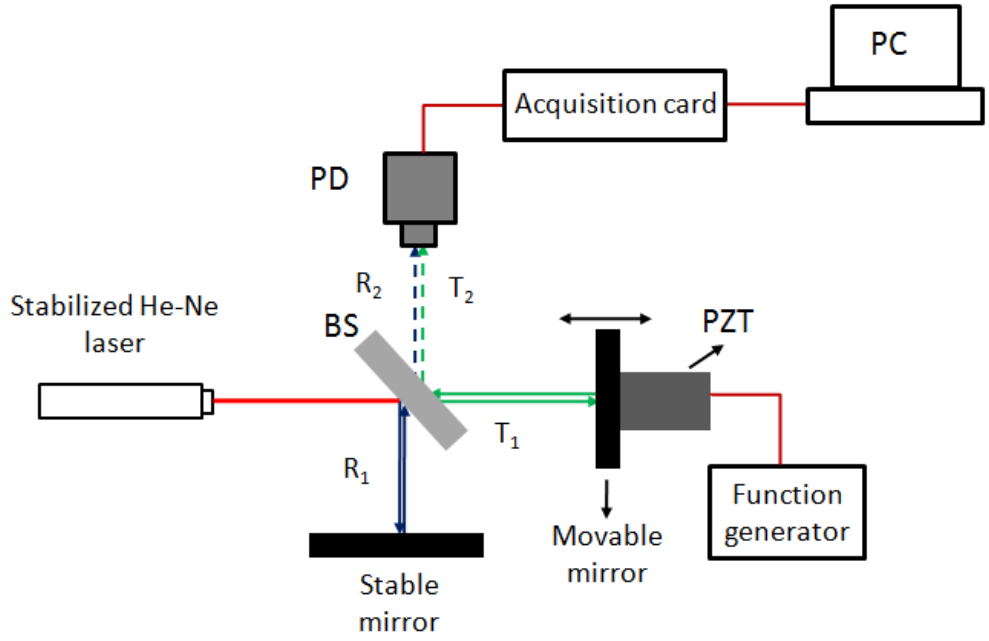

Figure 4.16: Experimental setup of the Michelson interferometer. BS: Beam splitter, PZT: Piezo electric transducer. The blue line represents the beam R_1 reflected on the beam splitter, whereas the green line is the transmitted beam T_1.

By changing the extension of the piezo through the applied input voltage, the optical path changes results in changing the intensity of the interference fringes that are produced on the PD. As a result, the light intensity on the photodiode changes from maximum (light fringe) to minimum (dark fringe) and produces a current which is converted to voltage. This output voltage signal is acquired by the National Instruments acquisition card (16 bits, 1 MHz sampling rate), and is processed on a PC.

Figure 4.17 presents the interference intensity (in red), and the signal of the photodiode (in blue) that is proportional to the interference intensity.

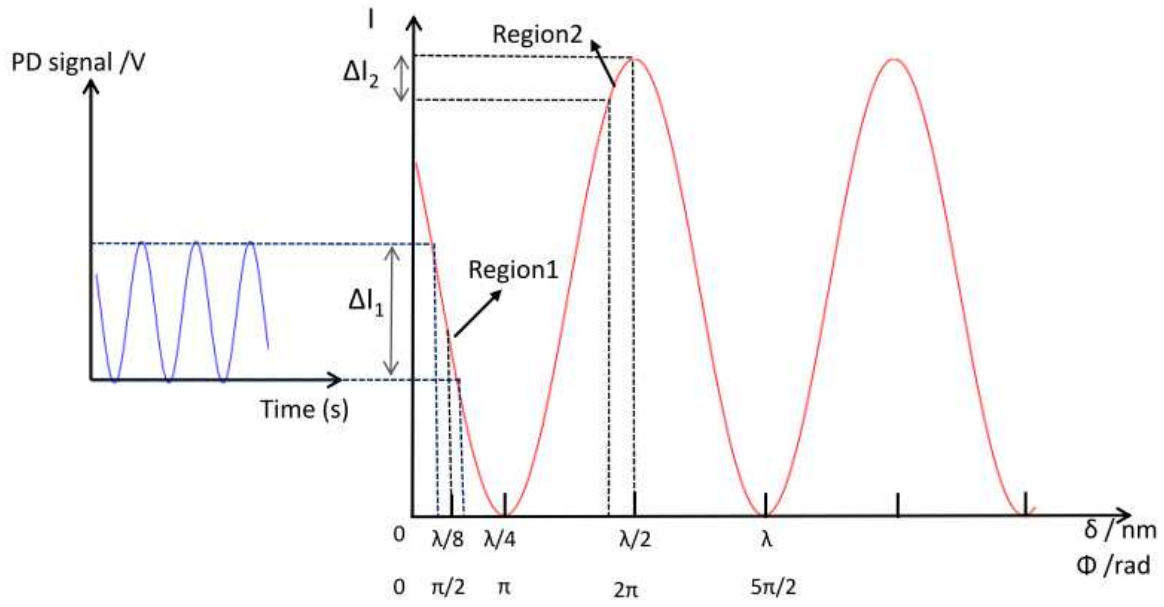

Figure 4.17: In red, Transfer function of intensity interference. In blue: PD signal which follows the intensity interference pattern. Region1: Displacement around λ/8, where the light intensity variation (ΔI_1) is a maximum. Region2: Displacement around λ/2, where the intensity variation (ΔI_2) takes its minimum.

To ensure that generated displacements will remain in a linear region, the piezo is excited with a voltage whose amplitude does not exceed 30 V. Additionally, Figure 4.17 shows displacement value close to λ/2 (region2), where the variation takes its minimum. It is possible to have a minimum intensity variation around λ /4, but we display the displacement around λ /2 for better illustration. We should underline that by changing the bias voltage (V_B) applied to the piezo, it is possible to move from the region1 to region2.

In the following measurements, the PD signal is acquired when the sensitivity is a maximum (region1), and to do this, the V_B value is kept around 15 volt, and the amplitude of the sinusoidal modulation signal (V_{AC}) is about 2 volts. To determine the resonance frequency of the piezo, V_B and V_{AC} are kept constant but the frequency of the modulation signals changes between 0 and 200 KHz. Before the resonance frequency, the amplitude of the piezo deflection does not change, thus the PD signal remain constant (oscillations amplitude is constant). When the resonance approaches, the piezo deflection increases which results in increasing the PD signal to reach its maximum value. After the resonance, the piezo deflection come back to its initial value as the voltages V_B and V_{AC} remain constants. The experimental result of testing the single piezo setup is shown in Figure 4.18. The corresponding resonance frequency is about 122 kHz which is close to the nominal value (129 kHz) for unloaded single PZT, and when both sides are unclamped. The small difference is due to the mass of the mirror (weight=0.2 g) which is small compared to the mass of the PZT (weight = 9 g).

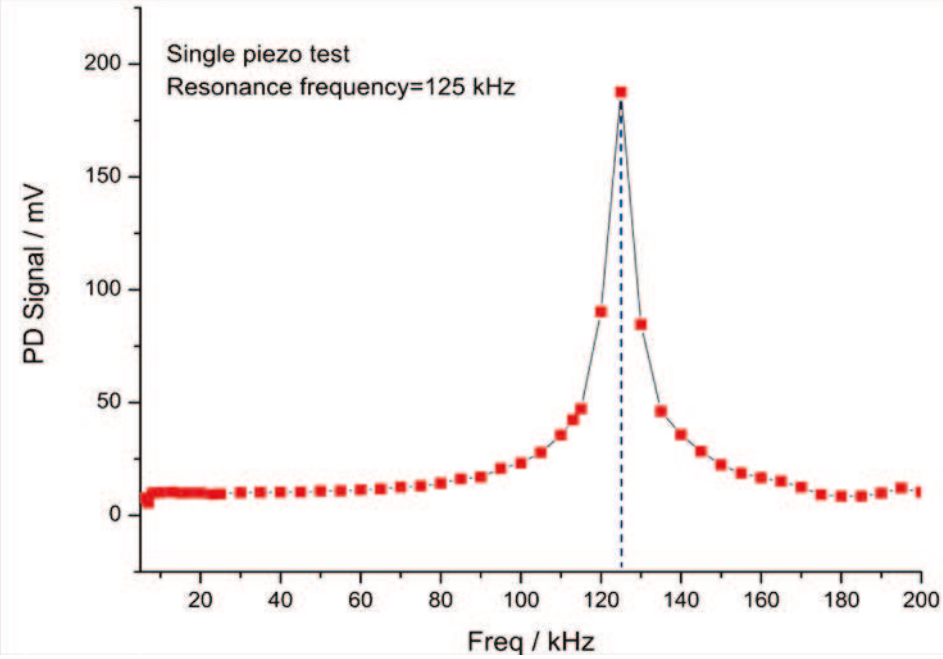

Figure 4.18: Resonance frequency of single piezo setup, red points are experimental measurements.

The double piezo setup is tested in the same way and the experimental result is shown in Figure 4.19. The corresponding resonance frequency is about 122 kHz.

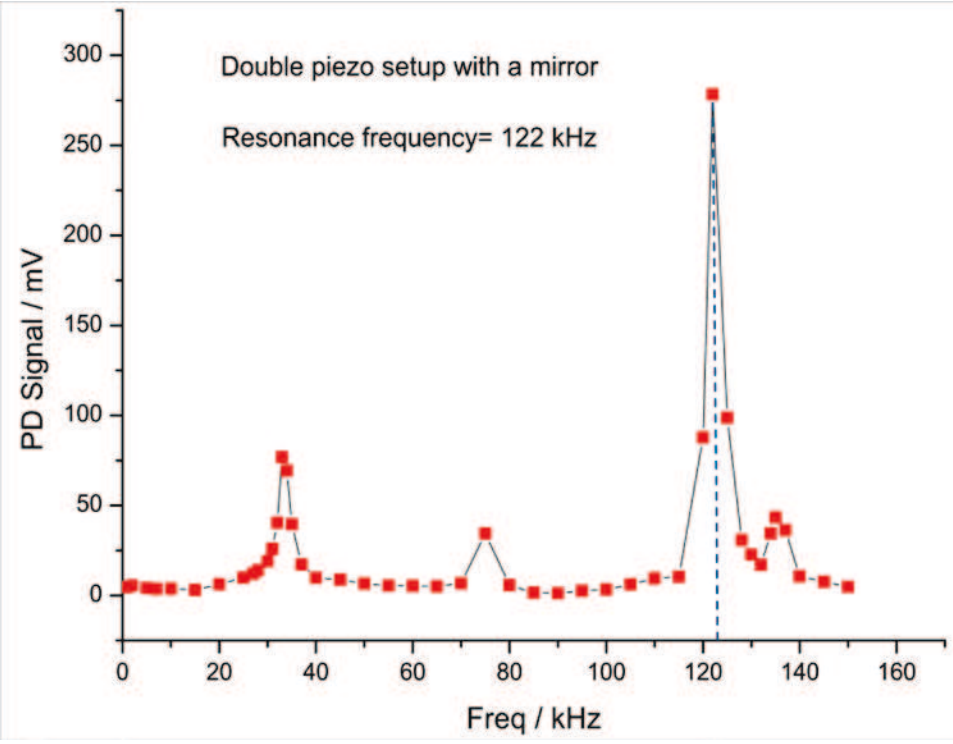

Figure 4.19: Resonance frequency of double piezo setup, red points are experimental measurements.

By this interference setup, we can also measure the tilt angle to be around 0.5 mrad at voltage value of about 100 volts.

In summary, the main resonance frequency of our double piezo setup is higher than the maximum frequency of the phase noise in mode locked Ti:Sa lasers which is known in literature to be around 100 kHz in free running regime.

4.4.3.3. Principle of the tilt lock technique

This technique exploits the interference between the fundamental cavity mode TEM_{00} and a nonresonant higher order spatial mode reflected from the input cavity mirror, to derive an error signal. The spatial transverse electromagnetic (TEM) modes of the cavity can be described by the Hermite–Gauss functions [12]. In general, tilt locking uses the higher order nonresonant TEM_{10} mode as a phase reference for the fundamental TEM_{00} cavity mode. The transverse electric field distributions of these modes are shown in Figure 4.20.a. The two modes are directed onto a two-element split detector which is positioned so that each lobe of the TEM_{10} mode is separately detected on each half of the detector as shown in Figure 4.20.b. The error signal is given by the subtraction of the photocurrent of the two halves of the split detector.

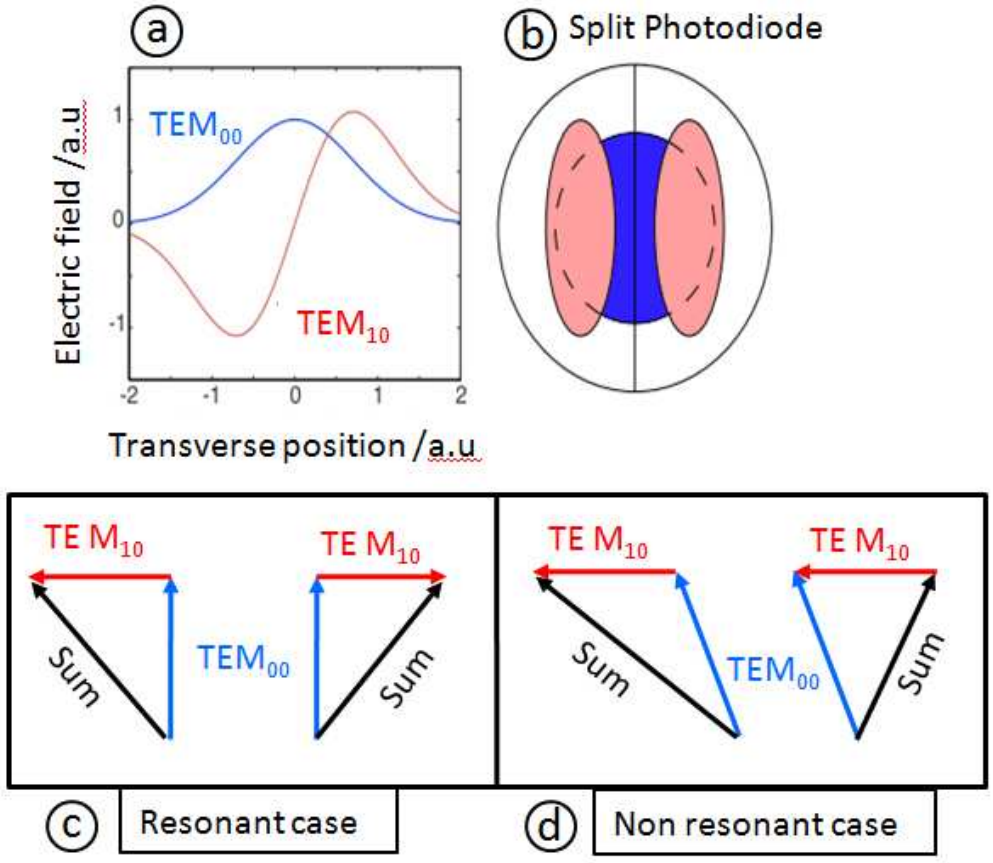

Figure 4.20: (a) TEM_{00} and TEM_{10} transverse electric field amplitude. (b) Intensity distribution of TEM_{00} (blue circle) and TEM_{01} (pink ellipses) on the split photodiode [43]. (c) Vector summation of electric fields on both diode halves with TEM_{00} on resonance and (d) slightly off resonance.

First, the laser beam is aligned and mode matched to the TEM_{00} cavity mode. Later, a small input misalignment will couple light into a non-resonant cavity TEM_{10} mode, which directly reflects off from the input cavity mirror. The input beam is misaligned by tilting a steering mirror in front of the reference cavity. The TEM_{10} mode has a $-\pi/2$ phase shift on one side and a $\pi/2$ phase shift on the other, relative to the TEM_{00} mode. When the TEM_{00} mode is exactly resonant in the cavity, it reflects off the cavity without any phase shift. The lower window of Figure 4.20 illustrates the diagram of the electric field vectors of the TEM_{00} and TEM_{10} modes on the two halves of the photodiode. The summation of the two relevant field vectors is important because the power is proportional to the square of the sum vector. In the case of the resonance, the TEM_{10} adds to the TEM_{00} on both sides of the PD, and each side monitors the same power. Thus, the error signal, obtained by subtracting the photocurrents from the two halves of the PD, is zero. When the TEM_{00} mode is slightly out of resonance with the cavity it acquires an equal phase shift in both photodiode halves as shown in Figure 4.20.d, while the nonresonant TEM_{10} mode remains unchanged, because it does not enter inside the reference cavity. As the TEM_{10} has opposite phase shift on both sides of the PD, the sum vector is different at those sides, yielding different power in each PD half. The electronically subtracted photocurrent is no longer zero and gives an error signal proportional to the phase shift.

4.4.3.3.1. Realization of the tilt lock technique and the cavities design

As the final aim is to make the Vernier effect measurement with a stabilized laser, we designed two cavities. One cavity with a low finesse (F=626) is used as a reference cavity to stabilize the laser, and the other cavity with a high finesse (10470) is used to detect the gas sample with the Vernier effect technique. The length of each cavity (L=62.4 cm) is the same which yields a cavity free spectral range three times the laser repetition rate. We shorten each cavity length to make the configuration compact and less sensitive to ambient vibrations. In addition, the mirror mounts are built in a way that requires only initial alignment. It then is possible to remove the mirrors for cleaning, and restore them without realignment. The tilt lock technique was tested, at this preliminary stage, only with the low finesse cavity. Because it is easier to start by low finesse for the alignment and for the locking process that the slope of the error signals depends strongly on the cavity finesse or on the mirrors reflectivity.

The error signal was obtained by using one split photodiode and a home-made electronic circuit to subtract the photocurrent of the two halves of the split PD and convert the difference to a voltage. The locking process didn't reach the final stage to control the laser parameters (f_{rep}, f_0) because the lack of time.

4.5. Conclusion and Perspectives

We presented a new technique of frequency comb spectroscopy whose potential performance depends on the optical properties of the mode-locked lasers, and that of the high finesse optical cavity. This technique provides large bandwidth, high sensitivity detection and a high spectral resolution as well as a rapid acquisition time. In the near future, the locking process will be completed to stabilize the laser source which permits to exploit the potential of this technique.

In perspectives, when the laser source will be stabilized, it will be possible to use more than one photodiode detector or a CCD. In this case, we will overcome the overlap problem which limits the deviated distance from the MP position, and hence limits the resolution. By using m detectors, it will be possible to get m beating peaks inside the laser bandwidth (the separation between two peaks is no longer limited by the laser bandwidth), and each peak will scan a part of the laser spectrum which enhances the resolution by a factor of m. For example, by using a cavity finesse of 10000, and only 4 photodiodes, to probe a laser bandwidth of 40 nm, we can get 40 000 spectral elements, to reach a spectral resolution of 1 pm, during less than 1 ms of acquisition time which is promising.

General conclusion and perspectives

In this thesis, we presented a compact, robust and transportable UV spectrometer exploiting the modelocked cavity enhanced absorption spectroscopy (ML-CEAS) technique to measure pptv and sub-pptv levels of atmospherically important halogen oxide radicals. Experimental measurements on trace gas detection were made, in the laboratory and in the field campaigns. It is remarkable that the performance of the instrument indoors and outdoors are identical, leading to the same stability results as well as the same detection limits.

Thanks to the double-cavity setup, alternative measurements of BrO and IO at 338.5 nm and 436 nm, respectively, are possible. The minimum absorption coefficients are $1.6 \times 10^{-10} cm^{-1} Hz^{-1/2}$ and $1.3 \times 10^{-11} cm^{-1} Hz^{-1/2}$ per spectral element, respectively. Due to the broad-band character of the instrument, H_2CO and NO_2 could also be measured together with the halogen oxides which were the principal target species of this development. This compact and robust instrument is suitable for *in situ* measurements of local concentrations of BrO/H_2CO and IO/NO_2, providing detection limits of 1 pptv (1 min), 96 ppt (1 min), 20 ppqv (5 min) and 3 pptv (5 min), respectively. The IO detection level of 20 ppqv in 5 min of acquisition is, to our knowledge, the best published result.

The large tunability of the system would allow to measure in the pptv range, other environmental important species such as OClO, HONO, OBrO, OIO, SO_2, etc., for which absorption cross sections in the near UV-visible are available in literature. Moreover, by frequency tripling the fundamental radiation, probing the strong rotational transitions of the OH radical at 308 nm is possible. The expected detection limit of 20 ppqv can be achieved, leading to sensitivity down to 10^5 radicals/cm^{-3}, which would be enough to detect the OH radical in the atmosphere.

More technical development is certainly necessary to realize the full potential of this instrument and to make the system more compact, more efficient and easier to operate. In the future developments, the procedure of switching from one wavelength to another will be automatically controlled by the computer including, changing the position of the BBO crystal and the Echelle grating. As the sensitivity of the developed system is limited by the photon shot noise, we can in principle achieve a better performance on our current setup by using a CCD detector allowing shorter exposure times and/or larger well capacity. In addition, the sensitivity can be increased at least by a factor of 3 (as long as the Rayleigh scattering is not dominant) by using higher reflectivity mirrors at both wavelengths, which will be commercially available in the near future. Thanks to the versatility of the instrument, applications in other domains such as industrial processes, national security or urban air quality (determination of toxic species, such as formaldehyde, NO_x, O_3) are anticipated. Furthermore, since this method is totally non-invasive and provides ultrasensitive detection

as well as rapid time measurements, interesting applications to clinical breath analysis are expected. Since the instrument has successfully completed the mission at Dumont d'Urville station in Antarctica by measuring BrO and IO, it is promising to send it to other relevant sites to contribute to field measurements of atmospheric interest. Additionally, we are motivated to use the instrument as a demonstrator in other domains mentioned before (urban air quality, medical diagnostics…), which may lead to industrialisation of the technology if a sufficiently large demand exists.

For the Vernier effect technique, I made the first demonstration in our laboratory, and I obtained preliminary results. Indeed, the achieved spectral resolution was modest, because the number of the spectral elements was limited by the laser mode width, and not by that of the cavity. In general, this technique provides a detection sensitivity enhanced by F/π like the ML-CEAS technique, and a spectral resolution given by the probed laser spectral window divided by the cavity finesse, if the laser source is stabilized. The expected resolution value can easily reach less than 1 pm. Furthermore, this technique has a simple setup compared to the ML-CEAS, where there is no need for the spectrograph. Additionally, the time required to measure one output absorption spectrum can be less than 1 ms.

The stabilization of the laser source has started and will surely continue in the future. The technique of tilt lock was deployed to lock the laser to a reference cavity. For this purpose, a reference cavity of low finesse, a double piezo setup, electronic circuits were realized. The double piezo setup was mounted on the end mirror after the prism sequence in the laser cavity, to allow a translation, and tilt movements to control both f_{rep} and f_0 of the laser comb with a response frequency higher than 100 kHz. The electronic circuits were used to generate error signals containing a mixture of information about the two laser parameters f_{rep} and f_0. A PID card was also designed to process the error signals and generate two bias voltages applied to the double piezo setup. In the near future, the laser stabilization procedure continues until the end and achieves its goal in reducing the laser mode width to be less than the cavity mode width. Then, it will be possible to increase the cavity finesse to enhance both the sensitivity and the resolution. One ambitious goal is to use several detectors instead of only one detector to increase the spectral resolution. Given that continuous improvements lie ahead, I expect the Vernier effect technique to be a powerful spectroscopic tool and to be employed more frequently in the future to respond to the needs of emerging scientific fields such as measurement of free radical kinetics in pulsed plasmas in the UV and VUV [82].

Conclusion Générale

Dans cette thèse, un spectromètre UV robuste, compacte et transportable a été construit. Il repose sur la technique ML-CEAS pour mesurer à des niveaux très faibles (pptv 1 particule sur mille milliards et même en dessous) des molécules réactives d'importance atmosphérique, en particulier, les radicaux d'oxyde d'halogènes. Des mesures expérimentales sur les détections de gaz à l'état de traces ont été faites en laboratoire et au cours de campagnes de terrain. Il est remarquable que les performances impressionnantes de l'instrument obtenues en laboratoire ont pu être reproduite à l'identique sur le terrain, conduisant aux mêmes résultats en termes de stabilité ainsi que pour la limite de détection.

Grace à la configuration de double cavité, des mesures alternatives de BrO et IO à 338.5 nm et 436 nm, respectivement, sont possibles. Les coefficients minimales d'absorption sont 1.6 × $10^{-10}$$cm^{-1}$ $Hz^{-1/2}$ et 1.3 × 10^{-11} cm^{-1} $Hz^{-1/2}$ par élément spectral, à 338.5 nm et 436 nm, respectivement. En raison du caractère large bande de l'instrument, les concentrations de H_2CO et de NO_2 peuvent également être mesurées avec les oxydes d'halogènes qui étaient les espèces cibles principales de ce projet. Cet instrument compact et robuste est adapté pour des mesures *in situ* de concentrations locales de BrO/H_2CO et IO/NO_2, offrant des limites de détection de 1 pptv (1 min), 96 ppt (1 min), 20 ppqv (5 min) et 3 pptv (5 min), respectivement. La limite de détection obtenue pour le radical IO est particulièrement impressionnante.

Par ailleurs, l'accordabilité importante du système permettrait de mesurer à des niveaux de l'ordre du pptv, d'autres espèces d'importance environnementale telle que OClO, HONO, OBrO, OIO, SO_2, etc, pour lesquels les sections efficaces d'absorption dans le proche UV-visible sont disponibles dans la littérature. De plus, par triplage de fréquence du rayonnement fondamental, il est possible d'atteindre 308 nm où se trouvent les fortes transitions rotationnelles du radical OH. La limite de détection prévue est de 20 ppqv, ce qui correspond à, concentration de 10^5 radical/cm^{-3}. Cette limite de détection est suffisante pour détecter le radical OH dans l'atmosphère en Antarctique.

Des développements techniques sont nécessaires pour aboutir au plein potentiel de cet instrument et rendre le système encore plus compact, plus performant et plus facile à utiliser. Un exemple d'évolution future est l'automatisation de la procédure qui permet de contrôler la position de crystal BBO et de changer en parallèle, la position du réseau utilisé dans le spectromètre. On pourrait ainsi passer de la mesure de BrO et du formaldéhyde à la mesure de IO et de NO_2 en quelques minutes.
Par ailleurs, comme la sensibilité du système est limitée par le bruit de photons, on peut en principe améliorer la sensibilité en utilisant un détecteur CCD permettant des temps d'exposition plus courts et/ou ayant des puits de plus grande capacité. La sensibilité peut

être aussi augmentée à l'aide de miroirs plus réfléchissants aux deux longueurs d'onde (338.5 nm, 436 nm). De tels miroirs devraient être disponibles dans le commerce dans un avenir proche. On peut ainsi espérer gagner jusqu'à un facteur 3 sur les limites de sensibilité. Grace à la versatilité de l'instrument, des applications dans d'autres domaines, tels que les procédés industriels, la sécurité nationale ou le contrôle de la qualité de l'air urbain (détermination des espèces toxiques, comme le formaldéhyde, NO_x, O_3) sont possible.

Puisque cette méthode est totalement non invasive et permet une détection ultrasensible et des mesures en temps rapides, des applications intéressantes à l'analyse d'air expiré pour un diagnostic médical ont été envisagées par cette technique. Comme l'instrument a été déployé avec succès à Dumont d'Urville, une station de mesures en Antarctique, il est prévu d'utiliser à nouveau l'instrument dans d'autres sites de mesures, afin d'améliorer nos connaissances et les modèles de chimie atmosphérique. Par ailleurs, il est probable que nous utiliserons à l'avenir notre instrument en tant que démonstrateur dans d'autres domaines de la physique mentionnés précédemment (qualité de l'air en milieu urbain, diagnostic médical ...), ce qui peut conduire à une industrialisation de la technologie si une demande suffisante existe.

En ce qui concerne l'effet Vernier, j'en ai réalisé la première démonstration dans notre laboratoire, et j'ai obtenu des résultats préliminaires prometteurs. Certes, la résolution spectrale obtenue est modeste, car elle était limitée par la largeur des modes du laser et non par la largeur des modes de la cavité, cependant le principe a pu être démontré. En général, cette technique fournit une sensibilité de détection accrue par F/π comme la technique ML-CEAS, et la résolution spectrale est donnée par la fenêtre spectrale du laser divisée par la finesse de la cavité. Pour se faire, il est nécessaire de stabiliser le laser de manière à ce que largeur des modes deviennent inférieures à la largeur des modes de la cavité. On devrait en pratique obtenir des résolutions meilleurs que 1 pm sur des fenêtres spectrales de plus de 30 nm, ce qui correspond à plus de 30 000 éléments spectraux. En outre, cette technique présente une configuration simplifiée par rapport à la ML-CEAS, vu que le spectrographe est alors supprimé. De plus, le temps nécessaire à l'enregistrement d'un spectre d'absorption peut être inférieur à 1 ms.

De grands efforts ont été déployés pour stabiliser la source laser. La technique de tilt-lock a été utilisée pour verrouiller le laser à une cavité de référence. A cet effet, une cavité de référence de faible finesse a été conçue ainsi qu'une configuration à double piezo et les circuits électroniques de contrôle. La configuration à double Piezo a été monté sur le miroir après la séquence de prisme dans la cavité laser, pour permettre les mouvements de translation et d'inclinaison pour contrôler à la fois f_{rep} et f_0 du laser avec une réponse fréquentielle pouvant aller jusqu'à 100 kHz. Les circuits électroniques ont été utilisés pour générer des signaux d'erreur contenant un mélange d'informations sur les deux paramètres du laser f_{rep} et f_0. Une carte « PID » est également conçu pour recevoir les signaux d'erreur

et générer deux tensions continues appliquées à la configuration de double piézo. J'espère que dans un proche avenir, la procédure de stabilisation du laser sera effective et atteindra son but, c'est-à-dire de réduire la largeur de mode laser pour être inférieure à la largeur de celle de la cavité. Ensuite, il sera possible d'augmenter la finesse de la cavité afin d'améliorer à la fois la sensibilité et la résolution. Un objectif ambitieux est d'utiliser plusieurs détecteurs au lieu d'un seul détecteur pour augmenter la résolution spectrale. Étant donné qu'un grand nombre d'améliorations sont encore possible, je m'attends à ce que cette technique utilisant un effet Vernier puisse être un puissant outil spectroscopique et être utilisé plus fréquemment à l'avenir pour répondre aux besoins des nouveaux domaines scientifiques tels que la mesure de la cinétique de radicaux libres dans les plasmas pulsés dans l'UV et VUV [82].

References

[1] R. L. Mauldin, III, F. L. Eisele, D. J. Tanner, E. Kosciuch, R. Shetter, B. Lefer, S. R. Hall, J. B. Nowak, M. Buhr, G. Chen, P. Wang, and D. Davis, "Measurements of OH, H2SO4, and MSA at the South Pole during ISCAT," *Geophys. Res. Lett.,* vol. 28, pp. 3629-3632, 2001.

[2] H. J. Beine, F. Dominè, A. Ianniello, M. Nardino, I. Allegrini, K. Teinilä, and R. Hillamo, "Fluxes of nitrates between snow surfaces and the atmosphere in the European high Arctic," *Atmos. Chem. Phys.,* vol. 3, pp. 335-346, 2003.

[3] T. Gherman and D. Romanini, "Modelocked Cavity-Enhanced Absorption Spectroscopy," *Opt. Express,* vol. 10, pp. 1033-1042, 2002.

[4] T. Gherman, S. Kassi, A. Campargue, and D. Romanini, "Overtone spectroscopy in the blue region by cavity-enhanced absorption spectroscopy with a mode-locked femtosecond laser: application to acetylene," *Chemical Physics Letters,* vol. 383, pp. 353-358, 2004.

[5] K. A. Read, Lewis, A. C., Bauguitte, S., Rankin, A. M., Salmon, R. A., Wolff, E. W., Saiz-Lopez, A., Bloss, W. J., Heard, D. E., Lee, J. D., and Plane, J. M. C., "DMS and MSA measurements in the Antarctic boundary layer: impact of BrO on MSA production," *Atmos. Chem. Phys.Discuss,* vol. 8, pp. 2657– 2694, 2008.

[6] S. Preunkert, B. Jourdain, M. Legrand, R. Udisti, S. Becagli, and O. Cerri, "Seasonality of sulfur species (dimethyl sulfide, sulfate, and methanesulfonate) in Antarctica: Inland versus coastal regions," *J. Geophys. Res.,* vol. 113, p. D15302, 2008.

[7] R. Holzwarth, T. Udem, T. W. Hänsch, J. C. Knight, W. J. Wadsworth, and P. S. J. Russell, "Optical Frequency Synthesizer for Precision Spectroscopy," *Physical Review Letters,* vol. 85, pp. 2264-2267, 2000.

[8] D. Romanini, A. A. Kachanov, N. Sadeghi, and F. Stoeckel, "CW cavity ring down spectroscopy," *Chemical Physics Letters,* vol. 264, pp. 316-322, 1997.

[9] C. Gohle, B. Stein, A. Schliesser, T. Udem, and T. W. Hänsch, "Frequency Comb Vernier Spectroscopy for Broadband, High-Resolution, High-Sensitivity Absorption and Dispersion Spectra," *Physical Review Letters,* vol. 99, p. 263902, 2007.

[10] J. Barbara J. Finlayson-Pitts James N. Pitts, *Chemistry of the upper and lower atmosphere*. London: Academic press, 1999.

[11] D. E. Spence, P. N. Kean, and W. Sibbett, "60-fsec pulse generation from a self-mode-locked Ti:sapphire laser," *Opt. Lett.,* vol. 16, pp. 42-44, 1991.

[12] A. E. Siegman, *Lasers*. Mill Valley, Calif.: University Science Books, 1986.

[13] U. Keller, "2.1 Ultrafast solid-state lasers," in *2 Short and ultrashort pulse generation*. vol. 11, G. Herziger, H. Weber, and R. Poprawe, Eds., ed: Springer-Verlag, 2007.

[14] W. F. Liu, P. S. J. Russell, and L. Dong, "Acousto-optic superlattice modulator using a fiber Bragg grating," *Opt. Lett.,* vol. 22, pp. 1515-1517, 1997.

[15] R. del Coso and J. Solis, "Relation between nonlinear refractive index and third-order susceptibility in absorbing media," *J. Opt. Soc. Am. B,* vol. 21, pp. 640-644, 2004.

[16] U. Keller, D. A. B. Miller, G. D. Boyd, T. H. Chiu, J. F. Ferguson, and M. T. Asom, "Solid-state low-loss intracavity saturable absorber for Nd:YLF lasers: an antiresonant semiconductor Fabry?Perot saturable absorber," *Opt. Lett.,* vol. 17, pp. 505-507, 1992.

[17] J.-y. Zhang, J. Y. Huang, H. Wang, K. S. Wong, and G. K. Wong, "Second-harmonic generation from regeneratively amplified femtosecond laser pulses in BBO and LBO crystals," *J. Opt. Soc. Am. B,* vol. 15, pp. 200-209, 1998.

[18] T. Udem, J. Reichert, R. Holzwarth, and T. W. Hänsch, "Accurate measurement of large optical frequency differences with a mode-locked laser," *Opt. Lett.,* vol. 24, pp. 881-883, 1999.

[19] S. T. Cundiff, J. Ye, and J. L. Hall, "Optical frequency synthesis based on mode-locked lasers," *Review of Scientific Instruments,* vol. 72, pp. 3749-3771, 2001.

[20] J. Willits, J. K. Wahlstrand, C. R. Menyuk, and S. T. Cundiff, "The quantum-limited comb lineshape for a mode-locked Ti:Sapphire laser," in *Precision Electromagnetic Measurements Digest, 2008. CPEM 2008. Conference on*, 2008, pp. 170-171.

[21] J. Y. a. S. T. Cundiff, *Femtosecond Optical Frequency Comb: Principle, Operation, and Applications,* : Kluwer Academic Publishers / Springer Norwell, MA 2004.

[22] L. Xu, C. Spielmann, A. Poppe, T. Brabec, F. Krausz, and T. W. Hänsch, "Route to phase control of ultrashort light pulses," *Opt. Lett.,* vol. 21, pp. 2008-2010, 1996.

[23] G. S. F. W. Helbing, J. Stenger, H. R. Telle, U. Keller, "Carrier-envelope offset dynamics and stabilization of femtosecond pulses," *Appl. Phys. B,* vol. 74, pp. S35-S42, 2002.

[24] K. W. Holman, R. J. Jones, A. Marian, S. T. Cundiff, and J. Ye, "Intensity-related dynamics of femtosecond frequency combs," *Opt. Lett.,* vol. 28, pp. 851-853, 2003.

[25] V. G. Dmitriev, G. G. Gurzadyan, and D. N. Nikogosyan, *Handbook of Nonlinear Optical Crystals*. New York, 1999.

[26] J.-C. D. W. RUDOLPH, *Ultrashort Laser Pulse Phenomena Fundamentals, Techniques, and Applications on a Femtosecond Time* Second Edition ed.: Elsevier Inc, 2006.

[27] A. Saiz-Lopez, A. S. Mahajan, R. A. Salmon, S. J.-B. Bauguitte, A. E. Jones, H. K. Roscoe, and J. M. C. Plane, "Boundary Layer Halogens in Coastal Antarctica," *Science,* vol. 317, pp. 348-351, July 20, 2007.

[28] L. A. Barrie, J. W. Bottenheim, R. C. Schnell, P. J. Crutzen, and R. A. Rasmussen, "Ozone destruction and photochemical reactions at polar sunrise in the lower Arctic atmosphere," *Nature,* vol. 334, pp. 138-141, 1988.

[29] S. E. Lindberg, S.B. Brooks, C-J. Lin, K. J. Scott, M. S. Landis, R. K. Stevens, M. Goodsite, and A. Richter, "Dynamic Oxidation of Gaseous Mercury in the Arctic Troposphere at Polar Sunrise," *Environ. Sci. Technol,* vol. 36, pp. 1245-1256, 2002.

[30] L. Whalley, K. Furneaux, T. Gravestock, H. Atkinson, C. Bale, T. Ingham, W. Bloss, and D. Heard, "Detection of iodine monoxide radicals in the marine boundary layer using laser induced fluorescence spectroscopy," *Journal of Atmospheric Chemistry,* vol. 58, pp. 19-39, 2007.

[31] M. S. B. Munson and F. H. Field, "Chemical Ionization Mass Spectrometry. I. General Introduction," *Journal of the American Chemical Society,* vol. 88, pp. 2621-2630, 1966/06/01 1966.

[32] J. Liao, H. Sihler, L. G. Huey, J. A. Neuman, D. J. Tanner, U. Friess, U. Platt, F. M. Flocke, J. J. Orlando, P. B. Shepson, H. J. Beine, A. J. Weinheimer, S. J. Sjostedt, J. B. Nowak, D. J. Knapp, R. M. Staebler, W. Zheng, R. Sander, S. R. Hall, and K. Ullmann, "A comparison of Arctic BrO measurements by chemical ionization mass spectrometry and long path-differential optical absorption spectroscopy," *J. Geophys. Res.,* vol. 116, p. D00R02, 2011.

[33] G. Hönninger and U. Platt, "Observations of BrO and its vertical distribution during surface ozone depletion at Alert," *Atmospheric Environment,* vol. 36, pp. 2481-2489, 2002.

[34] J. B. Burkholder, Curtius, J., Ravishankara, A. R., and Lovejoy, E. R, " Laboratory studies of the homogeneous nucleation of iodine oxides," *Atmos. Chem. Phys.,* vol. 4, pp. 19-34, 2004.

[35] R. Wada, J. Beames, and A. Orr-Ewing, "Measurement of IO radical concentrations in the marine boundary layer using a cavity ring-down spectrometer," *Journal of Atmospheric Chemistry,* vol. 58, pp. 69-87, 2007.

[36] J. U. White, "Very long optical paths in air," *J. Opt. Soc. Am.,* vol. 66, pp. 411-416, 1976.

[37] D. Herriott, H. Kogelnik, and R. Kompfner, "Off-Axis Paths in Spherical Mirror Interferometers," *Appl. Opt.,* vol. 3, pp. 523-526, 1964.

[38] J. B. McManus, P. L. Kebabian, and M. S. Zahniser, "Astigmatic mirror multipass absorption cells for long-path-length spectroscopy," *Appl. Opt.,* vol. 34, pp. 3336-3348, 1995.

[39] J. P. L. a. A. Jenouvrier, "Réalisation d'une cellule d'absorption à réflexions multiples de grande dimension (longueur : 50 m)," *Rev. Phys. Appl.,* vol. 20, pp. 869-875 (1985), 1985.

[40] K. K. Lehmann and D. Romanini, "The superposition principle and cavity ring-down spectroscopy," *Journal of Chemical Physics,* vol. 105, pp. 10263-10277, Dec 1996.

[41] C. J. Hood, H. J. Kimble, and J. Ye, "Characterization of high-finesse mirrors: Loss, phase shifts, and mode structure in an optical cavity," *Physical Review A,* vol. 64, p. 033804, 2001.

[42] R. Holzwarth, M. Zimmermann, T. Udem, and T. W. Hansch, "Optical clockworks and the measurement of laser frequencies with a mode-locked frequency comb," *Quantum Electronics, IEEE Journal of,* vol. 37, pp. 1493-1501, 2001.

[43] M. J. Thorpe and J. Ye, "Cavity-enhanced direct frequency comb spectroscopy," *Applied Physics B: Lasers and Optics,* vol. 91, pp. 397-414, 2008.

[44] R. W. P. Drever, J. L. Hall, F. V. Kowalski, J. Hough, G. M. Ford, A. J. Munley, and H. Ward, "Laser phase and frequency stabilization using an optical resonator," *Applied Physics B: Lasers and Optics,* vol. 31, pp. 97-105, 1983.

[45] D. A. Shaddock, M. B. Gray, and D. E. McClelland, "Frequency locking a laser to an optical cavity by use of spatial mode interference," *Opt. Lett.,* vol. 24, pp. 1499-1501, 1999.

[46] R. B. David Kriege, *The Dobsonian Telescope: A Practical Manual for Building Large Aperture Telescopes*, Willmann-Bell ed., 1977.

[47] J. Morville, "Thèse: Injection des cavités optiques de haute finesse par laser à diode-Application à la CW-CRDS et à la détection de traces atmosphériques.," ed. Grenoble, 2001.

[48] J. Morville, D. Romanini, M. Chenevier, and A. Kachanov, "Effects of Laser Phase Noise on the Injection of a High-Finesse Cavity," *Appl. Opt.,* vol. 41, pp. 6980-6990, 2002.

[49] W. Demtröder, *Laser Spectroscopy* vol. 1: Springer-Verlag Berlin Heidelberg, 2008.

[50] R. H. Kingston, *Optical Sources, Detectors, and Systems: Fundamentals and Applications*, 1 ed.: Elsevier Inc, 1995.

[51] R. Grilli, G. Méjean, C. Abd Alrahman, I. Ventrillard, S. Kassi, and D. Romanini, "Cavity-enhanced multiplexed comb spectroscopy down to the photon shot noise," *Physical Review A,* vol. 85, p. 051804, 2012.

[52] R. Grilli, G. Méjean, S. Kassi, I. Ventrillard, C. Abd-Alrahman, E. Fasci, and D. Romanini, "Trace measurement of BrO at the ppt level by a transportable mode-locked frequency-doubled cavity-enhanced spectrometer," *Applied Physics B: Lasers and Optics,* pp. 1-8, 2011.

[53] H. K. Haugen, E. Weitz, and S. R. Leone, "Accurate quantum yields by laser gain vs absorption spectroscopy: Investigation of Br/Br* channels in photofragmentation of Br[sub 2] and IBr," *The Journal of Chemical Physics,* vol. 83, pp. 3402-3412, 1985.

[54] A. O'Keefe and D. A. G. Deacon, "Cavity ring-down optical spectrometer for absorption measurements using pulsed laser sources," *Review of Scientific Instruments,* vol. 59, pp. 2544-2551, 1988.

[55] R. R. F. S.P. Sander, D.M. Golden, M.J. Kurylo, G.K. , H. K.-R. Moortgat, P.H. Wine, A.R. Ravishankara, C.E. Kolb,, and B. J. F.-P. M.J. Molina, R.E. Huie, V.L. Orkin, "Chemical Kinetics and Photochemical Data for Use in Atmospheric Studies, Evaluation Number 15," *NASA SLASH JPL Publication,* 2006.

[56] J. P. Burrows, A. Richter, A. Dehn, B. Deters, S. Himmelmann, S. Voigt, and J. Orphal, "ATMOSPHERIC REMOTE-SENSING REFERENCE DATA FROM GOME—2. TEMPERATURE-DEPENDENT ABSORPTION CROSS SECTIONS OF O3 IN THE 231–794NM RANGE," *Journal of Quantitative Spectroscopy and Radiative Transfer,* vol. 61, pp. 509-517, 1999.

[57] S. T. W. H. Press, W. Vetterling, B. Flannery, S.Teukolsky, *Numerical Recipes in C. The Art of Scientific Computing*- 2nd Edition, Cambridge University Press, 1992.

[58] D. M. Wilmouth, T. F. Hanisco, N. M. Donahue, and J. G. Anderson, "Fourier Transform Ultraviolet Spectroscopy of the A 2Π3/2 ← X 2Π3/2 Transition of BrO†," *The Journal of Physical Chemistry A,* vol. 103, pp. 8935-8945, 1999/11/01 1999.

[59] O. C. Fleischmann, M. Hartmann, J. P. Burrows, and J. Orphal, "New ultraviolet absorption cross-sections of BrO at atmospheric temperatures measured by time-windowing Fourier transform spectroscopy," *Journal of Photochemistry and Photobiology A: Chemistry,* vol. 168, pp. 117-132, 2004.

[60] C. A. Smith, F. D. Pope, B. Cronin, C. B. Parkes, and A. J. Orr-Ewing, "Absorption Cross Sections of Formaldehyde at Wavelengths from 300 to 340 nm at 294 and 245 K," *The Journal of Physical Chemistry A,* vol. 110, pp. 11645-11653, 2006.

[61] S. M. Newman, W. H. Howie, I. C. Lane, M. R. Upson, and A. J. Orr-Ewing, "Predissociation of the A 2[capital Pi]3/2 state of IO studied by cavity ring-down spectroscopy," *Journal of the Chemical Society, Faraday Transactions,* vol. 94, pp. 2681-2688, 1998.

[62] Y. Nakano, S. Enami, S. Nakamichi, S. Aloisio, S. Hashimoto, and M. Kawasaki, "Temperature and Pressure Dependence Study of the Reaction of IO Radicals with Dimethyl Sulfide by Cavity Ring-Down Laser Spectroscopy," *The Journal of Physical Chemistry A,* vol. 107, pp. 6381-6387, 2003.

[63] S. A. Nizkorodov, S. P. Sander, and L. R. Brown, "Temperature and Pressure Dependence of High-Resolution Air-Broadened Absorption Cross Sections of NO2 (415−525 nm)," *The Journal of Physical Chemistry A,* vol. 108, pp. 4864-4872, 2004.

[64] A. T. Young, "Revised depolarization corrections for atmospheric extinction," *Appl. Opt.,* vol. 19, pp. 3427-3428, 1980.

[65] V. A. K. W. E. EICHINGER, *ELASTIC LIDAR, Theory, Practice, and Analysis Methods*. New Jersey: John Wiley & Sons, Inc, 2004.

[66] P. Werle, "Accuracy and precision of laser spectrometers for trace gas sensing in the presence of optical fringes and atmospheric turbulence," *Applied Physics B: Lasers and Optics,* vol. 102, pp. 313-329, 2011.

[67] S. M. Ball, A. M. Hollingsworth, J. Humbles, C. Leblanc, P. Potin, and G. McFiggans, "Spectroscopic studies of molecular iodine emitted into the gas phase by seaweed," *Atmos. Chem. Phys.,* vol. 10, pp. 6237-6254, 2010.

[68] R. Vogt, R. Sander, R. von Glasow, and P. J. Crutzen, "Iodine Chemistry and its Role in Halogen Activation and Ozone Loss in the Marine Boundary Layer: A Model Study," *Journal of Atmospheric Chemistry,* vol. 32, pp. 375-395, 1999.

[69] A. S. Mahajan, H. Oetjen, J. D. Lee, A. Saiz-Lopez, G. B. McFiggans, and J. M. C. Plane, "High bromine oxide concentrations in the semi-polluted boundary layer," *Atmospheric Environment,* vol. 43, pp. 3811-3818, 2009.

[70] N. R. Newbury, I. Coddington, and W. Swann, "Sensitivity of coherent dual-comb spectroscopy," *Opt. Express,* vol. 18, pp. 7929-7945, 2010.

[71] M. Shirasaki, "Large angular dispersion by a virtually imaged phased array and its application to a wavelength demultiplexer," *Opt. Lett.,* vol. 21, pp. 366-368, 1996.

[72] F. Adler, M. J. Thorpe, K. C. Cossel, and J. Ye, "Cavity-enhanced direct frequency comb spectroscopy: technology and applications," *Annu Rev Anal Chem,* vol. 3, pp. 175-205, 2010.

[73] F. Herregodts, E. Kerrinckx, T. R. Huet, and J. V. Auwera, "Absolute line intensities in the v1 + 3v3 band of 12C2H2 by laser photoacoustic spectroscopy and Fourier transform spectroscopy," *Molecular Physics,* vol. 101, pp. 3427-3438, 2003/12/10 2003.

[74] R. Jason Jones, I. Thomann, and J. Ye, "Precision stabilization of femtosecond lasers to high-finesse optical cavities," *Physical Review A,* vol. 69, p. 051803, 2004.

[75] K. F. Kwong, D. Yankelevich, K. C. Chu, J. P. Heritage, and A. Dienes, "400-Hz mechanical scanning optical delay line," *Opt. Lett.,* vol. 18, pp. 558-560, 1993.

[76] F. W. Helbing, G. Steinmeyer, U. Keller, R. S. Windeler, J. Stenger, and H. R. Telle, "Carrier-envelope offset dynamics of mode-locked lasers," *Opt. Lett.,* vol. 27, pp. 194-196, 2002.

[77] A. Poppe, R. Holzwarth, A. Apolonski, G. Tempea, C. Spielmann, T. W. Hänsch, and F. Krausz, "Few-cycle optical waveform synthesis," *Applied Physics B: Lasers and Optics,* vol. 72, pp. 373-376, 2001.

[78] J. K. Ranka, R. S. Windeler, and A. J. Stentz, "Visible continuum generation in air-silica microstructure optical fibers with anomalous dispersion at 800 nm," *Opt. Lett.,* vol. 25, pp. 25-27, 2000.

[79] T. M. Fortier, D. J. Jones, and S. T. Cundiff, "Phase stabilization of an octave-spanning Ti:sapphire laser," *Opt. Lett.,* vol. 28, pp. 2198-2200, 2003.

[80] R. Jason Jones, J.-C. Diels, J. Jasapara, and W. Rudolph, "Stabilization of the frequency, phase, and repetition rate of an ultra-short pulse train to a Fabry–Perot reference cavity," *Optics Communications,* vol. 175, pp. 409-418, 2000.

[81] T. Hagglund, *PID Controllers: Theory, Design, and Tuning* 1995.

[82] G. Cunge, P. Bodart, M. Brihoum, F. Boulard, T. Chevolleau, and N. Sadeghi, "Measurement of free radical kinetics in pulsed plasmas by UV and VUV absorption spectroscopy and by modulated beam mass spectrometry," *Plasma Sources Science and Technology,* vol. 21, p. 024006, 2012.